



LUND UNIVERSITY

Antenna System Design for 5G and Beyond – A Modal Approach

Aliakbari Abar, Hanieh

2023

Document Version:

Publisher's PDF, also known as Version of record

[Link to publication](#)

Citation for published version (APA):

Aliakbari Abar, H. (2023). *Antenna System Design for 5G and Beyond – A Modal Approach*. [Doctoral Thesis (compilation), Communications Engineering]. Electrical and Information Technology, Lund University.

Total number of authors:

1

General rights

Unless other specific re-use rights are stated the following general rights apply:

Copyright and moral rights for the publications made accessible in the public portal are retained by the authors and/or other copyright owners and it is a condition of accessing publications that users recognise and abide by the legal requirements associated with these rights.

- Users may download and print one copy of any publication from the public portal for the purpose of private study or research.
- You may not further distribute the material or use it for any profit-making activity or commercial gain
- You may freely distribute the URL identifying the publication in the public portal

Read more about Creative commons licenses: <https://creativecommons.org/licenses/>

Take down policy

If you believe that this document breaches copyright please contact us providing details, and we will remove access to the work immediately and investigate your claim.

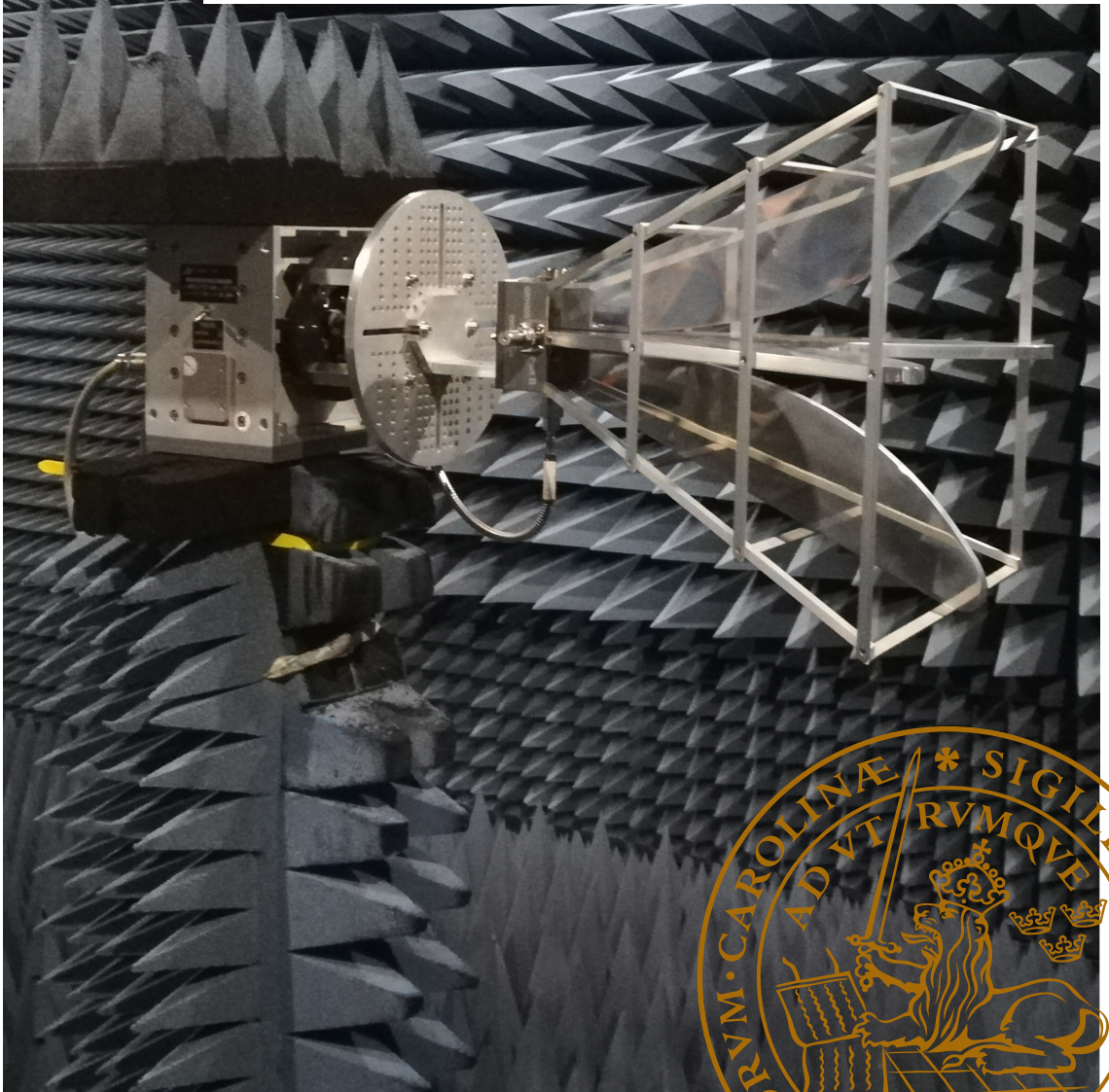
LUND UNIVERSITY

PO Box 117
221 00 Lund
+46 46-222 00 00

Antenna System Design for 5G and Beyond – A Modal Approach

HANIEH ALIAKBARI

DEPARTMENT OF ELECTRICAL AND INFORMATION TECHNOLOGY
FACULTY OF ENGINEERING | LTH | LUND UNIVERSITY



Antenna System Design for 5G and Beyond – A Modal Approach

by

Hanieh Aliakbari



LUNDS
UNIVERSITET

Doctoral Dissertation

To be presented, with the permission of the Faculty of Engineering, LTH at Lund University, for public defence in the auditorium E: 1406, E-building, Lund Institute of Technology, Ole Römers väg 3, 223 63 Lund, Sweden, Wednesday, June 14, 2023 at 9:15 am.

Faculty opponent

Prof. Yi Huang, University of Liverpool

Organization Department of Electrical and Information Technology Lund University Box 118, SE-221 00 Lund, Sweden		Document name Doctoral Dissertation	
		Date of disputation June 14, 2023	
Author Hanieh Aliakbari		Sponsoring organization	
Title and subtitle Antenna System Design for 5G and Beyond – A Modal Approach			
Abstract <p>Antennas are one of the key components that empower a new generation of wireless technologies, such as 5G and new radar systems. It has been shown that antenna design strategies based on modal theories represent a powerful systematic approach to design practical antenna systems with high performance. In this thesis, several innovative multi-antenna systems are proposed for wireless applications in different frequency bands: from sub-6 GHz to millimeter-wave (mm-wave) bands. The thesis consists of an overview (Part I) and six scientific papers published in peer-reviewed international journals (Part II). Part I provides the overall framework of the thesis work: It presents the background and motivation for the problems at hand, the fundamental modal theories utilized to address these problems, as well as subject-specific research challenges. Brief conclusions and future outlook are also provided. The included papers of Part II can be divided into two tracks with different 5G and beyond wireless applications, both aiming for higher data rates.</p> <p>In the first track, Papers [I] to [IV] investigate different aspects of antenna system design for smart-phone application. Since Long Term Evolution (LTE) (so-called 3.5G) was deployed in 2009, mobile communication systems have utilized multiple-input multiple-output antenna technology (MIMO) technology to increase the spectral efficiency of the transmission channel and provide higher data rates in existing and new sub-6 GHz bands. However, MIMO requires multi-antennas at both the base stations and the user equipment (mainly smartphones) and it is very challenging to implement sub-6 GHz multi-antennas within the limited space of smartphones. This points to the need for innovative design strategies. The theory of characteristic modes (TCM) is one type of modal theory in the antenna community, which has been shown to be a versatile tool to analyze the inherent resonance properties of an arbitrarily shaped radiating structure. Characteristic modes (CMs) have the useful property of their fields being orthogonal over both the source region and the sphere at infinity. This property makes TCM uniquely suited for electrically compact MIMO antenna design.</p> <p>In the second track, Papers [V]-[VI] investigate new integrated antenna arrays and subarrays for the two wireless applications, which are both implemented in a higher part of the mm-wave frequency range (i.e. <i>E</i>-band). Furthermore, a newly developed high resolution multi-layer “Any-Layer” PCB technology is investigated to realize antenna-in-package solutions for these mm-wave antenna system designs. High gain and high efficiency antennas are essential for high-speed wireless point-to-point communication systems. To meet these requirements, Paper [V] proposes directive multilayer substrate integrated waveguide (SIW) cavity-backed slot antenna array and subarray. As a background, the microwave community has already shown the benefits of modal theory in the design and analysis of closed structures like waveguides and cavities. Higher-order cavity modes are used in the antenna array design process to facilitate lower loss, simpler feeding network, and lower sensitivity to fabrication errors, which are favorable for <i>E</i>-band communication systems. However, waveguide/cavity modes are confined to fields within the guided media and can only help to design special types of antennas that contain those structures. As an example of the versatility of TCM, Paper [VI] shows that apart from smartphone antenna designs proposed in Papers [I]-[IV], TCM can also be used to find the desirable modes of the linear antenna arrays. Furthermore, apart from <i>E</i>-band communications, the proposed series-fed patch array topology in Paper [VI] is a good candidate for application in 79 GHz MIMO automotive radar due to its low cost, compact size, ability to suppress surface waves, as well as relatively wide impedance and flat-gain bandwidths.</p>			
Key words Millimeter-wave antennas, MIMO systems, Modal analysis, Substrate integrated waveguide antennas, Terminal antennas.			
Classification system and/or index terms (if any)			
Supplementary bibliographical information		Language English	
ISBN 978-91-8039-700-1 (print) 978-91-8039-701-8 (pdf)		ISSN 1654-790X160	
Recipient's notes		Number of pages 183	Price
		Security classification	

I, the undersigned, being the copyright owner of the abstract of the above-mentioned dissertation, hereby grant to all reference sources permission to publish and disseminate the abstract of the above-mentioned dissertation.

Signature *Hanieh Aliakbari*

Date : May 12, 2023

Antenna System Design for 5G and Beyond – A Modal Approach

Hanieh Aliakbari

Lund 2023

© Hanieh Aliakbari, 2023

“Antenna System Design for 5G and Beyond - A Modal Approach”

Published articles have been reprinted with permission
from the respective copyright holder.

Series of licentiate and doctoral theses

No. 160

ISSN 1654-790X160

ISBN 978-91-8039-700-1 (print)

ISBN 978-91-8039-701-8 (pdf)

This thesis is produced by using Microsoft Word

Printed in Sweden by *Tryckeriet i E-huset*, Lund.

Department of Electrical and Information Technology
Lund University, Box 118, SE-211 00 Lund, Sweden

*To
Hadi*

&

Hoda

"As you start to walk on the way, the way appears."

~ Rumi

Popular Science

Today's society relies more and more on the communications of various contents, especially in the form of data, with wireless communications taking the center stage. The most common form of wireless communications, mobile communications, is changing people's lives over the entire world. One example is the number of smartphone users that grows by hundreds of millions every year, many of whom do not previously have access to telephony or the many opportunities and conveniences it brings. Simultaneously, due to the popularity of bandwidth-hungry streaming video apps, the traffic generated by existing devices also increases by 30-40% annually. In addition, new wireless application areas are also emerging. For example, autonomous vehicles and drones must communicate with their surroundings to avoid collisions and other incidents. Hence, to support these different complex contents in wireless networks, higher data rates are needed.

Antenna is a critical component in wireless communications networks as it has the role of sending or receiving the aforementioned data as wireless signals over the air, which eliminates the need for wires. The wireless signals propagate through the medium or channel between the antennas at the transmitter and receiver in the form of electromagnetic waves. In this thesis, we utilize an antenna design paradigm based on modal methods to meet the antenna requirements for modern wireless systems. Basically, in modal analysis, an antenna's complex response is described by the weighted sum of multiple rather simpler responses called modes, with the modes being easier to characterize. This results in a more systematic design procedure, which is different from the traditional antenna design framework that mainly relies on intuition from past design experiences and blind numerical optimization of structural parameters.

Following the demand for ever increasing data rates, the antennas in mobile communication systems are required to provide more features and higher performance. One trend is to employ advanced multi-antenna technology to provide high data rates and link reliability. In the case of mobile communications, this means that smartphones are equipped with multi-antennas. It has been shown that, using multi-antenna technology, the achievable data rate is proportional to the number of the antenna elements, as long as the multi-antennas have "good enough" performance and the propagation environment offers many transmitter-to-receiver

paths. For multi-antennas to perform well, one important criterion is to minimize the interactions among the multi-antenna elements, and traditionally placing the antenna elements further apart would be beneficial for this purpose. However, as the physical size of an antenna is inversely related to the frequency of operation, it is rather challenging to design more than one antenna element in the limited size of a typical smartphone with low interaction, especially in lower frequency bands (i.e., sub-1GHz bands). Moreover, the smartphone multi-antennas also need to fulfill requirements relating to the physical appearance of the smartphone, such as small thickness and large display screen.

In this context, the first track of my research deals with some fundamental challenges of multi-antenna design for smartphones. My research shows how a classical modal theory can be utilized to overcome these challenges by exploring the fundamental electromagnetic properties of the smartphone's entire platform, i.e., a rectangular metal plate in its simplest form, to improve multi-antenna design. Furthermore, my research shows that, by using this modal approach, the mentioned physical constraints can even be used opportunistically to increase the number of antennas that can be fitted into the small platform while retaining good performance. My research further demonstrates the practicality of the modal approach to smartphone multi-antenna design by using it to design smartphone antennas that are robust to the influence of user hand and head.

The second trend to provide higher data rates for wireless communication is to move towards higher frequencies such as millimeter wave (mm-wave) bands in 5G due to the much larger bandwidths available in those bands than sub-6 GHz bands. However, sub-6 GHz bands will remain important for 5G and beyond systems due to significantly lower propagation loss than mm-wave bands, enabling better coverage and hence ubiquitous services. Following this trend another aspect that the first track of my PhD research investigated using modal analysis is the co-design of a smartphone antenna system that covers both the traditional cellular bands (i.e., sub-6 GHz) and a 5G mm-wave band (i.e. 28 GHz).

Continuing on the subject of 5G mm-wave antenna design, the trend has been to utilize even higher frequencies, beyond 28 GHz, due to the availability of even larger absolute frequency bandwidth. One such band of interest is the *E*-band (60-90 GHz). Apart from traditional wireless communications, a larger absolute bandwidth also enables a higher range resolution for radar/sensing applications. Furthermore, the higher frequency and hence the smaller wavelength also provides a higher angular resolution for radar/sensing applications, for the same antenna footprint. Therefore, the second track of my research investigates new concepts in integrated antennas for *E*-band wireless communications and/or radar systems using different modal theories.

Due to the high propagation loss incurred by small signal wavelength, the mm-wave antennas should be designed for high gains. Moreover, material losses such as conductor loss are much higher in *E*-band than in sub-6 GHz, which can result in antennas with low efficiencies. To overcome these challenges, high-gain multi-

antennas with high efficiency are needed. Another challenge is the fabrication cost of mm-wave antennas, which can be quite high due to the small wavelengths requiring more exotic materials and fabrication technologies. High fabrication cost can prevent mass production and successful roll-out of the mm-wave technology. Hence, in this part of the research, a new multi-layer printed-circuit board (PCB) fabrication technology is used and the main motivation for using this new technology is the high accuracy and the very low cost, which enable mass production. Several features of the new multi-layer PCB technology are exploited to facilitate performance benefits, such as lower loss, higher isolation, and larger impedance bandwidth.

Abstract

Antennas are one of the key components that empower a new generation of wireless technologies, such as 5G and new radar systems. It has been shown that antenna design strategies based on modal theories represent a powerful systematic approach to design practical antenna systems with high performance. In this thesis, several innovative multi-antenna systems are proposed for wireless applications in different frequency bands: from sub-6 GHz to millimeter-wave (mm-wave) bands. The thesis consists of an overview (Part I) and six scientific papers published in peer-reviewed international journals (Part II). Part I provides the overall framework of the thesis work: It presents the background and motivation for the problems at hand, the fundamental modal theories utilized to address these problems, as well as subject-specific research challenges. Brief conclusions and future outlook are also provided.

The included papers of Part II can be divided into two tracks with different 5G and beyond wireless applications, both aiming for higher data rates. In the first track, Papers [I] to [IV] investigate different aspects of antenna system design for smartphone application. Since Long Term Evolution (LTE) (so-called 3.5G) was deployed in 2009, mobile communication systems have utilized multiple-input multiple-output antenna technology (MIMO) technology to increase the spectral efficiency of the transmission channel and provide higher data rates in existing and new sub-6 GHz bands. However, MIMO requires multi-antennas at both the base stations and the user equipment (mainly smartphones) and it is very challenging to implement sub-6 GHz multi-antennas within the limited space of smartphones. This points to the need for innovative design strategies. The theory of characteristic modes (TCM) is one type of modal theory in the antenna community, which has been shown to be a versatile tool to analyze the inherent resonance properties of an arbitrarily shaped radiating structure. Characteristic modes (CMs) have the useful property of their fields being orthogonal over both the source region and the sphere at infinity. This property makes TCM uniquely suited for electrically compact MIMO antenna design. Moreover, as the conventional mobile chassis offers only one resonant CM in frequency bands below 1 GHz due to its small electrical size, it is even more challenging to design MIMO antennas for these bands. Therefore, the initial idea of Papers [I] to [III] is to utilize TCM to develop compact MIMO antenna systems for smartphones in frequency bands below 1 GHz. Using the CM-based

integrated antenna design concept, the chassis can be utilized as the radiator, and the conventional antenna elements can be replaced by physically smaller coupling elements, making it easier to design a compact antenna structure. As in the modal concepts utilized by the microwave community, the most valuable feature of CMs is that they are feed independent. Hence, a major challenge of using TCM for antenna design is to develop suitable feeding element(s) to excite the CMs of interest. Consequently, in this part of the thesis, the focus is on the proper excitation of the CMs of interest by an appropriate design of the feeding element(s) as well as minor alterations of the chassis structure that may be needed to first make available CMs with the desired properties to meet the requirements of the MIMO antenna.

In Paper [I], using the physical insight from TCM a step-by-step approach for the chassis' structural changes and multimode feed design is applied to simultaneously meet bandwidth and other practical requirements in a two-port MIMO antenna system. Then, in Paper [II], the smartphone's large metal screen is used to facilitate an additional uncorrelated MIMO port in a wideband tri-port design. Selective excitation technique is used, aided by the TCM, to design the feeding network. The performance under different practical situations is presented. Different from antennas for other applications which can be considered to operate in free space, the design of smartphone antennas should account for their interaction with the body of the user. To mitigate performance degradation due to user proximity, modes that are less affected by the body are found and selectively excited in Paper [III] to provide a more robust solution to user effects. Finally, Paper [IV] considers the trend of mobile communications expanding towards the higher frequencies due to the crowded radio spectrum in the existing sub-6 GHz bands. In this context, a co-designed antenna system covering both sub-6 GHz bands and a mm-wave band at 28 GHz is presented, where the mm-wave antennas that generate reconfigurable beams for beam steering are integrated in the capacitive coupling elements of the sub-6 GHz antennas. The aim was to achieve a compact and low-complexity antenna structure.

In the second track, Papers [V]-[VI] investigate new integrated antenna arrays and subarrays for the two wireless applications, which are both implemented in a higher part of the mm-wave frequency range (i.e. *E*-band). Furthermore, a newly developed high resolution multi-layer "Any-Layer" PCB technology is investigated to realize antenna-in-package solutions for these mm-wave antenna system designs.

High gain and high efficiency antennas are essential for high-speed wireless point-to-point communication systems. To meet these requirements, Paper [V] proposes directive multilayer substrate integrated waveguide (SIW) cavity-backed slot antenna array and subarray. As a background, the microwave community has already shown the benefits of modal theory in the design and analysis of closed structures like waveguides and cavities. Higher-order cavity modes are used in the antenna array design process to facilitate lower loss, simpler feeding network, and lower sensitivity to fabrication errors, which are favorable for *E*-band communication systems. However, waveguide/cavity modes are confined to fields

within the guided media and can only help to design special types of antennas that contain those structures. As an example of the versatility of TCM, Paper [VI] shows that apart from smartphone antenna designs proposed in Papers [I]-[IV], TCM can also be used to find the desirable modes of the linear antenna arrays. Furthermore, apart from *E*-band communications, the proposed series-fed patch array topology in Paper [VI] is a good candidate for application in 79 GHz MIMO automotive radar due to its low cost, compact size, ability to suppress surface waves, as well as relatively wide impedance and flat-gain bandwidths.

Preface

This doctoral thesis is comprised of two parts. The first part (Part I) gives an overview of the research field in which I have been working during the past 4 years at the Department of Electrical and Information Technology (EIT), Lund University, Sweden. The second part (Part II) contains the six included papers of my thesis work.

- [I] H. Aliakbari and B. K. Lau, “Low-profile two-port MIMO terminal antenna for low LTE bands with wideband multimodal excitation,” *IEEE Open J. Antennas Propag.*, vol. 1, pp. 368-378, Jul. 2020.
- [II] H. Aliakbari, L. Y. Nie, and B. K. Lau, “Large screen enabled tri-port MIMO handset antenna for low LTE bands” *IEEE Open J. Antennas Propag.*, vol. 2, pp. 911-920, Sep. 2021.
- [III] H. Aliakbari and B. K. Lau, “Low-band MIMO antenna for smartphones with robust performance to user interaction,” *IEEE Antennas Wireless Propag. Lett.*, vol. 20, no. 7, pp. 1195-1199, Jul. 2021.
- [IV] Q. Liang, H. Aliakbari, and B. K. Lau, “Co-designed millimeter-wave and sub-6 GHz antenna for 5G smartphones,” *IEEE Antennas Wireless Propag. Lett.*, vol. 21, no. 10, pp. 1995-1999, Jul. 2022.
- [V] H. Aliakbari, M. Mosalanejad, C. Soens, G. A. E. Vandenbosch, and B. K. Lau, “Wideband SIW-based low-cost multi-layer slot antenna array for E-Band applications,” *IEEE Trans. Compon. Packag. Manuf. Technol.*, vol. 9, no. 8, pp. 1568-1575, Aug. 2019.
- [VI] H. Aliakbari, M. Mosalanejad, C. Soens, G. A. E. Vandenbosch, and B. K. Lau, “79 GHz multilayer series-fed patch antenna array with stacked micro-via loading,” *IEEE Antennas Wireless Propag. Lett.*, vol. 21, no. 10, pp. 1990-1994, Jul. 2022.

During my Ph.D. studies, I have also contributed to the following journal and conference publications which are related to, but not considered part of, the thesis.

- [VII] I. M. Yousaf, H. Aliakbari, and B. K. Lau, “Quad-element car antenna system,” *In revision, IEEE Antennas Wireless Propag. Lett.*, Apr. 2023.
- [VIII] L. Y. Nie, B. K. Lau, S. Xiang, H. Aliakbari, B. Wang, and X. Q. Lin, “Wideband design of compact monopole-like circular patch antenna using modal analysis,” *IEEE Antennas Wireless Propag. Lett.*, vol. 20, no. 6, pp. 918-922, Jun. 2021.
- [IX] L. Y. Nie, B. K. Lau, H. Aliakbari, S. Xiang, B. Wang, and X. Q. Lin, “A low-profile wideband dual-resonance tri-port MIMO antenna,” *IEEE Trans. Antennas Propag.*, vol. 70, no. 6, pp. 4866-4871, Jun. 2022.
- [X] H. Aliakbari, A. Abdipour, A. Costanzo, D. Masotti, and V. Rizzolli, “Far-field based nonlinear optimization of millimeter-wave circularly polarized active antenna,” *IEEE Trans. Microw. Theory Techn.*, vol. 67, no. 7, pp. 2985-2997, Jul. 2019.
- [XI] H. Aliakbari and B. K. Lau, “Characteristic mode analysis of millimeter-wave series patch array,” in *Proc. IEEE Int. Symp. Antennas Propag.*, Denver, CO, Jul. 2022.
- [XII] H. Aliakbari and B. K. Lau, “On user effects of a low-profile MIMO terminal antenna with wideband multimodal excitation,” in *Proc. IEEE Int. Symp. Antennas Propag.*, Singapore, Dec. 2021.
- [XIII] H. Aliakbari and B. K. Lau, “Wideband excitation and matching of fundamental chassis mode using inductive coupling element,” in *Proc. IEEE Int. Symp. Antennas Propag.*, Montreal, Canada, Jul. 2020.
- [XIV] H. Aliakbari, Q. Liang, and B. K. Lau, “Enhanced low band MIMO terminal antenna based on selective feeding of chassis modes,” in *Proc. 14th Eur. Conf. Antennas Propag.*, Copenhagen, Denmark, Mar. 2020.
- [XV] I. Aziz, W. Liao, H. Aliakbari, and W. Simon, “Compact and low cost linear antenna array for millimeter wave automotive radar applications,” in *Proc. 14th Eur. Conf. Antennas Propag.*, Copenhagen, Denmark, Mar. 2020.

-
- [XVI] H. Aliakbari and B. K. Lau, “On modal excitation using capacitive coupling elements and matching network,” in *Proc. IEEE Int. Symp. Antennas Propag.*, Atlanta, GA, Jul. 2019.
- [XVII] H. Aliakbari and B. K. Lau, “Characteristic mode analysis of planar dipole antennas,” in *Proc. 13th Eur. Conf. Antennas Propag.*, Krakow, Poland, Apr. 2019.
- [XVIII] H. Aliakbari and B. K. Lau, “Impact of capacitive coupling element design on antenna bandwidth,” in *Proc. 12th Eur. Conf. Antennas Propag.*, London, UK, Apr. 2018.
- [XIX] Y. Chen, K. Schab, M. Capek, M. Masek, B. K. Lau, H. Aliakbari, Y. Haykir, W. J. Strydom, N. Peitzmeier, M. M. Jovicic, S. Genovesi, and F. Alessio Dicandia, “Benchmark problem definition and cross-validation for characteristic mode solvers,” in *Proc. 12th Eur. Conf. Antennas Propag.*, London, UK, Apr. 2018.

Acknowledgements

First and foremost, I would like to praise and thank God, the Almighty, who created and rules this amazing and largely undiscovered universe in which we live. I am truly grateful for His unconditional and endless love, mercy, and grace.

During the four years of my academic journey at the Department of Electrical and Information Technology (EIT) of Lund University, I experienced and learned a lot not only about research, but also about life. Time passed by in a flash, and I had the opportunity to meet many wonderful people who have left an indelible mark on my academic journey.

It is difficult to express my sincere gratitude to my advisor, Prof. Buon Kiong Lau (Vincent), for his limitless support during my journey at Lund University. Vincent, thank you for giving me an opportunity to develop and gain knowledge about the research area which I haven't had a chance to work on before coming to Sweden. Your dedicated supervision always helped me improve my work and I learned a lot from it. I will never forget your great sense of responsibility. Thank you for always listening to me, encouraging me, and guiding me throughout this journey.

I would like to thank Prof. Mats Gustafsson, my co-supervisor, for valuable advice during the earlier part of my journey at EIT. Thank you for always being open to discussions. Your positive attitude and passion for science truly inspire people around you. I am so grateful to Prof. Guy Vandenbosch at KU Leuven University in Belgium and Dr. Mohammad Mosalanejad at IMEC in Belgium for their great support, for sharing their knowledge and their access to technology and for what we accomplished together. I would like to thank the Characteristic Modes Special Interest Group (CM-SIG) for organizing a variety of meetings, seminars and training schools that had provided me with valuable knowledge and expertise in my field of research. My special thanks to Dr. Hui Li, Dr. Zachary Miers and Dr. Ivalyo Vasilev, whom unfortunately I didn't have a chance to meet personally, but the knowledge that they had left in the group during their stay at EIT provided me building blocks that helped me accelerate my research on antenna design using characteristic modes.

My gratitude also goes to the head of department as well as the administrative and technical staff at EIT. I am especially grateful to Prof. Daniel Sjöberg, Prof. Stefan Höst, Prof. Fredrik Tufvesson, Prof. Ove Edfors, Pia Bruhn, Linda Bienen, Anne Andersson, Erik Göthe, Elisabeth Nordstrom, Elisabeth Ohlsson, Erik Jonsson, Andreas Johansson and Sirvan Abdollah Poor, for their tireless support and guidance. Your continuous support had made it much easier for me to just focus on my research. I am also thankful for the technical support of Dr. Dmytro Pugachov from Sigma Connectivity.

I would also like to thank Prof. Yi Huang for taking the time to be the faculty opponent of my thesis, Prof. Gert Frolund Pedersen, Prof. Divitha Seetharamdoo, Prof. Samel Arslanagic, and Dr. Erik Bengtson for agreeing to be the grading committee members. I appreciate your willingness to review and critique my work.

I am grateful to the Swedish Research Council for providing the project grant which allowed for my research to be accomplished. Additionally, I would like to thank Ericssons forskningsstiftelse and Fysiografiska Sällskapet i Lund for the travel grants which allowed me to attend conferences and training schools.

Literally all of my current and former colleagues at EIT, especially my colleagues in the Division of Communications Engineering, should also be acknowledged. I have had the pleasure to meet, work with and get to know many amazing people – the list will be very long if I name everyone! I would like to also express my appreciation to my friends in Iran and my supervisors in Amirkabir University of Technology. I am so happy that I have had the support of all my friends and their families in Sweden, especially during the challenging time of the covid-19 pandemic. I cannot thank you enough for all the positive energy that you have given me and my family, and I cannot fully describe how valuable you are to us.

My words fail to express my overwhelming gratitude to my mother, father and brother. They love me unconditionally and support me with unwavering faith. Thank you for sacrificing everything so that I have a chance to know, to grow, to dream, and to reach for the sky.

I would like to thank my little one, Hoda, who was born in the later stage of this journey. Hoda, with you I started to discover more about my hidden abilities, which I haven't had a chance to use and develop before your birth. Thank you even for waking up during the late nights while I was writing this thesis; they reminded me that you are with me and encouraged me to work through the night.

Finally, from the bottom of my heart, I would like to say a big thank you to my wonderful husband, Hadi. Your pure love, encouragement and endless support is the main reason I stay strong in the most difficult moments. I learn from you every day. Whatever I write or say does not even get close to what you mean to me. So, I just say thank you for everything!

Hanieh Aliakbari
Lund, April 2023

List of Acronyms and Abbreviations

AoC	Antenna-on-Chip
AiP	Antenna-in-Package
ANN	Artificial Neural Network
BS	Base Station
CA	Characteristic Attribute
CCE	Capacitive Coupling Element
CM	Characteristic Mode
CTIA	Cellular Telecommunications Industry Association
ECC	Envelope Correlation Coefficient
EM	Electromagnetic
FCC	Federal Communications Commission
FDTD	Finite-Difference Time-Domain
FEM	Finite Element Method
FTBR	Front-to-Back Ratio
GA	Genetic Algorithm
HDI	High Definition Interconnect
HPBW	Half Power Beam Width
ICE	Inductive Coupling Element
IE	Integral Equation

IEEE	Institute of Electrical and Electronics Engineers
ITU	International Telecommunication Union
LCP	Liquid Crystal Polymer
LOS	Line-Of-Sight
LTCC	Low Temperature Co-fired Ceramic
LTE	Long Term Evolution
LWG	Laminated Wave Guide
MIMO	Multiple-Input Multiple-Output
MWC	Modal Weighting Coefficient
MMIC	Monolithic Microwave Integrated Circuit
MSRR	Medium and Short-Range Radar
MoM	Method of Moments
MS	Modal Significance
PCB	Printed Circuit Board
PEC	Perfect Electric Conductor
PIFA	Planar Inverted-F Antenna
RADAR	Radio Detection And Ranging
RF	Radio Frequency
RX	Receive
SISO	Single-Input Single-Output
SIW	Substrate Integrated Waveguide
SLL	Side Lobe Level
SNR	Signal-to-Noise Ratio
TCM	Theory of Characteristic Modes
TRP	Total Radiated Power
TX	Transmit
UMTS	Universal Mobile Telecommunications System
5G	Fifth Generation

Contents

Popular Science.....	vii
Abstract.....	xi
Preface.....	xv
Acknowledgements.....	xix
List of Acronyms and Abbreviations.....	xxi
Contents.....	xxiii
Part I: Thesis Overview.....	1
Chapter 1 Introduction.....	3
1.1 Background.....	3
1.2 Multiple Antenna Systems in Sub-6 GHz Bands.....	4
1.3 Multiple Antenna Systems in Mm-wave Bands.....	14
1.4 Antenna Design Strategies.....	22
1.5 Motivation of the Thesis.....	23
1.6 Organization of the Thesis.....	23
Chapter 2 Modal Analysis – An Overview.....	25
2.1 Waveguide/Cavity modes.....	25
2.2 Spherical Wave Modes.....	28
2.3 Modal Expansion Methods.....	29
2.4 Characteristic Modes.....	29

Chapter 3 Compact Multiport Terminal Antenna.....	41
3.1 General Design Procedure of Platform-Integrated Antennas.....	42
3.2 CM-based MIMO Antenna System Design.....	48
3.3 Antenna-user Interaction.....	52
3.4 Co-Integration of Sub-6 Antenna with Mm-wave Antennas.....	54
Chapter 4 Low-cost Millimeter-wave Multi-element Antennas.....	57
4.1 Any-Layer PCB Technology.....	58
4.2 Antenna Arrays for MRR Radar.....	62
4.3 Antenna Array for Point-to-point Communication.....	66
Chapter 5 Conclusions and Future Perspectives.....	73
5.1 Overview of Included Papers.....	73
5.2 Conclusions.....	78
5.3 Future works.....	80
References.....	83
Part II: Included Papers.....	97

Part I:

Thesis Overview

Chapter 1

Introduction

1.1 Background

AN antenna is an electrical component that can both transmit and receive radio waves; in the transmission mode it converts a guided wave into a radiating wave propagating in free space, and in the reception mode vice versa. Thus, the antenna is a necessary part of all wireless systems that involve wave propagation. Modern wireless technologies such as 5th generation (5G) communication and low-cost radar systems have attracted significant market interest and the successful deployment of these technologies require efficient antenna design over a wide range of frequencies, from sub-1 GHz bands to millimeter wave (mm-wave) bands (30-300 GHz). In wireless technologies, different antenna requirements are defined to satisfy different system targets and limitations. With the advent of data communications in 2.5G, a paradigm shift occurred in the use of wireless technology: increasing data rate became one of the desirable system level goals in modern wireless applications. For example, multi-gigabits per second data rates are targeted in 5G to support enhanced mobile broadband services (see Fig 1.1).

Higher data rates can be achieved in different ways. Based on Shannon's Theorem, one approach to obtain higher data rates is to utilize more bandwidth by implementing antennas in higher frequency bands, where more bandwidth is available than in lower bands [1]. Furthermore, increasing the number of antennas in multiple antenna systems has been introduced as a popular solution to achieve higher data rates and link reliability for systems operating at lower frequencies, especially at sub-6 GHz bands [3]. Notably, the so-called multiple-input multiple-output (MIMO) technology incorporates multi-antennas on both the mobile and base station sides of the radio access network to facilitate the transmission of parallel

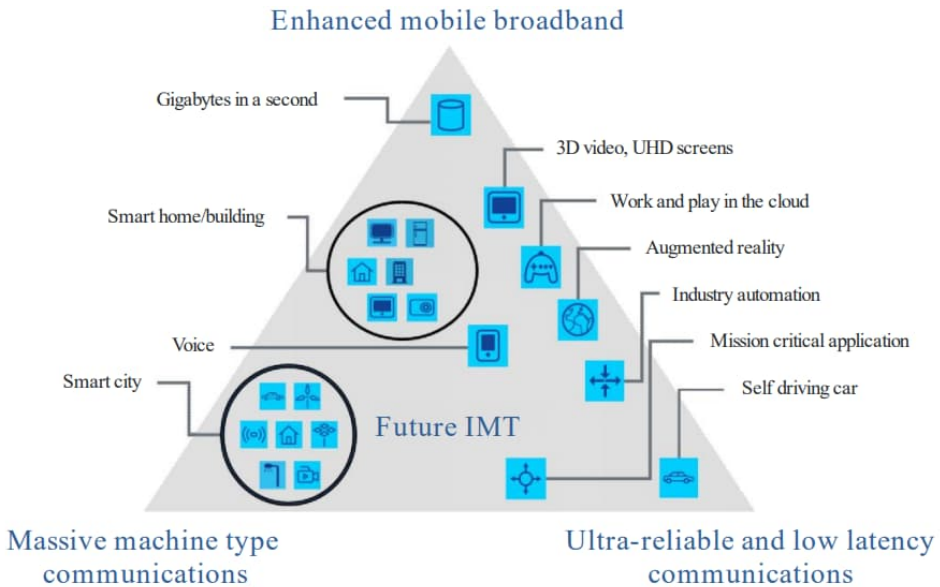


Fig 1.1 Usage patterns of 5G [2].

data streams, which dramatically increases the data rate [4]. It is noteworthy that sub-6 GHz bands are critical for providing reliable coverage of mobile services, due to lower propagation losses and higher signal penetration.

In this chapter, we present on the background and challenges of the antenna design for the above-mentioned applications in two different frequency bands. Then, the thesis motivation and thesis outline will be provided.

1.2 Multiple Antenna Systems in Sub-6 GHz Bands

The importance of the antennas in mobile radio handsets increased around the beginning of the 21st century. For aesthetic reasons, the traditional external handset antennas were replaced by internal ones. Moreover, the number of antennas, supported radio systems and other hardware (e.g., multiple cameras) that are implemented in the handset keep increasing while the thickness has been decreasing, making it harder and harder to find the space to integrate antennas. The interesting challenge of making compact and efficient internal antennas has attracted a surge of research interest in recent times, which has resulted in numerous theses, patents, and other scientific publications, as well as new solutions in the form of consumer products [5].

Mobile communication is a rapidly changing industry, and its products have short life cycles. The future of mobile handsets may be very different from the

current situation, and changes may come sooner than we can imagine. Nevertheless, although the platform for the antennas keeps changing, the challenges related to the antennas will remain, thanks to the laws of physics. These challenges will also motivate further academic research in the field for years to come. Designing the perfect antenna will always remain a worthy pursuit, given the constant evolution of the handset and its operating environment.

This section will briefly review the MIMO system model as well as key performance metrics for MIMO systems. For MIMO antenna designs, it is important to have a suitable metric to translate the antenna performance parameters to the system performance. In this context, the thesis utilizes multiplexing efficiency as the primary metric to enhance MIMO system performance. Several requirements and corresponding challenges in MIMO antenna design for mobile handsets are then discussed.

1.2.1 MIMO System Model

In recent years, the ever-increasing demand for high data rate wireless applications has required new wireless communication systems to have higher Shannon capacity for data transmission. Shannon or channel capacity is defined as the maximum mutual information which can be transferred through the wireless channel [6], [7]. Among various techniques to increase capacity, MIMO systems have attracted a great deal of attention in both the research community and the industry as a suitable solution to significantly enhance the capacity of band-limited wireless systems [7].

A MIMO system is essentially a wireless system with multiple antennas at both the transmitter and receiver ends, as illustrated in Fig 1.2 (a). Compared to single-input single-output (SISO) system, the main advantages of MIMO system include higher capacity (and data rates), higher link reliability (due to spatial diversity offered by multipath propagation), and wider coverage area (from array gain). As shown conceptually in Fig 1.2 (a), if different propagation paths can be resolved by multiple antennas, then ideally independent (or parallel) data streams can be transferred through each propagation path, and therefore, the channel capacity can be enhanced [8]. Since the independent data streams are transferred at the same frequency, MIMO system can provide a higher spectral efficiency than SISO system.

The general model of a MIMO antenna configuration is illustrated in Fig 1.2(b), showing M_T and M_R as the number of antenna elements at the transmitter and receiver sides, respectively, and H_{mn} represents the channel coefficient between the n -th transmitter and the m -th receiver. Using the dyadic channel response function $\overline{\overline{G}}(\omega, \Omega_R, \Omega_T)$, which relates the received field distribution $\overline{\overline{P}}_R(\omega, \Omega_R)$ to the radiated field pattern of the transmitter array, one can write:

$$\overline{\overline{P}}_R(\omega, \Omega_R) = \int \overline{\overline{G}}(\omega, \Omega_R, \Omega_T) \cdot \overline{\overline{P}}_T(\omega, \Omega_T) d\Omega_T, \quad (1.1)$$

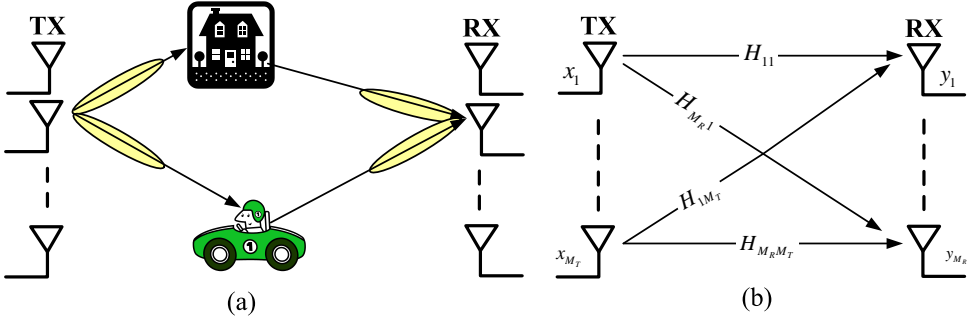


Fig 1.2. (a)The MIMO system in a multipath propagation environment, (b)The general model of MIMO antennas.

where Ω_R and Ω_T are the solid angles with respect to the receiver and transmitter coordinate systems, respectively. The radiated field pattern of the transmitter array can be written as follows [8]

$$\bar{P}_T(\omega, \Omega_T) = \sum_{n=1}^{M_T} x_n(\omega) \bar{F}_{T,n}(\omega, \Omega_T), \quad (1.2)$$

where x_n is the up-converted symbol fed to the n -th antenna element, and $\bar{F}_{T,n}$ is the vector field radiation pattern of the n -th transmitting antenna element in the presence of other antenna elements.

Using the channel dyadic function, the received signal by the m -th receiving antenna element can be found as

$$y_m(\omega) = \int_{\Omega_R} \bar{F}_{R,m}(\omega, \Omega_R) \cdot \bar{P}_T(\omega, \Omega_T) d\Omega_T, \quad (1.3)$$

where $\bar{F}_{R,m}$ is the field radiation pattern of the m -th receiving antenna element in the presence of the other antenna elements. Using (1.1) to (1.3), the vector signal received by the receiving antenna elements, after adding the additive noise contribution $\boldsymbol{\eta}(\omega)$, can be expressed as follows [8]

$$\mathbf{y}_m(\omega) = \mathbf{H}(\omega) \mathbf{x}(\omega) + \boldsymbol{\eta}(\omega), \quad (1.4)$$

$$H_{mn}(\omega) = \iint \bar{F}_{R,m}(\omega, \Omega_R) \cdot \bar{G}(\omega, \Omega_R, \Omega_T) \cdot \bar{F}_{T,n}(\omega, \Omega_T) d\Omega_T d\Omega_R.$$

For the flat fading or non-selective frequency channel, the channel transfer matrix \mathbf{H} is constant over the signal bandwidth. However, it can still vary over time, if there is movement in the transmitter, receiver or the propagation environment. As can be seen, the field radiation patterns of the receiver and transmitter antennas also

affect \mathbf{H} . Since the channel dyadic function is determined by the environment and cannot be manipulated, the antenna field patterns should be effectively designed so that the desired MIMO system performance is achieved.

1.2.2 MIMO Performance Metrics

Based on the system model presented in the previous subsection, several performance metrics that are particularly relevant to antenna and system performance will be introduced below.

Shannon Capacity

The main advantage of MIMO systems over conventional SISO systems is its ability to enhance capacity without requiring any additional transmit power or frequency spectrum. Under the assumptions that the channel is unknown for the transmitter and known for the receiver, MIMO capacity is given by [6], [7], [9]

$$C = \log_2 \det \left(\mathbf{I}_{M_R} + \frac{P_T}{M_T \sigma_n^2} \mathbf{H} \mathbf{H}^H \right), \quad (1.5)$$

where \mathbf{I}_{M_R} is an $M_R \times M_R$ identity matrix, P_T is the total transmit power, $\det(\bullet)$ is the determinant operator and $(\bullet)^H$ is the Hermitian conjugate operator. Assuming an orthogonal MIMO channel matrix \mathbf{H} and $M_T = M_R = M$, it has been shown in [6] that (1.5) simplifies to

$$C = M \log_2 \left(1 + \frac{P_T}{\sigma_n^2} \right). \quad (1.6)$$

The fundamental derivation in (1.6) implies that capacity scales linearly with the number of antenna elements without sacrificing the limited resources of frequency spectrum and transmit power. The linear scaling of capacity is possible since the MIMO channel can be effectively decomposed into M independent subchannels, which support the transmission of parallel data streams. This so-called spatial multiplexing (SM) capability enables a significant increase in information transfer as compared to conventional SISO systems. Beyond the increase in spectral efficiency, MIMO systems are also credited with increasing reliability and coverage in mobile communications through diversity and beamforming techniques.

Conventionally, diversity techniques are used to combat the multipath fading effects [6]. In various diversity schemes such as space, angle, polarization, and pattern diversities, multiple antennas are employed to transmit or receive independent radio signals that contain identical information. By obtaining

independent signals caused by the independent wireless channel effects, the probability of simultaneous fading in the independent signals will decrease and hence system reliability will improve [6]. With beamforming, MIMO systems aim at increasing signal-to-noise ratio (SNR) and reducing interference through forming more directive antenna system radiation or reception, thereby improving reliability and coverage.

In the SM mode, the actual capacity enhancement depends on the number of resolvable propagation paths which can be obtained through the wireless channel. For instance, if there is only one dominant propagation path in the wireless channel, the same information is extracted by multiple antennas and no capacity improvement can be obtained. Hence, it should be emphasized that MIMO systems are beneficial in rich multipath environments which contain multiple propagation paths resolvable by multiple antennas. In such an environment, MIMO systems can be employed to exploit the wireless channel's degrees of freedom.

However, the number of resolvable subchannels in a multipath environment depends on the correlation of the communication channel pipes, i.e., channels of all transmit-receiver antenna pairs, which in turn depends on the properties of the multipath propagation and antennas. If the communication channels obtained from the multipath environment are highly correlated, then similar information is obtained through different channel pipes, and therefore, there is little degrees of freedom in the channels to be extracted by the MIMO systems. Hence, the lower the correlation between the MIMO signals, the better the performance for the MIMO system.

In this procedure of determining channel resolvability, the electromagnetic (EM) properties of the MIMO antenna elements are usually considered as part of the wireless channel, where the MIMO antenna structures can play a crucial role to make MIMO signals uncorrelated. The electromagnetic effects of the MIMO antennas enforce fundamental limitations in the MIMO system performance. If the EM limitations and interactions of the antennas are ignored, then the MIMO system performance may be underestimated or overestimated, and as a result imprecise evaluation of the MIMO systems may be obtained. Hence, MIMO system design requires careful EM antenna considerations in addition to baseband signal processing.

Correlation

Correlation is known to significantly impair MIMO system performance. It is therefore one of the most crucial figures of merit in multiple antenna systems and of particular importance to a number of research activities in the field as well as to this thesis work. The complex correlation coefficient of the received signals between the i -th and j -th antenna elements can be written in the following general form [3]

$$\rho_{ij} = \frac{\langle \overline{F}_i, \overline{F}_j \rangle_P}{\left[\langle \overline{F}_i, \overline{F}_i \rangle_P \langle \overline{F}_j, \overline{F}_j \rangle_P \right]^{1/2}}, \quad (1.7)$$

where

$$\langle \overline{A}, \overline{B} \rangle_P = \iint_{4\pi} \overline{A} \cdot \overline{B}^* P(\Omega) d\Omega,$$

and $P(\Omega)$ is the probability distribution of the power angular spectrum (PAS) of the incoming waves impinging on the MIMO antenna elements, \overline{F}_i is the vector field radiation pattern of the i -th transmitting antenna element in the presence of other antenna elements, the solid angle $\Omega = (\theta, \phi)$ and $d\Omega = \sin\theta d\theta d\phi$. When maximizing the channel capacity, the cross-correlation coefficients should be minimized. In mobile communications, due to the accessibility of the signal envelopes, e.g., from the receive signal strength indicator (RSSI) voltages, the envelope correlation coefficient (ECC) is often used. The ECC between ports m and n is approximated by $\rho_e \approx |\rho_c|^2$.

For lossless antennas and uniform PAS ($P(\Omega)=1$), the cross-correlation coefficient in (1.7) can be expressed in terms of scattering parameters [10]

$$\overline{\rho}_{ij} = \frac{\sum_{p=1}^N S_{pi}^* S_{pj}}{\left[\left(1 - \sum_{p=1}^N S_{pi}^* S_{pi}\right) \left(1 - \sum_{p=1}^N S_{pj}^* S_{pj}\right) \right]^{1/2}}, \quad (1.8)$$

where S_{pi} is the scattering parameter between the p -th and i -th ports of the N -port antenna structure.

In many MIMO antenna designs, (1.8) has been used as a criterion to provide uncorrelated signals for wireless communication systems. Since the correlation coefficient defined in (1.8) does not include the wireless channel effects in the correlation calculations, there is no guarantee that the MIMO antenna design can lead to orthogonal signals in different channel realizations, whereas (1.7) allows for the performance evaluation of the designed MIMO antenna architecture in different environments modeled in the PAS. Moreover, (1.8) is in general not valid, especially when the radiation efficiency is low for the antenna elements [10]. Hence, equation (1.7), which contains the wireless channel information in addition to the vector field radiation pattern of the MIMO antenna modes, is a more suitable criterion for designing MIMO antenna system. At the same time, the scattering parameters of the MIMO antenna structure should also be evaluated to investigate the impedance matching of each antenna element as well as the isolation between the elements.

Multiplexing Efficiency

MIMO performance in the SM mode of operation, i.e., parallel data stream transmission that is feasible at higher SNRs, has been traditionally characterized by capacity in bits/s/Hz. However, in many occasions a power-related measure of efficiency is a more intuitive figure of merit for comparing multiple antenna systems operating in the SM mode.

In this context, multiplexing efficiency (ME) was proposed in [11] to combine antenna correlation and efficiency in a single, intuitive figure of merit. For a 2×2 MIMO setup ($M_R = M_T = 2$) at high SNRs and in a uniform 3D PAS, it is expressed as

$$\eta_{me} = \sqrt{\eta_1 \eta_2 (1 - \rho_e)}, \quad (1.9)$$

where η_1 and η_2 are the total antenna efficiencies at port 1 and 2, respectively and ρ_e is the ECC.

1.2.3 MIMO Antenna Design Challenges

There are many fundamental and practical challenges in designing MIMO antennas for wireless systems. These challenges relate to the ones attributed to the fundamental antenna element properties as well as those unique with multi-element configurations.

Compactness of Implementation Space

Modern mobile communication systems use wideband and MIMO antennas in both base stations and terminals to provide higher data rates over particular frequency ranges. However, especially in mobile terminals (i.e., smartphones), the antenna space is limited and integration of wideband and multiple antenna systems working in sub-6 GHz in the limited space of the printed-circuit board (PCB) (i.e., chassis) is a huge challenge. Previously these limitations were related to the form factor, i.e., the shape and size of the smartphones [12], [13]. However, recently the average length and width of the mobile handset have actually increased during the last few years due to the introduction of the touch screen technology and the demand for ever larger screens capable of displaying high quality videos, etc. The antenna size in the terminal has, however, not increased. One reason for this is that the battery size has grown due to the higher power consumption of the device. In addition, the average thickness of the handsets has decreased, due to the current trend of slim smartphones. So, the space occupied by the antenna systems tends to decrease due to these new trends in smartphones, relative to that of the earlier mobile handsets.

To summarize, consumers want to have a device with a large display screen (i.e., with high screen-to-body ratio) and a thin casing, yet offers long battery lifetime and many hardware features like multiple cameras. These requirements greatly limit the available space for antenna implementation, which will degrade antenna performance [14]. In addition, MIMO technology that is used to increase the data rate requires multiple antennas to be integrated in the already limited antenna space. To make things worse, the large PCB and screen imply that there is little off-ground clearance, which is important for good antenna performance.

Decoupling of MIMO Antennas

It has been shown in Section 1.2.2 that data rate can be increased linearly with the number of antennas in the MIMO context, as a larger number of antennas at both link ends increases the number of the independent sub-channels. And this performance increase can be achieved without sacrificing additional frequency spectrum and transmit power [8]. However, as mentioned, antenna and propagation channel properties influence the possibility to obtain independent sub-channels. For the multi-antennas, it is crucial that the antenna elements facilitate low correlation/coupling upon integration into the compact terminal device, to achieve good MIMO system performance [15]-[18]. But low correlation is hard to achieve in reality because all the antenna elements are mounted on the same chassis, which subjects these antennas to both high spatial correlation and strong mutual coupling [19].

The easiest method to decouple the multi-antennas is to increase the distance between the antenna elements. However, this method is only feasible to some extent due to the small size of the PCB limiting element spacing. Accordingly, many other effective decoupling techniques have been proposed in the literature, such as the use of multiport matching networks [20], ground plane modification [21]-[24], neutralization line [25], and parasitic scatterer [26]. In addition, the use of suspended lines has also been reported in the literature [27].

Unfortunately, most of the existing decoupling techniques are not practical for mobile terminals and the ones that are suitable mainly focus on relatively high frequency bands (i.e. those above 1 GHz), including WLAN, DCS1800 and UMTS bands [15]-[24], even though in practice the problem of coupling is more severe at lower frequencies. For cellular frequencies below 1 GHz (i.e., covering 698-960 MHz), the existing decoupling techniques are no longer adequate to facilitate good MIMO performance [28]-[31]. Existing literature shows that the isolation of multiple antennas in compact terminals is typically less than 6 dB for frequencies below 1 GHz (see e.g., [32]). The reason of this high coupling is that the mobile chassis, which only functions as a ground plane for the antenna elements at high frequency bands, becomes the main radiator at the lower frequency bands (i.e., the bands below 1 GHz) [12]. Thus, different antenna elements share the same radiator, making isolation worse. In [12], it has already been shown that the most effective

antenna in the low band is the one that employs the metallic chassis as the main radiator. Thus, the radiation patterns are strongly influenced by the shared chassis, such that angle and polarization diversities are difficult to achieve among the antennas for the purpose of decoupling. It has been shown earlier that radiation pattern overlap (i.e., lack of diversity) contributes to coupling [33].

Wideband Requirement

Traditional mobile terminal antennas are usually self-resonant at their frequencies of operation. The resonances are created within the antenna geometry and result in good impedance match between the antenna and its feed, without additional matching circuits. Among compact self-resonant antennas, internal planar inverted-F antennas (PIFAs) are the most commonly employed for GSM900/1800 cellular-phone handsets [34], [35]. PIFAs are quarter-wavelength resonating antennas that can be considered as probe-fed shorted patches over an infinite ground plane. However, PIFAs present two main drawbacks. The first is that as microstrip patches, they are inherently narrow-bandwidth antennas. Moreover, because of their compactness, their performance is subject to the well-known fundamental limits on small antennas [36]. That is because the wavelength, which for frequencies below 1 GHz is over 300 mm, is physically large compared to the size of a typical mobile terminal. Hence, it is very challenging to implement quarter wavelength-long radiators within the limited antenna space in typical mobile terminals, especially at lower frequencies.

Most of the earlier studies on antenna design in the low band (e.g., 698-960 MHz) focus their attention on single antenna design for mobile terminals, e.g., [34]-[41]. This is because, as discussed above, it is challenging in the low band to achieve multiple antenna elements (or ports) with low coupling and enough bandwidth, simultaneously. Recent results indicate that, in a rich scattering environment, the MIMO performance of closely spaced antennas can be improved by decoupling multiple antennas, with the tradeoff being a smaller bandwidth [20].

User Effects on Terminal Antennas

Different from antennas which always operate in free space, the design of handset antennas should also account for their interactions with the human body. As such, the above-mentioned mobile antenna system design challenges will be more complicated in realistic usage scenarios that often involve user interactions. The user of a handheld mobile device typically affects the antenna performance in a negative manner. However, users would typically assume that their handsets are operating reliably regardless of how they are interacting with the terminal device (e.g., holding it with one or two hands, and possibly also in proximity to the head). This problem can be partly overcome by careful design of the antenna system

(including the use of possible compensation methods) and by taking into account the realistic performance of the antenna already in the planning procedure of the whole radio system.

In addition, the antennas (or actually the whole terminal) must respect the specific absorption rate (SAR) regulations [42], [43] that are used to limit the radio frequency energy absorption per mass unit of the human tissue. Thus, SAR performance is also an important consideration in antenna design. In addition, lower SAR values are also desirable since typically less power is absorbed by the user and thus the radiation efficiency is higher.

Matching and Efficiency of Antenna Elements

There are several other practical limitations in the design of mobile terminal antenna. Firstly, the antenna designer has to acknowledge that the antenna is a part of a radio system. The interoperability with other parts of the system is important, as well as electromagnetic compatibility (EMC) in general. For example, the antenna should have good impedance matching properties not only for good efficiency, but also because the transmitter electronics may suffer if the impedance mismatch causes a strong standing wave. The standards of each communication system also set requirements with respect to noise, linearity, maximum transmitter power, etc. The 3G Partnership Project (3GPP), which is a cooperation body of companies and institutes in the field of mobile communications, prepares standards for the mobile communication systems [2]. Acceptable matching should also be maintained in the close vicinity of the user's head and hand.

Generally, the efficiency should be as high as possible to guarantee reliable operation of the radio system and long operation time. In practice, relatively large losses introduced by the impedance mismatch and conductive loss of the terminal, as well as additional losses caused by the user, must be tolerated in the design.

Pattern and Polarization of Antenna Elements

An omnidirectional pattern in the azimuth plane is desirable for terminal antennas due to the random orientation of the terminal and the incident waves. Due to the inherently properties of small antennas, the antenna designer has limited possibility to influence the near-omnidirectional pattern and distinct polarization, especially in the sub-1 GHz frequency range. However, the polarization of the antenna is not very important due to the complex multipath propagation environment expected in typical usage scenarios, since the scatterers in the environment can substantially depolarize the waves so that the signals can still be received irrespective of the polarization properties of the antennas.

1.3 Multiple Antenna Systems in Mm-wave Bands

As already mentioned, the frequency band of 30-300 GHz (corresponding to the wavelength of 10-1 mm) is broadly defined as the mm-wave band [45]. There are some specific advantages in using the mm-wave band for wireless systems. First, the physical sizes of components in mm-wave band is significantly smaller compared to those of the traditional cellular band. The small component sizes are very beneficial for realizing highly integrated and lightweight systems. Further, due to the smaller antenna elements, array concept can be used in the antenna part of the system, which leads to higher gain and narrower beamwidth. Second, the mm-wave band also offers significantly larger available absolute bandwidth. The narrower beamwidth and wider bandwidth at the mm-wave band lead to higher angular and range resolutions for radar and imaging applications [44]. On the other hand, due to the availability of wider absolute bandwidth, higher data rates are obtainable in mm-wave communications networks [45]-[46].

1.3.1 Mm-wave Antenna Design Challenges

Despite the advantages of the mm-wave band, one critical bottleneck for mm-wave wireless communication is the increased path-loss (PL), which is proportional to frequency squared. As an illustration, the PL increases from 32.45 dB to 61.35 dB as the frequency increases from 1 GHz to 28 GHz. Apart from this PL property of the mm-wave band, there are also unique challenges in the development of antennas and RF components in the mm-wave band, which will be discussed in the following subsection.

Propagation and Antenna Losses

The first and main challenge is the atmospheric scattering and absorption caused by rain, snow and fog. Indeed, signals with frequencies below 30 GHz experience relatively little atmospheric losses. Fig 1.3 shows that the atmospheric attenuation of the signal increases as the frequency increases [47]. It illustrates some O₂ and H₂O attenuation peaks that happen along the frequency axis. These peaks can be beneficial for applications that require higher security and less signal transmission range. Unlike visible light and infrared, millimeter waves can penetrate fog, smoke and dust in the in the frequency bands between the attenuation peaks in Fig 1.3, which is a very beneficiary property.

Generally, mm-waves are mainly impacted by precipitation, atmospheric gases (e.g., water vapor and O₂), and obstruction and diffraction by objects (e.g., foliage) [48]. When some of these sources are present together, then the range attenuation significantly increases.

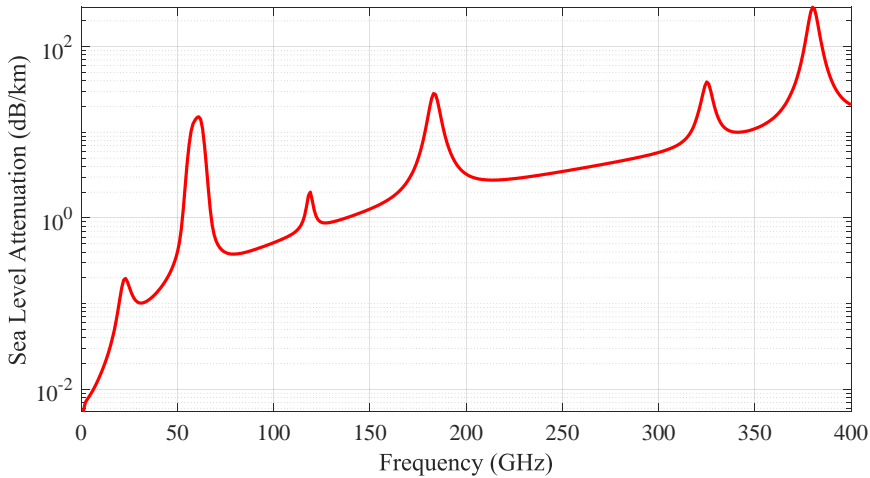


Fig 1.3 Average mm-wave atmospheric absorption.

Material and surface roughness cause more severe signal attenuation from reflection and diffraction at mm-wave frequencies than lower frequencies. This is because the roughness becomes comparable to the wavelength, which is between 1 mm and 10 mm, resulting in increased scattering of the incident waves. In systems without line of sight between the transmitting and receiving sources, attenuation becomes much more severe. Unlike the lower frequency signals, mm-wave signals suffer from high loss when incident on solid materials, which implies they can be easily blocked by objects [49]. In addition, measurements have shown that the attenuation through 10 meters of foliage can be as high as 23.5 dB at 80 GHz, which is very substantial.

Apart from the propagation loss and sensitivity to blockage, antenna losses such as conductor loss, dielectric loss, and degradation caused by transition structures are also more substantial at mm-wave frequencies than sub-6 GHz frequencies.

Due to the aforementioned severe losses experienced by mm-wave signals, high-gain antennas operating over a large band are mandatory to offset these losses, in order to sustain the desired link performance.

Fabrication Technology

Another important challenge is high fabrication (i.e., tape-out) cost of mm-wave antennas. This is because in the mm-wave regime, the free space wavelength (1-10 mm) is very much smaller than that in traditional cellular bands (i.e., sub-6 GHz bands), which leads to much smaller radio-frequency (RF) component sizes. Consequently, there is a need for greater precision in the manufacturing process to reduce fabrication errors, which translates to very expensive tape-out cost compared to that in lower bands. Furthermore, the possibility of the antenna design for mass

production is another critical criterion to ensure marketplace adoption. It is also important to choose an antenna fabrication technology that allows for easy integration with the mm-wave silicon transceiver. There are two ways to integrate the antennas with the transceiver at mm-wave frequencies, i.e., the antenna-on-chip (AoC) concept and the antenna-in-package (AiP) concept.

In AoC concept, the need for a circuit-antenna interface is eliminated [50]. In fact, the reduced carrier wavelength at mm-wave frequencies allows for the antenna size to be shrunk to less than a millimeter, thus making an on-chip implementation feasible. However, these antennas do not work very well because of the high permittivity and low resistivity of silicon substrate [51].

On the other hand, the materials used for the second concept, AiP, have relatively lower losses, which means that AiP can facilitate higher antenna efficiency. Hence, AiP solutions have, over the last decade, attracted significant interest for mm-wave applications [50]. Many different solutions based on different materials have been reported. Among the main candidate technologies for fabricating such antennas are Low Temperature Cofired Ceramics (LTCC), standard PCB (Printed Circuit Board) and Liquid-crystal polymer (LCP). LTCC is the most popular fabrication technology for AiP [52]. It supports compact size with multilayer structure configuration, and it is known to have more design freedom with via placement and tight tolerance. However, it suffers from high cost and manufacturing complexity. In contrast, PCB technology is low cost since it can be mass produced but it has more design restrictions, making the design process at higher frequencies more difficult. As another fabrication technology for AiP, LCP[53] supports similar multilayer structures as LTCC but at a lower price [53]. However, it has a long production cycle, and the technology is not suitable for mass production.

The above discussions show the need for a new or improved mm-wave antenna fabrication technology that is low-cost, low loss and easy to integrate with the active circuitry, especially for the higher part of mm-wave band. Due to more PL and material loss in the mm-wave band than sub-6 GHz bands, designing low-cost mm-wave antenna with enough gain to compensate for the losses is a real challenge.

1.3.2 Automotive Radar Systems

Due to the advantages of mm-wave band in providing superior angular and range resolution, it is popular to implement radars in this band, including those for automotive application [44]. In this subsection, automotive radars are introduced.

The discussion on the use of radar systems on vehicles to prevent collisions started in 1964 [54]. In the 1970s, automotive radar prototypes were built and tested on roads [55]-[57]. However, the high cost and large dimensions of the radar modules were the limiting factors for commercial application. As early as 1990, the major automotive industries and suppliers started again to do research on automotive radar applications. In 1992, Doppler radar systems working at 24 GHz

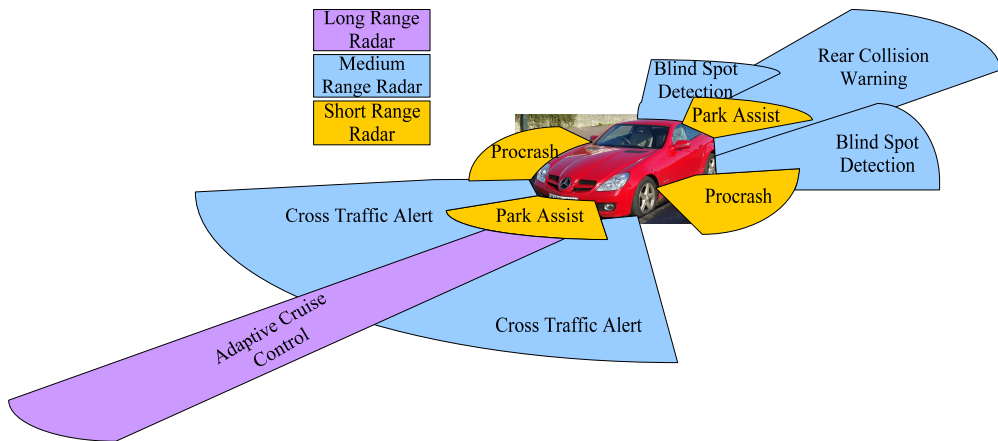


Fig 1.4 Various automotive radar applications.

were installed on 1700 Greyhound buses in the US by Eaton VORAD Technologies, and the accident rate was reduced by 25% [58]. In the late 1990s, Mercedes-Benz was the first automobile company that introduced the 77 GHz radar based DISTRONIC system [59]. Since then, other car manufacturers started following Mercedes-Benz in introducing radar into their car models. Today, most high- and middle-class vehicles are equipped with radar sensors.

Pulse radar and FMCW (Frequency Modulated Continuous Wave) radar are the two most common types of radar currently used in commercial products [60]. A Pulse radar transmits short pulses while an FMCW radar sends out a linearly modulated signal. A pulse radar determines the target range by measuring the time delay between the transmitted and received signals, but an FMCW radar determines the distance based on the difference in the transmitted and received signal frequencies.

Today, two frequency bands around 24 GHz and 77 GHz are used for automotive radar applications. The 77 GHz radars are more promising for future evolution as it offers advantages such as smaller dimension, better angular resolution and broader bandwidth, but they are more challenging in design and implementation, and the final radar modules are costlier. The 77 GHz band can be divided into two sub-bands: 76-77 GHz and 77-81 GHz (also called 79 GHz band). The former has been approved by most countries, whereas the latter is only available in Europe so far but is under discussion in other regions/countries.

In addition to the existing automotive frequency band of 76 to 77 GHz used for long-range radar (LRR) applications such as autonomous cruise control (ACC), the 79-GHz band (77-81 GHz) has been allocated by the European Commission in 2004 for future short- and mid-range (SRR, MRR) high-resolution automotive radar systems (see Fig 1.4). Therefore, safety and comfort applications such as collision warning, blind spot detection, and precrash vehicle preparation [61] will benefit

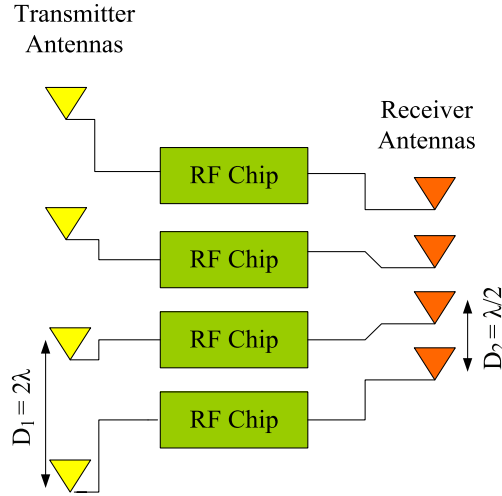


Fig 1.5 Configuration of the MIMO radar array.

from higher sensor performance and smaller sensor size compared to the established sensor technology at 24 GHz [62], [63]. Among the radar applications of different ranges, LRR applications require the narrowest FOV (Field of View) and highest antenna directivity. The antenna module is usually mounted behind the front car grill to determine the distance of objects ahead, with a range of up to 250 meters. SRR offers the widest FOV and can be used to monitor the vicinity of a vehicle within the range of 30 m. MRR has a FOV between LRR and SRR, and can be installed on the front, rear, or side area of the vehicle for different applications. Detailed comparisons of the three sensor types and their corresponding applications are given in [64].

MIMO Radar and its Requirements

MIMO radar is a relatively new concept in radar technologies, and it has been noted as an emerging technology in comparison to classical digital beamforming radars. The main difference between these two types of radar is that in MIMO radar, we can transmit different signals over multiple transmit (TX) antennas, while keeping these signals separable at the receive (RX) antennas. The signal separation is the major characteristic of all MIMO radar systems, and it leads to several advantages. The first advantage is that, since we use several TX antennas, the target is illuminated from several directions, therefore the negative effect of strongly direction-dependent radar cross section is reduced [65]. To use this advantage maximally, the TX antennas must be placed far away from one another, but at the expense of making the radar module bigger. However, the MIMO concept offers more benefits. In [66], it has been demonstrated that with the MIMO concept, it is

possible to synthesize virtual antenna arrays with larger numbers of elements, which enables a larger number of targets to be tracked in the same range. Another benefit is that the virtual RX antenna positions are the spatial convolution of the TX and RX antenna positions, which leads to a larger virtual array aperture, and therefore to a higher resolution [67], [68].

A MIMO radar array configuration is shown in Fig 1.5. Antenna sub-arrays can be used instead of each antenna. Indeed, with a spatial convolution of the 4 sub-arrays both in the TX and RX arrays, a virtual linear array with 16 elements in the receiver part is formed. The concept of the virtual array is described in further details in [66].

For mm-wave MIMO radars, the set of requirements is quite strict. First, regarding the virtual array concept, the distance between RX sub-arrays must be less than half of the free space wavelength, to mitigate the side lobe level (SLL) as much as possible, which results in quite small elements. Second, since the signal level in the RX array is low, the mutual coupling between the TX and RX sub-arrays must be as low as possible, otherwise the functionality of radar will degrade substantially. Third, aiming at high production volumes for the consumer market, the cost of fabrication has to be as low as possible. Designing and fabricating antennas that satisfy all these requirements is challenging. It is worth mentioning that if this radar is designed for ranges under 30 meters (SRR), the number of elements in the subarray will be less than radars for ranges up to 100 (MRR) or 250 (LRR) meters. This means that we need more gain in the MRR (or LRR) case and placing more than one element in a row, and making a sub-array out of them can help us to make the antenna more directive. However, wide beams are beneficial for SRRs, where the scanning range must be wide.

Fat-gain behavior along the frequency bandwidth is highly advantageous for the targeted radar applications. The reason is that, with a flat-gain characteristic, it is easier for the radar designer to have full control over the TX and RX filters in radar-waveform design. If the frequency response of the antenna is not flat, then the designer must then take it into account in the design of the TX and RX filters [69].

1.3.3 5G Cellular Network

As mentioned, apart from radar systems, the mm-wave band has also been adopted by wireless communications [46]. The exploitation of the mm-wave spectrum is essential to tackle the current dizzying growth of mobile data traffic [70]. The legacy bands are lower than 6 GHz (referred to as sub-6 GHz bands), have limited bandwidth and are currently heavily used. To meet the growth in data traffic, 28 GHz and 38 GHz bands have recently been made available for 5G networks [71]. The 5G New Radio (5G NR) air interface has been developed to meet the requirements of the 5G networks, which covers the wide range of frequency bands from sub-1 GHz bands to mm-wave bands. This means that the antennas used to

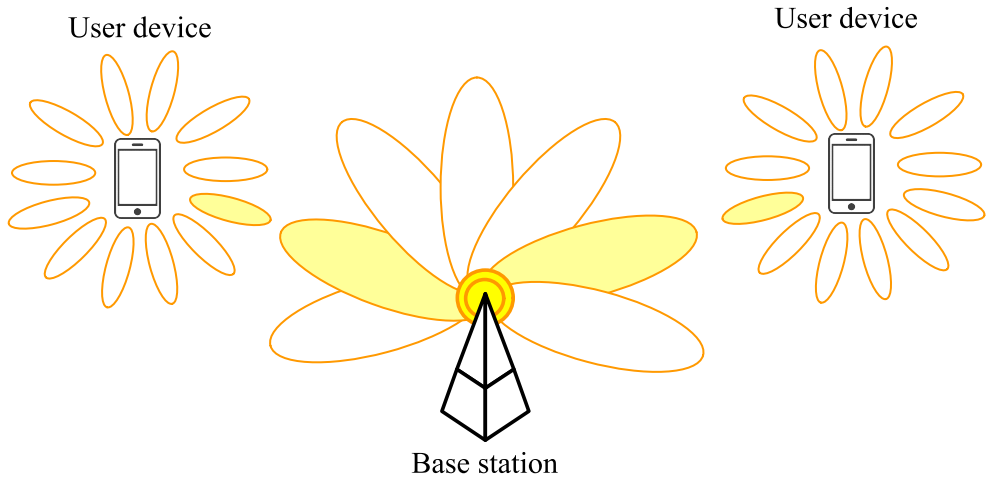


Fig 1.6 Beam distributions of base stations and user devices in mm-wave bands.

support 5G networks need to be capable of operating in these frequency bands.

As mentioned in Section 1.3.1, when compared to the lower frequency bands, the electromagnetic waves in the higher frequency bands experience more noticeable losses. To compensate for the high propagation losses, the antennas operating in higher frequency bands need to generate radiation patterns or beams with higher gains. However, the higher gain is achieved at the cost of narrower half-power beamwidth thus reduced angular coverage. Therefore, both the base stations and user devices in high frequency wireless communication systems need to be capable of finer beam steering to maintain the same coverage area as in low frequency bands (see Fig 1.6).

1.3.4 *E*-band Communication

Wireless point-to-point communication between fixed locations is another common mm-wave application that has evolved alongside the automotive radar application. Indeed, in dense small cell networks, using fiber connections for backhaul is expensive, whereas using copper wire connections is complex and increases latency. In this situation, point-to-point wireless links are great alternatives. They provide high-speed data like fiber connections, which is very beneficial for transferring voice, video and data between commercial locations.

Two frequency bands within the *E*-band, i.e., 71–76 GHz and 81–86 GHz, can together offer a huge frequency spectral resource of up to 10 GHz, and their free space atmospheric absorption is less than 1 dB/km (Fig 1.3). Therefore, they have been allocated by the Federal communication Commission (FCC) for long-range

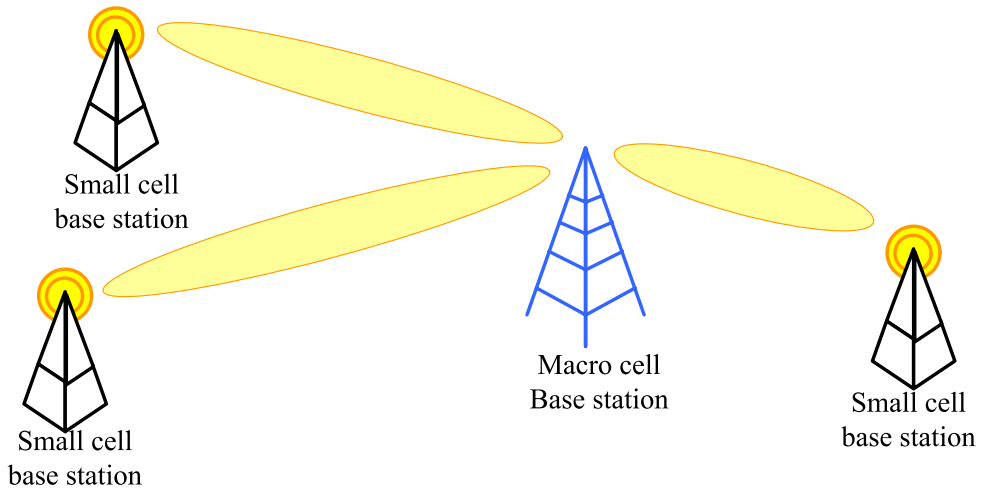


Fig 1.7 Point-to-point wireless links for backhaul.

gigabyte wireless point-to-point communication [72]. This 10 GHz spectrum is the largest frequency band ever allocated by the FCC for any application. This broad bandwidth is 50 times larger than the entire cellular spectrum. As mentioned in [73]-[74], the potential applications for these frequency bands are: 1) network fiber (backbone) POP (point-of-presence) access, 2) high definition video, 3) redundant access-network diversity, 4) enterprise campus connectivity, 5) broadband local area network (LAN) extension, 6) local loop, 7) metropolitan area network (MAN), 8) wide area network (WAN) access, 9) central office bypass, 10) storage access, and 11) fixed cellular backhaul links. All these applications are explained in detail in [74], but the main application is wireless backhaul, which is illustrated in Fig 1.7.

Achieving gigabit or even higher data rates is easily achieved by using the 5+5 GHz bandwidth for the communication channel. In this case, the radio architecture can be reasonably simple too. Simulation study shows 10 Gbps backhaul capacity can be achieved with 2 GHz bandwidth and 64-QAM modulation at *E*-band [75].

For the abovementioned wideband wireless systems, the antenna is one of the key components for obtaining high system performance. However, owing to the very high operating frequency of up to 86 GHz, there are many challenges in the design and implementation of *E*-band antennas, including the relatively high conductor loss, high cost, and very high fabrication sensitivity.

Practically, it is desirable to develop wideband, high-gain, high-efficiency *E*-band antennas in planar form and at low-cost for future large-scale commercial *E*-band wireless systems that utilize the entire system bandwidth.

1.4 Antenna Design Strategies

Closed-form equations can be used to design some specific types of antennas. But as the specific antenna problems or geometries become more complicated, there is often no convenient formulation that can be used to analyze it. Instead, the use of numerical methods or information which can be obtained from Maxwell's equations and a set of boundary conditions becomes necessary. Consequently, the designers of modern antennas generally rely on the use of in-house numerical codes or commercial software implementing traditional port-based computational electromagnetic solvers, e.g., Finite-Difference Time-Domain (FDTD) [77], Finite Element Method (FEM) [78], and Method of Moments (MoM) [79], to evaluate and manually optimize the antenna performance in a trial and error fashion before a physical prototype is fabricated. Under this circumstance, even with the support of computers, the success of the final design depends upon intuition.

An alternative approach is to use automated optimization techniques based on pseudo-random search algorithms [80]. Typical examples of these techniques are genetic algorithms (GAs), artificial neural networks (ANNs), particle swarm optimization (PSO) or bees algorithms. Their main advantage is that once the optimization algorithm is programmed, little interaction with the designer is required, as the computer is supposed to arrive at the expected specifications autonomously. Another feature of most computational electromagnetic solvers is that they require a predefined excitation to simulate the electromagnetic properties of an object. Once a solution is obtained from these types of computational solvers, only a single current distribution that produces a specific radiation pattern is obtained. This approach gives little insight into the suitability of the predefined excitation type and location.

The common problem in the aforementioned design strategies is that they do not directly provide useful physical insights of the radiating structure or its operating principles, and hence it is difficult to provide rigorous antenna design guidelines. On the other hand, another design strategy that utilizes the concept of electromagnetic modes can mitigate these limitations by offering physical explanations to the (modal) behavior of the antenna system, which can then yield systematic guidelines for antenna design.

In some special types of modal theories, analysis of arbitrary shape structures is possible. Furthermore, a predefined excitation is not required for the modal-based strategy. In contrast, excitation types and positions in traditional antenna design are found through visual inspection and analysis of excited currents of similar antennas, or by means of trial-and-error excitation placement.

1.5 Motivation of the Thesis

As it has been mentioned in section 1.4, clear and intuitive explanations should be provided for various phenomenon observed from antenna design examples in different scenarios. Such insights are essential to achieve better antenna performance. In this context, this work focuses on using modal theories to provide innovative antenna solutions that enable 5G and beyond systems to meet their stringent performance requirements, particularly with respect to data rates. These solutions cover different 5G frequency bands: sub-6 GHz bands and mm-wave bands.

For the sub-6 GHz bands, the studies focused on addressing the fundamental challenges of designing high-performance multiple antennas for compact MIMO terminals. The results reveal that the influence of the terminal chassis is the most critical factor in designing MIMO antennas at low frequency bands, especially for sub-1 GHz bands. On the other hand, for the mm-wave bands, the focus is on antenna design for mm-wave automotive radar and communication systems. In this body of work, the challenge is in designing wideband, low-cost, high efficiency and high-gain antennas. Such antennas will also require multiple elements, but as opposed to the requirements of low coupling and correlation in MIMO operation, these array antennas are designed for beamforming gain.

In this context, modal theories have been used as the primary tool to effectively overcome the design challenges and provide systematic design guidelines for the antennas in both sub-6 GHz and mm-wave bands. The specific excitation of the modes and the contribution of individual modes to the radiated power are given particular attention in this thesis. The experimental studies in this thesis are mainly used to validate electromagnetic (EM) field and circuit simulations. The main scientific contributions of the thesis are presented in Papers [I]-[VI], which are included in Part II of the thesis.

1.6 Organization of the Thesis

The thesis consists of two parts: **Part I** and **Part II**.

Part I provides an overview of the research field covered in the included papers in Part II and it contains five chapters. After the general introduction in **Chapter 1** about the antenna challenges and requirements in different applications, **Chapter 2** gives a short introduction of different modal theories and their related parameters, which can yield insight into the radiation phenomena of antennas and thereby a framework for systematic antenna design. This chapter can be seen as an introduction of the theory needed to better understand the systematic antenna design approaches developed and utilized in Papers [I]-[VI].

Chapter 3 examines how the modal theory called Theory of Characteristic Modes (TCM) can be applied for general platform-based antenna design, such as designing MIMO antenna system on a compact mobile terminal by using the terminal chassis as the radiator. This approach is also called the structural antenna concept because it explores the use of the platform structure as the radiator and manipulates/excites the CMs of the structure for antenna design. Another topic in this chapter is about using the TCM to account for user interaction in the design process. Finally, the last section concerns the need for co-designed antenna system for mobile terminals to cover both 28 GHz and sub-6 GHz bands.

Chapter 4 is devoted to multiple antenna design in the mm-wave band (i.e., 30-300 GHz). Among different applications of mm-wave frequencies, *E*-band radar and communication systems are the focus of this Chapter. Two different antenna arrays with different feeding networks are studied and a suitable technology for their implementation in mm-wave frequencies is introduced. Chapter 4 also examines how waveguide/cavity modes are beneficial in the development of high-gain slot array antennas.

Chapter 5 concludes the overview part of the thesis (**Part I**) and summarizes the contributions of each of the doctoral candidate's included papers in this field of research. Possible future work is also discussed.

Part II of the thesis contains the six original research papers that cover the research areas described in Part I. Specifically, Papers [I]-[IV] are mainly related to Chapter 3 in Part I, and Papers [V]-[VI] are related to Chapter 4 in Part I.

Chapter 2

Modal Analysis – An Overview

This thesis is aimed at giving a systematic design strategy for different types of antennas. To some extent, modal analysis can leverage this objective, as it yields information about the modes that can contribute to the radiation of a given antenna structure, how to excite the desired mode(s) with practical feed(s), as well as the actual modal contribution for the chosen excitation. In this chapter, an overview of some types of modal analysis which are useful for systematic antenna design is provided.

2.1 Waveguide/Cavity modes

For many electromagnetic boundary-value problems, there are usually many field configurations (modes) that are solutions that satisfy Maxwell's equations and the boundary conditions. The most known modes are those that are referred to as Transverse ElectroMagnetic (TEM), Transverse Electric (TE), and Transverse Magnetic (TM).

TEM modes are field configurations whose electric and magnetic field components are transverse to a given direction. Often, but not necessarily, that direction is the path that the wave is travelling. TE modes are field configurations whose electric field components are transverse to a given direction, for TM modes the magnetic field components are transverse to a given direction [81]. For example, if the desired fields are TM to z (TM^z), this implies that $H_z = 0$. The other two magnetic field components (H_x and H_y) and three electric field components (E_x , E_y ,

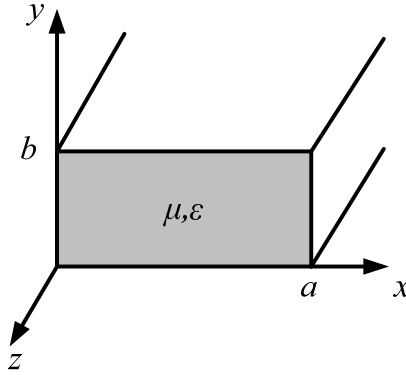


Fig 2.1 Geometry of a rectangular waveguide.

and E_z) may or may not all exist.

There are some methods that utilize the vector potentials (denoted by \mathbf{A} and \mathbf{F} in [82]) to construct TEM, TE, and TM modes. Based on the described procedure in [82] to derive the field expressions that are TM to a given direction, it is sufficient to let the vector potential \mathbf{A} have only a component in the direction in which the fields are desired to be TM. The remaining components of \mathbf{A} as well as all of \mathbf{F} are set to zero.

For example, for TM^z

$$\begin{aligned}\mathbf{A} &= \hat{a}_z A_z(x, y, z), \\ \mathbf{F} &= 0.\end{aligned}\tag{2.1}$$

Then A_z will be derived from a wave equation and the boundary conditions. Once A_z is found, the next step is to use the below equations to find the \mathbf{E} and \mathbf{H} field components below, which is derived from Maxwell's equations [82].

$$\begin{aligned}E_x &= -j \frac{1}{\omega\mu\epsilon} \frac{\partial^2 A_z}{\partial x \partial z}, & H_x &= \frac{1}{\mu} \frac{\delta A_z}{\delta y}, \\ E_y &= -j \frac{1}{\omega\mu\epsilon} \frac{\partial^2 A_z}{\partial y \partial z}, & H_y &= -\frac{1}{\mu} \frac{\delta A_z}{\delta x}, \\ E_z &= -j \frac{1}{\omega\mu\epsilon} \left(\frac{\partial^2}{\partial z^2} + \beta^2 \right) A_z, & H_z &= 0.\end{aligned}\tag{2.2}$$

TE modes can be derived in a fashion similar to the TM fields. This time, however, we let the \mathbf{F} vector potential have a nonvanishing component in the direction in which the TE fields are desired, and all the remaining components of \mathbf{F} and \mathbf{A} are set equal to zero. For example, for TE^z

$$\begin{aligned}\mathbf{A} &= \mathbf{0}, \\ \mathbf{F} &= \hat{a}_z F_z(x, y, z).\end{aligned}\tag{2.3}$$

Then

$$\begin{aligned}E_x &= -\frac{1}{\varepsilon} \frac{\delta F_z}{\delta y}, & H_x &= -j \frac{1}{\omega \mu \varepsilon} \frac{\partial^2 F_z}{\partial x \partial z}, \\ E_y &= \frac{1}{\varepsilon} \frac{\delta F_z}{\delta x}, & H_y &= -j \frac{1}{\omega \mu \varepsilon} \frac{\partial^2 F_z}{\partial y \partial z}, \\ E_z &= 0, & H_z &= -j \frac{1}{\omega \mu \varepsilon} \left(\frac{\partial^2}{\partial z^2} + \beta^2 \right) F_z.\end{aligned}\tag{2.4}$$

where F_z satisfies the wave equation and boundary conditions.

TEM modes are usually the simplest forms of field configurations, and they are usually referred to as the lowest-order modes. Often, we seek solutions for higher-order modes, other than TEM modes. Some of the higher order modes, often required to satisfy boundary conditions, are designated as TM and TE. A classical example of the need for TE and TM modes are the modes of propagation in waveguides. As discussed above, the modes that can be supported by these structures must satisfy Maxwell's equations or the wave equation, and the corresponding boundary conditions.

Waveguides are basically a device for transporting electromagnetic energy from one region to another. Typically, waveguides are hollow metal tubes (often rectangular or circular in cross section). They are capable of directing power precisely to where it is needed, can handle large amounts of power and function as a high pass filter. Hence, most of the energy above a certain frequency (the cutoff frequency) will pass through the waveguide, whereas most of the energy that is below the cutoff frequency will be attenuated by the waveguide [83]. On the other hand, a simple short-end waveguide is usually serving as a cavity. A cavity is a special type of resonator, consisting of a closed (or largely closed) metal structure that confines electromagnetic fields. The cavity structure can be either hollow or filled with dielectric material [83].

An empty rectangular waveguide of lateral dimensions a and b and with infinite length is shown in Fig 2.1. It can be shown that modes TE^x , TM^x , TE^y , TM^y , TE^z , and TM^z satisfy the boundary conditions of Fig 2.1, which are

$$\begin{aligned}E_x(0 \leq x \leq a, y = 0, z) &= E_x(0 \leq x \leq a, y = b, z) = 0 \\ E_z(0 \leq x \leq a, y = 0, z) &= E_z(0 \leq x \leq a, y = b, z) = 0 \\ E_y(x = 0, 0 \leq y \leq b, z) &= E_y(x = a, 0 \leq y \leq b, z) = 0 \\ E_z(x = 0, 0 \leq y \leq b, z) &= E_z(x = a, 0 \leq y \leq b, z) = 0.\end{aligned}\tag{2.5}$$

Then the appropriate expressions for the TE_{mn}^z modes using (2.4) and (2.5) are [82]

$$\begin{aligned} E_x &= A_{mn} \frac{\beta_y}{\varepsilon} \cos(\beta_x x) \sin(\beta_y y) e^{-j\beta_z z}, & H_x &= A_{mn} \frac{\beta_x \beta_z}{\omega \mu \varepsilon} \sin(\beta_x x) \cos(\beta_y y) e^{-j\beta_z z}, \\ E_y &= -A_{mn} \frac{\beta_x}{\varepsilon} \sin(\beta_x x) \sin(\beta_y y) e^{-j\beta_z z}, & H_y &= A_{mn} \frac{\beta_y \beta_z}{\omega \mu \varepsilon} \cos(\beta_x x) \sin(\beta_y y) e^{-j\beta_z z}, \\ E_z &= 0, & H_z &= -jA_{mn} \frac{\beta_c^2}{\omega \mu \varepsilon} \cos(\beta_x x) \cos(\beta_y y) e^{-j\beta_z z}. \end{aligned} \quad (2.6)$$

where β_{mn} are propagation constants and A_{mn} is an arbitrary amplitude constant. The cutoff frequency of a given mn mode is derived from

$$(f_c)_{mn} = \frac{1}{2\pi\sqrt{\mu\varepsilon}} \sqrt{\left(\frac{m\pi}{a}\right)^2 + \left(\frac{n\pi}{b}\right)^2}. \quad \begin{cases} m=0,1,2,\dots \\ n=0,1,2,\dots \\ m=n \neq 0 \end{cases} \quad (2.7)$$

Modal analysis has long been used in electromagnetism for the analysis of close structures like waveguides and cavities (with canonical shape), in which it is relatively easy to arrive at close solutions such as (2.6), even for structures of non-separable geometry, by applying boundary conditions [83], [84]. For a closed Perfect Electric Conductor (PEC) object, the internal resonances can be related to non-radiating resonant cavity modes. This kind of modal analysis is only helpful for the design of special type of antennas which are based on waveguide or cavity structures (See Chapter 4). Otherwise, the calculation of modes in open radiating structures is needed, which is more complex and usually quite time-consuming.

In Paper [V], cavity modes are used to design the slot antenna array, including the SIW cavity. This choice is based on the special antenna type and the physical insights cavity modes bring to the radiating phenomena taking place on the antenna.

2.2 Spherical Wave Modes

Unlike cavity/waveguide modes, which are confined within guided media, modal theory in the form of spherical wave expansion [85] can deal with radiating currents and fields. The radiating properties of canonical structures (e.g., a sphere or a spherical shell) can be quantified in analytical form, which improves the understanding of radiation mechanisms and how to manipulate them.

The Spherical Vector Waves (SVWs) form a complete set of orthogonal Eigenvector functions for the radiated electromagnetic fields [86]-[89]. A review of the available literature on modal analysis shows that the first modal approach to analyze antennas was devised by Chu in 1948 [90], and subsequently Harrington in 1960

[14], when they tried to determine the fundamental limitations of antennas. They postulated that, since any radiating electromagnetic field can be written as a sum of SVWs, the antenna can be enclosed in a sphere. Then, the radiated power of the antenna is calculated from the propagating modes within the sphere, while all modes contribute to reactive power. Hence, studying the behavior and interactions of these vector waves in a specific propagation condition will fully characterize the wireless environment [91], [92].

2.3 Modal Expansion Methods

In the seventies, other more general modal expansion methods were developed [93], [94]. These methods are based on expanding the fields radiated by an antenna in terms of planar, cylindrical or spherical wave functions. Next, the coefficients in the expansion are determined by measuring the near fields of the antenna.

When applying modal expansion methods, first the entire domain of interest should be divided into a number of subregions. Then, field expressions in all these subregions are expanded into the summation of their modal functions weighted by unknown coefficients. By enforcing the continuity conditions of tangential field components across the regional interfaces, one can then determine these expansion coefficients. Based on the obtained field expressions, the current distribution along the surface of the antenna can be readily calculated. Finally, the input impedance and radiation pattern of the antenna can be computed from the known current distribution.

2.4 Characteristic Modes

Unlike SWVSs, characteristic modes (CMs) provide a versatile and straightforward tool to analyze the inherent resonance properties of any arbitrarily shaped radiating structure [95], [96]. TCM is an analysis tool that allows resonant antennas to be understood in the same way as a guitar string resonating when it is played [99]. Similar to a guitar string resonating and releasing acoustic waves in different frequencies and harmonics according to string tension and boundary conditions, upon being plucked (i.e., excited), an object can resonate to radiate electromagnetic waves in different “harmonics” (modes) in response to an external excitation, be it near field (i.e., an antenna feed) or far field (i.e., an incident plane wave). The ability to extract the detailed resonance properties independently of the excitation makes CMs particularly suitable for designing and analyzing radiating and scattering objects [99]. CMs share with SVWs in Section 2.2 the property of orthogonal far fields and they further introduce a modal ratio of the reactive power to the radiated power, which is an important physical measure. Moreover, as in the waveguide/cavity modes in Section 2.1, the most valuable feature of CMs is that

they provide the resonance properties of the object in question without considering the excitation source [96]. In publications [I]-[IV], [VI] antennas are designed using TCM. The choice is based on the mathematical properties of CMs, and on the physical insights they bring to the radiating phenomena taking place on the antenna.

2.4.1 Introduction to TCM

TCM was originally formulated in the late 1960's in an effort to fundamentally understand how an object scatters electromagnetic energy [95]. CMs was formulated by Garbacz in 1968. The CMs defined by Garbacz correspond to the eigenvectors of a weighted eigenvalue equation [95]. These modes have the useful property of being orthogonal over both the source region and the sphere at infinity.

In 1971, Harrington and Mautz obtained the same modes defined by Garbacz by diagonalizing the operator relating the current to the tangential electric field on the body [96], [97]. The advantage of the formulation described in [96], known as the TCM, is that it leads to a simpler derivation of the theory than the one proposed by Garbacz in [95], and it is valid for conducting bodies of arbitrary shape. Afterwards, Harrington et al. extended the formulation of the Theory of Characteristic Modes to encompass dielectric, magnetic, and both dielectric and magnetic bodies [98].

Garbacz only calculated the CMs of a few canonical obstacles [95]. Today, more than 50 years later, the theory is almost the same. But advances in computing power, computational electromagnetics and modern algorithms have enabled CMs to be calculated and used for far more complex structures [100].

2.4.2 TCM Formulation for Conducting Bodies

The formulation of the TCM for conducting bodies begins with the definition of an operator equation that relates the current \mathbf{J} on the surface S of a conducting body with the tangential incident electric field \mathbf{E}^i [96]

$$\left(\ell(\mathbf{J}) - \mathbf{E}^i\right)_{tan} = 0, \quad (2.8)$$

where the ℓ operator represents an integral equation that relates the tangential current to the electric field and the null on the right-hand side of the equation indicates the absence of the excitation source. The ℓ operator has a dimension of impedance (Ω), as it transforms the surface current density (A/m) into an electric field (V/m) [96]

$$\mathbf{Z}(\mathbf{J}) = (\ell(\mathbf{J}))_{tan}. \quad (2.9)$$

The impedance operator \mathbf{Z} is complex, and it can be written as $\mathbf{R} + j\mathbf{X}$, where \mathbf{R} and \mathbf{X} are the real and imaginary parts of the impedance operator \mathbf{Z} .

The characteristic attributes (CAs) of an object can be used to obtain many physical insights including the proper location of an excitation element, variability between structures, and isolation between excitation ports. CAs can be feed-independent (e.g., characteristic eigenvalues, modal significance, characteristic currents and characteristic currents far-fields) or feed-dependent (e.g., modal excitation coefficient (MEC) and modal weighting coefficient (MWC)), which will be discussed further in the next two subsections.

2.4.3 Feed-independent Characteristic Attributes

Characteristic current modes can be obtained as the eigenfunctions of the following particular weighted eigenvalue equation

$$\mathbf{X}(\mathbf{J}_n) = \lambda_n \mathbf{R}(\mathbf{J}_n), \quad (2.10)$$

where λ_n are the eigenvalues, \mathbf{J}_n are the eigenfunctions or eigencurrents. It is known from reciprocity theorem that if \mathbf{Z} is a linear symmetric operator, then, its Hermitian parts (\mathbf{R} and \mathbf{X}) will be real and symmetric operators. From this, it follows that all eigenvalues λ_n are real, and all the eigencurrents \mathbf{J}_n can be chosen to be real or equiphase over the surface in which they are defined [96]. Moreover, the choice of \mathbf{R} as a weighting operator in (2.10) is responsible for the orthogonality properties of CMs described in [96], which can be summarized as

$$\begin{aligned} \langle \mathbf{J}_m, \mathbf{R}(\mathbf{J}_n) \rangle &= \delta_{mn}, \\ \langle \mathbf{J}_m, \mathbf{X}(\mathbf{J}_n) \rangle &= \lambda_n \delta_{mn}, \\ \langle \mathbf{J}_m, \mathbf{Z}(\mathbf{J}_n) \rangle &= (1 + j\lambda_n) \delta_{mn}. \end{aligned} \quad (2.11)$$

where δ_{mn} is the Kronecker delta function (i.e., taking the value of 0 if $m \neq n$ and 1 if $m = n$).

Consistent with (2.10), the characteristic currents \mathbf{J}_n can be defined as the real currents on the surface of a conducting body that only depend on its shape and size and are independent of any specific source or excitation. Moreover, the characteristic electric far fields (i.e., \mathbf{E}_n) produced by characteristic currents \mathbf{J}_n on the surface of a conducting body, form an orthogonal set [96]

$$\frac{1}{2Z_0} \iint_{S^\infty} \mathbf{E}_m \cdot \mathbf{E}_n^* dS = \delta_{mn}, \quad (2.12)$$

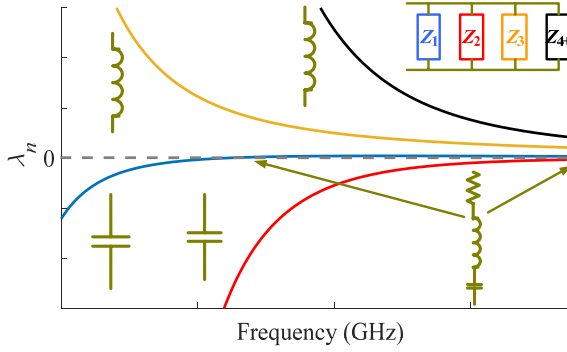


Fig 2.2 Interpretation of characteristic eigenvalues in frequency.

The eigenvalues can be defined mathematically by

$$\lambda_n = \frac{\langle J_m, X(J_n) \rangle}{\langle J_m, R(J_n) \rangle} = \frac{2\omega(\overline{W}_m - \overline{W}_e)}{P_e}, \quad (2.13)$$

where W_e and W_m are stored magnetic and electric energy, respectively, and P_e is the radiated power defined in the Poynting theorem.

Hence, the eigenvalue of a CM can be used for a physical interpretation. The difference between the stored energies defines when an object is in a resonant, capacitive, or inductive state. These energy states are akin to a simple Resistive, Inductive, Capacitive (RLC) circuit where the electric and magnetic energies are stored by a capacitor or an inductor, and power is dissipated in the circuit by means of a resistor (see Fig 2.2). When analyzing a lossless object using TCM, the resistor represents the power dissipated by the antenna through far-field radiation. When $\lambda_n = 0$, the stored energies are equal, as can be seen in (2.11). When $\lambda_n < 0$, there is more electric energy than magnetic energy stored over any given frequency cycle, and the CM is defined to be capacitive. Finally, when $\lambda_n > 0$, more magnetic energy than electric energy, and the CM is inductive.

Based on the definition of λ_n , it has a range of $[-\infty, +\infty]$. Another CA, the so-called modal significance (MS) has the range of $[0, 1]$ and it is defined as

$$MS_n = \left| \frac{1}{1 + j\lambda_n} \right|. \quad (2.14)$$

The modal resonances coincide with the maxima of the MS_n curves (i.e., $MS_n = 1$), where no net energy will be stored in the near field and the contribution of each mode to the radiation reaches the maximum. MS_n can also be used to determine the

modal radiation bandwidth, i.e., the modal bandwidth (BW_n). The half-power radiating bandwidth can be approximated using

$$BW_n \approx \frac{f_H(MS_n = 1/\sqrt{2}) - f_L(MS_n = 1/\sqrt{2})}{f_{res}(MS_n = 1)}. \quad (2.15)$$

In (2.15), f_H and f_L are the high and low frequency band edges of any local maximum, at which the MS is equal to or greater than 0.707. f_{res} is the resonant frequency where $MS_n = 1$ or at the maximum value. It is important to understand that the modal bandwidth corresponds to the radiated pattern's half-power bandwidth (for single-mode excitation) and not the impedance bandwidth of an excited structure.

The base eigenvalue equation for TCM as shown by (2.10) can be solved through discretization of the operators using MoM, where \mathbf{Z} is decomposed into a discrete set of popular Rao-Wilton-Glisson (RWG) basis functions [97]. When properly carried out, the MoM reduces the operators \mathbf{Z} , \mathbf{R} , and \mathbf{X} into a set of $N \times N$ matrices defined by $[\mathbf{Z}]$, $[\mathbf{R}]$, and $[\mathbf{X}]$. Additionally, the eigenvector \mathbf{J}_n is transformed into the $N \times 1$ vector $[\mathbf{J}_n]$. This transforms the TCM operator equation (2.10) into the TCM matrix equation.

2.4.4 Feed-dependent Characteristic Attributes

CMs are real current modes that can be computed numerically for conducting bodies of arbitrary shape. Since CMs form a set of orthogonal functions, they can be used to expand the total current on the surface of the body. Once the characteristic currents are found, different associated feed-dependent CAs can be derived.

Due to the mentioned orthogonality properties over both the surface of the body and the enclosing sphere at infinity, characteristic modes radiate power independently of one another. Because of this attractive feature, characteristic modes can be used as a basis set in which to expand the unknown total current \mathbf{J} on the surface of the conducting body as

$$\mathbf{J} = \sum_{n=1}^N \alpha_n \mathbf{J}_n, \quad (2.16)$$

where α_n are the MWCs. By substituting (2.16) in to (2.8) and some simple calculations α_n can be calculated as

$$\alpha_n (1 + j\lambda_n) = V_n^i, \quad (2.17)$$

$$V_n^i = \langle \mathbf{J}_n, \mathbf{E}^i \rangle = \iint_S \mathbf{J}_n \cdot \mathbf{E}^i dS. \quad (2.18)$$

Equation (2.18) is referred to as MEC, and it defines a characteristic current's relationship to the position, magnitude, phase and polarization of an applied excitation. Once coefficients α_n have been obtained from (2.17), equation (2.16) can be expressed as

$$\mathbf{J} = \sum_{n=1}^N \frac{V_n^i J_n}{1 + j\lambda_n}. \quad (2.19)$$

Formulation (2.19) shows the key factors influencing the significance each CM has to a radiated field. Apart from the MECs which represent the influence of an excitation source, the weighting factor (2.19) is the MS in (2.14), as it represents the amplitude each characteristic current contributes to the total radiated field.

2.4.5 Eigenvalue Tracking

TCM provides insights into the electromagnetic characteristics of an object when calculated at a single frequency. However, when characteristic eigenvalues are plotted, the eigenvalues are traditionally ordered with respect to the frequency at which each eigenvalue crosses its resonance. To combat the randomness of plotting eigenvalues across frequency, different eigenvalue tracking algorithms have been used [101]-[103]. In this thesis, the eigenvalue tracking is based on the far-field tracking method in [103]. In this method, the far-field pattern of each individual mode is tracked over frequency.

The first step in the algorithm for far-field tracking is to sort the eigenvalues in ascending order from the lowest to the highest. Second, the far-field patterns must be individually cross-correlated with the far-field patterns at subsequent frequency steps. If modes are highly correlated, the linking matrix is recorded to track those two modes across frequency [103].

2.4.6 Application of TCM to Antenna Design

Typically, antennas are synthesized using different computational electromagnetic solvers through a complex optimization process, where the feeding structure, feed location and object shape are all changed independently in an effort to obtain the best antenna performance. That is mainly because computational electromagnetic solvers (e.g., FEM, FDTD, and MoM) are based on numerical approximations of Maxwell's Equations. These solvers often require a physical excitation to excite an object before insights can be obtained. Although an antenna's radiation performance is fundamentally limited by its shape and material, typical analysis tools are not well suited for antenna optimization as feeding structures are required. Whereas all

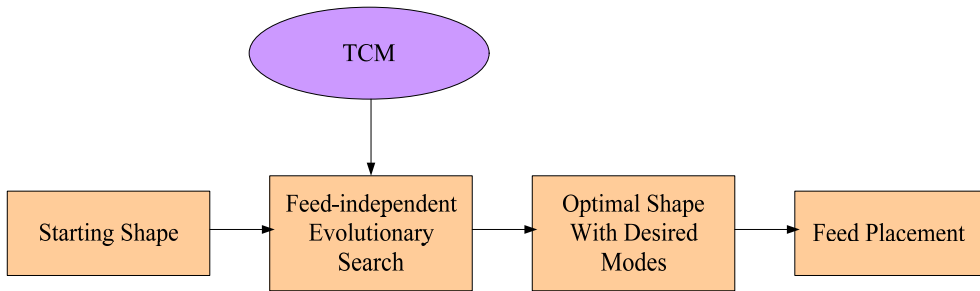


Fig 2.3 The design flow for TCM-assisted feed-independent antenna synthesis.

computational electromagnetic solvers have specific advantages, TCM is rather unique. This is due in part to TCM not requiring the placement of excitation sources when determining the electromagnetic properties of an analyzed object. This makes TCM perfectly suited for antenna synthesis algorithms, as it can analyze the radiation performance of the object without requiring any excitation structure.

Broadly speaking, TCM offers two distinctive properties for antenna design: 1) It decomposes the antenna response into constitutive parts (i.e., the CMs), which make it easier to study and control the antenna's radiation properties than relying only on the total response, 2) It gives valuable information about the properties of the antenna structure irrespective of the feed, which allows for a more fundamental analysis of the structure, which is not limited by a specific feed choice.

However, as the CM concept was originally explored for electromagnetic scattering [95], TCM were at first applied to scattering [104]-[106]. As TCM provides a complete set of the orthogonal radiated far-field patterns that an object can radiate, it is perfectly suited for pattern synthesis and scattering problems.

A few years later, the antenna applications of TCM were introduced, firstly on platform-based small antenna analysis [107] and antenna shape synthesis [108]. However, strictly speaking TCM did not initially receive much attention from the antenna community, until the first TCM overview article was published in 2007 [109], which showed the practical value of acquiring the modal reactive power, current and fields, by using these attributes to simplify the design of various real-life antennas, including patch antenna, reflect array, planar monopole and mobile terminal antennas.

After TCM is introduced as a viable and efficient tool for the analysis and design of antennas, many antenna researchers started working in this area and showed how TCM provides a step-by-step deterministic approach to antenna design [109]-[113]. In the following, the progress of antenna design on conducting bodies using TCM are summarized in three different categories: 1) single-element antennas, 2) platform antennas, and 3) multi-element antennas.

Single-Element Antenna

TCM has been shown to be effective for enhancing the performance of existing single-element antenna structures. In this section, we investigate the progress on the design of some single-element antenna structures, including multiport antennas, circularly polarized antennas, reconfigurable antennas, wideband antennas and dielectric resonator antennas (DRAs).

- Multiport Antennas

The orthogonal radiation patterns of CMs make TCM a very proper choice for MIMO antenna design. If two different CMs are selectively excited by two different antenna ports, then the ports are guaranteed to yield low mutual coupling. Unlike the platform antenna design concept, which will be discussed in the next section, in this part the focus is on redesigning the antenna element to support multiple modes and normally the design process will start with a canonical shape. For example, by analyzing a canonical structure such as a wide-loop antenna in [114], it was found to support four modes with low eigenvalues and different resonant frequencies. By selectively placing capacitive gaps at positions where some modes have current nulls, their eigenvalues, and thus resonant frequencies, can be controlled somewhat independently and the resonances are moved near each other for MIMO operation.

Another way of implementing multimode operation for multiport antennas is via shape synthesis. One advantage of using TCM-based antenna synthesis approach for multiport antennas is that it avoids imposing unnecessary constraints arising from pre-defining a feed, which allows for a more thorough exploration of the design space. For instance, in [115], a feed-independent shape synthesis technique for multiport antennas is developed, where the modal properties (resonant frequency and Q factor) of several modes are included in the cost function for the shape synthesis. A two-port MIMO antenna system is designed in [116] using the TCM-assisted shape-first, feed-next design technique, which is illustrated in Fig 2.3.

After the shape synthesis using TCM, the feed design is the next step. However, the feed design of a MIMO antenna is challenging, since a single feed which is intended to excite one mode will often excite multiple modes, and this increases the coupling between the ports. Again, TCM can give insight to this problem, which can be addressed by using a mode-decoupling technique for MIMO antenna design [117]. In this technique, a mode-decoupling network maps the physical antenna ports that excite several CMs to MIMO terminal ports by combining their currents with varying magnitude and phase. For instance, [118] shows a four-port MIMO antenna that extracts the desired modes over the four ports from eight physical excitation points (on each single-element antenna) using a combination of power dividers.

- Circularly Polarized (CP) Antennas

CMs can help us obtain CP radiation as they have orthogonality in the currents and radiated fields. The conditions to obtain CP of the field radiated by an antenna can be easily defined in terms of CMs: first, two modes with orthogonal linear polarization must exist with the necessary 90° phase difference between their CAs, and second, both modes must exhibit the same MS at the working frequency f_0 .

We can start the process with known designs and enhance their CP operation by analyzing the modal currents and eigenvalues [119], [120]. For example, by the insights provided from TCM, more than two CMs can be produced in a microstrip patch antenna with the proper amplitude–phase condition to widen the CP frequency bandwidth [119]. The physical insight provided by TCM also allows for control over the levels of the cross-polar radiated fields. Furthermore, the CP bandwidth can be broadened by using three pairs of CMs [120].

- Reconfigurable Antennas

The reconfigurability function of an antenna can involve its radiation pattern shape, polarization as well as working frequency. Reactive loading is one of the techniques that can be used for controlling the modal resonance [105].

Again, TCM is well suited for utilizing reactive loading as the impedance matrix \mathbf{Z} in (2.9) provides valuable insights into how to modify a structure's radiation properties using reactive components. It also provides a set of characteristic currents that offer critical insights into the optimal placement of reactive elements. By the proper use of TCM, this method can lead to enhanced antenna bandwidth [121], frequency reconfigurability [122], main lobe reconfigurability [123] and polarization reconfigurability [124].

- Wideband Antennas

Strictly speaking, TCM offers two techniques for designing wideband antennas: 1) the excitation of wideband mode(s) and 2) a combination of multiple nearby narrowband modal resonances. These two techniques can also be combined to significantly enhance the bandwidth of an antenna element [125]. As an example of the first technique in [126], the bandwidth of a microstrip patch has been increased to 46% by optimizing the feed structure. For the second technique, nearby resonant modes can be synthesized by modifying the geometry of the antenna or by loading the antenna with foster or non-foster elements to shift the resonant frequencies of some mode(s) close to those of the other modes, thus increasing the total bandwidth. By using the second technique [127] the bandwidth of a simple dipole has been increased from 1.8% to 11.2% [127].

- Dielectric resonator antennas (DRAs)

Traditionally, DRAs based on canonical geometries are analyzed by using approximate analytical formulas. However, TCM leverages similar physical insights to DRAs of more complex geometries, where analytical solutions are impossible. That is mainly because TCM enables the direct study of stored energies and Q factors of DRAs unconstrained by the feed choice, which leads to new design strategies for noncanonical DRAs [128]. The TCM-based shape synthesis techniques that have been discussed earlier for multiport antennas can also be applied to DRAs, to enable DRAs to be used for MIMO and wideband applications [129].

Platform Antennas

In the previous subsection, a few CM-based standalone antenna elements were highlighted. However, antennas are usually placed on platforms in practical applications, which in most cases have the role of supporting structure for antennas. These platforms are normally conducting bodies and the size of the platforms is comparable to the operating wavelength in some antennas such as vehicular [130]-[132] and terminal antennas [31], [40]. In those applications, using stand-alone antennas with large sizes is not possible. Hence, electrically small antennas that utilize the CMs of their platforms for radiation have recently attracted much attention, especially since the platform's CMs can compensate for the small antennas' inherently limited bandwidth and low radiation efficiency [90]. CM-based platform-integrated antenna design takes advantage of the resonant modes of the platforms to achieve the desired properties, such as multiband/wideband operation, polarization or pattern reconfigurability, high isolation among the ports (in the case of multiport antennas) and high gain. Two main platform-based antennas have been vehicular antennas and terminal antennas. In Chapter 3, more details on CM-based platform antenna design for mobile terminal is provided.

Multi-Element Antennas

Multiple element antennas include antenna arrays of multiple radiating elements fed by one single signal port, arrays of multiple antennas fed by multiple signal ports simultaneously, and combinations thereof. CMs are useful for tackling the challenges at the different levels of multi-element antenna design, including the element, inter-element, and array levels.

At the element level, as discussed in the subsection of "Single-Element Antenna", CMs can be used to control important parameters for the overall array design, for instance, the control of the element radiation pattern [133] and polarization [124], the element size, the impedance bandwidth [134], and the number of uncorrelated ports [135].

At the inter-element level, CMs can be used to explore the interaction of two or more antenna elements in close proximity [136]-[138]. The principal task is to identify those modes that are responsible for the mutual coupling. Having identified the principal coupling mechanisms, countermeasures can be utilized to suppress those modes that are responsible for the coupling. In this case, more modes need to be taken into account as compared to a conventional modal analysis, as mutual coupling does not rely only on radiation mechanisms due to significant modes, but also on reactive coupling due to higher-order modes [138].

Finally, at the array level, a modal analysis of the whole array can be conducted to gain a more thorough understanding about its electromagnetic behavior, e.g., with respect to edge effects or surface wave propagation. As antenna arrays belong to the class of electrically large problems, efficient computation techniques are useful for such analyzes [139]. An alternative analysis technique for antenna arrays is the characteristic port-mode method in [106], [117], which instead of performing a modal analysis of the whole array, the array is represented by its port impedance matrix. This technique has the advantage of considerably reducing the computation space. By this technique, the implementation of multi-element antenna features, such as pattern synthesis, beam shaping and beam steering, are also enabled [140],[118].

The far-field pattern shape is determined only by the currents on the object, and as TCM provides a unique set of currents that provide orthogonal far-field patterns, it can be used to better understand multi-element antenna systems.

Chapter 3

Compact Multiport Terminal Antenna

The ground planes of the printed circuit board (PCB), EMC shielding and other electrically conductive parts (like display and its frame) of a handheld device create an RF ground plane, called a chassis. The chassis, being the platform of the terminal antennas, brings some challenges to terminal antenna design. Due to the inherent physical limitations described in Chapter 1, the implementation of small internal wideband cellular antennas is challenging across the low band (below 1 GHz), with the typical matching criterion (6 dB return loss) of current cellular antennas. The traditional self-resonant antenna solutions, as introduced in Chapter 1, might not be viable to provide wideband operation with rather thin and small antenna structures. In addition to bandwidth, as also described in Chapter 1, severe mutual coupling caused by the limited implementation space also makes multi-antenna design in terminal devices more challenging.

The chassis in terminal antennas can easily become part of the radiator, which contributes to the antenna performance and has a significant effect on the impedance and radiation properties of the antennas. It can even become the dominant radiator especially in the low band used in mobile communications [141]. That is because the modern handset chassis length is typically around 150 mm, which roughly corresponds to half-a-wavelength for the low band used in mobile communications. Therefore, the chassis needs to be considered in the antenna design process. It will be shown in this chapter that the CM-based platform-integrated antenna concept described in Chapter 2 can be of great help, as the entire platform is considered as part of the radiator. This concept leads to the increased radiation aperture due to the

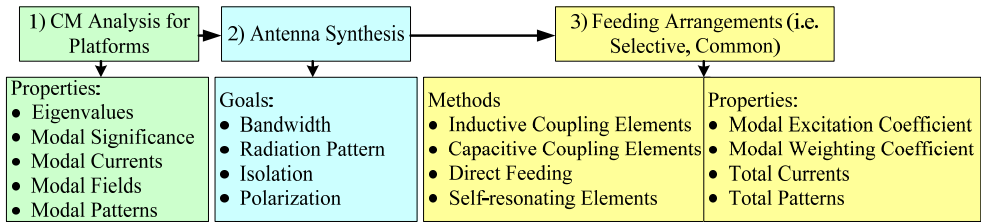


Fig 3.1 A general flow chart for platform- based antenna designs using TCM.

large platform (i.e., chassis) size. Furthermore, the coupling between the antenna and chassis is explicitly considered and even exploited during the design process, which transforms the problem of coupling into an opportunity. Thus, the original antennas function primarily as electromagnetic coupling elements for CMs, making it easier to design a low-profile, compact antenna structure that does not affect the chassis' original structural characteristics. Specifically, in Chapter 2 it is demonstrated that TCM is also suited for MIMO antenna systems and different CMs can be used for different ports. On the other hand, unlike the CM-based antennas described in Chapter 2, which always operate in free space, the design of handset antennas should also consider their interactions with the human body.

This chapter describes the way the chassis can be exploited as a part of the MIMO antenna system in future smartphones using CMs. It will be shown how CMs can be excited through various coupling-based feeds. Based on this idea, the optimal location and configuration of such coupling feed elements on the chassis are investigated for several scenarios. In the meantime, TCM can also alleviate the negative interactions among the antenna ports in the MIMO antenna system, leading to higher antenna efficiency and lower SAR values. Finally, co-integration of sub-6 GHz antennas with 5G mm-wave antennas in the 28 GHz band in a mobile terminal is investigated.

Based on the results obtained for this topic in Papers [I]-[IV] of this thesis, it can be concluded that TCM is beneficial in the development of 5G and beyond terminal antenna systems.

3.1 General Design Procedure of Platform-Integrated Antennas

In addition to benefiting from the possible usage of the platform (e.g., chassis), the physical insights from TCM allow us to formulate a practical and systematic procedure to design platform-integrated antennas. Fig 3.1 presents a general flowchart for platform-based antenna design using CMs, which follows three stages:

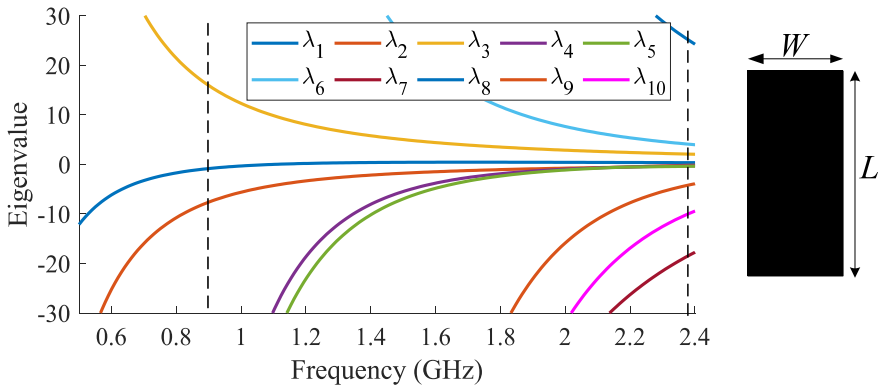


Fig 3.2 Characteristic eigenvalues of solid PEC chassis. $W = 60, L = 120$ (units: mm).

- 1) Perform CM analysis for the target platform in the frequency bands of interest and obtain critical modal information, such as modal currents, modal fields, modal patterns, and modal significances (see Chapter 2). Identify desired and unwanted modes.
- 2) Synthesize antennas based on the CMs of platforms for achieving the required properties, including, but not limited to, the bandwidth, beam shape, polarization, and number of ports.
- 3) Design exciters for the synthesized currents or near fields. Find appropriate feeding schemes including the exciter, power divider, and matching networks and integrate them onto the platform.

The above-mentioned design stages will be described in more details in the following subsections, especially in the case of MIMO antenna design for handsets.

3.1.1 Characteristic Attribute Analysis

TCM provides a useful tool to study the radiation characteristics of the CMs of a platform. It is possible to numerically calculate the resonant frequencies and the maximum obtainable radiation bandwidth of each mode can be obtained from the frequency response of the eigenvalue. For instance, Fig 3.2 shows the eigenvalues of a typical-size PEC rectangular plate (used as a chassis model) from 0.4-2.4 GHz. As also mentioned, the chassis of the handset is an important radiator, as its largest typical dimension (i.e., the length) corresponds to 0.5–1.5 wavelengths for the different cellular bands within 0.9-3 GHz. As can be seen in Fig 3.2, for the chassis of a single rectangular plate, there is only one mode resonating in frequency bands below 1 GHz (i.e., λ_1), and it has a large bandwidth. As the frequency increases, more significant modes appear. At around 2.4 GHz, the number of significant rises to four or five. Due to the different number of available modes, the method to design

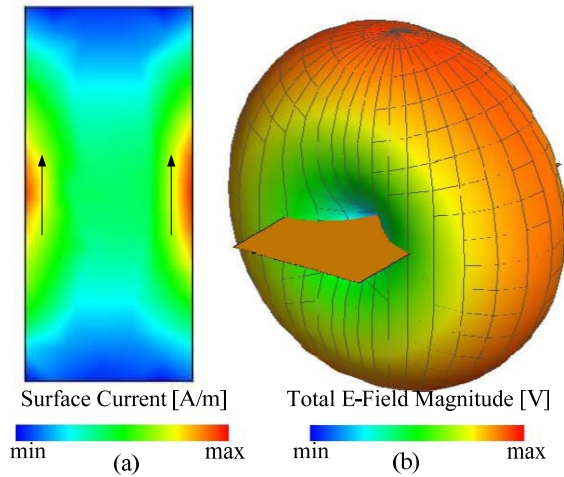


Fig 3.3 Characteristic (a) current and (b) far-field pattern of the first mode of the solid 120 mm \times 60 mm PEC chassis.

low-band antennas is different to that for high-band ones. Fig 3.3 shows the modal current and far-field pattern of the fundamental mode (i.e., λ_1) of the 120 mm \times 60 mm chassis at the resonant frequency.

3.1.2 Antenna Synthesis

Generally, if the required bandwidth or number of ports is not met by any single CM, this means that the structure may not support the intended application or multi-mode excitation may be required. However, if any near-resonant mode (e.g., $|\lambda| < 15$) supports the requirements, the resonant properties of that mode should be further analyzed to determine if the structure can be optimized to force that mode into resonance. This can be done for example through modifying the structure's shape. For example, in Paper [I], minor structural changes can yield up to four additional resonant modes below 1 GHz, and in Paper [II]-[III], new modes were introduced by considering the display screen in the chassis model.

The insights gained from CM analysis in stage 1 provide an engineer with the knowledge necessary to correctly optimize an object before designing the excitation for each antenna port in the next stage.

3.1.3 Coupling-based Exciter Design

The original TCM described in Chapter 2 is based on applying a plane wave excitation on a chassis. However, in mobile terminals a certain coupling structure is

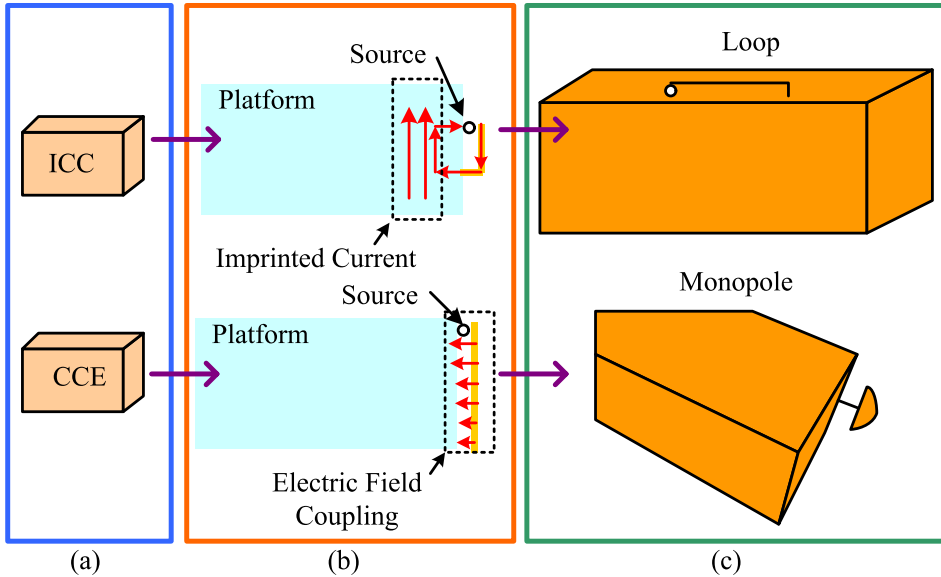


Fig 3.4 (a) Typical coupling element (exciter) types, (b) working principles, (c) exciter structures.

required to excite the chassis CMs. This coupling structure can be either the self-resonant or non-resonant type.

Traditional mobile terminal antennas, such as PIFA, create the antenna resonance and couple to the CMs' electric near fields of the chassis. A large part of the antenna element volume is "wasted" for creating the resonance [12]. Since the antenna element itself is not a significant radiator below 1 GHz, the volume occupied by the element can be decreased significantly by introducing compact non-resonant coupling elements, whose principal function is to only couple the ports to the CMs without contributing too much to the radiation [37]. Since the coupling-element structure itself is non-resonant, separate matching circuitry outside the coupling structure is needed. Therefore, to achieve the minimum volume of the coupling structure while providing sufficient bandwidth, one needs to exploit the chassis by maximizing the coupling to the chassis CMs [37]. Although the inclusion of circuit simulations makes the antenna design more complex, it is worthwhile to consider non-resonant antennas in mobile terminals. This is because the coupling element has a higher bandwidth-to-element-volume ratio than the PIFA by its ability to excite the chassis CMs more strongly than the PIFA. Self-resonant antennas can also be optimized to efficiently excite CMs. However, due to the considerable size of self-resonating antennas, the CMs of the platform should be recalculated for accurate analysis (if the self-resonant antennas are used as the exciters). Self-resonating antenna is more feasible as an exciter at higher bands due

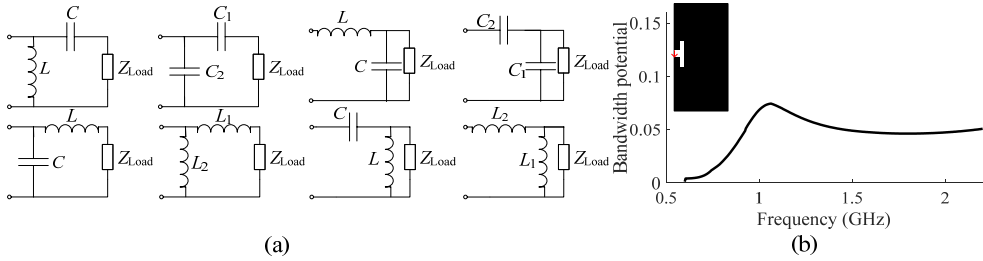


Fig 3.5 (a) Eight possibilities for single-frequency lumped element matching network, (b) bandwidth potential of the single ICE.

to its smaller physical size at those bands.

Different non-resonant coupling structures can be categorized according to the way the coupling is achieved. The CM currents on the edges of the chassis can be created via electric or magnetic fields and/or using galvanic coupling, all of which are well-known electromagnetic near-field phenomena. The galvanic coupling is often implemented through a direct feed (i.e., a voltage source) across an impedance discontinuity, such as a slot. In addition to the direct feed and self-resonating elements, there are two kinds of coupling elements for CM excitation, namely, inductive coupling elements (ICEs) and capacitive coupling elements (CCEs) [142], [18]. Fig 3.4 illustrates the element types, working principles, structures, and locations of excitors. An ICE excites its corresponding mode by the impressed current, as shown in the top part of Fig 3.4(b). Thus, an ICE is usually placed at a maximum of the modal current (minimum of the modal electric field), as shown in Fig 3.6(a). The basic structure of an ICE is a loop [144]. In contrast, a CCE excites its corresponding mode through electric field coupling, as shown in the bottom part of Fig 3.4(b). Thus, a CCE is usually placed at a maximum of the modal electric field (a minimum of the modal current) to be able to couple most strongly to the desired CM (see Fig 3.6(a)). The basic structure of a CCE is a monopole whose performance can be enhanced by loading and bending techniques [18]. In Papers [I], [II], [III], and [IV], direct/self-resonant feeds, CCE/direct feeds, ICE/direct feeds, and CCE feed are applied, respectively.

Effect of CM Frequency Evolution on Excitation

The performance of a chosen excitation type and location will be influenced by CA variation over frequency. Since characteristic currents, near fields, and far fields constantly evolve over frequency, it is often necessary to determine how the effect of an excitation will change over the bandwidth to which it is applied. If the CMs of an object have large bandwidths, the frequency evolution often becomes more relevant. For instance, if a rectangular PEC plate's CMs are computed across the full bandwidth of the fundamental resonance, the near fields change significantly

over the fundamental mode's bandwidth, whereas the location of maximum currents does not change. This indicates that the object can be more effectively excited across the entire modal bandwidth if it is fed using an ICE in Paper [XVIII] rather than a CCE as in Paper [XVI].

Tools for Excitation (Feed) Design

TCM-based algorithms can be developed to synthesize or optimize the shape and material of an object and predict the best locations to implement excitation structures. After an object is optimized, other computational analysis tools can be utilized to synthesize and optimize the feeding structures in the areas predetermined by TCM analysis. Here, we focus on the use of non-resonant coupling elements as the feed. There are a few useful tools which can help the coupling element design process. Firstly, we need to use a merit called bandwidth potential, which can reveal the maximum obtainable bandwidth of each mode. Moreover, feed-dependent CM-based merits called MEC and MWC show the effectiveness of the modal excitation. In Papers [I]-[IV], these concepts are found to be very useful as supporting tools in the optimization of coupling element designs.

- Bandwidth Potential

Non-resonant antennas must be matched with external circuits to realize satisfactory impedance matching, and thus the simulated port impedance does not directly reveal the potential performance of the antenna. Since the non-resonant antenna does not work well without impedance matching, the simulated antenna would need to be matched at each frequency band of interest to evaluate its operation. Circuit simulations are needed for this purpose and a metric called bandwidth potential has been found useful.

The bandwidth potential metric was originally proposed in [37] as a pragmatic way to measure the extent to which the bandwidth of an antenna can be improved by suitable matching components. This metric helps to speed up the antenna design process. It is based on numerically matching the input impedance of an antenna with two-component lossless L-section matching circuits to 50Ω at a given frequency, for a given return loss level. An L-section is a two-component matching circuit consisting of two reactances in L-shape configuration: A series or shunt inductor or capacitor with a shunt or series inductor or capacitor (see Fig 3.5 (a)). The L-section is used because it is the simplest general matching topology which can match an arbitrary load impedance having a positive real part to a generator impedance (which also needs to have a positive real part). To obtain the bandwidth potential, the L-section matching is applied at each frequency of interest. The maximum achievable relative bandwidth as a function of frequency (over all possible L-section topologies shown in Fig 3.5 (a)) then constitute the bandwidth potential. Normally, two or four topologies out of the eight in Fig 3.5 (a) are feasible

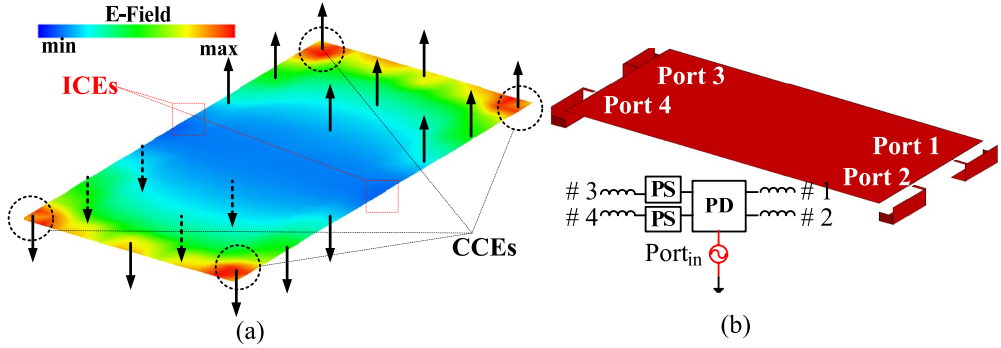


Fig 3.6 (a) Electric field of the fundamental mode and the excitors placement on the platform, (b) multiple CCE with matching elements on the platform, phase shifters (PS), and power divider (PD).

depending on the coupling element impedance.

Bandwidth potential can be calculated using a post-processing template in CST [145] or Beta Match Software [146]. For instance, as discussed in this subsection regarding the modal currents of the fundamental mode in Fig 3.3(a), an ICE can be placed in the middle of the chassis to couple energy to the fundamental mode of the chassis. Fig 3.5 (b) shows the corresponding bandwidth potential of the ICE.

- Modal Weighting Coefficient (MWC)

To evaluate how purely the desired modes can be excited MWC can be calculated using (2.18) and (2.19)

$$\alpha_n = \frac{\langle \mathbf{J}_n, \mathbf{E}^i \rangle}{1 + j\lambda_n}. \quad (3.1)$$

Compared with the MS in (2.14), the MWC also considers the interaction between the excitation and the characteristic modes.

3.2 CM-based MIMO Antenna System Design

Multi-antenna (or multipoint) design in MIMO terminal devices is challenging due to the severe mutual coupling caused by the limited implementation space. As explained in the previous section, the number of resonant modes is very limited for typical terminal device form factors in frequency bands below 1 GHz, which often results in antenna ports with highly correlated radiation patterns. Therefore, novel antenna solutions are required. For higher frequency bands, though more resonant

modes are available, the required number of antenna ports is increased to four or even eight. This means that it is also very challenging to design MIMO antennas (with enough ports and low enough coupling/correlation) for higher frequency bands.

The first method for alleviating coupling at the low frequency bands is to avoid the sharing of the single chassis mode by two or more ports. For the two-antenna case, this can be achieved by placing one antenna at the shorter edge of the chassis and the other at the center of the chassis [31]. By this layout, the single chassis mode will be excited by the edge antenna but not by the center one, due to the zero modal electric field in the center as shown in Fig 3.6(a). If a three-antenna configuration is desired, then for the third port a magnetic antenna, e.g., an electrically small loop antenna, can be placed at a shorter edge of the chassis. This means that the third antenna will also not share the chassis mode for radiation, since the modal magnetic field is zero on the shorter edges of the chassis [141]. Another efficient method to mitigate coupling is to create more resonant modes in the low band by modifying the structure of the chassis, e.g., by loading it with a T-shaped metal frame [146] or bezel [148] or by changing the chassis geometry [149]. Thus, multiple orthogonal modes are obtained, and different coupling elements can be applied to excite these modes. Papers [I]-[III] shows different ways to create more excitable modes (i.e., resonant modes) in the low band to be used for achieving more bandwidth or increasing the number of ports.

To practically design MIMO antenna using the multiple resonant CMs of the modified chassis, suitable feeding structures need to be synthesized for exciting them. The feeding structures can be any feed structure, either a resonant or non-resonant coupling element. As discussed in the previous section, TCM can also be used to study the combined performance of the coupling-based exciters and the chassis as well as the optimal location of the coupler relative to the chassis. In general, the effect of the coupling element on the chassis' CMs can be mitigated by limiting the size of the coupling element. To confirm that the desired modes are unchanged (or not appreciably affected), the modal analysis step can be repeated with the feed structure included, and MWC in (3.1) can be calculated to verify that the desired modes are indeed excited. Then, the exciters arrangement can be utilized to optimize the antenna performance (e.g., bandwidth potential, radiated power, absolute power delivered to the antenna, etc.) in different operation frequencies. In this section, we present two different exciter arrangements for improving the bandwidth and isolation among the antenna ports in MIMO antenna for low frequency bands.

The ability to uniquely excite a single desired CM (i.e., selective excitation), or a specific set of CMs with the same exciter (i.e., common excitation), is important in many applications.

3.2.1 Selective Excitation of CMs

Selective excitation of a single mode by a coupling element is a sufficient requirement to maintain far-field orthogonality relationships among the antenna ports, which is vital for many applications, including MIMO. The main challenge becomes how to selectively excite modes to ensure good isolation among all ports. As an example, selective excitation is achieved for the proposed two-port design in Paper [III]. However, the coupling problem becomes more severe in MIMO terminal antennas design with more than two ports with respect to related two-port designs in the literature. In this case, selective excitation becomes more critical, as shown in the design process of the proposed tri-port antenna in Paper [II]. There are two approaches to excite only one mode with zero coupling into other modes: 1) multiple coupling element excitation and 2) single coupling element excitation.

Multiple Coupling Element Excitation

Pure selective excitation is impossible in practice, especially when there are many resonant modes at the frequency of interest – in other words, when the structure is not electrically small. Nevertheless, the contribution of other modes can be minimized by increasing the number of properly placed/phased feeders or by reactive loading. To purely excite a given mode in practice in an electrically small object, multiple feed locations with certain phase relationships can be utilized for each antenna port. For instance, based on the modal analysis of a PEC plate, the maximum electric near fields of the fundamental mode (i.e., λ_1 in Fig 3.2) are mainly at the four corners, with a 180° phase shift between the two smaller edges (see Fig 3.6 (a)). To purely excite this mode to be used as one port in MIMO antenna design, it is better to increase the number of elements placed at the right locations (with each suitably phased). This will also help to utilize the volume of the CCE more efficiently. As an example, four CCEs with their matching circuits can be placed in the maximum modal electric field regions as shown in Fig 3.6 (b). The two CCEs at the same shorter edge is co-phased and those on the other shorter edge should be fed antiphase (using 180° phase shifters) to be able to purely excite the desired mode. Practically, a power divider (PD) is also needed to distribute the signal from the port to the four CCEs.

In Paper [III], the multiple coupling element approach is used to excite one of the desired modes by port 2, selectively. Furthermore, the same approach has been applied for the feeding of port 2 in Paper [II].

Single Coupling Element Excitation

To excite one mode without coupling into another, the proper location of a coupling element can be found through the analysis of different CAs. CM interdependence calculates the dependencies between two different characteristic currents or near

fields over a surface (region) of interest [150]. In the case of characteristic near-fields, the CM interdependence matrix for a given component (x , y , or z) is defined by

$$[\mathbf{II}_\gamma] = \left(\left| \frac{[F_m]}{\max([\![F_{x,m}]\!], [\![F_{y,m}]\!], [\![F_{z,m}]\!])} \right| \circ \left| \frac{[F_n]}{\max([\![F_{x,n}]\!], [\![F_{y,n}]\!], [\![F_{z,n}]\!])} \right| \right)^{\frac{1}{2}}. \quad (3.2)$$

In (3.2), $[F_m]$ and $[F_n]$ are the CA matrices of the CMs m and n for the given component over the surface being analyzed and normalized by the maximum near-field value over the surface and over all components (x , y , and z), and \circ is the Hadamard product. If the interdependence of two CMs at the same frequency ($f_1 = f_2$) is calculated, the dependence of the near fields is obtained. The interdependence information can be used to determine which excitation locations can be exploited to excite a single CM. This analysis will provide the optimal locations for placing a single-source. This approach has been used in Paper [II] for single mode excitation.

3.2.2 Common Excitation of CMs

In contrast to the selective excitation, it is often necessary to excite multiple CMs (i.e., common excitation) either to extend the exciter's bandwidth, or to allow the exciter to obtain a multiband behavior. In these cases, the previously described excitation analysis cannot be directly applied. However, (3.2) can be applied to two different modes at two separate frequencies. When this is effectively applied, locations of large correlation describe which modes (at the two frequencies) have common high current or field densities. These specific locations can then be exploited to allow for a single excitation source to excite multiple CMs at separate frequencies.

When multiple CMs are excited by any of several excitations, the orthogonality relationships between the different excitations are no longer guaranteed. However, there is an exceptional case which we can achieve decorrelated MIMO handset antennas by exciting orthogonal mixed modes, whose MWCs in (3.1) satisfy

$$\left| \sum_{n=1}^N \alpha_{n,i} \alpha_{n,i}^* \right| = 0, \quad (3.3)$$

where $\alpha_{n,i}$ and $\alpha_{n,j}$ are the MWCs of i th and j th port excitations for mode n (for N significant modes). In Paper [I] this approach is used to implement a two-port MIMO antenna with wideband multimode excitation.

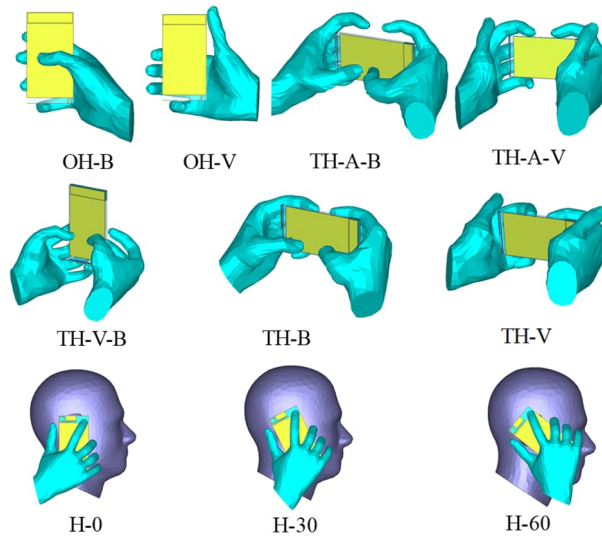


Fig 3.7 User scenario simulation setups. Talk modes with different inclination angles (H-0, H-30, and H-60). Browse modes in both one and two hands (OH-B, TH-B, TH-A-B, and TH-V-B). Video modes in both one and two hands (OH-V, TH-V, and TH-A-V).

3.3 Antenna-user Interaction

Terminal antennas are different from other antennas which are both designed and utilized in free space, since in practice they can be used in proximity to parts of a human body, i.e., the hands and head. Ten realistic user scenarios are shown in Fig 3.7. User interaction can significantly degrade terminal antenna performance via absorption of electromagnetic waves in body tissues and impedance mismatch due to resonance frequency offset [151], which severely reduce the SNR. Therefore, reducing the influence of the human body on the terminal antennas and reducing the SAR in the human body are critical issues for terminal antennas [151]- [154]. There are two main research activities in the topic of antenna-user interactions: 1) human exposure to electromagnetic radiation and 2) antenna performance degradation. As the first aspect is outside the scope of this work, in the following paragraphs we will focus on user induced performance degradation.

A pioneering contribution in [155] employed a custom-developed FDTD simulation software to investigate antenna performance in the presence of users. In [155], the user's influence on radiation pattern, input impedance, radiation efficiency, and near-field magnitude was investigated. It was established that when an antenna is used by an operator, the resonance frequency drops, the radiation pattern changes significantly, and on average 45% of the power is lost in the hand

and head. It also indicates that the power absorption is more severe for antennas at the lower frequency bands.

In most of the existing literature, handset antennas are designed in free space and then their performances are investigated in user scenarios to check whether the efficiency degradation is acceptably low. If the degradation is severe, then different solutions (e.g., adaptive impedance matching [151]) may be proposed to compensate for the user effect. However, it would be more efficient to consider user influence in the antenna design process and so a unified design strategy targeting user interaction is needed. Until now, only a few papers have provided theoretical analysis on the hand effect or systematical method to consider the user effect in the design procedure. Two different CM-based approaches that can be used for investigating and alleviating the interaction between terminal antennas and the human body, i.e., mixed structures' CMs and characteristic mode mapping, will be described in the following subsections.

3.3.1 Mixed Structures' CMs

As a straightforward method, human tissues have been included in the calculation of CMs, where the modes are extracted for mixed structures with lossy materials [152], [153]. The CMs of lossy materials are calculated based on surface integral operator [153], which successfully separates the dissipative power from the stored power and radiated power. The modal efficiency for each mode is then calculated using modal currents, and the mode with the highest efficiency is selected to build robust terminal antennas. This method is comprehensive, but it is time-consuming.

3.3.2 Characteristic Mode Mapping

An alternative method for reducing the effect of the human body is CM mapping, which has been used in Paper [III]. According to [96], the far field of any antenna can be decomposed into the superposition of weighted characteristic far fields, i.e.,

$$E_{total} = \sum_n \alpha_n E_n, \quad (3.4)$$

where α_n and E_n are the weighting coefficient and the characteristic far-field for the n^{th} mode, respectively. Thus, the radiation patterns of the antenna in free space and in the presence of the human body are mapped to the characteristic patterns of the structure, respectively, for finding the contribution of each mode.

According to [156], the weighting coefficients can be calculated from the correlation between the total radiation pattern and the characteristic patterns ($\rho_{total,n}$)

$$\alpha_n = \sqrt{P_{\text{rad}}} \rho_{\text{total},n}^*, \quad (3.5)$$

where P_{rad} is the total power radiated by the antenna. P_{rad} is normalized to unity for simplicity, since it is irrelevant to the relative contribution of each mode. Thus, (3.5) is reduced to

$$\rho_{n,\text{desired}} = \alpha_n^*, \quad (3.6)$$

and the weighting coefficients satisfy

$$\sum_n |\alpha_n|^2 = 1. \quad (3.7)$$

By comparing the MWCs of the same mode in different scenarios, robust modes that are not sensitive to the environment can be retained. Those modes are then selected as the target modes for pattern synthesis, leading to handset antennas that are robust to user effects.

Some types of antennas operating at 0.9 GHz have been investigated in [154] following this procedure. A conclusion is that the pattern with less radiation toward the boresight and backward directions is more robust to the hand/head loading.

3.4 Co-Integration of Sub-6 Antenna with Mm-wave Antennas

Since the invention of the mobile phone, the content delivered to users has become more and more diverse: voice, text, pictures, videos and live streaming, which requires higher and higher data rates. One approach to provide higher data rates in 5G is to utilize the larger available bandwidth in higher bands, especially mm-wave bands. Thus, mobile terminals for 5G communication are starting to cover both sub-6 GHz and mm-wave bands. This means that the sub-6 GHz band antennas and mm-wave antennas need to coexist in the limited space of mobile terminals. So, the codesign of sub-6 GHz and mm-wave antenna for mobile terminals are attracting more and more research interest.

To compensate for high losses in the propagation of electromagnetic waves, mm-wave antennas are required to generate high gain and steerable beams to maintain the same coverage area as in low frequency bands. Currently, the most prevalent antenna type for mm-wave antennas is phased array antenna with feeding networks [157]. By connecting the antenna elements with phase shifters and other RF elements, the amplitude and phase distributions of the phased array can be controlled flexibly for more diverse beampatterns.

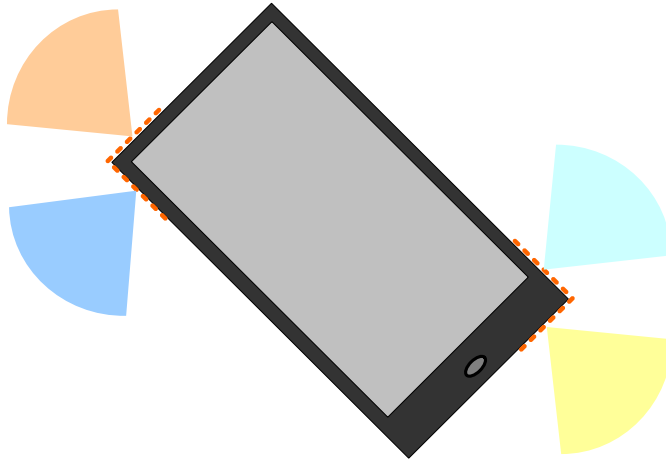


Fig 3.8 Enhancing the spatial coverage of mm-wave 5G smartphones using beam-reconfigurable antenna array.

The codesign of sub-6 GHz and mm-wave antennas for mobile antennas aims to provide wide frequency bands and high space utilization. The current co-designed antennas suffer from poor space utilization, which is caused by two main factors: the large size of sub-6 GHz antenna and the considerable area occupied by the feeding networks of mm-wave phased array antennas, which also bring extra insertion losses.

It is shown in Papers [II] -[III] that TCM can help to make use of the CMs of the handset chassis to reduce the size of the sub-6 GHz antenna in mobile terminals with respect to traditional design of electrically small/compact antenna (e.g., simple monopole and printed inverted-F antennas). Hence, small non-resonant coupling elements, which were introduced in Section 3.2.3 and also used in Paper [II], are useful for the co-design approach. Paper [IV] proposes a co-designed sub-6 GHz and mm-wave antenna system with higher space utilization, where compact beam reconfigurable mm-wave antennas are integrated with the CCEs of the sub-6 GHz antennas. The CCE in Paper [III] is designed to excite the fundamental dipole mode below 1 GHz with a single matching network, whereas in paper [IV] the chassis CMs are excited by two CCEs (i.e., common mode excitation) to cover two sub-6 GHz bands with the aid of two different matching networks.

Compared with the conventional phased array, the proposed beam-reconfigurable array features a low-complexity structure and occupies less space. Each mm-wave array can realize a 90-degree beam scanning range with two states of the PIN diodes and four arrays are mounted on the two corner CCEs that are diagonally placed on the chassis (see Fig 3.8).

Chapter 4

Low-cost Millimeter-wave Multi-element Antennas

In traditional single-input single-output (SISO) linear systems, one TX antenna and one RX antenna are used for communication, whereas the propagation environment is commonly represented by the channel impulse response. In such a condition, the received signal can be expressed as

$$y = hx + n , \quad (4.1)$$

where y is the received signal, h is the channel impulse response, x is the transmitted signal and n is the additive white Gaussian noise (AWGN) [7]. The spectral efficiency of such a channel to support communication between the TX and RX is upper bounded by the Shannon capacity, which can be expressed in bits per second per Hertz (bits/s/Hz) as

$$C = \log_2 \left(1 + \frac{P_T}{\sigma_n^2} |h|^2 \right), \quad (4.2)$$

where P_T is the transmit power, σ_n^2 is the noise variance, and $|h|^2$ is the gain of the scalar SISO channel. As seen in (4.2), to increase the total amount of information transferred through the SISO channel in bits/s, we can either increase the transmit power or increase the system bandwidth. The first solution is not viable due to the energy efficiency requirement limiting the available total transmit power. On the

other hand, as has been discussed in Chapter 1, we can utilize the higher part of the mm-wave band (e.g., *E*-band), where larger absolute bandwidths are available.

As said in Section 1.3.4, *E*-band wireless technologies have grown significantly during recent years. With the development of modern wireless systems with the requirements of low transmitted power and high data rate, antennas that are wideband, high-gain, and easily integrated with planar circuits have become an essential component in the *E*-band front-end system.

In this chapter, antenna technologies suitable for *E*-band are introduced. Further, the newly developed low-cost high-resolution multi-layer “Any-Layer” PCB technology for implementing antenna-in-package solutions at *E*-band frequencies is described. Then, the new integrated subarray and array antenna topologies for *E*-band future point-to-point wireless communication and radar systems as proposed in Papers [V] and [VI] will be introduced. In particular, two different subarray/array antenna topologies with different feeding schemes (i.e., series, corporate) are designed with the help of cavity/ waveguide modes and CMs, respectively. The mentioned topologies satisfy the scenario-dependent requirements in Chapter 1 for wireless point-to-point communication and mm-wave MIMO radar, respectively. All the antennas were fabricated with the “Any-Layer PCB” technology.

4.1 Any-Layer PCB Technology

As mentioned in Chapter 1, the mm-wave band has been adopted for a variety of applications, such as communication systems and radars. In these systems, high-density of digital and analogue signal routings are needed behind or next to the antenna elements. As such, having a cost-effective multi-layer build-up in the mm-wave band is a great advantage. In this context, both of the antenna arrays proposed in Papers [V] and [VI] were fabricated with the Any-Layer PCB technology, which allows for the solder bump flip-chip technology to be used to attach them to the monolithic microwave integrated circuit (MMIC) for system-level assembly. In this section, the Any-Layer PCB fabrication technology is compared with some other common antenna fabrication technologies in the mm-wave band.

Technologies with multi-layer build-up for the implementations of integrated mm-wave antennas are key enablers in the development of broadband large-scale mm-wave systems with high-density digital and analog signal routings. In the multilayer build-up, it is possible to integrate the feeding structure and radiators of the antennas using perpendicular interconnections. Currently, multi-layer process technologies that can be used at mm-wave frequencies for integrating chip packages and antenna arrays are limited. Thin-film LTCC and standard HDI (High Definition Interconnect) PCB technologies mostly based on LCP or Teflon are currently the most common and attractive ones in the industry. The main advantage associated with these technologies is the high resolution in the manufacturing process. For

instance, new advances in LTCC promise ceramic thicknesses down to 50 μm , fine line widths down to 35 μm , and slim micro-via diameters down to 50 μm . These features make this technology suitable for applications at frequencies even higher than 100 GHz. Almost the same is true for LCP and Teflon-based HDI PCB technologies. On top of that, their substrates can offer lower permittivities and lower losses in the mm-wave band. On the other hand, the main disadvantages of these technologies are the cost and the manufacturing complexity. For instance, the LTCC technology requires temperatures above 850 degrees Celsius during fabrication. At this high temperature, active devices are completely destroyed. So, in contrast to passive devices, active devices have to be integrated into the package after the firing process [69], which results in a very high complexity process.

Although standard HDI PCB technology has high accuracy and resolution, it has a prominent disadvantage: machine drilled vias have to be used to connect two non-stacked metal layers, whereas laser drilled micro-vias can be used to connect just two stacked metal layers. In other words, in this technology, stacking micro-vias on top of each other is not possible.

The Any-Layer technology is an improvement of the standard HDI PCB technology, with a different fabrication process [158]. The Any-Layer PCB technology is the technology that has been used for the fabrication of *E*-band antenna arrays in Papers [V] and [VI]. The antenna applications include large scale 5G systems, and automotive radar modules. The main advancement of the Any-Layer technology over the standard HDI technology is that stacking micro-vias is possible. This feature makes it possible that each layer or connection on a specific layer can be connected to every other layer within the PCB build-up. In this case, there is no need to use conventionally drilled, blind, or through hole vias anymore. They are replaced by copper-filled stacked micro-vias. Machine-drilled vias, non-stacked micro-vias and stacked micro-vias are illustrated in Paper [VI]. It is noteworthy that stacked micro-vias provided by the Any-Layer PCB technology play a major role in the feeding mechanism and overall array design in Papers [V]-[VI]. The minimum hole and pad size for machine drilled vias are 200 μm and 400 μm respectively, whereas for laser-drilled micro-vias, they are 75 μm and 175 μm , respectively. It is worth mentioning that in the Any-Layer and standard HDI technology, since the features for track widths and clearance between traces are much smaller than for standard PCBs, the routing density may be significantly increased. For example, in standard PCBs, the minimum track width and clearance are 100 μm , but for standard HDI and Any-Layer PCBs they are 40 μm .

Any-Layer or standard HDI PCB technologies must be combined with special substrate materials suitable for the mm-wave band. These substrate materials must have low losses and a stable permittivity in the sub-band(s) of interest. Currently LCP and Teflon based substrates are the most common materials that are used in PCB technologies in the mm-wave band [158], [159]. But these materials have their own disadvantages. LCP and Teflon-based PCBs work with layers with considerably different coefficients of thermal expansions (CTEs) compared to

Table 4.1 Comparison between Any-Layer, HDI PCB, and LTCC technologies.

Features	Any-Layer with Megtron 6	HDI PCB with LCP and FR4	HDI PCB with Teflon	LTCC
Minimum substrate thickness (um)	50	50	50	50
Minimum track width (um)	40	40	40	35
Minimum microvia diameter (um)	75	75	75	50
Minimum track clearance (um)	40	40	40	35
Integration with chip package	Easy	Easy	Easy	Hard
Maximum number of layers	14 \geq	8-10	8-10	30

metals. Therefore, when the temperature rises, the PCB board tends to bend, and there is a serious possibility that the micro-vias crack or that the metallic layers depart from the board. Hence, with LCP or Teflon based technologies, it is usually not possible to provide more than 8 layers. Another disadvantage of LCP and Teflon substrates is that in multi-layer PCBs, they must be used in mixed build-ups with other substrates like FR4 or Rogers RO4000. The main reason is that, in LCP, grass cloth cannot be used to keep the x-y coordinates exactly in place during the fabrication process. If they are used alone and without other substrates like FR4, then the fabrication becomes very complex and the fabrication cost increases enormously. The last problem with LCP is that liquid crystal polymers are polar materials, so when the environment temperature goes up, different parts of the substrates become crystalized differently, which leads to anisotropic permittivity in the substrates. It is worth mentioning that although LCP is not classified as an expensive material, Teflon is very expensive by nature, and this also increases the fabrication cost.

The substrates used in the build-ups in Papers [V] and [VI] are of the Panasonic Megtron 6 type [159]. Although these materials have higher losses compared to Teflon and LCP substrates in *E*-band (tangent delta of 0.006 versus 0.003, according to the datasheet), they do not suffer from the problems associated with LCP and Teflon. For example, they can be used in build-ups of up to 14 layers. In addition, they are very cheap by nature. Moreover, since the fabrication procedure is much simpler with these materials than with LCP and Teflon, the fabrication cost is much lower too.

The technical characteristics of the Any-Layer and standard HDI PCB technologies with different substrates are compared with LTCC in Table 4.1. The values are very close, while the tape-out cost for the Any-Layer PCB technology combined with Panasonic Megtron 6 substrates are less than one third of that for

LTCC in mass production. It is worth mentioning that for mass production, the cost of LTCC increases more rapidly with the board size relative to Any-Layer and HDI PCB technologies. For multi-layer PCB technologies, the cost for the final PCB board relates to both the technology and substrate materials. In the literature, several authors have used LCP and Teflon substrates in a HDI PCB technology [159], [161], but in this thesis Panasonic Megtron 6 substrates were used in the Any-Layer technology. The Any-Layer technology is more advanced and more expensive than the standard HDI technology, but Megtron 6 substrates are much cheaper than LCP and Teflon substrates, and easier to process. The overall result is a reduced final cost. Therefore, the Megtron 6 substrates play a big role in the final cost reduction. As a conclusion, the thesis work has advanced the use of a new technology in antenna design, which together with the use of cheaper substrates enables lower overall fabrication cost. It is worth mentioning that, according to the knowledge of the authors, this is the first time that this advanced multi-layer PCB technology is assessed in the design and fabrication of mm-wave antennas. In addition, our reported build-ups with 8 layers have the largest number of layers compared to the PCB build-ups reported in the literature.

4.1.1 Panasonic Megtron 6

This thesis utilizes one of the most common multi-layer build-ups. As an example, an antenna with 2 stacked patches is embedded in the 8-layer stack-up of Fig 4.1, which contains 7 different substrates and 8 metal layers. Also, there is a transition between “signal layer3” and “bottom layer” to feed the bottom patch. “Internal Planes” 1, 2, 3 are ground planes, and others are reserved for signal routing. Since in radar modules there are many digital and analog signal routings, the ground layers mitigate the interaction of different signal lines on each other. Furthermore, Internal Planes 1 stops the waves from radiating back to the build-up, which can severely distort the radiation pattern. The five middle substrates, substrates 2, 3, 4, 5, and 6 are the thicker ones in Papers [V] and [VI] to achieve more bandwidth. The top and bottom substrates are chosen to be thinner to get an acceptable width for the transmission lines. According to the Any-Layer PCB manufacturer, in this technology the layers’ thicknesses and specifications change, depending on the type of substrate used in the build-up. Micro-vias have a conical shape and their diameters depend on the substrate thickness. All the presented data in Fig 4.1, including permittivity, loss tangent and thickness are according to the datasheet provided by Panasonic [159].

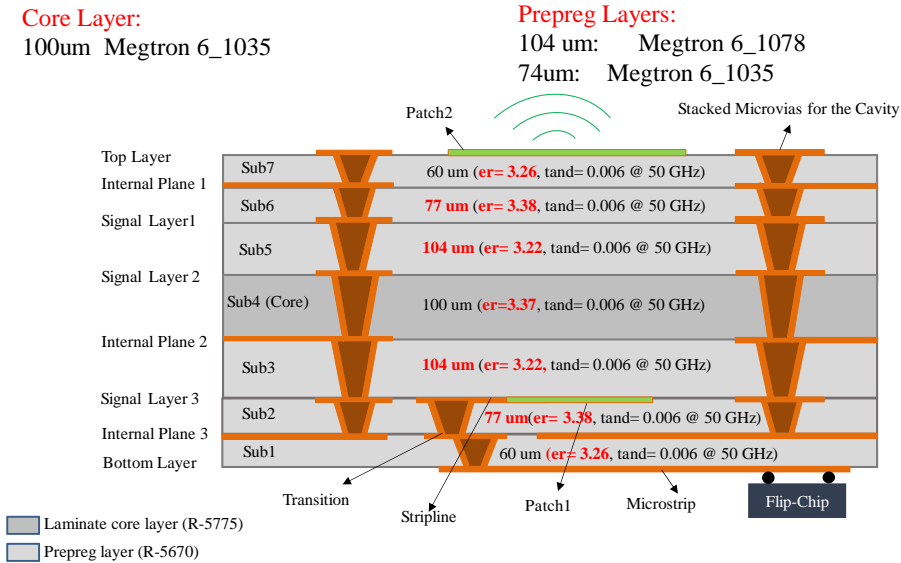


Fig 4.1 Build-up for in-set antenna.

4.1.2 Disadvantages

In the previous section, the fabrication accuracy of the Any-Layer technology was compared with well-known technologies in the mm-wave band. Even though this comparison shows that this new PCB technology is accurate enough for mm-wave applications, it has several drawbacks. The first major drawback is associated with dimensional tolerances. This problem becomes severe when considering the high relative dimensional tolerances for small widths, e.g., track widths. Hence, sensitivity analysis needs to be performed after each design. The second major drawback originates from the substrate and copper thicknesses in the multi-layer build-up. The copper thickness of the metal layers in a multi-layer build-up can vary by about $\pm 3 \mu\text{m}$ over the entire PCB board. As a conclusion, if the Any-Layer PCB technology is applied to large arrays, then the tolerance sources must be compensated very accurately before or during the fabrication process.

4.2 Antenna Arrays for MRR Radar

Mm-wave radar systems can detect the presence, position, direction of travel and relative speed of remote objects with small delays. The main driving force behind

them is the automotive industry. 77-81 GHz radar sensors will soon be used in every car for enabling emergency braking systems [68].

As discussed in Chapter 1, for MRR radar systems, it is favorable to have antenna arrays with large impedance bandwidth as well as low sidelobe level (SLL) and flat gain within the required band. Typically, the arrays must have a narrow beam (10° - 15°) in one plane to scan the elevation, and a wide beam (60° - 80°) in another plane to scan the azimuth. Further, their distance range is 1-100 m, and typically their broadside gain must be higher than 10 dBi. In Paper [VI], a series-fed patch antenna array is designed as a subarray for medium range MIMO radar applications. This subarray satisfies all the necessary features (low mutual coupling when concatenated, width of less than half a wavelength and cheap fabrication) for integration into the transmitter and receiver arrays of a mm-wave MIMO radar and it is superior in performance to existing series-fed patch designs in the literature. For designing the subarray, a multi-layer build-up is used.

Microstrip patch antenna has drawn the attention of antenna engineers since the 1970s and it is one of the best antennas for automotive radar systems, due to its numerous advantages. Microstrip antenna is light weight, low cost, low profile and amenable to low-cost PCB fabrication processes. The use of a corporate feeding network is common in microstrip antenna arrays, since it can provide in-phase radiation of all radiating elements over a wide frequency range. However, these feeding networks have large dissipation losses and hence are not proper for high gain applications. It has been shown that, above 30 GHz, the losses of the feeding network of parallel-fed patch arrays become severe and they result in poor total efficiency in the order of 20% [162]. The series feeding technique is a suitable alternative. In this type of feeding, the feed losses are significantly lower, due to the smaller feed line lengths. Some designs based on patch arrays have been reported [163]-[165], but they are either narrowband, expensive in fabrication, or incapable of suppressing the mutual coupling.

Another type of series-fed arrays, suitable for automotive radar applications, are microstrip comb-line arrays, which have been extensively reported in the literature [166]-[170]. Even though they have good SLL suppression at the center frequency, they have a big drawback, i.e., the high sensitivity of their radiation patterns to frequency. Indeed, at frequencies away from the center frequency, the broadside beam squints by about 1 - 2° /GHz and the SLL degrades substantially. Further, all the array antennas in the related literature [163]-[170] have other problems pertaining to the two dominant requirements in MIMO radars, as discussed in Chapter 1. First, the cross talk between the receiver and transmitter arrays must be mitigated as much as possible. Second, the subarray antenna width must be less than half a wavelength, to suppress potential sidelobes as much as possible.

Microstrip grid antenna array is another topology that has recently been applied in automotive radar applications [171]-[172]. Since the distance between the radiating arms in all grid antenna arrays described in literature is around one guided wavelength, they have two main drawbacks when they are used in radar systems.

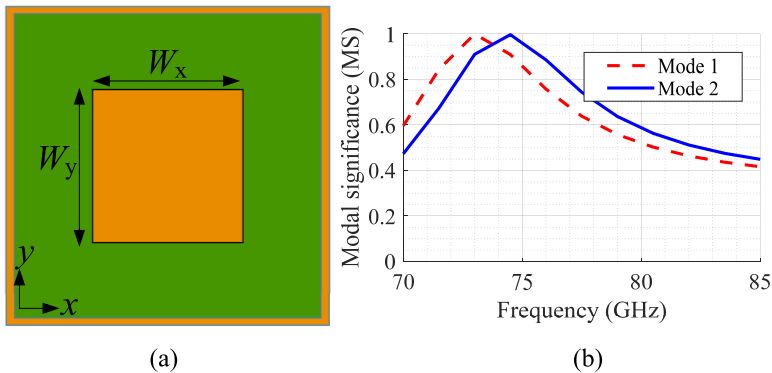


Fig 4.2 (a) Rectangular patch with $W_x=0.98$ mm, $W_y=1$ mm, and (b) modal significance of Modes 1 and 2.

First, the field of view (FOV) in the scanning plane (H-Plane) is limited for MRR. Second, the minimal spacing between the adjacent channels in a MIMO system is relatively large. This leads to high SLLs, which is very destructive for the functionality of radar systems.

4.2.1 Conventional Series-Fed Patch

Fig 4.2 (a) shows the geometry of a single patch antenna, where a rectangular PEC patch antenna is formed on a single layer substrate with the height of 0.2 mm and the dielectric constant of 3.25. In Fig 3.2 and Fig 3.3, modal analysis was only applied on a PEC plate. However, modal analysis can also be performed on the single patch in Fig 4.2 (a) using Altair FEKO 2019, assuming infinite substrate. Two other examples of applying TCM to patch antenna design are found in Papers [VIII] and [IX]. The modal significances of two characteristic modes (CMs) with broadside patterns and resonant frequencies within 70-80 GHz are shown in Fig 4.2(b). It can be seen that the CMs have ~8% modal bandwidth. The modes are similar and orthogonally polarized. However, as the patch is slightly shorter in the x direction than in the y direction, the resonant frequency of the x -directed mode (Mode 2) is slightly higher than that of the y -directed mode (Mode 1), as shown in Fig 4.2 (b). For illustration, the electric fields (under the patch), normalized surface current on the patch, and far-field pattern of Mode 2 are provided in Fig 4.3.

As mentioned in previous section, series-fed patch arrays are one of the most interesting array topologies for automotive radar applications. A simple series fed antenna array is shown in Fig 4.4 (a). In this type of antenna array topology, patch antenna elements are used, and they are connected in series by interconnecting lines. The length of patch elements and interconnect lines are around half a guided

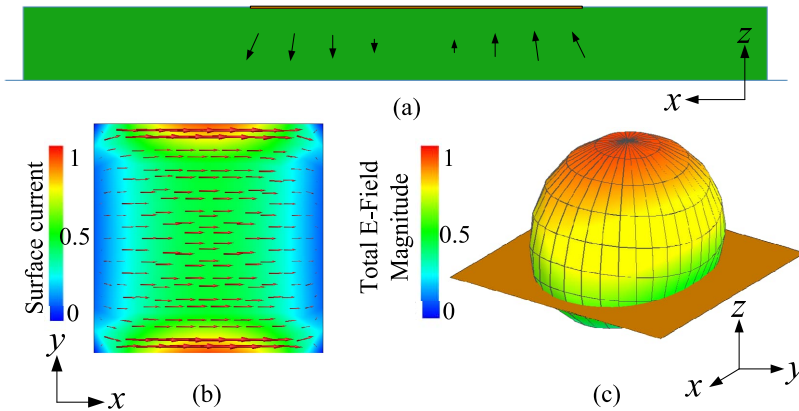


Fig 4.3 (a) Electric field, (b) surface current distribution, and (c) far-field pattern at the resonant frequency of Mode 2.

wavelength at the intended frequency, so all the patches are excited in phase. The main advantage is avoiding corporate feeding network, which occupies a large area on the PCB board, and causes huge loss along the lines. But there are two main disadvantages, including nonuniform amplitude distribution and phase tolerance enhancement of array elements along the array, which lead to narrow impedance and gain bandwidth. A circuit model for the array shown in Fig 4.4 (a) is shown in Fig 4.4 (b). In the circuit model, Z_{CL} is the characteristic impedance of the interconnecting lines, Z_{CP} is the characteristic impedance of the patch elements, and R_{rad} is the radiation impedance of patch elements. Series-fed array can be modeled as a periodically loaded high-impedance transmission line terminated at each end by a low impedance transmission line (patches) [173].

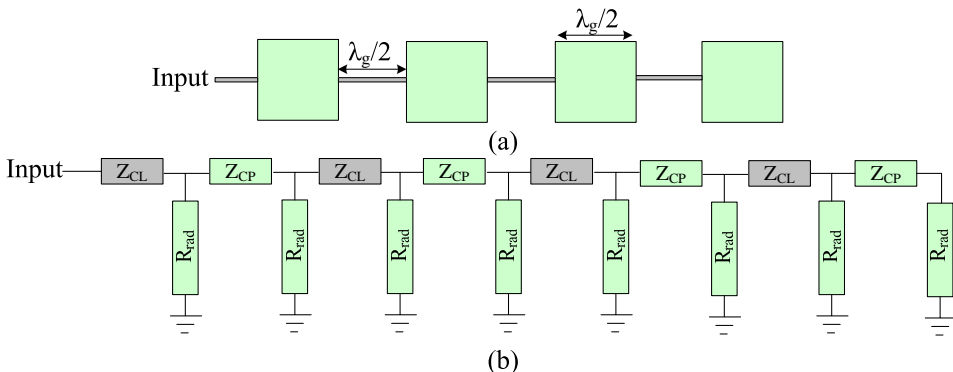


Fig 4.4 (a) Simple series-fed patch antenna array, (b) circuit model.

4.2.2 Cavity-backing Technique

As we discussed in Chapter 1, low mutual coupling between transmitter and receiver is crucial for MIMO radars. There are different ways to reduce the mutual coupling between the elements in microstrip antenna arrays. In [174] and [175], the authors changed the shape of the patch elements to reduce the mutual coupling. The use of defected ground structures (DGS) is another common way for decoupling [176]. Different studies on decoupling have been done based on applying electromagnetic band gap structures (EBG) and metamaterials [23], [177]-[178]. Moreover, parasitic elements [179] or a neutralization link between the array elements [180], can be used to suppress the mutual coupling. Although all these methods can achieve mutual coupling suppression, they suffer from low bandwidth and manufacturing difficulties.

It is noteworthy that since we have three ground planes in the build-up in Fig 4.1, there is a high potential for surface waves and parallel plate modes to be excited. The cavity-backing technique is used in the proposed design in the microstrip patch array in Paper [VI] to suppress the parallel plate modes. Moreover, the role of the cavities is to suppress cross talk and mutual coupling between the RX and TX sub-arrays in the MIMO radar module shown in Fig 1.5. In microstrip patch arrays, using cavities around the patches has several benefits. First, it is easily implemented through stacked micro-vias. Second, such a configuration does not suffer from small bandwidth. Third, the cavity prevents surface waves from being excited in the substrate. This features result in a direct benefit at the element level: thicker substrates can be used to increase the bandwidth, without the danger of generating large surface waves. The suppression of the surface waves also offers a fourth benefit at the array level: the mutual coupling among the elements of the antenna is reduced [181].

The cavities are implemented using laser drilled copper filled stacked micro-vias in Paper [VI]. The small laser drilled micro-vias in the Any-Layer PCB technology have two main advantages. First, since their hole size is much smaller than the size of machine drilled vias in standard HDI PCB technology, they can be placed closer together, further mitigating the surface waves and the mutual coupling between the TX and RX sub-arrays.

4.3 Antenna Array for Point-to-point Communication

As also discussed in Chapter 1, large chunks of spectra within *E*-band have been allocated in most countries worldwide. Antenna is one of the most important components in *E*-band point-to-point wireless systems with 10 GHz of bandwidth.

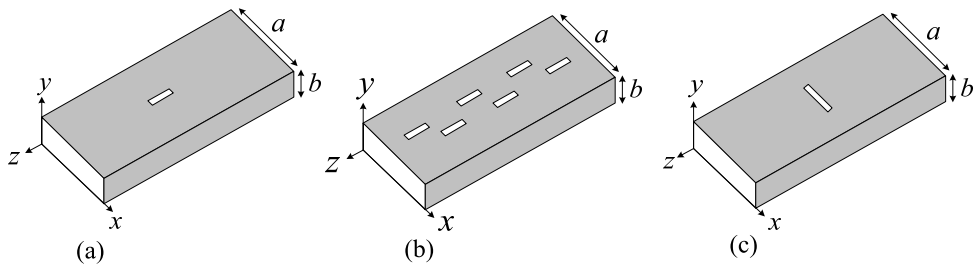


Fig 4.5 Waveguide with thin slot(s) in different positions.

A low-cost, high gain, and high-efficiency antenna that at the same time covers the whole system bandwidth is highly desired.

4.3.1 Waveguide/Cavity Antennas

Very high-gain, wideband and efficient antennas are required for *E*-band wireless point-to-point communication. Over the past decades, numerous efforts have been made to develop high performance *E*-band antennas. To satisfy the stringent requirements in gain, bandwidth and efficiency, the antenna solutions developed include 3D structures such as horn arrays [182], lenses [183], and reflector antennas [184]. Such antennas are bulky, heavy, expensive and difficult to construct. On the other hand, classical waveguide (slot) array antennas [185] and cavity-backed slot antennas [186] are also widely used in *E*-band radar and communication systems and they have been shown to provide high performance and good alternatives to the bulky 3D structures. An appropriate operating mode in the waveguide/cavities can bring excellent radiation beam and adequate operating bandwidth for the antenna. Waveguide slot array antennas are an important class of array antennas for *E*-band owing to high gain, high power capacity, high efficiency, low cross-polarization levels and accurate control of the radiation patterns. Moreover, the cavity-backed slot antenna topology has large front-to-back ratio (FTBR) and high isolation from its environment. The analysis and design procedures for these antennas have been established by Elliott [187] and Coetzee et al. [188]. However, the waveguide/cavity antennas are still bulky, heavy, expensive, and difficult to construct.

A typical waveguide slot array antenna is shown in Fig 4.5. In waveguide slotted antennas we will need to understand the modal electric and magnetic fields within the waveguide first, as also discussed in Chapter 2. Then, there will be induced modal current on the top wall of the waveguide, where thin slots can be etched [189]. Slot antennas are one of the basic electromagnetic energy radiators. The position, shape and orientation of the slots will determine how (or if) they will radiate, which can be defined by the waveguide mode. In addition, the shape of the waveguide and

frequency of operation will play a major role. The slots are typically thin in order to not affect the modal fields inside the waveguide. Radiation occurs when the currents go around the slots in order to continue in their desired direction.

Assuming $a > b$ in Fig 2.1 and Fig 4.5, the mode with the smallest cut off frequency, called the dominant mode of a rectangular waveguide, is the TE₁₀ mode. The existing field for this mode is given by (2.6)

$$\begin{aligned} H_x &= \frac{-E_0}{2\pi f \mu} \sqrt{k^2 - \left(\frac{\pi}{a}\right)^2} \sin\left(\frac{\pi x}{a}\right) e^{-j\sqrt{k^2 - \left(\frac{\pi}{a}\right)^2} z}, \\ E_y &= E_0 \sin\left(\frac{\pi x}{a}\right) e^{-j\sqrt{k^2 - \left(\frac{\pi}{a}\right)^2} z}, \\ H_z &= \frac{jE_0}{2af\mu} \cos\left(\frac{\pi x}{a}\right) e^{-j\sqrt{k^2 - \left(\frac{\pi}{a}\right)^2} z}. \end{aligned} \quad (4.3)$$

In the above equations, f is the frequency of interest, k is the wavenumber and E_0 is a constant that specifies how much power is added to the waveguide. The cutoff frequency depends on the shape and size of the cross section of the waveguide. The larger is the waveguide, the lower is the cutoff frequency for that waveguide. The formula for the cutoff frequency of a rectangular cross-sectioned waveguide as given by (2.7) is in this case

$$f_c = \frac{1}{2a\sqrt{\mu\epsilon}} = \frac{c}{2a}. \quad (4.4)$$

Magnetic fields tangent to a conductor produces electric currents on the surface. The resulting surface current density \mathbf{J} (measured in Amps/meter) can be determined using the unit normal to the surface (\mathbf{n}) as

$$\mathbf{J} = \hat{\mathbf{n}} \times \mathbf{H}. \quad (4.5)$$

On the top wall of the waveguide the induced current will be

$$\begin{aligned} J_x &= \frac{-jE_0}{2\pi f \mu} \cos\left(\frac{\pi x}{a}\right) e^{-j\sqrt{k^2 - \left(\frac{\pi}{a}\right)^2} z}, \\ J_z &= \frac{-E_0}{2\pi f \mu} \sqrt{k^2 - \left(\frac{\pi}{a}\right)^2} \sin\left(\frac{\pi x}{a}\right) e^{-j\sqrt{k^2 - \left(\frac{\pi}{a}\right)^2} z}. \end{aligned} \quad (4.6)$$

As an example, consider a narrow slot in the center of the waveguide as shown in Fig 4.5 (a). In this case, the z -component of the current will not be disturbed, because the slot is thin and the z -current would not need to travel around the slot. Hence, the x -component of the current will be responsible for the radiation. However, at this location ($x = a/2$), the x -component of the current density is zero, i.e., no current and therefore no radiation. As a result, slots should not be placed in the center of the waveguide, as shown in Fig 4.5 (a).

If the slots are displaced from the centerline as shown in Fig 4.5 (b), the x -directed current will not be zero and will need to travel around the slot. Hence, radiation will occur. Note that the distance from the edge will determine the magnitude of the current. As a result, the power that the slot radiates can be altered by moving the slots closer or farther from the edge. In this manner, a phased array can be designed with varying excitation to each element. If the slot is oriented as shown in Fig 4.5 (c), the slot will disturb the z -component of the current density. This slot will then radiate. If this slot is displaced away from the center line, the amount of power that it radiates can be adjusted.

4.3.2 Substrate-integrated Waveguide (SIW) Technology

The antennas mentioned in the previous subsection are bulky, heavy, and incur high fabrication cost, which make them unstable for mass production. Additionally, their nonplanar structure leads to poor integration capability with active components. Planar antennas are desirable for E -band wireless systems because of their excellent integration capability and low profile. As a typical planar antenna, a microstrip array generally has low profile, is light-weight and incurs low fabrication cost, but it suffers from relatively low element gain and serious parasitic radiation loss from the feeding network in the mm-wave region. Fortunately, “laminated waveguide (LWG)” or “substrate integrated waveguide (SIW)” has been proven to improve the element gain and mitigate the severe feeding network loss in E -band or W -band planar antennas [190]-[194]. The SIW has the advantages of waveguide, but it is also low-cost and in planar form. The structure can be easily connected to coplanar waveguides (CPWs) and microstrip lines. As such, antennas based on SIW can easily be integrated with active devices.

SIW structures are generally fabricated by using two rows of conducting cylinders embedded in a dielectric substrate that connects two parallel metal plates and they permit the implementation of various microwave circuits with improved performance compared to microstrip circuits. Fig 4.6 (a) shows the structure of SIW that is synthesized with linear arrays of metallic via-holes on a substrate and the top and bottom copper foils of the substrate. The tunnel is then equivalent to a dielectric-filled rectangular waveguide, where the two rows of metallic vias are equivalent to its side walls. In order to make the SIW cavity equivalent to

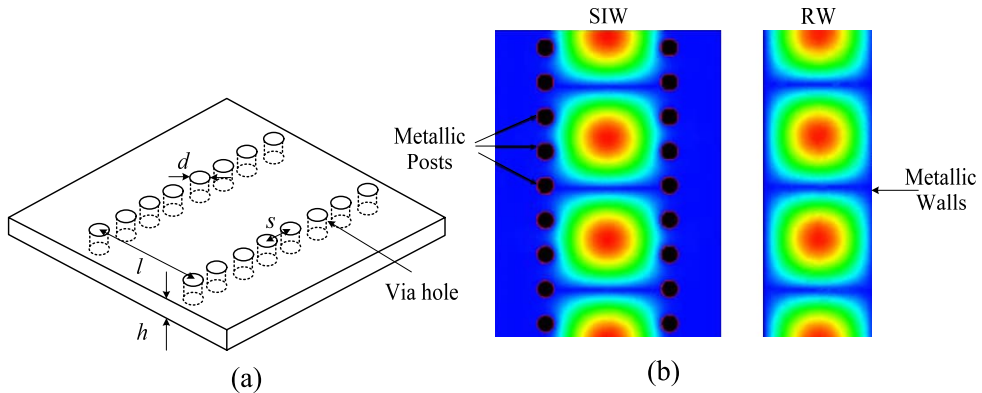


Fig 4.6 (a) Configuration of SIW synthesized using metallic via-hole arrays, (b) Quasi- TE_{10} and TE_{10} mode in the top surface of SIW and RW.

conventional metallic cavity, the conditions of $d/s \geq 0.5$ and $d/\lambda_0 \leq 0.1$ must be satisfied, where λ_0 denote free space wavelength [194]. When these guidelines are met, the attenuation constant is small enough such that the leakage wave from the clearance between two neighboring vias can be neglected. Fig 4.6(b) depicts the simulated electric field distribution of the dominant TE_{10} mode and quasi- TE_{10} mode on the top surface of a rectangular waveguide (RW) and a SIW, which are very similar. Experiments and simulations have proven that the dispersion characteristics of the SIW are the same as those of its equivalent rectangular waveguide [193]. It is noteworthy that only TE_{n0} modes ($n = 1, 2, \dots$) can be supported by SIW structures.

With the development of SIWs, classical waveguide-like structures can be synthesized using via rows embedded in a dielectric substrate with top and bottom metallization. Therefore, completely planar designs of slotted waveguide arrays can be realized [195], offering the same planar interconnectivity as standard microstrip antennas. Owing to their simple manufacturing process, low-cost and lightweight features are possible.

In the past few decades, cavity-backed slot antennas based on SIW technology have been attracting increasing attention for mm-wave applications as they combine the advantages of conventional solid cavity-backed antenna, namely large FTBR and high isolation from its environment, with the advantages of planar antennas, i.e., low-profile, low fabrication cost, high-quality factor, and ease of fabrication and integration with planar microwave circuits with self-consistent electrical shielding [194]. Given their very high isolation from their environment and high suppression of unwanted surface waves, such cavity-backed SIW slot antennas are excellent building blocks for compact antenna arrays with low mutual coupling and stable characteristics when installed in different desk configurations.

In Paper [V], a SIW cavity-backed slot antenna is proposed for the gigabyte mobile radio application in *E*-band. Unlike the series fed patch array in Paper [VI], the corporate feeding is realized underneath the radiating cavities. Thanks to the use of the multi-layer Any-Layer PCB technology, the antenna array is compact and small stacked microvias are used as the cavity walls and for impedance matching in the middle of the cavity. It can be seen how machine drilled via size in conventional PCB technology instead of small stacked vias can negatively affect the impedance bandwidth and total gain of the proposed slot array antenna. Apart from a reduction of the total gain, the radiation pattern has also changed significantly in the band of operation as a result of the larger vias disrupting the distribution of the electromagnetic field in the cavity. Moreover, the minimum distance between machine drilled vias in conventional PCB process are two times the distance between stacked micro-vias in Any-Layer PCB technology, which by itself makes the performance of the SIW cavity more non-ideal, which can lead to worse results. This shows the importance of the small stacked micro-vias provided by the Any-Layer PCB technology in *E*-band.

Chapter 5

Conclusions and Future Perspectives

In this chapter, the main contributions of the publications that are included in the thesis will be overviewed. The six included papers in this thesis can be found in Part II. Furthermore, an overall conclusion and a discussion on possible future work are also provided.

5.1 Overview of Included Papers

Paper [I]: Low-profile two-port MIMO terminal antenna for low LTE bands with wideband multimodal excitation

Research Contributions: In this article, the framework presented in Chapter 3 is used to design a two-port MIMO terminal (or smartphone) antenna with low antenna correlation and wide bandwidth. As described in Chapter 3, since there is only one resonant chassis mode at frequencies below 1 GHz, it is challenging to design MIMO antennas with high total efficiency, low correlation, and large bandwidth. It is even more challenging if the design goals also include achieving a low-profile structure with no ground clearance and equal bandwidth for the ports. Moreover, it is desirable for the antennas to not occupy the top or bottom end of the chassis. Our proposed MIMO antenna satisfies all the mentioned goals, and it is

achieved by using a systematic design process, aided by CM analysis. A new approach is proposed to design minor structural changes on the terminal chassis as well as, multimode feeds, using the magnitude and phase information of the near-fields and currents of CMs over frequency. This approach has resulted in a low profile, two-port MIMO antenna, where both ports simultaneously cover the common LTE bands below 1 GHz with high total efficiencies and low envelope correlation. Furthermore, as the top and bottom sides of the chassis are not used in the two-port design, it is used to achieve, for the first time, a low-band three-port MIMO antenna.

Personal Contributions: I was the main contributor and lead researcher for all parts of this scientific work, including but not limited to developing the idea, performing the full-wave/circuit simulations and CM analysis, post-processing with MATLAB codes, creating and measuring the prototype, as well as writing the paper, with guidance and support of Buon Kiong Lau.

Paper [II]: Large screen enabled tri-port MIMO handset antenna for low LTE bands

Research Contributions: In this article, a tri-port MIMO antenna for large screen mobile handsets (or smartphones) is proposed by using a systematic design process, aided by the CM-based framework presented in Chapter 3. It was shown in Chapter 2 that, assuming a rich multipath propagation environment and multi-antennas with high efficiencies and low correlations, the capacity of a MIMO system is linearly dependent on the number of the antenna elements. However, as mentioned in Chapter 3, terminal antennas at cellular bands below 1 GHz rely on the chassis for radiation, and there is only one resonant chassis mode below 1 GHz. This single-mode property makes it challenging to design low-band N -port MIMO antennas (especially for $N > 2$) with uncorrelated ports, high total efficiencies and moderate bandwidths. Recently, the screen-to-body ratio of mobile handsets has been increasing. In the literature, the metal covered screen is mainly seen as a component that negatively affects antenna performance. In this work, we take advantage of the two resonant modes introduced by the screen to facilitate an additional uncorrelated MIMO port in a tri-port design for frequency bands below 1 GHz. The CM analysis of the double-plate model of the handset enabled a sufficient number of resonant modes to be created and tuned. Then, a step-by-step feeding design/excitation procedure was used to selectively excite

the modes for the three ports, notably with wide bandwidth, high total efficiencies, and low correlations.

Personal Contributions: I was the main contributor and lead researcher for all parts of this scientific work, including but not limited to developing the idea, performing the full-wave/circuit simulations and CM analysis, post-processing with MATLAB codes, creating and measuring the prototype, as well as writing the paper, with guidance and support of Buon Kiong Lau.

Paper [III]: Low-band MIMO antenna for smartphones with robust performance to user interaction

Research Contributions: In this letter, a two-port MIMO terminal (or smartphone) antenna design that is robust to user effects is proposed for frequencies below 1 GHz. The systematic design process is aided by the CM-based framework and the mode mapping technique given in Chapter 3 helped to find the modes that are less affected by the presence of the human body than the classical dipole modes. Like Paper [II], CM analysis is carried out on a simulation model that includes a large screen. Then, the desired modes are tuned by considering the modal near-fields and currents. Finally, these modes are selectively excited by a careful feeding network design, to simultaneously achieve sufficient impedance bandwidth and isolation for some low-band applications. The design is confirmed to be significantly more robust in MIMO performance to user effects (i.e., a one-hand data mode and a talk mode) than other two-port antennas in the literature. Furthermore, the proposed antenna does not require any adaptive circuit to compensate for user effects.

Personal Contributions: I was the main contributor and lead researcher for all parts of this scientific work, including but not limited to developing the idea, performing the full-wave/circuit simulations and CM analysis, post-processing with MATLAB codes, creating and measuring the prototype, as well as writing the paper, with guidance and support of Buon Kiong Lau.

Paper [IV]: Co-designed millimeter-wave and sub-6GHz antenna for 5G smartphones

Research Contributions: In this letter, a smartphone antenna system with shared-aperture configuration is proposed to accommodate four mm-wave arrays and two sub-6 GHz antennas in a compact space. The mm-wave array employs parasitic elements loaded with PIN diodes, providing beam-steering capability without lossy feeding network. The CCEs that excite the sub-6 GHz bands are shared by the mm-wave arrays as ground plane, facilitating high space utilization and low-complexity structure.

Personal Contributions: Qiuyan Liang was the main contributor of this paper. I designed the sub-6 GHz antenna, and I was involved in the process of designing the overall layout of the millimeter-wave and sub-6 GHz antennas. Qiuyan Liang took the lead in writing the paper, with the guidance and support from me and Buon Kiong Lau.

Paper [V]: Wideband SIW-based low-cost multi-layer slot antenna array for E-Band applications

Research Contributions: In this transactions paper, a substrate integrated waveguide slot antenna array is proposed for the gigabyte point-to-point application in *E*-band. As discussed in Chapter 3, the implementation of a low loss corporate feeding network is a challenge, especially in higher mm-wave bands. In this paper, a higher order cavity mode is utilized for the unit cell of the *E*-band slot antenna array, which results in simpler feeding network with reduced loss than slot arrays applying the fundamental cavity mode. Moreover, the design provides more relaxed fabrication tolerance and higher accuracy, the effects of which are more pronounced in *E*-band than lower frequencies, leading to enhanced stability of performance. A differential feeding network is also implemented to mitigate beam deviation problems in this band. Finally, the antenna is implemented using “Any-Layer HDI PCB technology”, which is the most advanced PCB technology available. Stacked micro-vias is an interesting feature in the Any-layer PCB technology. The importance of stacked micro-vias compared with machine drilled vias in conventional PCB technology has also been investigated. Considering the possibility for planar 2-D array application, cost and efficiency, as well as impedance and gain bandwidths, this work gives the best performance in the targeted band relative to existing substrate integrated

waveguide *E*-band slot arrays. The simulation and measurement results presented in this paper verified that the designs are valid for modules, which can be used as subarrays of very large arrays needed for *E*-band applications.

Personal Contributions: I was the main contributor and lead researcher for all parts of this scientific work, including but not limited to developing the idea, performing the full-wave simulations and analysis, modifying the design after the first type out, working with the new Any-Layer PCB Technology, and postprocessing with MATLAB codes. The KU Leuven and IMEC collaborators were responsible for prototype creation and measurements. I took the lead in writing the paper, with guidance and support of Buon Kiong Lau.

Paper [VI]: 79 GHz multilayer series-fed patch antenna array with stacked micro-via loading

Research Contributions: In this letter, a multilayer patch array is designed to satisfy the requirements of *E*-band mid-range MIMO automotive radar applications as presented in Chapter 1. For instance, the crosstalk between the transmitting and receiving arrays can be mitigated to a large extent due to the metallic walls in the design. In addition, the cavity width is very close to half-a-wavelength in free space ($\lambda_0/2$) at 79 GHz, which helps to suppress sidelobes when several patch arrays are placed side by side to form the transmitting or receiving array. In contrast to Paper [V], series feeding is used, which as discussed in Chapter 4 is known to have narrowband characteristics. However, the proposed array achieves wide impedance-gain bandwidth by vertically loading the patches. The vertical loading is realized by stacked micro-vias (SMVs) in the low cost Any-Layer PCB Technology. The SMVs have an equivalent capacitance and inductance loading effect that can help to match the array over a larger frequency band. This is the first time that the fundamental technical advancement (i.e., SMV implementation) of “Any-Layer PCB technology” is explicitly utilized in the design process. The wide band operation is highly advantageous for the mentioned applications as it provides flat-gain behavior and increases the robustness of the fabricated antenna in covering the desired band. However, the proposed patch-loading concept for bandwidth enhancement can be applied, in general, to any series-fed patch array (e.g., those for lower frequencies).

Personal Contributions: I was the main contributor and lead researcher for all parts of this scientific work, including but not limited to developing the idea, performing the full-wave simulations and analysis, modifying the design after the first type out, working with the new Any-Layer PCB Technology, and postprocessing with MATLAB codes. The KU Leuven and IMEC collaborators were responsible for prototype creation and measurements. I took the lead in writing the paper, with guidance and support of Buon Kiong Lau.

5.2 Conclusions

This contains research outputs in two aspects of antenna design for high data rate systems, including MIMO antenna system design for mobile terminals (i.e., Papers [I]-[IV]) and mm-wave antenna array design for two different *E*-band applications (i.e., Papers [V] and [VI]). Characteristic modes and wave guide/cavity modes have been found to be useful as tools for the systematic design of these MIMO and array antennas.

Papers [I]-[IV] contribute to advancing the design of efficient antenna systems for mobile terminals based on the TCM. Systematic applications of TCM reveal how the complexity of terminal antenna design can be substantially reduced. For instance, it was shown that, despite that CM analysis is based on structures without feed, it can provide insights into how to efficiently feed the desired modes. Specifically, different kinds of mode coupling mechanisms were evaluated and the independent control of CMs were devised for efficient antenna design in terminals. This body of work has demonstrated the respective advantages of selective inductive excitation as well as common capacitive excitation of the CMs on the chassis.

In this context, Paper [I] utilizes the insights from TCM to develop a complete systematic design approach for a low profile two-port MIMO antenna for terminals. A new concept of designing MIMO terminal antennas in frequencies below 1 GHz is introduced in Paper [I]. The concept relies on the joint excitation of multiple chassis modes with proper phase shifts to drastically improve the impedance bandwidth in the low band while retaining low correlation between the two ports. This design concept also helped to save space on the chassis and increase the number of isolated ports from two to three. However, the bandwidth of the third port was not enough to cover a typical low band. This problem was solved in Paper [II], where based on new modes introduced by the large metal-covered screen, a tri-port MIMO antenna is proposed for the first time for large-screen smartphones, to cover cellular bands below 1 GHz. Paper [III] takes the TCM design process one

step further by considering the user effect and designing a high efficiency MIMO antenna in the presence of the user. Finally, in Paper [IV], mm-wave antennas with beam-steering capability were tightly integrated with two sub-6 GHz antennas. It was shown that the capacitive coupling element that served as the feeding element of a sub-6 GHz antenna in Paper [II] can be shared by the mm-wave antennas without changing the fundamental radiation modes of the chassis. Likewise, the operation of the mm-wave antenna is also relatively unaffected.

Papers [V] and [VI] investigate new antenna array topologies in combination with a new multilayer PCB technology called “Any-Layer” PCB technology for future *E*-band MIMO radar and communication applications. This new technology has high accuracy and very low cost in mass production and it is found to be reliable and accurate enough for antenna design in *E*-band. Antenna arrays in Papers [V] and [VI] can be readily combined with active circuits (e.g., monolithic microwave integrated circuits (MMICs)). The presented antenna arrays are with various feeding networks, including series feeding [VI] and corporate feeding [V]. It was shown that the results were different for the different antenna designs, but for each design the requirements for the intended application is satisfied. In the design process, waveguide/cavity modes and CMs were found to be helpful.

In this context, 2×2 unit cell wideband differential-fed slot array is proposed in Paper [V], for the *E*-band multi-gigabits fixed wireless application. Based on the electric field properties of the higher order cavity mode, both the resonance cavity and the antenna feeding network for the unit cell can be realized efficiently, resulting in a simplified feeding network and relatively low loss in *E*-band. Moreover, the use of higher order mode makes the structure less sensitive to fabrication errors, which is desirable for *E*-band applications. The proposed low-cost *E*-band SIW antenna array has the merits of simple feeding structure, wide bandwidth, low loss, and ease of integration with active circuits.

On the other hand, in Paper [VI], a novel compact patch antenna array loaded with SMVs is presented. SMV is an interesting feature in the Any-Layer technology. The SMV loading enables an array topology with wide combined impedance-gain bandwidth. The proposed series-fed patch array topology is a good candidate for 79 GHz MIMO automotive radar due to the low cost, compact size, ability to suppress surface waves, as well as relatively wide impedance and flat-gain bandwidths. Further, due to the fact that an 8-layer build-up has been used in the design process, it is expected that the digital and analogue signal routings behind the antenna arrays in the radar module can be placed in different layers, and hence the final module becomes more compact. This is a huge commercial advantage of the technology.

5.3 Future works

Many aspects within and beyond the studied topics can be interesting subjects for future work. The following is a selection of the most interesting and promising extensions of the work presented in this thesis:

- 1) The platform-integrated antenna design concept using TCM, which was discussed in Chapter 3, truly opens up the design space for spatially confined antennas. It may also find important application in the Internet-of-Things (IoT) technology, as almost every object can be designed as a sensor and/or actuator. In addition, large performance improvements are still possible through research efforts in the following aspects: (A) the selective excitation of platform CMs or even dynamic selective excitation for reconfigurable antenna systems, (B) the opportunistic use of dielectric materials in platforms to facilitate more design freedom for performance enhancement as compared to focusing only on the metallic part of the platforms, (C) advanced antenna array developments based on the structure of the platform for beamforming and other advanced applications, and (D) robust MIMO antenna design for terminals, which take more user hand scenarios into account than Paper [III].
- 2) In Chapter 4, several technologies for AiP solutions were discussed. However, for applications above 100 GHz (e.g., 140 GHz radar systems, beyond 5G terabits/s wireless communications), it is feasible to integrate antennas into the chip, due to the small wavelength and subsequently the small antenna elements and arrays. By using AoC solutions, the interconnection losses incurred between the antennas and the chip are eliminated and the mm-wave packaging design is simplified. However, the main problem associated with antenna designs based on mainstream silicon technologies is the very low efficiency (around 10-20%). This is due to the high permittivity and the low resistivity of silicon substrates. Exploiting electromagnetic band gap (EBG) structures is a great solution to deal with this problem. These structures can help to suppress the surface waves and increase the radiated power from the antenna element, which leads to higher efficiency. EBG structures are reported to work well in the literature at lower frequencies, but their combination with on-chip antennas at very high frequencies is quite a new research direction and it may attract the interest of academia and industry in the near future.

- 3) As already mentioned in Chapter 1, automotive radars are categorized into three different types: short, medium, and long-range radars. In the automotive industry, it is very interesting to have an antenna that can be used in two out of three radar types, which means that the antenna characteristics have to pass the requirements of both radar types. For example, designing an antenna array that is operational in both short and medium range radar mode can eliminate the switching between these two functional modes. The antenna array with shaped beam is a high-potential solution to solve this problem and a totally new concept in automotive radars. Shaped beam antenna arrays have been utilized in some particular applications, for example in satellite communications, but are certainly not widely studied in automotive radars. In this case, several antenna topologies, including cascaded patch, combline, grid, and slot antenna arrays can be surveyed to check the feasibility of the MIMO MSRR (Medium-short range radar) module.

References

- [1] Y. Wang, *et al.* “5G mobile: Spectrum broadening to higher-frequency bands to support high data rates,” *IEEE Veh. Technol. Mag.*, vol. 9, no. 3, pp. 39-46, 2014.
- [2] “Framework and overall objectives of the future development of IMT for 2020 and beyond,” ITU-R, Tech. Rep. M.2083, Sep. 2015. [Online]. Available: <https://www.3GPP.org>.
- [3] R. G. Vaughan and J. B. Andersen, “Antenna diversity in mobile communications,” *IEEE Trans. Veh. Technol.*, vol. 36, no. 4, pp. 149-172, 1987.
- [4] R. Hussain and M. S. Sharawi, “5G MIMO antenna designs for base station and user equipment: Some recent developments and trends,” *IEEE Antennas Propag. Mag.*, vol. 64, no. 3, pp. 95-107, 2021.
- [5] Z. Ying, M. Ohtsuka, Y. Nishioka, and K. Fujimoto, “Antennas for mobile terminals,” in *Mobile Antenna Systems Handbook*, K. Fujimoto, Ed. Norwood, MA: Artech House, 2008, pp. 213-319.
- [6] D. Tse and P. Viswanath, *Fundamentals of Wireless Communication*, Cambridge University Press, 2005.
- [7] A. Paulraj, R. Nabar, and D. Gore, *Introduction to Space-Time Wireless Communications*. New York, U.S.: Cambridge University Press, 2003.
- [8] M. A. Jensen and J. W. Wallace, “A review of antennas and propagation for MIMO wireless communications,” *IEEE Trans. Antennas Propag.*, vol. 52, no. 11, pp. 2810-2824, 2004.
- [9] A. J. Paulraj, *et al.*, “An overview of MIMO communications—A key to gigabit wireless,” *Proc. IEEE*, vol. 92, no. 2, pp. 198-218, 2004.
- [10] S. Blanch, J. Romeu, and L. Corbella, “Exact representation of antenna system diversity performance from input parameter description,” *Electron. Lett.*, vol. 39, no. 9, pp. 705-707, 2003.
- [11] R. Tian, B. K. Lau, and Z. Ying, “Multiplexing efficiency of MIMO antennas,” *IEEE Antennas Wireless Propag. Lett.*, vol. 10, pp. 183-186, 2011.

- [12] P. Vainikainen, J. Ollikainen, O. Kivekas, and I. Kelder, "Resonator-based analysis of the combination of mobile handset antenna and chassis," *IEEE Trans. Antennas Propag.*, vol. 50, no. 10, pp. 1433-1444, 2002.
- [13] S. R. Best, "A discussion on small antennas operating with small finite ground planes," in *Proc. IEEE Int. Workshop Antenna Technol.*, White Plains, NY, Mar. 2006, pp. 152-155.
- [14] R. F. Harrington, "Effect of antenna size on gain, bandwidth, and efficiency," *J. Res. Natl. Inst. Stand. Technol.*, vol. 64D, pp. 1-12, 1960.
- [15] C. Gómez-Calero, L. González, and R. Martínez, "Tri-band compact antenna array for MIMO user mobile terminals at GSM 1800 and WLAN bands," *Microw. Opt. Technol. Lett.*, vol. 50, no. 7, pp. 1914-1918, 2008.
- [16] S. Zhang, K. Zhao, Z. Ying, and S. He, "Adaptive quad-element multi-wideband antenna array for user-effective LTE MIMO mobile terminals," *IEEE Trans. Antennas Propag.*, vol. 61, no. 8, pp. 4275-4283, 2013.
- [17] S. Zhang, A. A. Glazunov, Z. Ying, and S. He, "Reduction of the envelope correlation coefficient with improved total efficiency for mobile LTE MIMO antenna arrays: mutual scattering mode," *IEEE Trans. Antennas Propag.*, vol. 61, no. 6, pp. 3280-3291, 2013.
- [18] Z. Miers, H. Li, and B. K. Lau, "Design of bandwidth-enhanced and multiband MIMO antennas using characteristic modes," *IEEE Antennas Wireless Propag. Lett.*, vol. 12, pp. 1696-1699, 2013.
- [19] B. K. Lau, "Multiple antenna terminals," in *MIMO: From Theory to Implementation*, C. Oestges, A. Sibille, and A. Zanella, Eds. San Diego, CA, USA: Academic, 2011, pp. 267-298.
- [20] B. K. Lau, J. B. Andersen, G. Kristensson, and A. F. Molisch, "Impact of matching network on bandwidth of compact antenna arrays," *IEEE Trans. Antennas Propag.*, vol. 54, no. 11, pp. 3225-3238, Nov. 2006.
- [21] H. Li, J. Xiong, and S. He, "A compact planar MIMO antenna system of four elements with similar radiation characteristics and isolation structure," *IEEE Antennas Wireless Propag. Lett.*, vol. 8, pp. 1107-1110, 2009.
- [22] H. Li, J. Xiong, Z. Ying, and S. He, "High isolation compact four-port MIMO antenna systems with built-in filters as isolation structure," in *Proc. 4th Eur. Conf. Antennas Propag.*, Rome, Italy, Apr. 2010, pp. 1-4.
- [23] F. Yang and Y. Rahmat-Samii, "Microstrip antennas integrated with electromagnetic band-gap (EBG) structures: a low mutual coupling design for array applications," *IEEE Trans. Antennas Propag.*, vol. 51, no. 10, pp. 2936-2946, 2006.
- [24] M. Karaboikis, C. Soras, G. Tsachtsiris, and V. Makios, "Compact dual-printed inverted-F antenna diversity systems for portable wireless devices," *IEEE Antennas Wireless Propag. Lett.*, vol. 3, pp. 9-14, 2004.

- [25] A. Diallo, C. Luxey, P. Le Thuc, R. Staraj, and G. Kossiavas, "Enhanced two-antenna structures for universal mobile telecommunications system diversity terminals," *IET Microw. Antennas Propag.*, vol. 2, pp. 93-101, 2008.
- [26] B. K. Lau and J. B. Andersen, "Simple and efficient decoupling of compact arrays with parasitic scatterers," *IEEE Trans. Antennas Propag.*, vol. 60, no. 2, pp. 464-472, 2012.
- [27] A. Diallo, C. Luxey, P.L. Thuc, R. Staraj, and G. Kossiavas, "Study and reduction of the mutual coupling between two mobile phone PIFAs operation in the DCS 1800 and UMTS bands," *IEEE Trans. Antennas Propag.*, vol. 54, no. 11, pp. 3063-3074, 2006.
- [28] R. A. Bhatti, S. Yi, and S. O. Park, "Compact antenna array with port decoupling for LTE-standardized mobile phones," *IEEE Antennas Wireless Propag. Lett.*, vol. 8, pp. 1430-1433, 2009.
- [29] G. Park, M. Kim, T. Yang, J. Byun, and A. S. Kim, "The compact quadband mobile handset antenna for the LTE700 MIMO application," in *Proc. IEEE Int. Symp. Antennas Propag.*, Charleston, SC, Jun. 2009, pp. 1-4.
- [30] M. S. Han and J. Choi, "Multiband MIMO antenna with a band stop filter for high isolation characteristics," in *Proc. IEEE Int. Symp. Antennas Propag.*, Charleston, SC, Jun. 2009, pp. 1-4.
- [31] H. Li, Y. Tan, B. K. Lau, Z. Ying, and S. He, "Characteristic mode based tradeoff analysis of antenna-chassis interactions for multiple antenna terminals," *IEEE Trans. Antennas Propag.*, vol. 60, no. 2, pp. 490-502, 2012.
- [32] V. Plicanic, B. K. Lau, A. Derneryd, and Z. Ying, "Actual diversity performance of a multiband antenna with hand and head effects," *IEEE Trans. Antennas Propag.*, vol. 57, no. 5, pp. 1547-1556, 2009.
- [33] S. Stein, "On cross coupling in multi-beam antennas," *IEEE Trans. Antennas Propag.*, vol. 10, no. 5, pp. 548-557, 1962.
- [34] C. Rowell and R. Murch, "A compact PIFA suitable for dual-frequency 900/1800-MHz operation," *IEEE Trans. Antennas Propag.*, vol. 46, no. 4, pp. 596-598, 1998.
- [35] T. Taga and K. Tsunekawa, "Performance analysis of a built-in planar inverted-F antenna for 800 MHz band portable radio units," *IEEE J. Select. Areas Commun.*, vol. ACE-5, no. 5, pp. 921-929, 1987.
- [36] R. C. Hansen, "Fundamental limitations in antennas," *Proc. IEEE*, vol. 69, no. 2, pp. 170-182, 1981.
- [37] J. Villanen, J. Ollikainen, O. Kivekas, and P. Vainikainen, "Coupling element based mobile terminal antenna structure," *IEEE Trans. Antennas Propag.*, vol. 54, no. 7, pp. 2142-2153, 2006.
- [38] J. Holopainen, R. Valkonen, O. Kivekäs, J. Ilvonen, and P. Vainikainen, "Broadband equivalent circuit model for capacitive coupling element-based mobile terminal antenna," *IEEE Antennas Wireless Propag. Lett.*, vol. 9, pp. 716-719, 2010.

- [39] W. L. Schroeder, A. A. Vila, and C. Thome, "Extremely small wideband mobile phone antenna by inductive chassis mode coupling," in *Proc. 36th Eur. Microw. Conf., Manchester, U.K.*, Sep. 2006, pp. 1702-1705.
- [40] W. L. Schroeder and C. T. Famdie, "Utilisation and tuning of the chassis modes of a handheld terminal for the design of multiband radiation characteristics," in *Proc. IEE Wideband Multiband Antennas and Arrays*, Sep. 2005, pp. 117-122.
- [41] S. R. Best, "The significance of ground-plane size and antenna location in establishing the performance of ground-plane-dependent antennas," *IEEE Antennas Propag. Mag.*, vol. 51, no. 6, pp. 29-42, Dec. 2009.
- [42] International Commission on Non-Ionizing Radiation Protection (ICNIRP), "Guidelines for limiting exposure to time-varying electric, magnetic, and electromagnetic fields (up to 300 GHz)," *Health Physics*, vol. 74, no. 4, Apr. 1998, pp. 494-522.
- [43] ANSI/IEEE Std C95.1, 1999 Edition, *IEEE Standard for Safety Levels with Respect to Human Exposure to Radio Frequency Electromagnetic Fields, 3 kHz to 300 GHz*, New York, USA, Apr. 1999, pp. 73.
- [44] R. Feger, C. Wagner, S. Schuster, S. Scheibelhofer, H. Jager, and A. Stelzer, "A 77-GHz FMCW MIMO radar based on an SiGe single chip transceiver," *IEEE Trans. Microw. Theory Techn.*, vol. 57, no. 5, pp. 1020-1035, 2009.
- [45] 6G Flagship, "Key Drivers and Research Challenges for 6G Ubiquitous Wireless Intelligence," 2019.
- [46] H. Zirath, T. Masuda, R. Kozhuharov, and M. Ferndahl, "Development of 60-GHz front-end circuits for a high-data-rate communication system," *IEEE J. Solid-State Circuits*, vol. 39, no. 10, pp. 1640-1649, 2004.
- [47] H. Liebe, "MPM89 — An atmospheric mm-wave propagation model," *Int. J. Infrared Millim. Waves*, vol. 10, no. 6, pp. 631-650, 1989.
- [48] J. du Preez, and S. Sinha, *Introduction to the World of Millimeter-Wave Systems*, Springer, 2016.
- [49] Z. Pi, and F. Khan, "An introduction to millimeter-wave mobile broadband systems," *IEEE Commun. Mag.*, vol. 49, no. 6, pp. 101-107, 2011.
- [50] H. M. Cheema and A. Shamim, "The last barrier: On-chip antennas," *IEEE Microw. Mag.*, vol. 14, no. 1, pp. 79-91, 2013.
- [51] N. Demirel *et al.*, "Codesign of a PA-antenna block in silicon technology for 80-GHz radar application," *IEEE Trans. Circuits Syst., II, Exp. Briefs*, vol. 60, no. 4, pp. 177-181, 2013.
- [52] J. Xu, Z. N. Chen, X. Qing, and W. Hong, "140-GHz TE₂₀-mode dielectric-loaded SIW slot antenna array in LTCC," *IEEE Trans. Antennas Propag.*, vol. 61, no. 4, pp. 1784-1793, 2013.
- [53] Y. Zhang, S. Shi, R. D. Martin, and D. W. Prather, "High-gain linearly tapered antipodal slot antenna on LCP substrate at E- and W-bands," *IEEE Antennas Wireless Propag. Lett.*, vol. 15, pp. 1357-1360, 2016.

- [54] A. L. Merlo, "Automotive radar for the prevention of collisions," *IEEE Trans. Ind. Electron.*, vol. IECI-11, no. 1, pp. 1-6, 1964.
- [55] F. R. Holmstrom, J. B. Hopkins, A. T. Newfell, and E. F. White, "A microwave anticipatory crash sensor for activation of automobile passive restraints," *IEEE Trans. Veh. Technol.*, vol. 22, no. 2, pp. 46-54, 1973.
- [56] J. E. Stevens and L. L. Nagy, "Diplex Doppler radar for automotive obstacle detection," *IEEE Trans. Veh. Technol.*, vol. 23, no. 2, pp. 34-44, 1974.
- [57] T. Tamama, A. Iwabe, K. Ban, M. Tsudo, S. Mitsui, K. Baba, M. Kiyoto, H. Endo, and N. Fujiki, "Radar sensor for automotive collision prevention," in *IEEE MTT-S Int. Microwave Symp. Dig.*, Ottawa, Canada, Jun. 1978, pp. 168-170.
- [58] J. D. Woll, "Monopulse Doppler radar for vehicle applications," in *Proc. IEEE Symp. Intell. Veh.*, Detroit, MI, Sep. 1995, pp. 42-47.
- [59] J. Wenger, "Automotive radar – status and perspectives," in *Proc. IEEE Compd. Semicond. Integr. Circuit Symp.*, Palm Springs, CA, Oct. 2005, pp. 21-24.
- [60] M. I. Skolnik, *Radar Handbook*, 3rd Edition, New York: McGraw Hill, 2008.
- [61] K. Strohm, H. L. Bloecher, R. Schneider, and J. Wenger, "Development of future short range radar technology," in *Proc. Eur. Radar Conf. (EuRAD)*, Paris, France, Oct. 2005, pp. 165-168.
- [62] H. Rohling, "Development milestones in 24 GHz automotive radar systems," in *Proc. 11th Int. Radar Symp. (IRS)*, Vilnius, Lithuania, Jun. 2010, pp. 1-5.
- [63] I. Gresham, A. Jenkins, R. Egri, C. Eswarappa, N. Kinayman, N. Jain, R. Anderson, F. Kolak, R. Wohlert, S. Bawell, J. Bennett, and J. P. Lanteri, "Ultra-wideband radar sensors for short-range vehicular applications," *IEEE Trans. Microw. Theory Tech.*, vol. 52, no. 9, pp. 2105-2122, 2004.
- [64] M. Kohler, J. Hasch, H. L. Blocher, and L. P. Schmidt, "Feasibility of automotive radar at frequencies beyond 100 GHz," *Int J. Microw. Wirel. T.*, vol. 5., no.1, pp. 49-54, 2013.
- [65] A. Haimovich, R. Blum, and L. Cimini, "MIMO radar with widely separated antennas," *IEEE Signal Process. Mag.*, vol. 25, no. 1, pp. 116-129, 2008.
- [66] F. Robey, S. Coumts, D. Weikle, J. McHarg, and K. Cuomo, "MIMO radar theory and experimental results," in *Proc. 38th Asilomar Conf. Signals, Syst., Comput. Conf.*, vol. 1, Pacific Grove, CA, Nov. 2004, pp. 300-304.
- [67] N. Kees, E. Schmidhammer, and J. Detlefsen, "Improvement of angular resolution of a millimeter wave imaging system by transmitter location multiplexing," in *Proc. IEEE Microw. Syst. Conf.*, May 1995, pp. 105-108.
- [68] M. Steinhauer, H. O. Ruo, H. Irion, and W. Menzel, "Millimeter-wave radar sensor based on a transceiver array for automotive applications," *IEEE Trans. Microw. Theory Techn.*, vol. 56, no. 2, pp. 261-269, 2008.
- [69] O. Khan, J. Meyer, K. Baur, and C. Waldshmidt, "Hybrid thin film antenna for automotive radar at 79 GHz," *IEEE Trans. Antennas Propag.*, vol. 65, no. 10, pp. 5076-5085, 2017.

- [70] C. Dehos, J. L. González, A. D. Domenico, D. Kténas, and L. Dussopt, "Millimeter-wave access and backhauling: The solution to the exponential data traffic increase in 5G mobile communications systems?" *IEEE Commun. Mag.*, vol. 52, no. 9, pp. 88-95, 2014.
- [71] T. Rappaport, *et al.* "Millimeter wave mobile communications for 5G cellular: It will work!" *IEEE Access*, vol. 1, pp. 335-349, 2013.
- [72] *Allocation and Service Rules for the 71-76 GHz, 81-86 GHz, and 92-95 GHz Bands*, document FCC 03-248, Federal communication Commission, Nov. 2003.
- [73] *Planning of the 71-76 GHz and 81-86 GHz Bands for Millimeter Wave High Capacity Fixed Link Technology*, document SPP 2006-11, Australian communication and Media Authority, 2006.
- [74] "Australian communications and media authority" [online]. Available: <https://pdfs.semanticscholar.org/4f6f/8507de0d7edc2b23b19cece8d87913ea23cc.pdf>.
- [75] D. del Rio, A. Rezola, R. Berenguer, I. Gurutzeaga, I. Velez, and J. F. Sevillano, "A wideband millimeter-wave up-conversion mixer for future backhaul E-band point-to-point links with a 0 dBm 1-dB compression point," in *Proc. IEEE International Conference on Ubiquitous Wireless Broadband (ICUWB)*, 2015, pp. 1-5.
- [76] T. Potelon, M. Ettorre, L. Le Coq, T. Bateman, J. Francey, R. Sauleau, "Reconfigurable CTS antenna fully integrated in PCB technology for 5G backhaul applications," *IEEE Trans. Antennas Propag.*, vol. 67, no. 6, pp. 3609-3618, 2019.
- [77] K. Kunz, *The Finite Difference Time Domain Method for Electromagnetics*. Boca Raton: CRC Press, 1993.
- [78] J. M. Jin, *The Finite Element Method in Electromagnetics*. Hoboken. New Jersey: John Wiley & Sons Inc, 2014.
- [79] R. F. Harrington, *Field Computation by Moment Methods*. Malabar, FL: Krieger Pub Co, 1968.
- [80] E. K. P. Chong, S. H. Žak, *An Introduction to Optimization*, Wiley-Interscience Series in Discrete Mathematics and Optimization. John Wiley & Sons, New York, 2001.
- [81] R. E. Collin, *Foundations for Microwave Engineering*, 2nd ed. Hoboken, NJ, USA: Wiley-IEEE Press, 1992.
- [82] C. Balanis, *Advanced Engineering Electromagnetics*, USA: Wiley-IEEE Press, 1989.
- [83] R. E. Collin, *Field Theory of Guided Waves*. McGraw Hill, New York, 1960.
- [84] R. Mittra and S. W. Lee, *Analytical Techniques in the Theory of Guided Waves*, Macmillan, New York, 1971.
- [85] J. A. Stratton, *Electromagnetic Theory*. Hoboken, NJ, USA: Wiley-IEEE Press, 2007.

- [86] P. M. Morse and H. Feshbach, *Methods of Theoretical Physics*, New York: McGraw-Hill, 1953.
- [87] J. A. Stratton, *Electromagnetic Theory*, New York: McGraw-Hill, 1941.
- [88] C. T. Tai, *Dyadic Green's Functions in Electromagnetic Theory*, San Francisco: Intext Educational Publishers, 1971.
- [89] R. F. Harrington, *Time Harmonic Electromagnetic Fields*, New York, McGraw-Hill, 1961.
- [90] L. J. Chu, "Physical Limitations of Omnidirectional Antennas," *J. Appl. Phys.*, vol. 19, pp. 1163-1175, 1948.
- [91] A. A. Glazunov, M. Gustafsson, A. F. Molisch, F. Tufvesson, and G. Kristensson "Spherical vector wave expansion of Gaussian electromagnetic fields for antenna-channel interaction analysis," *IEEE Trans. Antennas Propag.*, vol. 57, no. 7, pp. 2055-2067, 2009.
- [92] M. Mohajer, S. Safavi-Naeini, and S. K. Chaudhuri, "Spherical vector wave method for analysis and design of MIMO antenna systems," *IEEE Antennas Wireless Propag. Lett.*, vol. 9, pp. 1267-1270, 2010.
- [93] R. G. Parkinson and M. M. Z. Kharadly, "Optimum determination of scattered field coefficients from near-field measurements," *Proc. IEEE*, vol. 58, no. 9, pp. 1396-1397, 1970.
- [94] D. Wilton and R. Mittra, "A new numerical approach to the calculation of electromagnetic scattering properties of two-dimensional bodies of arbitrary cross section," *IEEE Trans. Antennas Propag.*, vol. 20, no. 2, pp. 310-317, 1972.
- [95] R. J. Garbacz, "A generalized expansion for radiated and scattered fields," Ph.D. dissertation, The Ohio State Univ., USA, 1968.
- [96] R. Harrington and J. Mautz, "Theory of characteristic modes for conducting bodies," *IEEE Trans. Antennas Propag.*, vol. 19, no. 5, pp. 622-628, 1971.
- [97] R. F. Harrington and J. R. Mautz, "Computation of characteristic modes for conducting bodies," *IEEE Trans. Antennas Propag.*, vol. AP-19, no. 5, pp. 629-639, 1971.
- [98] R. F. Harrington, J. R. Mautz, and Y. Chang, "Characteristic modes for dielectric and magnetic bodies," *IEEE Trans. Antennas Propag.*, vol. AP-20, pp. 194-198, 1972.
- [99] B. K. Lau, M. Capek, and A. M. Hassan, "Characteristic modes: Progress, overview, and emerging topics," *IEEE Antennas Propag. Mag.*, vol. 64, no. 2, pp. 14-22, 2022.
- [100] Y. Saad, *Numerical Methods for large Eigenvalue Problems*. Society for Industrial and Applied Mathematics (SIAM), 2001.
- [101] A. Krewski, W. L. Schroeder, and K. Solbach, "MIMO LTE antenna design for laptops based on theory of characteristic modes," in *Proc. 6th Eur. Conf. Antennas Propag.*, Prague, Czech Republic, Mar. 2012, pp. 1894-1898.

- [102] C. Deng, Z. Xu, A. Ren, and S. V. Hum, "TCM-based bezel antenna design with small ground clearance for mobile terminals," *IEEE Trans. Antennas Propag.*, vol. 67, no. 2, pp. 745-754, 2019.
- [103] Z. Miers and B. K. Lau, "Wide band characteristic mode tracking utilizing far-field patterns," *IEEE Antennas Wireless Propag. Lett.*, vol. 14, pp. 1658-1661, 2015.
- [104] R. Harrington, and J. Mautz, "Control of radar scattering by reactive loading," *IEEE Trans. Antennas Propag.*, vol. 20, no. 4, pp. 446-454, 1972.
- [105] J. Mautz, and R. Harrington, "Modal analysis of loaded n-port scatterers," *IEEE Trans. Antennas Propag.*, vol. 21, no. 2, pp. 188-199, 1973.
- [106] R. Harrington and J. Mautz, "Optimization of radar cross section of N-port loaded scatterers," *IEEE Trans. Antennas Propag.*, vol. 22, no. 5, pp. 697-701, 1974.
- [107] E. Newman, "Small antenna location synthesis using characteristic modes," *IEEE Trans. Antennas Propag.*, vol. 27, no. 4, pp. 530-531, 1979.
- [108] R. Garbacz and D. Pozar, "Antenna shape synthesis using characteristic modes," *IEEE Trans. Antennas Propag.*, vol. 30, no. 3, pp. 340-350, 1982.
- [109] M. Cabedo-Fabres, E. Antonino-Daviu, A. Valero-Nogueira, and M. F. Bataller, "The theory of characteristic modes revisited: A contribution to the design of antennas for modern applications," *IEEE Antennas Propag. Mag.*, vol. 49, no. 5, pp. 52-68, 2007.
- [110] H. Morishita, Y. Kim, and K. Fujimoto, "Design concept of antennas for small mobile terminals and the future perspective," *IEEE Antennas Propag. Mag.*, vol. 44, no. 5, pp. 30-43, 2002.
- [111] J. J. Adams, S. Genovesi, B. Yang, and E. Antonino-Daviu, "Antenna element designs using characteristic modes analysis," *IEEE Antennas Propag. Mag.*, vol. 64, no. 2, pp. 32-40, 2022.
- [112] H. Li, Y. Chen, and U. Jakobus, "Synthesis, control, and excitation of characteristic modes for platform integrated antenna designs," *IEEE Antennas Propag. Mag.*, vol. 64, no. 2, pp. 41-48, 2022.
- [113] D. Manteuffel, F. H. Lin, T. Li, N. Peitzmeier, and Z. N. Chen, "Characteristic mode inspired advanced multiple antennas," *IEEE Antennas Propag. Mag.*, vol. 64, no. 2, pp. 49-57, 2022.
- [114] E. Antonino-Daviu, M. Cabedo-Fabres, M. Ferrando-Bataller, and M. Gallo, "Design of a multimode MIMO antenna using the theory of characteristic modes," *Radioengineering*, vol. 18, no. 4, pp. 425-430, 2009.
- [115] B. Yang and J. J. Adams, "Systematic shape optimization of symmetric MIMO antennas using characteristic modes," *IEEE Trans. Antennas Propag.* vol. 64, no. 7, pp. 2668-2678, 2015.
- [116] B. Yang, J. Zhou, and J. J. Adams, "A shape-first, feed-next design approach for compact planar MIMO antennas," *Prog. Electromagn. Res.*, vol. 77, pp. 157-165, Jan. 2019.

- [117] J. Ethier and D. A. McNamara, "An interpretation of mode-decoupled MIMO antennas in terms of characteristic port modes," *IEEE Trans. Magn.*, vol. 45, no. 3, pp. 1128-1131, 2009.
- [118] D. Manteuffel and R. Martens, "Compact multimode multielement antenna for indoor UWB massive MIMO," *IEEE Trans. Antennas Propag.*, vol. 64, no. 7, pp. 2689-2697, 2016.
- [119] Y. Chen and C. F. Wang, "Characteristic-mode-based improvement of circularly polarized U-slot and E-shaped patch antennas," *IEEE Antennas Wireless Propag. Lett.*, vol. 11, pp. 1474-1477, 2012.
- [120] H. H. Tran, N. Nguyen-Trong, and A. M. Abbosh, "Simple design procedure of a broadband circularly polarized slot monopole antenna assisted by characteristic mode analysis," *IEEE Access*, vol. 6, pp. 78,386-78,393, 2018.
- [121] E. Safin and D. Manteuffel, "Manipulation of characteristic wave modes by impedance loading," *IEEE Trans. Antennas Propag.*, vol. 63, no. 4, pp. 1756-1764, 2015.
- [122] Z. Mahlaoui, E. Antonino-Daviu, A. Latif, and M. Ferrando-Bataller, "Design of a dual-band frequency reconfigurable patch antenna based on characteristic modes," *Int. J. Antennas Propag.*, vol. 2019, p. e4512532, 2019.
- [123] Y. Chen and C. F. Wang, "Synthesis of reactively controlled antenna arrays using characteristic modes and DE algorithm," *IEEE Antennas Wireless Propag. Lett.*, vol. 11, pp. 385-388, 2012.
- [124] K. Li, Y. Shi, H. Shen, and L. Li, "A characteristic-mode-based polarization reconfigurable antenna and its array," *IEEE Access*, vol. 6, pp. 64,587-64,595, 2018.
- [125] A. Bhattacharyya, J. Pal, K. Patra, and B. Gupta, "Bandwidth-enhanced miniaturized patch antenna operating at higher order dual-mode resonance using modal analysis," *IEEE Antennas Wireless Propag. Lett.*, vol. 20, no. 2, pp. 274-278, 2021.
- [126] M. Khan and M. Chowdhury, "Analysis of modal excitation in wideband slot-loaded microstrip patch antenna using theory of characteristic modes," *IEEE Trans. Antennas Propag.*, vol. 68, no. 11, pp. 7618-7623, 2020.
- [127] Y. Luo, Z. N. Chen, and K. Ma, "Enhanced bandwidth and directivity of a dual-mode compressed high-order mode stub-loaded dipole using characteristic mode analysis," *IEEE Trans. Antennas Propag.*, vol. 67, no. 3, pp. 1922-1925, 2019.
- [128] B. Yang and J. J. Adams, "Quality factor calculations for the characteristic modes of dielectric resonator antennas," in *Proc. 2017 USNC-URSI Nat. Radio Sci. Meeting (USNC-URSI NRSM)*, Boulder, CO, Jan. 2017, pp. 1-2.
- [129] H. Alroughani and D. A. McNamara, "The shape synthesis of dielectric resonator antennas," *IEEE Trans. Antennas Propag.*, vol. 68, no. 8, pp. 5766-5777, 2020.

- [130] Y. Chen and C. F. Wang, "HF band shipboard antenna design using characteristic modes," *IEEE Trans. Antennas Propag.*, vol. 63, no. 3, pp. 1004-1013, 2015.
- [131] M. Li and N. Behdad, "Dual-band platform-mounted HF/VHF antenna design using the characteristic mode theory," *IET Microw. Antennas Propag.*, vol. 12, no. 4, pp. 452-458, 2018.
- [132] K. Obeidat, R. G. Rojas, and B. Raines, "Design of antenna conformal to V-shaped tail of UAV based on the method of characteristic modes," in *Proc. 3rd Eur. Conf. Antennas Propag.*, Berlin, Germany, Mar. 2009, pp. 2493-2496.
- [133] D. Wen, Y. Hao, H. Wang, and H. Zhou, "Design of a wideband antenna with stable omnidirectional radiation pattern using the theory of characteristic modes," *IEEE Trans. Antennas Propag.*, vol. 65, no. 5, pp. 2671-2676, 2017.
- [134] R. Xu, *et al.*, "Analysis and design of ultrawideband circularly polarized antenna and array," *IEEE Trans. Antennas Propag.*, vol. 68, no. 12, pp. 7842-7853, 2020.
- [135] N. Peitzmeier, T. Hahn, and D. Manteuffel, "Systematic design of multimode antennas for MIMO applications by leveraging symmetry," *IEEE Trans. Antennas Propag.*, vol. 70, no. 1, pp. 145-155, 2021.
- [136] Q. Wu, W. Su, Z. Li, and D. Su, "Reduction in out-of-band antenna coupling using characteristic mode analysis," *IEEE Trans. Antennas Propag.*, vol. 64, no. 7, pp. 2732-2742, 2016.
- [137] Z. Ma, Z. Yang, Q. Wu, and D. Su, "Out-of-band mutual coupling suppression for microstrip antennas using characteristic mode analysis and shorting pins," *IEEE Access*, vol. 7, pp. 102,679-102,688, 2019,
- [138] P. Liang and Q. Wu, "Characteristic mode analysis of antenna mutual coupling in the near field," *IEEE Trans. Antennas Propag.*, vol. 66, no. 7, pp. 3757-3762, 2018.
- [139] P. Gu, Z. He, J. Xu, K. W. Leung, and R. S. Chen, "Design of wide scanning sparse planar array using both matrix-pencil and space-mapping methods," *IEEE Antennas Wireless Propag. Lett.*, vol. 20, no. 2, pp. 140-144, 2021,
- [140] C. Y. Chiu, B. K. Lau, and R. Murch, "Bandwidth enhancement technique for broadside tri-modal patch antenna," *IEEE Open J. Antennas Propag.*, vol. 1, pp. 524-533, 2020.
- [141] H. Li, B. K. Lau, Z. Ying, and S. He, "Decoupling of multiple antennas in terminals with chassis excitation using polarization diversity, angle diversity and current control," *IEEE Trans. Antennas Propag.*, vol. 60, no. 12, pp. 5947-5957, 2012.
- [142] D. Manteuffel and R. Martens, "Multiple antenna integration in small terminals," in *Proc. Int. Symp. Antennas Propag. (ISAP)*, Nagoya, Japan, Oct. 2012, pp. 211-214.

- [143] R. Martens, E. Safin, and D. Manteuffel, "Inductive and capacitive excitation of the characteristic modes of small terminals," in *Proc. Loughborough Antennas Propag. Conf. (LAPC)*, Loughborough, U.K., Nov. 2011, pp. 1-4,
- [144] R. Castillo, R. Ma, and N. Behdad, "Platform-based, electrically-small HF antenna with switchable directional radiation patterns," *IEEE Trans. Antennas Propag.*, vol. 69, no. 8, pp. 4370-4379, 2021.
- [145] "CST Studio Suite 3D EM Simulation and Analysis Software, version 2023," Dassault Systemes. Accessed: Apr. 14, 2023. [Online]. Available: <https://www.3ds.com/products-services/simulia/products/cst-studio-suite/>
- [146] Betamatch, version 3.7.6. (2019). MNW Scan Pte Ltd. Accessed: Mar. 16, 2020. [Online]. Available: <http://www.mnw-scan.com>
- [147] H. Li, Z. Miers, and B. K. Lau, "Design of orthogonal MIMO handset antennas based on characteristic mode manipulation at frequency bands below 1 GHz," *IEEE Trans. Antennas Propag.*, vol. 62, no. 5, pp. 2756-2766, 2014,
- [148] K. K. Kishor and S. V. Hum, "A two-port chassis-mode MIMO antenna," *IEEE Antennas Wireless Propag. Lett.*, vol. 12, pp. 690-693, 2013.
- [149] C. Deng, Z. Feng, and S. V. Hum, "MIMO mobile handset antenna merging characteristic modes for increased bandwidth," *IEEE Trans. Antennas Propag.*, vol. 64, no. 7, pp. 2660-2667, 2016.
- [150] Z. T. Miers, "Systematic antenna design using the theory of characteristic modes," Ph.D. Dissertation, Lund University, Sweden, 2016.
- [151] I. Vasilev and B. K. Lau, "On user effects in MIMO handset antennas designed using characteristic modes," *IEEE Antennas Wireless Propag. Lett.*, vol. 15, pp. 758-761, 2016.
- [152] Z. Miers and B. K. Lau, "Post-processing removal of non-real characteristic modes via basis function perturbation," in *Proc. Int. Symp. Antennas Propag.*, Fajardo, Puerto Rico, Jun. 2016, pp. 419-420.
- [153] R. Luomaniemi, P. Ylä-Oijala, A. Lehtovuori, and V. Viikari, "Designing hand-immune handset antennas with adaptive excitation and characteristic modes," *IEEE Trans. Antennas Propag.*, vol. 69, no. 7, pp. 3829-3839, 2021.
- [154] H. Li, M. Wu, W. Li, and Y. Yu, "Reducing hand effect on mobile handset antennas by shaping radiation patterns," *IEEE Trans. Antennas Propag.*, vol. 69, no. 8, pp. 4279-4288, 2021.
- [155] J. Toftgard, S. N. Hornsleth, and J. B. Andersen, "Effects on portable antennas of the presence of a person," *IEEE Trans. Antennas Propag.*, vol. 41, no. 6, pp. 739-746, 1993.
- [156] H. Li, S. Sun, and B. Wang, "Automatic feeding arrangement based on theory of characteristic mode," in *Proc. 6th Asia-Pacific Conf. Antennas Propag.*, Xian, China, Oct. 2017, pp. 1-3.

- [157] S. M. Moon, S. Yun, I. B. Yom, and H. L. Lee, "Phased array shaped-beam satellite antenna with boosted-beam control," *IEEE Trans. Antennas Propag.*, vol. 67, no. 12, pp. 7633-7636, 2019.
- [158] "HDI Circuit Boards (2023)," AT&S Products and Technologies. Accessed: Apr. 14, 2023. [Online]. Available: <https://ats.net/en/products/hdi-printed-circuit-boards/>
- [159] A. Enayati, G. A. E. Vandenbosch, and W. D. Raedt, "Millimeter-wave horn-type antenna-in-package solution fabricated in a teflon-based multilayer PCB technology," *IEEE Trans. Antennas Propag.*, vol. 61, no. 4, pp. 1581-1590, 2013.
- [160] "Matrix Circuit Board Materials (2023)," Accessed: Apr. 14, 2023. [Online]. Available: <https://www.matrixelectronics.com/products/panasonic/megtron-6/>
- [161] D. G. Kam, D. Liu, A. Natarajan, S. K. Reynolds, and B. A. Floyd, "Organic packages with embedded phased-array antennas for 60-GHz wireless chipsets," *IEEE Trans. Antennas Propag.*, vol. 1, no. 11, pp. 1806-1814, 2011.
- [162] Y. J. Cheng, Y. X. Guo, and Z. G. Lin, "W-band large-scale high-gain planar integrated antenna array," *IEEE Trans. Antennas Propag.*, vol. 62, no. 6, pp. 3370-3373, 2014.
- [163] I. Slomian, K. Wincza, and S. Gruszczynski, "Series-fed microstrip antenna array with inclined-slot couplers as three-way power dividers," *IEEE Antennas Wireless Propag. Lett.*, vol. 12, pp. 62-64, 2013.
- [164] P. K. Li, Z. H. Shao, Y. J. Cheng, and Q. Wang, "A single layer wideband differential-fed patch antenna array with SIW feeding networks," in *Proc. IEEE Int. Conf. Commun. Problem-solving*, Beijing, China, Dec. 2014, pp. 665-667.
- [165] F. Sickinger, E. Weissbrodt, and M. Vossiek, "76-81 GHz LTCC antenna for an automotive miniature radar frontend," in *Proc. 47th Eur. Microw. Conf.*, Nuremberg, Germany, Oct. 2017, pp. 1222-1225.
- [166] H. Moheb, L. Shafai, and M. Barakat, "Design of 24 GHz microstrip travelling wave antenna for radar application," in *Proc. IEEE Int. Symp. Antennas Propag.*, Newport Beach, CA, Jun. 1995, pp. 350-353.
- [167] L. Zhang, W. Zhang, and Y. P. Zhang, "Microstrip grid and comb array antennas," *IEEE Trans. Antennas Propag.*, vol. 59, no. 11, pp. 4077-4084, 2011.
- [168] S. Sugawa, K. Sakakibara, N. Kikuma, and H. Hirayama, "Low-sidelobe design of microstrip comb-line antennas using stub integrated radiating elements in the millimeter-wave band", *IEEE Trans. Antennas Propag.*, vol. 60, no. 10, pp. 4699-4709, 2012.
- [169] S. Afoakwa, and Y. B. Jung, "Wideband microstrip comb-line linear array antenna using stubbed- element technique for high sidelobe suppression", *IEEE Trans. Antennas Propag.*, vol. 65, no. 10, pp. 5190-5199, 2017.

- [170] Y. Hayashi, K. Sakakibara, M. Nanjo, Sh. Sugawa, N. Kikuma, and H. Hirayama, "Millimeter-wave microstrip comb-Line antenna using reflection-canceling slit structure," *IEEE Trans. Antennas Propag.*, vol. 59, no. 2, pp. 398-406, 2011.
- [171] B. Zhang, and Y. P. Zhang, "Analysis and synthesis of millimeter-wave microstrip grid-array antennas," *IEEE Antennas Propag. Mag.* vol. 53, no. 6, pp. 42-55, 2011.
- [172] X. Chen, G. Wang, and K. Huang, "A novel wideband and compact microstrip grid array antenna", *IEEE Trans. Antennas Propag.*, vol. 58, no. 2, pp. 596-599, 2010.
- [173] P. C. Stickland, "Series-fed microstrip patch arrays with periodic loading," *IEEE Trans. Antennas Propag.*, vol. 43, no. 12, pp. 1472-1474, Dec. 1995.
- [174] Y. Ge, K. P. Esselle, and T. S. Bird, "E-shaped patch antennas for high-speed wireless networks," *IEEE Trans. Antennas Propag.*, vol. 52, no. 12, pp. 3213-3219, 2004.
- [175] K. W. Wong, L. Chiu, and Q. Xue, "A 2-D Van Atta array using star shaped antenna elements," *IEEE Trans. Antennas Propag.*, vol. 55, no. 4, pp. 1204-1206, 2007.
- [176] S. Xiao, M. C. Tang, Y. Y. Bai, S. Gao, and B. Z. Wang, "Mutual coupling suppression in microstrip array using defected ground structure," *IET Microw. Antennas Propag.*, vol. 5, no. 12, pp. 1488-1494, 2011.
- [177] S. Assimonis, T. Yioultis, and C. Antonopoulos, "Design and optimization of uniplanar EBG structures for low profile antenna applications and mutual coupling reduction," *IEEE Trans. Antennas Propag.*, vol. 60, no. 10, pp. 4944-4949, 2012.
- [178] X. M. Yang, X. G. Liu, X. Y. Zhou, and T. J. Cui, "Reduction of mutual coupling between closely packed patch antennas using waveguided metamaterials," *IEEE Antennas Wireless Propag. Lett.*, vol. 11, pp. 389-391, 2012.
- [179] S. Farsi, H. Aliakbarian, D. Schreurs, B. Nauwelaers, and G. Vandenbosch, "Mutual coupling reduction between planar antennas by using a simple microstrip U-section," *IEEE Antennas Wireless Propag. Lett.*, vol. 11, pp. 1501-1503, 2012.
- [180] A. Chebihi, C. Luxey, A. Diallo, P. Le Thuc, and R. Staraj, "A novel isolation technique for closely spaced PIFAs for UMTS mobile phones," *IEEE Antennas Wireless Propag. Lett.*, vol. 7, pp. 665-668, 2008.
- [181] F. Zavosh and J. Aberle, "Infinite phased arrays of cavity-backed patches," *IEEE Trans. Antennas Propag.*, vol. 42, no. 3, pp. 390-398, 1994.
- [182] M. B. Gueye, H. H. Ouslimani, S. N. Burokur, A. Priou, Y. Letestu, and A. Le Bayon, "Antenna array for point-to-point communication in E-band frequency range," in *Proc. IEEE Int. Symp. Antennas Propag.*, Spokane, WA, Jul. 2011, pp. 2077-2079.

- [183] M. K. T. Al-Nuaimi, W. Hong, and Y. Zhang, "Design of high-directivity compact-size conical horn lens antenna," *IEEE Antennas Wirel. Propag. Lett.*, vol. 13, pp. 467-470, 2014.
- [184] I. Papageorgiou, A. Derneryd, L. Manholm, and J. Yang, "An E-band cylindrical reflector antenna for wireless communication systems," in *Proc. 7th Eur. Conf. Antennas Propag.*, Gothenburg, Sweden, Apr. 2013, pp. 524-528.
- [185] M. Zhang, J. Hirokawa, and M. Ando, "An E-Band partially corporate feed uniform slot array with laminated quasi double-layer waveguide and virtual PMC terminations," *IEEE Trans. Antennas Propag.*, vol. 59, no. 5, pp. 1521-1527, 2011.
- [186] J. Hirokawa, H. Arai, and N. Goto, "Cavity backed wide slot antenna," *Proc. Inst. Elect. Eng.*, vol. 136, no. 1, pt. H, pp. 29-33, Feb. 1989.
- [187] R. S. Elliott, *Antenna theory and design*, John Wiley & Sons Inc., 2003.
- [188] J. C. Coetzee, J. Joubert, and D. A. McNamara, "Off-center-frequency analysis of a complete planar slotted-waveguide array consisting of subarrays," *IEEE Trans. Antennas Propag.*, vol. 48, no. 11, pp. 1746-1755, 2000.
- [189] H.-Y. Yee and P. Richardson, "Slotted waveguide antenna arrays," *IEEE Antennas Propag. Soc. Newslett.*, vol. 24, no. 6, pp. 4-8, 1982.
- [190] K. Wu, "Substrate integrated circuits (SICs) for low-cost high-density integration of millimeter-wave wireless systems," in *Proc. Radio Wirel. Symp.*, Orlando, FL, Jan. 2008, pp. 683-686.
- [191] H. Uchimura, T. Takenoshita, and M. Fujii, "Development of a laminated waveguide," *IEEE Trans. Microw. Theory Tech.*, vol. 46, no. 12, pp. 2438-2443, 1998.
- [192] F. Xu and K. Wu, "Guided-wave and leakage characteristics of substrate integrated waveguide," *IEEE Trans. Microw. Theory Tech.*, vol. 53, no. 1, pp. 66-73, 2005.
- [193] Y. Cassivi, L. Perregrini, P. Arcioni, M. Bressan, K. Wu, and G. Conciauro, "Dispersion characteristics of substrate integrated rectangular waveguide," *IEEE Microw. Wirel. Compon. Lett.*, vol. 12, pp. 333-335, 2002.
- [194] J. C. Bohórquez, H. A. Forero Pedraza, I. C. Herrera Pinzón, J. A. Castiblanco, N. Peña, and H. F. Guarnizo, "Planar substrate integrated waveguide cavity-backed antenna," *IEEE Antennas Wireless Propag. Lett.*, vol. 8, pp. 1139-1142, 2009.
- [195] J. Hirokawa and M. Ando, "Single-layer feed waveguide consisting of posts for plane TEM wave excitation in parallel plates," *IEEE Trans. Antennas Propag.*, vol. 46, no. 5, pp. 625-630, 1998.
- [196] M. Vogel, G. Gampala, D. Ludick, and C. Reddy, "Characteristic mode analysis: Putting physics back into simulation," *IEEE Antennas Propag. Mag.*, vol. 57, no. 2, pp. 307-317, 2015.

Part II:

Included Papers

Paper I

Low-Profile Two-Port MIMO Terminal Antenna for Low LTE Bands With Wideband Multimodal Excitation

HANIEH ALIAKBARI¹ (Graduate Student Member, IEEE), AND BUON KIONG LAU¹ (Senior Member, IEEE)

Department of Electrical and Information Technology, Lund University, 221 00 Lund, Sweden

CORRESPONDING AUTHOR: B. K. LAU (e-mail: buon_kiong.lau@eit.lth.se)

This work was supported by Vetenskapsrådet under Grant 2010-00468 and Grant 2018-04717.

ABSTRACT Multiple-input multiple-output (MIMO) is a key enabler for high data rates in mobile communications. However, it is challenging to design MIMO terminal antennas for LTE bands below 1 GHz, due to the conventional chassis offering only one resonant characteristic mode (CM). Recently, it was shown that minor structural changes can yield up to two additional resonant modes for designing two-port MIMO antennas. Nonetheless, the resulting bandwidth for the second port is relatively small. To simultaneously meet bandwidth and other practical requirements (including low profile and no off-ground clearance), a step-by-step approach for structural changes and feed design is applied in this work to exemplify the use of physical insights from CM analysis to achieve a competitive wideband two-port solution. The main novelty is that an entirely new mode is identified and appropriately tuned by structural modification for creating an additional resonance below 1 GHz. Moreover, two simple probe-feed ports are designed to jointly excite different subsets of four modes over frequency. In addition, far-field pattern orthogonality is guaranteed by the different phase shifts of the characteristic electric fields at the port locations. Furthermore, bulkier self-resonant antenna elements are avoided. To show design flexibility, a three-port version is also demonstrated.

INDEX TERMS MIMO systems, terminal antennas, wideband antennas, complex correlation coefficient, characteristic modes.

I. INTRODUCTION

MULTIPLE-INPUT multiple-output (MIMO) technology enables data rate to scale linearly with the number of antennas for a fixed transmit power and bandwidth [1]. It is in widespread use in Long Term Evolution (LTE), IEEE 802.11ac and other wireless communication systems [1].

A. MIMO TERMINAL ANTENNA DESIGN CHALLENGES

Implementing more than one antenna port per band for MIMO operation is challenging in user terminals, especially in frequency bands below 1 GHz, due to their compact form factor [2]. The small electrical size of the terminal chassis offers limited degrees of freedom (in terms of the number of resonant modes) to fulfill strict requirements of orthogonal MIMO antenna and wideband design. Moreover, the current trend points to lesser space for antennas in smartphones, e.g., decreasing thickness and ground clearance. On

the other hand, these lower bands are critical for reliable coverage, due to lower propagation losses and larger signal penetration.

In recent years, many MIMO terminal antennas have been proposed, e.g., [3]–[23]. For the designs above 1 GHz [3]–[9], low coupling and correlation can be more easily achieved across the antenna ports via space, angle or polarization diversities, due to the electrically larger chassis facilitating more resonant orthogonal radiation modes, i.e., characteristic modes (CMs) [9]. In fact, high-end smartphones are equipped with four-port MIMO antennas for higher LTE bands.

On the other hand, below 1 GHz, the largest dimension of the terminal chassis is typically less than half-wavelength ($\lambda_0/2$). This results in the chassis having only one resonant mode [10], [11] (often called fundamental chassis mode), which has a large bandwidth. Hence, early designs

of two-port MIMO antennas often lead to either a narrow-band solution for the second port, by avoiding the use of the wideband single resonant mode [10]–[12], or solutions that mainly excite the single-mode using both ports, which cause high coupling and correlation [17]–[20], [24]. The latter approach may require additional isolation improvement techniques to meet system specific isolation requirements [24]. In addition, the profile (thickness) of modern terminals is typically less than 10 mm, which is electrically very small for frequencies below 1 GHz. This requirement often necessitates larger off-ground clearance (typically ~ 15 mm) as a tradeoff for acceptable bandwidth and MIMO performance. Because of the above fundamental challenges, MIMO terminal antennas for low LTE bands are so far confined to only two-port designs [10]–[23].

B. ASYMMETRIC BANDWIDTH TWO-PORT DESIGNS BELOW 1 GHz

CM analysis (CMA) has been used in [10]–[16] to reduce the correlation of the two ports in the low band. This is motivated by the far-field orthogonality of CMs, which offers an effective framework to design orthogonal MIMO antennas. In [10], it is shown a slot-monopole and a planar inverted-F antenna (PIFA) give the measured isolation and envelope correlation coefficient (ECC) of 13 dB and 0.04, if the slot monopole placed at a short end is used to excite the fundamental chassis mode, whereas the PIFA is located at the chassis center to avoid exciting the chassis mode. However, without using the chassis for radiation, the 6 dB bandwidth of the PIFA is as small as 1%, which is impractical. A magnetic antenna at either short end of the chassis can be used to replace the PIFA [11]. But again, since the magnetic antenna's location is chosen to avoid exciting the chassis, the high isolation of over 20 dB and low ECC of below 0.01 are obtained at the expense of small bandwidth (i.e., 2%).

To increase the bandwidth of the second port while retaining high isolation, two more modes were made resonant in the low band by chassis modification [13]. However, since only one of the two modes was utilized by the second port, the resulting bandwidth is still small (9%) and the profile is still large (8 mm). In [14], both of the additional modes were tuned and excited for the second port, slightly increasing the bandwidth to 11%, but the profile is unchanged. Generally in [13]–[16], using different modes for each port in resulted in lower bandwidth for one of the ports. Whereas asymmetrical bandwidths may be suitable for early LTE releases (e.g., Rel. 8 only requires MIMO for the downlink), symmetrical bandwidths are utilized in later releases, e.g., Rel. 10 (LTE-Advanced), to improve the uplink.

C. SYMMETRIC BANDWIDTH TWO-PORT DESIGNS BELOW 1 GHz

In the meantime, several two-port designs that offer wide symmetric bandwidth and moderate to low correlation below

TABLE 1. Recent and proposed two-port designs with symmetric bandwidth.

Ref.	Antenna type	Chassis size (mm ²)	Profile/height (mm)	Port spacing (λ_0)	BW (%)	Max $ S_{21} $ (dB)/Max correlation	Ground clearance (mm)	Min η_r (%)
[18]	Dual-monopole	120 × 60	7	0.20	25	-6.5 / 0.5	12	46
[21]	2 IFAs at shorter sides	150 × 78	7	0.50	30	NA/0.1	16	45
[22]	Coupled-line+branches	153 × 77	7.5	0.52	30	-10/0.35	10	47
[23]	2 IFAs at longer sides	148 × 68	5	0.23	13*	-10 / 0.5	2	50
This work	2 probe feeds	130 × 60	4	0.2	25	-13/0.15	None	67
This work (v.2)	2 probe feeds	150 × 78	4	0.26	30	-14.2 / 0.08	None	72

NB: NA (not available), η_r (measured total efficiency), BW (bandwidth).
 * ON state BW (Fig. 7(a) in [23]). 30% bandwidth with ON/OFF switching.

1 GHz were proposed [18], [21]–[23] (see Table 1). These designs do not make use of CMA. However, each port in [18] is claimed to be exciting a combined current mode. Defined by means of observing the chassis' current distributions, the two combined modes are formed from the monopole antennas' self-resonant mode and the chassis' dipole mode. Even though the ECC is as high as 0.5 and the total efficiency relatively low ($>46\%$) at the low LTE bands, this work shows that two different modes can be excited jointly at each port for MIMO operation, which also conveniently result in symmetric bandwidths.

In fact, the same principle has been demonstrated earlier using CMA at a higher frequency (2.3 GHz) [8], where two modes are simultaneously excited by two MIMO antenna ports. It is shown using modal weighting coefficients that pattern orthogonality between the ports is achieved by means of phase difference in the excitation of one of the two ports. These pioneering designs [8], [18] focus on the analysis of the antenna operation after the feeding ports are chosen, rather than directly applying this principle to design the feeds. Nevertheless, they provide the insight that it is not necessary to excite different CMs in different ports as in [13], [14]. Moreover, self-resonant antenna structures (e.g., PIFA, monopole and slot antennas), bulkier than non-resonant coupling elements, are typically used for excitation by at least one of the two ports [10]–[15], [18], [19], [21]–[23]. Hence, efforts were made to avoid using self-resonant structures in MIMO antennas [9], [26].

D. NEW LOW-PROFILE, SYMMETRIC WIDEBAND TWO-PORT DESIGN

Considering the limitations of the state-of-the-art solutions, we show in this article that CMA provides the physical insights needed to systematically transform the two-port MIMO antenna in [13], [14] to simultaneously meet the requirements of low profile, wideband, low coupling and correlation, no ground clearance and adding a third port for

LTE coverage under 1 GHz. Bulkier self-resonant structure is also avoided.

Specifically, based on the addition of shorted strips (T-strips) along the longer sides of the flat chassis in [13], [14], the profile was reduced by folding the strips. The folding slightly increased the resonant frequency and decreased the modal bandwidth of the strip-induced mode. In addition, the center position of the shorting pin along each strip was adjusted to decrease the resonant frequencies and increase the bandwidth potential. Then, a slot was added to each of the two longer sides of the chassis, just below the strips, to utilize an additional mode to enhance bandwidth at the higher frequency edge. Utilizing mainly those three resonant modes over the desired frequency range, two probe feeds were designed to replace the shorting pins to capacitively couple power into these modes to achieve wideband behavior for both ports and low ECC over the operating band. The feed design ensures that the condition for orthogonality is retained over the entire band of interest. In particular, the chosen feed location excites one mode with the same phase but the other mode in an out-of-phase fashion. This feeding approach is simple and it does not require a complex feeding network or power divider as utilized in [25] for modal excitation.

To our knowledge, the proposed antenna is the first low profile (4 mm), on-ground (i.e., no ground clearance) design that concurrently provides low correlation ($ECC < 0.15$) and wide bandwidth of 0.75-0.96 GHz (25%) over the low LTE band (see “This work” in Table 1). Moreover, the two ports are spaced by only $0.2\lambda_0$ and no switch or decoupling structure is needed. It is also noted that a typical mid-size chassis, smaller than those of [21]–[23], is used for our reference design. A larger chassis tends to improve bandwidth potential at the lower frequency edge, thus enabling a larger bandwidth, as confirmed by the simulated results of applying the proposed design steps on the larger chassis size of [21] (see “This work (v.2)” in Table 1). To highlight another advantage of the design, which does not occupy either the top or bottom part of the chassis normally reserved for conventional self-resonant antennas, a third port is added to the top end to create a low-band three-port MIMO antenna, for the first time. The third port consists of a frequency tunable narrow-band antenna [11], which has little effect on the existing ports. Further, it is noted that an early version of our proposed design has only 11% simulated bandwidth (0.85-0.95 GHz) [27]. The relatively poor performance is due to the new resonant mode introduced by the slots in the chassis not being utilized by this early design to enhance bandwidth, which is rectified in this work by means by detailed step-by-step CMA.

II. MIMO ANALYSIS USING CHARACTERISTIC MODE THEORY

In this section, CMA is briefly revisited, in the context of MIMO antenna design. CMs are real current modes that

can be computed numerically for conducting bodies of arbitrary shape, obtained by solving the weighted eigenvalue equation [28]

$$X\mathbf{J}_n = \lambda_n R\mathbf{J}_n, \quad (1)$$

where \mathbf{J}_n is the n th characteristic current associated with the n th eigenvalue λ_n . R and X are the real and imaginary parts of the symmetric impedance operator Z . Specifically, the CM far-fields produced by \mathbf{J}_n are orthogonal to each other [28]. Thus, for the electric farfield \mathbf{E}_n

$$\frac{1}{2Z_0}(\mathbf{E}_m \cdot \mathbf{E}_n^*) = \delta_{mn} = \begin{cases} 1, & m = n \\ 0, & m \neq n \end{cases}, \quad (2)$$

where δ_{mn} is the Kronecker delta and Z_0 is the wave impedance of free space and $*$ denotes complex conjugate operation. Also, the symmetric product of the two vector functions in (2), for \mathbf{A} and \mathbf{B} on the surface at infinity S_∞ (i.e., far-field) is defined as

$$\langle \mathbf{A}, \mathbf{B} \rangle = \iint_{S_\infty} \mathbf{A} \cdot \mathbf{B}^* ds. \quad (3)$$

The orthogonality feature of CM far-fields is ideally suited for MIMO antenna design and analysis. This is because MIMO systems (e.g., LTE) are typically used in rich multipath environments, where the angular power spectrum of the outgoing or incoming signal is nearly uniform. In such a propagation environment, orthogonal patterns of MIMO antenna elements are sufficient to guarantee uncorrelated signals across the antenna ports [2]. Therefore, as long as each antenna port excites one or more than one unique modes, with no mode being excited by more than one port, all the resulting patterns will be pairwise uncorrelated, as illustrated by (2), and likewise the received signals at antenna ports will be pairwise uncorrelated.

However, selective excitation of resonant CMs is sufficient, but not necessary to guarantee orthogonal antenna ports, as explained in the following. Consider a P -port MIMO antenna ($P = 2$ in this work), \mathbf{E}^p is denoted as the excited electric field (E-field), when the p th port is excited by an impressed E-field \mathbf{E}_i^p . Since CM far-fields form a set of orthogonal functions, they can be used to expand the excited field \mathbf{E}^p [28]

$$\mathbf{E}^p = \sum_{n=1}^{\infty} \alpha_{n,p} \mathbf{E}_n \approx \sum_{n=1}^N \alpha_{n,p} \mathbf{E}_n \quad (4)$$

where N is the number of dominating modes (with small absolute values of λ_n) and $\alpha_{n,p} = \langle \mathbf{J}_n, \mathbf{E}_i^p \rangle / (1 + j\lambda_n)$ denotes the modal weighting coefficient of the n th CM for the p th port.

To evaluate the magnitude and phase of the contribution of the n th CM to the far-field radiation pattern of the p th port, the complex correlation coefficient (CCC) between \mathbf{E}^p and \mathbf{E}_n is given by [29]

$$\rho_{n,p} = \alpha_{n,p} / \sqrt{P_{rad}}, \quad (5)$$

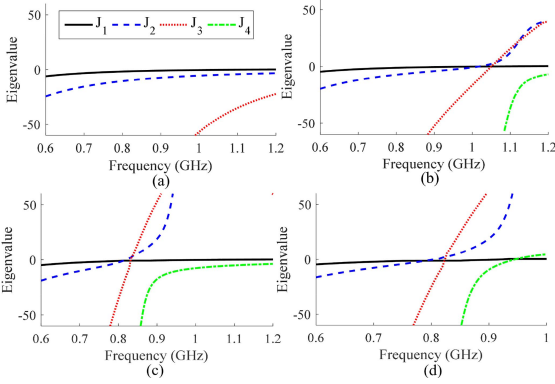


FIGURE 1. Eigenvalues of four CMs of interest for the: (a) chassis, (b) chassis with folded strips and center shorting pins, (c) chassis with folded strip and offset shorting pins on the same side, (d) slotted chassis with folded strip and offset shorting pins on same side. Only modes relevant to the design are shown.

where P_{rad} is the constant total radiated power at each port, and the power budget implies that

$$\sum_{n=1}^N |\rho_{n,p}|^2 \approx 1. \quad (6)$$

Using (4), if $P = 2$ and $N = 2$, the E-fields for the ports are

$$\begin{aligned} \mathbf{E}^1 &= \alpha_{1,1} \mathbf{E}_1 + \alpha_{2,1} \mathbf{E}_2 \\ \mathbf{E}^2 &= \alpha_{1,2} \mathbf{E}_1 + \alpha_{2,2} \mathbf{E}_2, \end{aligned} \quad (7)$$

The CCC of the far-field patterns for ports becomes

$$\begin{aligned} \rho_{E^1, E^2} &= \frac{\langle \mathbf{E}^1, \mathbf{E}^2 \rangle}{\sqrt{\langle \mathbf{E}^1, \mathbf{E}^1 \rangle \langle \mathbf{E}^2, \mathbf{E}^2 \rangle}} \\ &= \frac{\alpha_{1,1} \alpha_{1,2}^* + \alpha_{2,1} \alpha_{2,2}^*}{\sqrt{|\alpha_{1,1}|^2 + |\alpha_{2,1}|^2} \sqrt{|\alpha_{1,2}|^2 + |\alpha_{2,2}|^2}} \\ &= \rho_{1,1} \rho_{1,2}^* + \rho_{2,1} \rho_{2,2}^* \end{aligned} \quad (8)$$

Therefore, in the equivalent context of modal currents, the individual terms $\alpha_{1,1} \alpha_{1,2}^*$ and $\alpha_{2,1} \alpha_{2,2}^*$ do not need to be zero for the sum to be zero, i.e., the general case when ports 1 and 2 do not excite different modes. For example, if ports 1 and 2 excite modes 1 and 2 by the same magnitude ($|\alpha_{1,1}| = |\alpha_{2,1}| = |\alpha_{1,2}| = |\alpha_{2,2}|$), but in a co-phase manner at port 1 ($\angle \alpha_{1,1} = \angle \alpha_{1,2}$) and 180° out-of-phase at port 2 ($\angle \alpha_{2,1} = \angle \alpha_{2,2} + \pi$), then $\rho_{E^1, E^2} = 0$ despite nonzero individual terms.

Another important point in CMA is that the tracking of eigenvalues obtained from (1) over a wide frequency band is very challenging, especially when new modes are introduced by chassis modification [13]–[15], [26]. The orthogonality of far-field patterns in (2) at a given frequency is also a suitable property to be used for modal tracking [30]. The eigenvalues of four CMs of interest in this work (see Fig. 1) were classified by the far-field tracking method of [30], which correlates

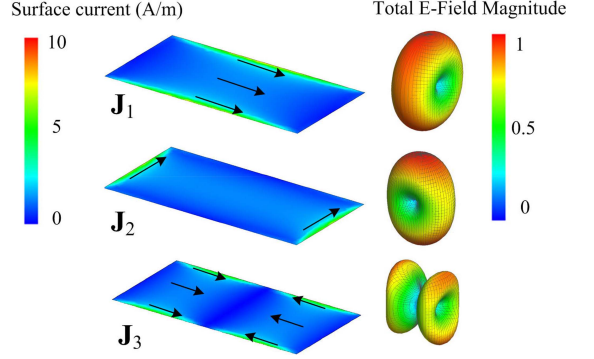


FIGURE 2. Eigencurrent distribution and normalized pattern of CMs in the chassis with resonant frequencies of: 1.08 GHz (J_1), 2.85 GHz (J_2), 2.5 GHz (J_3).

the far-field patterns of each individual mode over frequency. The method was also applied for MIMO antenna design [14]. In contrast, in the preliminary study [27], a current-based tracking method [26] was used, and it failed to identify and track one of the modes, resulting in the missing mode (J_4) not being used to enhance bandwidth.

III. CM MODIFICATION AND EXCITATION

In Fig. 1, the evolutions of the CMs of interest with minor chassis modifications for the entire design procedure are summarized in eigenvalue plots. The size of the terminal chassis was chosen to be $130 \text{ mm} \times 60 \text{ mm}$, intended for a typical mid-size smartphone. It is noted that the overall *outer* dimensions of a smartphone are bigger than those of its chassis. As the first design step, the characteristic eigenvalues for the $130 \text{ mm} \times 60 \text{ mm}$ perfect electric conductor (PEC) chassis were computed and shown in Fig. 1(a). As can be seen, the chassis supports only one resonant mode (J_1) close to 1 GHz. Two non-resonant modes of interest to this study (J_2 and J_3) are also shown in Fig. 1(a). In Fig. 2, the currents and the corresponding electric far-field patterns of J_1 to J_3 are shown as a reference. It can be seen that mode 1 (J_1) is the fundamental dipole mode, with a current flowing along the length of the chassis. Mode 2 (J_2) supports a current distribution like a dipole oriented along the chassis width. Mode 3 (J_3) is a longitudinal full-wave dipole mode. The plain chassis is then modified in stages to obtain the desired characteristic properties, as will be described in this section. Figures 3(a)-3(c) illustrate the currents and electric far-field patterns of the CMs associated with the eigenvalues in Fig. 1(b)-(d), respectively, for different design stages.

A. FOLDING OF T-STRIPS AND CENTER FEED POSITIONS

It is known that capacitive loading along the longer sides of the flat chassis using shorted metal strips (T-strips) enables two additional modes to be resonant below 1 GHz [13], [14], apart from the fundamental dipole mode. Specifically, these

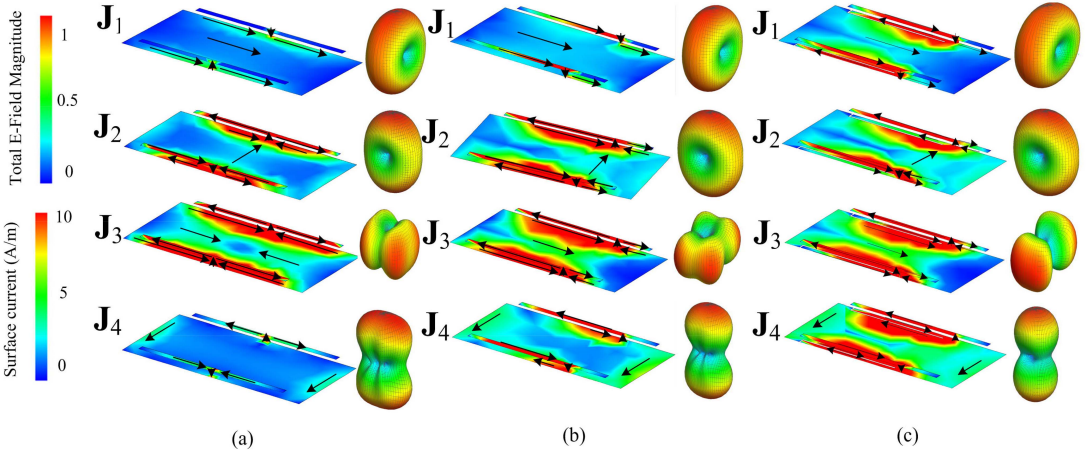


FIGURE 3. Eigencurrent distribution and normalized pattern of CMs of chassis with folded strips and (a) center shorting pins with resonant frequencies of: 1.08 GHz (J_1), 1.01 GHz (J_2), 1.05 GHz (J_3), 2.8 GHz (J_4), (b) offset shorting pins in the same side with resonant frequencies of 1.08 GHz (J_1), 0.8 GHz (J_2), 0.83 GHz (J_3), 1.84 GHz (J_4), and (c) offset shorting pins in the same side with extra slot on the chassis with resonant frequencies of 1.02 GHz (J_1), 0.78 GHz (J_2), 0.83 GHz (J_3), 0.94 GHz (J_4).

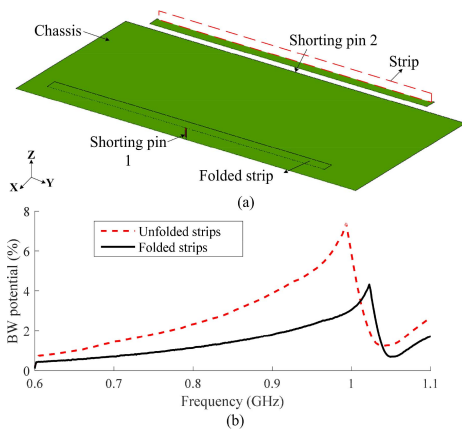


FIGURE 4. (a) Chassis layout with unfolded (dashed outline)/folded (solid outline) strips at the two longer sides and with center shorting pins, (b) bandwidth potential of center excited probe feed with unfolded/folded strips.

are the dipole mode along the width of the chassis as well as a mode resulting from the slots formed between the chassis and the shorted metal strips. However, as described earlier, the proposed antennas in [13] and [14] offer only a modest bandwidth (of up to 11%), with asymmetric bandwidths obtained across the two ports. Moreover, they require a profile of 8 mm and the addition of capacitive coupling elements (CCEs) and/or off-ground self-resonant antenna elements. In this work, the chassis structure with T-strips (shorted in the center) in [13] was adopted as the initial design, based on which all of its limitations were addressed in the following step-by-step design procedure.

The first step was to lower the profile of the chassis structure by folding the T-strips into horizontal orientations,

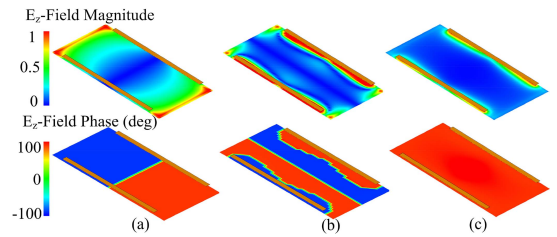


FIGURE 5. Magnitude and phase of z-directed modal E-field distribution of (a) J_1 , (b) J_2 , and (c) J_3 , 2 mm above the chassis at resonant frequencies.

as shown in Fig. 4(a). This lowered the overall profile to 4 mm. The resulting eigenvalues, depicted in Fig. 1(b), reveal that the three resonant modes under 1 GHz (see Fig. 2(b) in [13]) are still available, despite the folding. However, by folding the strips, the resonant frequency of J_2 approaches that of J_3 , and the maximum bandwidth potential [31] of the folded structure (with a shorting pin replaced by a probe feed) reduces from 7% to 4.3% (see Fig. 4(b), calculated using BetaMatch) and the frequency of maximum bandwidth potential increases from 0.99 to 1.02 GHz. In addition, as seen in Fig. 1(b), the slopes of J_2 and J_3 are steep (steeper than those of the unfolded case shown in Fig. 2(b) of [13]), whereas that of J_1 is unchanged with the folding. Moreover, J_4 has large eigenvalues below 1 GHz.

Figure 3(a) shows the corresponding eigencurrents and far-field patterns for the chassis with folded strips and centered shorting pins. J_1 has strong currents along the two longer sides of the chassis, giving the classic half-wave dipole pattern along the chassis length. This verifies that the J_1 is the fundamental dipole mode of the chassis. J_2 has strong currents flowing along the strips and the chassis underneath

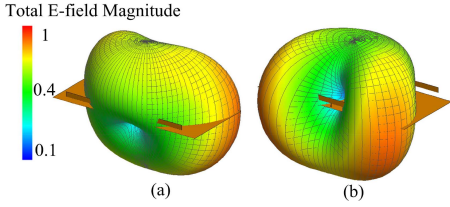


FIGURE 6. 3D normalized radiation pattern by exciting individual ports at 1.04 GHz: (b) Port 1; (c) Port 2.

them, due to the capacitive loading of the strips. However, these currents flow in opposite directions, hence it is the currents along the chassis width that contributes to the dipole pattern. In comparison to \mathbf{J}_1 and \mathbf{J}_4 , the currents in the \mathbf{J}_2 and \mathbf{J}_3 are stronger around the metal strips and shorting pins. Nonetheless, the far-field patterns of \mathbf{J}_2 and \mathbf{J}_3 are different, since the currents' directions at two shorting pins are opposite in \mathbf{J}_2 , but the same in \mathbf{J}_3 . In contrast to \mathbf{J}_1 , the far-field patterns of \mathbf{J}_2 and \mathbf{J}_4 are both along the chassis width; however, it is more directional for \mathbf{J}_4 , since the currents on the strips also contribute to the pattern.

Figure 5 shows the magnitude and phase of the z component of the E-field 2 mm above the chassis for the first three modes (i.e., $\mathbf{J}_1 - \mathbf{J}_3$). As shown in Fig. 5(b), it is expected that if the shorting pins in the center of the chassis are replaced by two (z -oriented) feeding ports (unmatched, unless otherwise stated), the electric near-field excitation of \mathbf{J}_2 by ports 1 and 2 will be 180° out-of-phase. In contrast, as shown in Fig. 5(c), \mathbf{J}_3 is excited by the two ports without any phase shift. Moreover, as the fundamental mode (\mathbf{J}_1) has a lower E-field magnitude at the ports, as compared with those of \mathbf{J}_2 and \mathbf{J}_3 (see Fig. 5(a)), the contribution of \mathbf{J}_1 to the overall radiation should be low. This can be confirmed by computing the magnitude and phase of the CCC using (5) for each port at three different frequencies around the resonances of \mathbf{J}_2 and \mathbf{J}_3 (see Table 2). The percentage power in each mode for a given port is given by the magnitude square of the CCC, i.e., $|\rho_{p,n}|^2$. From Table 2, it is computed that 99% of the total radiation power in each port is radiated by \mathbf{J}_2 and \mathbf{J}_3 , with little contribution from \mathbf{J}_1 . As expected from Fig. 5(b), it is confirmed in Table 2 that the excitation of \mathbf{J}_2 by ports 1 and 2 are 180° out-of-phase and \mathbf{J}_3 is excited in-phase.

Due to the lower eigenvalue of \mathbf{J}_2 at 1.02 GHz, it has more contribution to the far-field patterns than \mathbf{J}_3 . Hence, the total patterns of both ports are similar to the pattern of \mathbf{J}_2 , indicating high correlation. However, at 1.04 GHz, the far-field patterns are almost equally contributed by \mathbf{J}_2 and \mathbf{J}_3 , with 180° phase difference in the excitation of \mathbf{J}_2 by the two ports. Thus, the CCC of the two ports is nearly zero at 1.04 GHz. The pattern orthogonality can be visualized by significant differences in the far-field patterns of the two unmatched ports (see Fig. 6). However, as the frequency increases further to 1.05 GHz, the patterns of two ports are

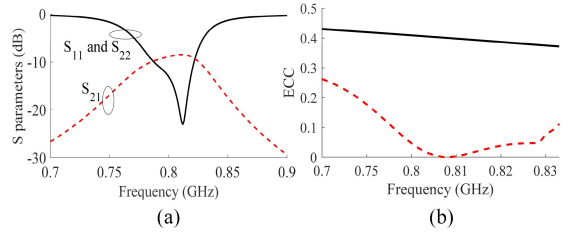


FIGURE 7. (a) S parameters of the two matched ports for the offset feed in the same direction and (b) ECC of two matched ports in the operating bandwidth for offset feed in opposite direction (solid) and same direction (dashed).

TABLE 2. CCC between embedded radiation patterns and characteristic far-field patterns in Fig. 3(a).

	Mode 1	Mode 2	Mode 3
@1.02 GHz			
Port 1	0.05 $\angle 0^\circ$	0.97 $\angle -16.4^\circ$	0.24 $\angle -96^\circ$
Port 2	0.05 $\angle 180^\circ$	0.97 $\angle 163^\circ$	0.24 $\angle -96^\circ$
@1.04 GHz			
Port 1	0.01 $\angle -4.6^\circ$	0.72 $\angle -55.3^\circ$	0.69 $\angle 73.8^\circ$
Port 2	0.01 $\angle 178^\circ$	0.72 $\angle 123.2^\circ$	0.69 $\angle 73.8^\circ$
@1.05 GHz			
Port 1	0.02 $\angle -11^\circ$	0.3 $\angle 39^\circ$	0.95 $\angle -65.8^\circ$
Port 2	0.02 $\angle 168^\circ$	0.3 $\angle -148^\circ$	0.95 $\angle -65^\circ$

dominated by \mathbf{J}_3 , degrading the pattern orthogonality of the two ports. Therefore, it is concluded that pattern orthogonality is only achieved for a small bandwidth. Moreover, as mentioned, Fig. 4(a) shows that the maximum bandwidth that can be achieved for the folded strips' case with the center-fed ports is also small 4.3%. To match both ports at the frequency of maximum bandwidth potential (1.02 GHz, see Fig. 4(a)), a two Murata element matching network consisting of a parallel inductor ($L = 2$ nH) and a series capacitor ($C = 12$ pF) was used at each port.

Although the folding the strips has resulted in a smaller bandwidth (from 7% to 4.3%) and poor ECC performance, the performance limitation is mostly due to the two center-fed ports not exciting the wideband \mathbf{J}_1 mode. Therefore, to enlarge the bandwidth, \mathbf{J}_1 should also be excited by two ports.

B. OFFSET FEED POSITIONS

To utilize \mathbf{J}_1 , it is necessary to offset the two feeding ports (probe feeds) from the center of the strips, so to excite its electric near-field (see magnitude distribution of Fig. 5(a)). Based on this consideration, there are two options, i.e., offsetting the two ports from the center position in the same or the opposite directions along the longer sides. However, from the phase response of Fig. 5(a), it can be seen that these two cases differ in that the same-direction offset results in in-phase excitation of \mathbf{J}_1 , whereas the opposite-direction offset result in 180° out-of-phase excitation. On the other hand, both offset cases result in equal magnitude but 180° out-of-phase excitation of \mathbf{J}_2 (see Fig. 5(b)). Therefore, according to (8) as well as the discussions in Section II,

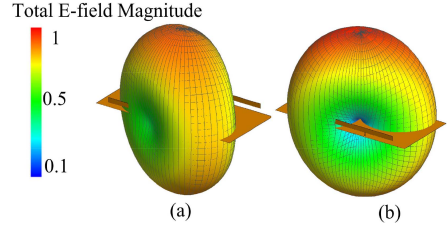
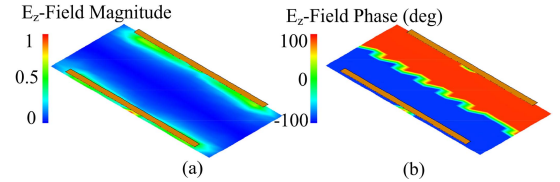
TABLE 3. CCC between embedded radiation patterns and characteristic far-field patterns of Fig. 3(b).

	Mode 1	Mode 2	Mode 3
@0.79 GHz			
Port 1	0.68 \angle 43.6°	0.72 \angle 36°	0.16 \angle -92°
Port 2	0.68 \angle 43°	0.72 \angle -137°	0.16 \angle -92°
@0.82 GHz			
Port 1	0.70 \angle 25.9°	0.68 \angle -31.6°	0.2 \angle 51.4°
Port 2	0.70 \angle 24°	0.68 \angle 140°	0.2 \angle 51.4°
@0.83 GHz			
Port 1	0.61 \angle 26.1°	0.66 \angle 118°	0.43 \angle 79.3°
Port 2	0.61 \angle 25°	0.66 \angle -75°	0.43 \angle 79.3°

the same-direction offset should provide low correlation between the two ports, whereas the opposite-direction offset should result in high correlation. These predictions are verified in Fig. 7(b), where the ECC exceeds 0.4 for the opposite-direction case but lower than 0.1 for the same-direction offset, within their respective 6 dB impedance bandwidth. As before, both ports in the same-direction offset case were matched at the frequencies of maximum bandwidth (0.8 GHz) with two Murata element matching networks. The parallel inductor value and the series capacitor value were 3.4 nH and 11.4 pF, respectively. Relative to the center fed chassis, the maximum bandwidth potential with the same-direction offset feed increases from 4.3% to 7%, due to the excitation of \mathbf{J}_1 . Also, as shown in Fig. 7(b), the isolation is larger than 9 dB in the bandwidth (0.77-0.83 GHz).

For further validation of the same-direction offset case, the CCC between each mode and each port was calculated using (5) and summarized in Table 3 at three frequencies within the 6 dB impedance bandwidth. Similar to the previous case in Table 2, it can be observed that \mathbf{J}_2 is excited with 180° phase shift and \mathbf{J}_3 is excited in phase between the ports. However, contrary to the center-feed chassis, the contribution of \mathbf{J}_1 is higher, and it is excited in-phase by the two ports (as expected from Fig. 5(a)). Moreover, the excitation of \mathbf{J}_3 is less than that of \mathbf{J}_1 and \mathbf{J}_2 in the band because of \mathbf{J}_3 's narrower bandwidth (compare Figs. 1(b) and 1(c)). Therefore, the total patterns (see Fig. 8) is a combination of the far-field dipole patterns of \mathbf{J}_1 and \mathbf{J}_2 , with a rotation of $\phi \approx 45^\circ$ relative to either modal pattern.

Furthermore, it is shown in Fig. 3(b) that by moving the shorting pins from the center, \mathbf{J}_1 has more surface currents around the metal strips and shorting pins (than that in Fig. 3(a)). Compared to the center shorting pins, due to the longer slots formed between the metal strips and the chassis, the resonance frequency of the \mathbf{J}_2 and \mathbf{J}_3 will shift to lower frequencies and resonance of the \mathbf{J}_1 remains almost unchanged (see Fig. 1(c)). The resonant frequency of \mathbf{J}_4 is also reduced but it is still far those of the other three modes (i.e., \mathbf{J}_1 , \mathbf{J}_2 and \mathbf{J}_3 resonate under 1 GHz). However, in comparison to Fig. 1(b), the slope of \mathbf{J}_3 is larger in Fig. 1(c), thus its modal bandwidth is smaller. The resonant frequency of \mathbf{J}_2 and \mathbf{J}_3 can be tuned with the longer slots (i.e., L_2 in Fig. 10) on both sides.


FIGURE 8. 3D normalized radiation pattern by exciting individual ports at 0.83 GHz: (a) port 1; (b) port 2.

FIGURE 9. (a) Magnitude, and (b) phase of z-directed modal E-field of \mathbf{J}_4 , 2 mm above the chassis at resonant frequencies.

Despite the good ECC performance of the same-direction offset feed structure shown in Fig. 7(b), the bandwidth of 7% (see Fig. 7(a)) is still small and cannot cover the low LTE bands. The isolation performance is likewise only moderate (above 9 dB). Furthermore, even though the impedance bandwidth can be increased using more complex matching networks in BetaMatch (10% bandwidth was achieved with four matching elements), the ECC will increase towards the lower frequencies (e.g., 0.75 GHz) and higher frequencies (e.g., 0.96 GHz). This is because the excitation of \mathbf{J}_2 will decrease in those frequencies and \mathbf{J}_1 is the only mode which will be excited by the two ports.

C. SLOTTED CHASSIS

To increase the bandwidth of both ports at the higher frequency edge, while retaining low ECC, another mode needs to be jointly excited alongside with \mathbf{J}_1 , to replace the role of \mathbf{J}_2 at lower frequencies. Since the E-fields of \mathbf{J}_1 excited by the two offset feeds are of equal magnitude and phase (with the feed positions chosen for proper lower frequency excitation of \mathbf{J}_1 and \mathbf{J}_2), the two feeds should excite the E-fields of the new mode with equal magnitude and 180° out-of-phase at the two feeds (as was the case for \mathbf{J}_2) to ensure that ECC is low, as predicted by (8). As shown in Fig. 1(c), \mathbf{J}_4 's resonance is above 1 GHz, so by nature it cannot be used to extend the bandwidth and \mathbf{J}_2 has lower modal significance in higher frequencies. However, the E-field distribution of \mathbf{J}_4 has the desired property of being equal in magnitude but 180° out-of-phase at the feed locations, (see Fig. 9). This makes \mathbf{J}_4 a good candidate for the new mode.

Therefore, the structure should be modified to allow \mathbf{J}_4 to contribute to the radiation in the higher frequencies,

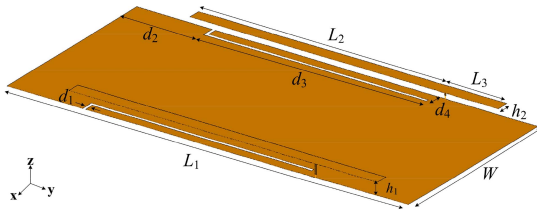


FIGURE 10. Final simulated prototype with the total dimensions of $130 \times 60 \times 4 \text{ mm}^3$. The design parameters are: $L_1 = 130 \text{ mm}$, $L_2 = 81 \text{ mm}$, $L_3 = 20 \text{ mm}$, $h_1 = 4 \text{ mm}$, $h_2 = 4 \text{ mm}$, $d_1 = 1 \text{ mm}$, $d_2 = 27 \text{ mm}$, $d_3 = 74 \text{ mm}$, $d_4 = 3 \text{ mm}$, $W = 60 \text{ mm}$.

TABLE 4. CCC between embedded radiation patterns and characteristic far-field patterns of Fig. 3(c).

@0.82 GHz	Mode 1	Mode 2	Mode 3	Mode 4
Port 1	$0.68 \angle -5.6^\circ$	$0.72 \angle -29.4^\circ$	$0.13 \angle -93.9^\circ$	$0.1 \angle -90.5^\circ$
Port 2	$0.69 \angle -5.7^\circ$	$0.69 \angle -151^\circ$	$0.13 \angle -93.9^\circ$	$0.12 \angle -89.5^\circ$
@0.75 GHz				
Port 1	$0.65 \angle -79.9^\circ$	$0.71 \angle -160^\circ$	$0.2 \angle -42.5^\circ$	~ 0
Port 2	$0.65 \angle -79.9^\circ$	$0.71 \angle -16.7^\circ$	$0.2 \angle -42.5^\circ$	~ 0
@0.94 GHz				
Port 1	$0.69 \angle -12.7^\circ$	~ 0	$0.28 \angle -89^\circ$	$0.69 \angle -62.8^\circ$
Port 2	$0.67 \angle -15.6^\circ$	~ 0	$0.22 \angle -89^\circ$	$0.70 \angle -120^\circ$

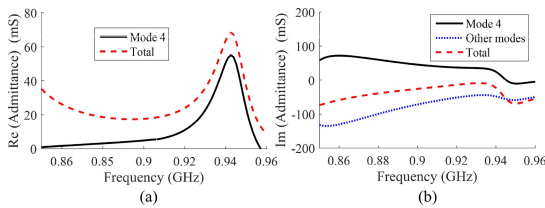


FIGURE 11. (a) Real part and (b) Imaginary part of the modal and total admittance.

alongside with \mathbf{J}_1 . To this end, by inspecting the current distribution of \mathbf{J}_4 in Fig. 3(b), the resonant frequency of \mathbf{J}_4 can be decreased to below 1 GHz (i.e., 0.94 GHz) by inserting two slots along the longer sides of the chassis, as shown in Fig. 10. In this way, the current path along the chassis width is increased. Similarly, the resonant frequency of \mathbf{J}_2 is also decreased to 0.78 GHz, which can contribute to the radiation and improve the ECC at lower frequencies. By the length of this slot (i.e., d_3 in Fig. 10), the resonant frequency of \mathbf{J}_4 can be tuned. The computed CCC between each mode and each port is shown in Table 4 for three frequencies. As can be seen, \mathbf{J}_4 offers almost equal contribution as \mathbf{J}_1 in magnitude, but nearly 180° out-of-phase excitation as compared to \mathbf{J}_1 's nearly co-phase excitation. Furthermore, by adding the slot, the frequency of maximum bandwidth potential increases to 0.9 GHz, and the bandwidth potential improves because of one more resonant mode: \mathbf{J}_4 adds some reactive admittance (see Fig. 11(b)) to the other modes' reactive admittances and also increases the real part of input admittance at the higher frequencies (see Fig. 11(a)).

Finally, both ports were matched using the BetaMatch software. To match the ports, a three element Π matching network consisting of a 4.3 nH series Murata inductor

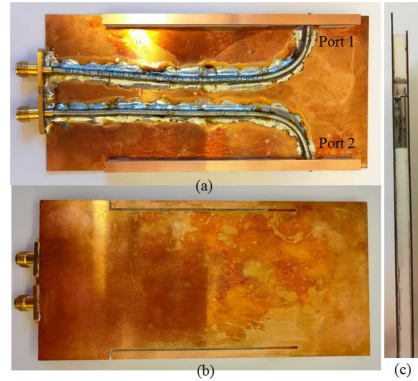


FIGURE 12. Fabricated two-port prototype: (a) top, (b) back and (c) side views.

together with 18 pF and 10 pF parallel Murata capacitors was used. One more matching element was used here than the previous cases (in Section III-A and Section III-B), as it was needed to improve the matching at the lower frequencies. As mentioned in the Introduction, this work focuses on the design and analysis of wideband MIMO antenna below 1 GHz, which is a challenging problem due to the small electrical size of the chassis. However, multiband operation can also be achieved by noting that the same feed points can also be used to excite CMs that are resonant at higher frequencies, by following the procedure in [14]. To achieve wide-band impedance matching for both the low band as well as a higher band, a more complex single-port dual-branch matching network [32] can be used. The dual-band single-CCE based antenna in [32] achieves the total efficiency of 55-76% at the low band (0.698-0.96 GHz) and 54-91% at the higher band (1.71-2.69 GHz).

IV. PROTOTYPE VERIFICATION

The proposed antenna was fabricated, as shown in Fig. 12. A copper plate (thickness of 0.5 mm) was used as the chassis of the prototype and Rohacell foams were used to keep the feeding structures at the two longer sides more stable. The foams are electrically neutral ($\epsilon_r = 1$), so it does not load the modes and change the simulated results. The feed cables were well soldered to the chassis to mitigate cable influence. The simulated and measured S parameters agree well (see Fig. 13(a)). The final design offers the 6 dB impedance bandwidths of 0.75-0.96 GHz (25%). The measured far-field patterns, shown in Fig. 14, illustrate that a high level of orthogonality is achieved between the two ports at three sample frequencies. The measured ECC is below 0.15 (see Fig. 13(b)) and the measured total efficiency is above 67% (average of 71%) over the impedance bandwidth. It was found that adding realistic components such as a large battery to the MIMO antenna in [13], based on which the proposed design is developed, reduced the total efficiency by few percent due to the shifting of the CM resonances. However,

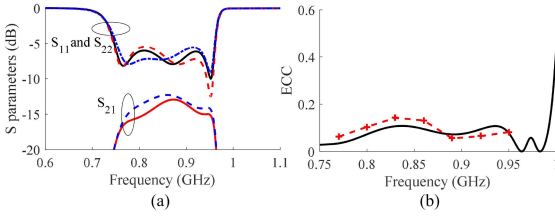


FIGURE 13. (a) S parameters and (b) ECC of the simulated (solid lines) and measured (dashed lines) prototype of two-port antenna designed using CMA.

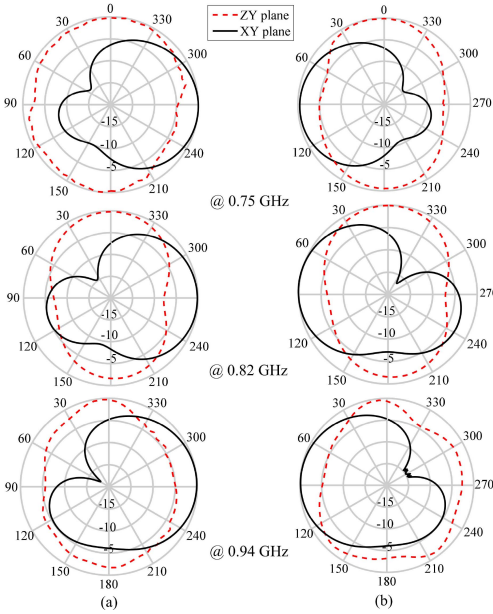


FIGURE 14. Measured total radiation patterns of the two-port prototype at three frequencies: (a) port 1 excitation. (b) port 2 excitation.

this effect could be partly compensated by retuning. Similar situation applies to the proposed antenna.

V. FEASIBILITY OF THREE-PORT ANTENNA AT LOW FREQUENCY BAND

As mentioned earlier, one advantage of the proposed two-port antenna is that it does not need to occupy the top or bottom end of the chassis, typically used for self-resonant antenna elements. Moreover, because of the chassis' electrically small dimensions, achieving more than two uncorrelated ports in the low frequency band is challenging. In [33], a four-port dual-band MIMO terminal antenna is formed using four non-resonant elements with 11 mm^2 of ground clearance. The bandwidth is 15% at the low band (824-960 MHz). Although all four ports mainly excite the fundamental mode of the large chassis ($157 \times 90 \text{ mm}^2$) at the lower band, the placement of the non-resonant elements at the four corners of the chassis helps to reduce the

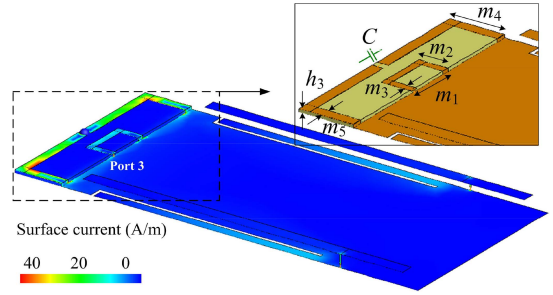


FIGURE 15. Current distribution of the 3-port antenna at 0.95 GHz when the loop antenna is excited. The parameters of the loop antenna are: $m_1 = 15 \text{ mm}$, $m_2 = 10 \text{ mm}$, $m_3 = 2 \text{ mm}$, $m_4 = 15 \text{ mm}$, $m_5 = 3 \text{ mm}$, $h_3 = 0.8 \text{ mm}$, $C = 0.17 \text{ pF}$. The substrate has a permittivity of 2.45, a loss tangent of 0.003 and a thickness h_3 . All other dimensions are the same as those in Fig. 15.

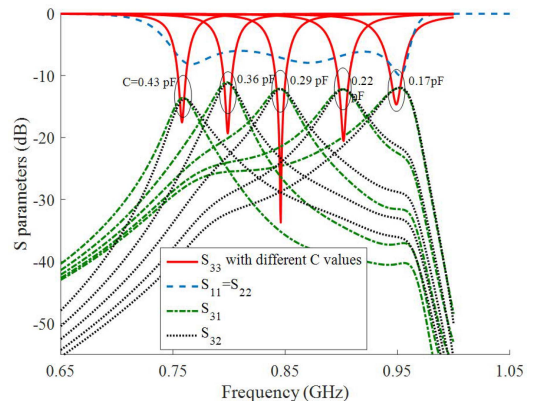


FIGURE 16. Simulated S parameters of the coupled loop, with different values of C .

ECC. However, in part due to high coupling (up to -8 dB), the minimum port efficiency is only 24.9%.

In this section, extending the proposed two-port wideband design, the feasibility of a three-port structure for low band coverage is studied. In particular, the planar-coupled feed loop in [34] was employed to realize the self-resonant magnetic antenna as the third port. The loop antenna [34] was previously adopted in [11] to provide an uncorrelated but narrowband second port for a traditional chassis top/bottom antenna. The antenna occupies $15 \text{ mm} \times 60 \text{ mm}$ at the top end of the two-port structure (see Fig. 15), with the total chassis length (130 mm) unchanged. As observed in Fig. 15, the coupled feed loop is implemented on a substrate and consists of two half-square rings, with the inner ring acting as the matching feed and the outer ring as the main radiator [34]. Although the coupled loop makes use of the shorter edge of the chassis, the resonant modes of the chassis is not excited over the existing two ports' 6 dB bandwidth (i.e., magnetic fields of $\mathbf{J}_1 - \mathbf{J}_4$ are weak at this location). Therefore, only the loop is excited (as a self-resonant structure) and the current is mostly confined around the outer loop (see Fig. 15).

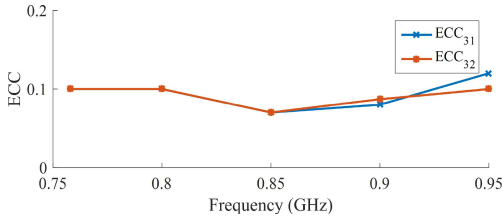


FIGURE 17. Simulated ECC of the three port antenna based on far-field patterns.

Only small amounts of currents are coupled to the slots on the chassis. The parameters of the coupled loop antenna are shown in Fig. 16. It is noted that the operation of the ports 1 and 2 will not be affected by adding the third port so the parameters of the chassis are the same as Fig. 10 and no re-optimization is needed.

A major drawback of the coupled loop antenna is the narrow bandwidth [11], [34]. However, it can still be used as a diversity antenna, where a relatively small instantaneous bandwidth is needed (e.g., up to 20 MHz for LTE). To provide coverage over the entire low band, the resonant frequency of the coupled loop antenna (or third port) can be tuned by replacing the fixed capacitor between the two-arm separations of the outer loop (i.e., C in Fig. 15) with a varactor. The S parameters with different capacitance values are shown in Fig. 16. The required tuning range of the varactor is between 0.17-0.43 pF to cover the bandwidth of the other two ports shown in Fig. 13(a). No matching network is needed. The achieved isolation is above 12 dB, which is enough for frequency bands below 1 GHz. More importantly, the ECC between the third port and any of the other ports is below 0.11 for all varactor states (see Fig. 17). The total simulated efficiency of port 3 is above 83% for all the different C values. Finally, it is noted that a fourth port can also be accommodated in the proposed design by adding another coupled loop antenna to the bottom end of the chassis in Fig. 15. This is possible due to the self-resonant coupled loop antenna not exciting the CMs utilized by the first two ports.

VI. CONCLUSION

This paper presents a concept design of MIMO terminal antennas that relies on the joint excitation of multiple chassis modes with proper phase shifts to drastically improve the impedance bandwidth in the low band while retaining low correlation. To this end, the characteristic currents as well as the amplitude and phase of the electric near-fields of the modes were used to guide the stepwise modifications of a previous strip-loaded chassis. The proposed low-profile two-port design, utilizing direct probe feeds at the loading strips and two added slots on the chassis, achieves the same bandwidth over both ports, covering 0.75-0.96 GHz (25% bandwidth). Moreover, utilizing a slightly larger chassis will allow the proposed design to cover the entire LTE low band 0.698-0.96 GHz (30%, see Table 1). In addition, it is shown

that a narrowband but tunable third antenna port can be added to the unused space typically occupied by traditional self-resonant antenna elements, to provide a three-port MIMO antenna. Possible future works include the enhancement of the bandwidth of the third port and the study of user effects on the proposed design using new CMA methods such as that proposed in [35].

ACKNOWLEDGMENT

The authors would like to thank Andreas Johansson at Lund University for his help in fabricating the antenna prototype.

REFERENCES

- [1] E. Dahlman, S. Parkvall, and J. Sköld, *4G LTE-Advanced Pro and The Road to 5G*, 3rd ed. London, U.K.: Academic, 2016.
- [2] H. Li and B. K. Lau, "MIMO systems and antennas for terminals," in *Handbook of Antenna Technologies*, Z. N. Chen, Ed. Singapore: Springer, 2015, pp. 1–35.
- [3] M.-Y. Li *et al.*, "Eight-port orthogonally dual-polarized antenna array for 5G smartphone applications," *IEEE Trans. Antennas Propag.*, vol. 64, no. 9, pp. 3820–3830, Sep. 2016.
- [4] J. Guo, L. Cui, C. Li, and B. Sun, "Side-edge frame printed eight-port dual-band antenna array for 5G smartphone applications," *IEEE Trans. Antennas Propag.*, vol. 66, no. 12, pp. 7412–7417, Dec. 2018.
- [5] Z. Qin, W. Geyi, M. Zhang, and J. Wang, "Printed eight-element MIMO system for compact and thin 5G mobile handset," *Electron. Lett.*, vol. 52, no. 6, pp. 416–418, Mar. 2016.
- [6] G. Li, H. Zhai, Z. Ma, C. Liang, R. Yu, and S. Liu, "Isolation-improved dual-band MIMO antenna array for LTE/WiMAX mobile terminals," *IEEE Antennas Wireless Propag. Lett.*, vol. 13, pp. 1128–1131, 2014.
- [7] M. Ikram, R. Hussain, A. Ghalib, and M. S. Sharawi, "Compact 4-element MIMO antenna with isolation enhancement for 4G LTE terminals," in *Proc. IEEE Int. Symp. Antennas Propag. (APSURSI)*, Fajardo, Puerto Rico, Jun. 2016, pp. 535–536.
- [8] K. K. Kishor and S. V. Hum, "A two-port chassis-mode MIMO antenna," *IEEE Antennas Wireless Propag. Lett.*, vol. 12, pp. 690–693, 2013.
- [9] R. Martens and D. Manteuffel, "Systematic design method of a mobile multiple antenna system using the theory of characteristic modes," *IET Microw. Antennas Propag.*, vol. 8, no. 12, pp. 887–893, Sep. 2014.
- [10] H. Li, Y. Tan, B. K. Lau, Z. Ying, and S. He, "Characteristic mode based tradeoff analysis of antenna-chassis interactions for multiple antenna terminals," *IEEE Trans. Antennas Propag.*, vol. 60, no. 2, pp. 490–502, Feb. 2012.
- [11] H. Li, B. K. Lau, Z. Ying, and S. He, "Decoupling of multiple antennas in terminals with chassis excitation using polarization diversity, angle diversity and current control," *IEEE Trans. Antennas Propag.*, vol. 60, no. 12, pp. 5947–5957, Dec. 2012.
- [12] I. Szini, A. Tatomiresscu, and G. F. Pedersen, "On small terminal MIMO antennas, harmonizing characteristic modes with ground plane geometry," *IEEE Trans. Antennas Propag.*, vol. 63, no. 4, pp. 1487–1497, Apr. 2015.
- [13] H. Li, Z. Miers, and B. K. Lau, "Design of orthogonal MIMO handset antennas based on characteristic mode manipulation at frequency bands below 1 GHz," *IEEE Trans. Antennas Propag.*, vol. 62, no. 5, pp. 2756–2766, May 2014.
- [14] Z. Miers, H. Li, and B. K. Lau, "Design of bandwidth-enhanced and multiband MIMO antennas using characteristic modes," *IEEE Antennas Wireless Propag. Lett.*, vol. 12, pp. 1696–1699, 2013.
- [15] C. Deng, Z. Feng, and S. V. Hum, "MIMO mobile handset antenna merging characteristic modes for increased bandwidth," *IEEE Trans. Antennas Propag.*, vol. 64, no. 7, pp. 2660–2667, Jul. 2016.
- [16] K. K. Kishor and S. V. Hum, "Multiport multiband chassis-mode antenna design using characteristic modes," *IEEE Antennas Wireless Propag. Lett.*, vol. 16, pp. 609–612, 2016.
- [17] A. A. Al-Hadi and R. Tian, "Impact of multiantenna real estate on diversity and MIMO performance in mobile terminals," *IEEE Antennas Wireless Propag. Lett.*, vol. 12, pp. 1712–1715, 2013.

- [18] S. Zhang, K. Zhao, Z. Ying, and S. He, "Investigation of diagonal antenna-chassis mode in mobile terminal LTE MIMO antennas for bandwidth enhancement," *IEEE Antennas Propag. Mag.*, vol. 57, no. 2, pp. 217–228, Apr. 2015.
- [19] Y. L. Ban, Z. X. Chen, Z. Chen, K. Kang, and J. L. W. Li, "Decoupled closely spaced heptaband antenna array for WWAN/LTE smartphone applications," *IEEE Antennas Wireless Propag. Lett.*, vol. 13, pp. 31–34, 2013.
- [20] J. Holopainen, J. Ilvonen, R. Valkonen, A. A. H. Azremi, and P. Vainikainen, "Study on the minimum required size of the low-band cellular antenna in variable-sized mobile terminals," in *Proc. 6th Eur. Conf. Antennas Propag. (EuCAP)*, Prague, Czech Republic, Mar. 2012, pp. 2754–2758.
- [21] I. Barani and K. Wong, "Integrated inverted-F and open-slot antennas in the metal-framed smartphone for 2×2 LTE LB and 4×4 LTE M/HB MIMO operations," *IEEE Trans. Antennas Propag.*, vol. 66, no. 10, pp. 5004–5012, Oct. 2018.
- [22] D. Huang, Z. Du, and Y. Wang, "A quad-antenna system for 4G/5G/GPS metal frame mobile phones," *IEEE Antennas Wireless Propag. Lett.*, vol. 18, pp. 1586–1590, 2019.
- [23] J. Choi, W. Hwang, C. You, B. Jung, and W. Hong, "Four-element reconfigurable coupled loop MIMO antenna featuring LTE full-band operation for metallic-rimmed smartphone," *IEEE Trans. Antennas Propag.*, vol. 67, no. 1, pp. 99–107, Jan. 2019.
- [24] J. Ilvonen, J. Holopainen, K. Rasilainen, A. Lehtovuori, and V. Viikari, "Suitable multi-antenna placement in mobile handsets based on electromagnetic isolation," in *Proc. 10th Europ. Conf. Antennas Propag. (EuCAP)*, Davos, Switzerland, Apr. 2016, pp. 1–4.
- [25] N. Peitzmeier and D. Manteuffel, "Upper bounds and design guidelines for realizing uncorrelated ports on multimode antennas based on symmetry analysis of characteristic modes," *IEEE Trans. Antennas Propag.*, vol. 67, no. 6, pp. 3902–3914, Jun. 2019.
- [26] C. Deng, Z. Xu, A. Ren, and S. V. Hum, "TCM-based bezel antenna design with small ground clearance for mobile terminals," *IEEE Trans. Antennas Propag.*, vol. 67, no. 2, pp. 745–754, Feb. 2019.
- [27] H. Li and B. K. Lau, "Design of low profile MIMO antennas for mobile handset using characteristic mode theory," in *Proc. IEEE 5th Asia-Pac. Conf. Antennas Propag.*, Kaohsiung, Taiwan, Jul. 2016, pp. 63–64.
- [28] R. Harrington and J. Mautz, "Theory of characteristic modes for conducting bodies," *IEEE Trans. Antennas Propag.*, vol. 19, no. 5, pp. 622–628, Sep. 1971.
- [29] E. Safin and D. Manteuffel, "Reconstruction of the characteristic modes on an antenna based on the radiated far field," *IEEE Trans. Antennas Propag.*, vol. 61, no. 6, pp. 2964–2971, Jun. 2013.
- [30] Z. Miers and B. K. Lau, "Wide band characteristic mode tracking utilizing far-field patterns," *IEEE Antennas Wireless Propag. Lett.*, vol. 14, pp. 1658–1661, 2015.
- [31] J. Villanen, J. Ollikainen, O. Kivekäs, and P. Vainikainen, "Coupling element based mobile terminal antenna structures," *IEEE Trans. Antennas Propag.*, vol. 54, no. 7, pp. 2142–2153, Jul. 2006.
- [32] R. Valkonen, M. Kalliokallio, and C. Icheln, "Capacitive coupling element antennas for multi-standard mobile handsets," *IEEE Trans. Antennas Propag.*, vol. 61, no. 5, pp. 2783–2791, May 2013.
- [33] J. Anguera, A. Andújar, R. M. Mateos, and S. Kahng, "A 4×4 MIMO multiband antenna system with non-resonant elements for smartphone platforms," in *Proc. 11th Eur. Conf. Antennas Propag. (EuCAP)*, Paris, France, Mar. 2017, pp. 2705–2708.
- [34] A. Erentok and R. W. Ziolkowski, "Metamaterial-inspired efficient electrically small antennas," *IEEE Trans. Antennas Propag.*, vol. 56, no. 3, pp. 691–707, Mar. 2008.
- [35] P. Ylä-Oijala, A. Lehtovuori, R. Luomaniemi, and V. Viikari, "Characteristic mode analysis of user's effect on mobile handset antennas," in *Proc. 13th Eur. Conf. Antennas Propag. (EuCAP)*, Krakow, Poland, Apr. 2019, pp. 1–4.

Paper II

Large Screen Enabled Tri-Port MIMO Handset Antenna for Low LTE Bands

HANIEH ALIAKBARI¹ (Graduate Student Member, IEEE), LI YING NIE²,
AND BUON KIONG LAU¹ (Senior Member, IEEE)

¹Department of Electrical and Information Technology, Lund University, 221 00 Lund, Sweden

²School of Computer Science and Information Engineering, Hefei University of Technology, Hefei 230601, China

CORRESPONDING AUTHOR: B. K. LAU (e-mail: buon_kiong.lau@eit.lth.se)

This work was supported by Vetenskapsrådet under Grant 2018-04717.

ABSTRACT In recent years, the screen-to-body ratio of mobile handsets has been increasing. Today, the screen nearly fills up the entire front side. Conventionally, the screen is mainly seen as a metallic object that adversely affects antenna performance. In this paper, the large screen is used for the first time to facilitate an additional uncorrelated MIMO port in a tri-port design, for several LTE bands below 1 GHz. To this end, the screen and the terminal chassis are modeled as two metal plates and their characteristic modes are analyzed. Four modes are then tuned to resonance and selectively excited to yield three uncorrelated MIMO ports. Simulation and measurement results are in good agreement. The measured bandwidths are 23%, 17% and 21%. Within the operating band, the measured isolation is above 13 dB, envelope correlation coefficient below 0.16 and average total efficiency above 72%.

INDEX TERMS Characteristic mode analysis, handset antenna, MIMO systems, mobile antenna, mutual coupling.

I. INTRODUCTION

ONE KEY technology for increasing the channel capacity (ideal data rate) of wireless communication systems is multiple-input multiple-output (MIMO) system. The capacity of a MIMO system is closely related to the number of the antenna elements, as well as the antenna efficiencies and the correlation of signals among these antennas.

Many MIMO terminal antennas with more than two ports have been proposed for sub-6 GHz cellular bands in recent years. However, most of these multipoint antenna systems are designed for frequencies above 1.71 GHz (i.e., conventional “high bands”) [1]–[3]. The popularity with high band designs is not only because MIMO was first deployed on a massive scale in the LTE band around 2.6 GHz. More importantly, it is technically very challenging to design MIMO antenna with high efficiency and low correlation for cellular bands below 1 GHz, e.g., LTE Band 5 (0.824-0.894 GHz). The reason is that such low-band antennas rely on the entire chassis for radiation and large bandwidth, and generally the electrically compact chassis with only one resonant mode (dipole mode

along chassis length) cannot support low coupling and correlation desired for multipoint MIMO operation [4]. For example, the quad-element design in [5] is only intended for dual-port MIMO operation by antenna selection. Moreover, the isolation in the 0.75-0.96 GHz band is only above 6 dB and the envelope correlation coefficient (ECC) is as high as 0.75.

Nonetheless, dual-port MIMO antennas with moderate to low coupling/correlation have been successfully designed for frequency bands below 1 GHz [4], [6]–[12], either by having a second self-resonant narrowband antenna that does not radiate through the chassis [4], [6] or facilitating a second resonant mode by making use of minor changes in the chassis [7]–[12]. The minor changes include the use of loading strips [7], [8] and a bezel frame [9]–[11], some in combination with a larger chassis width (~80 mm) [10]–[12].

Recently, a tri-port MIMO antenna with low correlation has been designed for these frequencies [13]. However, the focus of [13] is to significantly extend the bandwidth of the previous dual-port design in [7] from 9% to 25%.

The addition of the third port is mainly to show that a well-isolated tri-port antenna can be achieved by placing one magnetic antenna at the top end of the chassis. However, since the magnetic antenna does not rely on the chassis for radiation, its bandwidth is only around 2%, and tuning is needed to cover the operating band [13]. Therefore, the challenge is to find a tri-port solution with sufficient isolation and bandwidth over all three ports, without the need for frequency tuning [13] or decoupling structures [12]. Importantly, a tri-port antenna can offer 50% higher data rate than a two-port antenna in MIMO operation, if the correlation is low among the ports.

Increasing the screen-to-body ratio of smartphones is an ongoing trend, with it growing from 30.1% to 93.8% over the last 12 years [14], [15]. As a result, the screen covers nearly the entire front side, except for a few millimeters at the sides [16]. The screen is metal covered to enhance its structural strength [16]. In [1], the screen is modeled with only a dielectric plate (i.e., glass with a relative permittivity of 5.5). Hence, it has a limited influence on the antenna performance in the 3.5 GHz 5G band. As a more accurate model, a copper sheet has been used to model the screen [17]. However, the screen-to-body ratio is small (45%) and the effect of the screen is less prominent. To the best of the authors' knowledge, there are very few literatures on smartphone antenna design that explicitly model the large metal-covered screen in the design procedure [16], [18].

The effect of the large metal-covered screen was studied in [16] for a metal-framed monopole antenna or a planar inverted-F antenna (PIFA) mounted on the top end. The screen, which in practice is grounded to the terminal chassis, was found to severely degrade the bandwidth. In [18], the study of metal-covered screen is extended to design a multi-band single-port antenna, covering several LTE and 5G bands. Specifically, characteristic mode analysis (CMA) [19] was used to address the bandwidth degradation effect of the large screen observed in [16]. This is because the screen can be included in the design procedure through CMA, and the bandwidth impact can be mitigated by selectively exciting and merging as many resonant characteristic modes (CMs) as possible. However, no effort has so far been made to take advantage of the metal-covered screen to enable one more antenna port with a relatively large bandwidth, relative to the no-screen chassis model used for antenna design.

In this paper, the large screen is explicitly utilized by CMA to enable the design of a tri-port MIMO antenna below 1 GHz. The design procedure is based on two new resonant modes generated by the addition of the large screen, which facilitates the increase of the number of CMs (per frequency) in [7] from two to four. These two modes were then jointly and selectively excited by port 1 to improve bandwidth and correlation performances, respectively. Differential feeding is used by port 2 to avoid exciting the new modes, which is different from the single-feed design in [7]. Finally, the dipole mode along the chassis length is selectively excited by port 3 by adding a shorting pin to connect between the

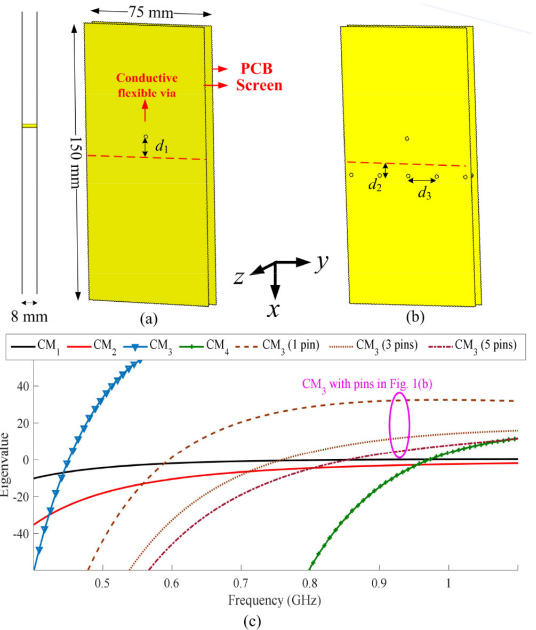


FIGURE 1. (a) Geometry and parameters of the connected metal plates ($d_1 = 15$ mm). (b) geometry with 5-metal pins added ($d_2 = 5$ mm, $d_3 = 17$ mm), and (c) Eigenvalues of the modes of interest for the dual-plate model with and without pins.

top end of the screen and the PCB. The proposed design concept yields at least 17% bandwidth for the tri-port antenna, showing that a tri-port design is feasible from both bandwidth and correlation perspectives even for MIMO operation below 1 GHz. Furthermore, as mentioned above, the tri-port design with low ECC (<0.16) can ideally offer 50% higher data rate for 3×3 MIMO, relative to a dual-port design for 2×2 MIMO.

II. LARGE-SCREEN INDUCED MODES AND SINGLE-PORT EXCITATION

A. CMA OF CONNECTED DOUBLE-PLATE MODEL

For a large-screen smartphone, the entire metal chassis is more accurately modelled as two connected parallel metal plates, i.e., the screen and the printed circuit board (PCB) (see Fig. 1(a)). As shown in the smartphone model in Fig. 1(a), there is normally a conductive flexible via (represented by a conductive pin of 1 mm in diameter, located d_1 above the center of each plate) that connects the screen assembly to the PCB [16]. The total model size is $150 \times 75 \times 8$ mm³, which can be considered typical for smartphones (e.g., Samsung S9 [15]). The addition of a large parallel plate to the single-PCB model is expected to significantly change the CMs of the chassis structure.

In this section, CMA is performed using 2018 Altair FEKO to explore the available modes in this connected

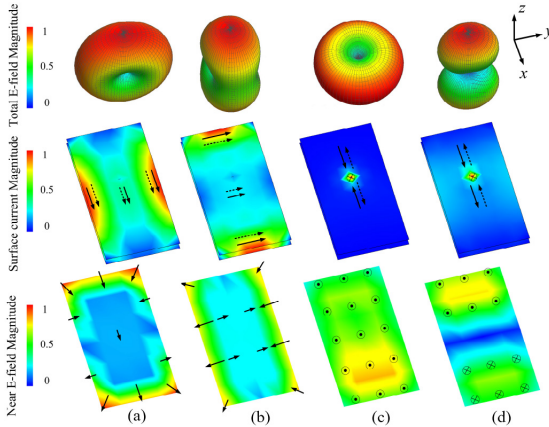


FIGURE 2. The normalized far-field patterns, surface currents on the two plates and electric near-field in between the two plates for (a) CM₁, (b) CM₂, (c) CM₃, and (d) CM₄ at their respective resonant frequencies. “⊙” and “⊗” represent E-field/current in positive and negative z directions, respectively. Solid and dashed arrows show the currents on the screen and PCB, respectively.

double-plate chassis, assumed to be a perfect electric conductor (PEC). For the initial analysis, the screen size is set to be the same as the PCB size (see Fig. 1(a)). As also found in [18] for slightly different plate sizes, the new structure of the smartphone chassis will bring different and new resonating CMs in comparison with a single PEC plate of the same dimension (see Fig. 1(c)). The first mode (CM₁) in Fig. 1(c) is the longitudinal half wavelength (0.5λ) dipole mode and the second one (CM₂) is the transversal 0.5λ -dipole mode, both of which also exist in single-PCB models. The lowest-order mode (CM₃) is a monopole-like mode that is due to two connected plates and the fourth mode (CM₄) is a patch-like mode due to adding the screen at the distance of h to the PCB ($h = 8$ mm in Fig. 1(a)). The parameter h has little effect on the resonant frequency of CM₁ and CM₂ in Fig. 1(c).

The characteristic far-field patterns, surface current distributions and electric field (E-field) distribution half-way between the two plates are shown for CM₁-CM₄ in Fig. 2. For CM₃, the surface currents on the screen flow into the metallic pin and then exit the pin into the PCB. The directions of the currents are reversed on the two plates and the currents reach a maximum value on the conductive flexible via (pin). The characteristic E-field of CM₃ is almost consistently in the positive z -direction in the volume between the plates. In contrast, the E-field for CM₄ is in both positive (top half) and negative (bottom half) z -directions, with a minimum E-field magnitude at the middle line. Depending on the position of the conductive flexible via (i.e., d_1 in Fig. 1(a)), the position of the minimum near E-field line of CM₄ can depart from the center. Moreover, the currents for CM₄ are in the same direction over the entire screen, whereas they flow in the opposite direction over the entire

PCB. But like CM₃, the currents are maximum along the via. Contrary to CM₃ and CM₄, the directions of the surface currents are the same on the two plates for CM₁ and CM₂, and the current is minimum on the conductive flexible via. Moreover, the E-field direction between the plates is in the xy -plane for CM₁ and CM₂.

As shown in Fig. 1(c), the resonant frequency of CM₃ in the initial structure (i.e., 452 MHz) is lower than the desired operating frequency range (~ 0.8 -1.0 GHz). According to [20], when a circular patch (i.e., two parallel circular plates) is not shorted with a pin, the resonant frequency of the lowest order mode (i.e., TM₀₁ or monopole mode in a circular patch antenna) is zero. To increase the modal resonant frequency, shorting pins were introduced to shorten the current paths [20]. Similarly, shorting pins can be added between the two plates in the initial structure (see Fig. 1(a)) to increase CM₃'s resonant frequency, resulting in the structure depicted in Fig. 1(b). As shown in Fig. 1(c), as the number of pins increases, the resonant frequency of CM₃ increases. However, the resonant frequencies of CM₁ and CM₂ remain unchanged, mainly due to their E-fields not being in the z -direction. To minimize any influence from the pins on the resonance of CM₄, the pins should be positioned along the line of minimum E-field magnitude for CM₄. As mentioned earlier, the minimum E-field region of CM₄ depends on d_1 and it can be moved downward from the middle if d_1 increases. Thus, d_1 and d_2 were optimized to tune the resonant frequencies of both CM₃ and CM₄ to the desired band. The result is that $d_1 = 15$ mm and $d_2 = 5$ mm for the five-pin case.

B. EXCITATION OF NEW CMS BY THE 1ST PORT

Having tuned the resonant frequencies of CM₃ and CM₄ to the desired band, the next step is to design the feed to simultaneously excite these two modes to achieve a wide-band dual-resonance, for the five-pin model. By comparing the characteristic currents and E-fields of modes with small eigenvalues within the desired frequency range (0.8-1.0 GHz) in Fig. 1(c), it can be seen that the currents of CM₃ and CM₄ have similar behavior along the via (i.e., maximum and in the same negative z -direction). So, a single feed at that location should be able to excite both CM₃ and CM₄, giving dual-resonance. Moreover, this single feed should not excite either CM₁ or CM₂, as their currents are very small along the via (see Figs. 2(a) and 2(b)). The selective excitation of CM₃ and CM₄ was verified using the modal weighting coefficients for this port (P₁) (see Fig. 3(a)). This strategy also allows CM₁ and CM₂ to be used for other ports, and low correlation with other ports is guaranteed as long as they do not excite CM₃ and CM₄.

As shown in Fig. 3(b), as the distance between the pins (i.e., d_3) increases, the resonant frequency of CM₃ increases and that of CM₄ remains almost unchanged. The latter is due to the pins being in a region of low E-field for CM₄. Finally, both modes were matched using a three-element

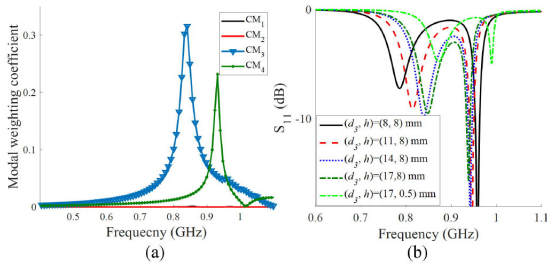


FIGURE 3. (a) Modal weighting coefficient of the modes of interest for P_1 excitation, (b) S_{11} before matching for different parameters (d_3, h).

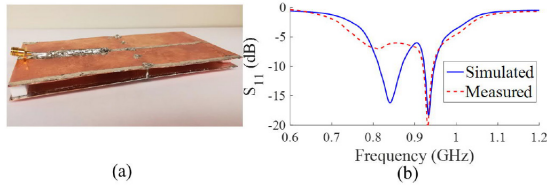


FIGURE 4. (a) Prototype of the single-port antenna, (b) measured and simulated S_{11} .

matching network consisting of a 3.9 pF series capacitor, as well as 19.8 nH and 14 nH parallel inductors. It is noted that the number of elements and configuration of the matching networks for achieving the maximum bandwidth potential [21] were found using BetaMatch [22]. To validate this new concept, the optimized single-port antenna was fabricated and shown in Fig. 4(a). A 20% bandwidth (792-968 MHz) is achieved with this matching network (see Fig. 4(b)). The measured $|S_{11}|$ in Fig. 4(b) is slightly different from the simulated ones, but it still covers the targeted band. This discrepancy is mainly due to imperfect Murata matching component modeling, imperfect soldering, and component aging.

Moreover, even if the gap between two plates model is drastically decreased, e.g., to $h = 0.5$ mm, to account for very extremely small gaps (in reality, the components between the layers should result in larger gaps), the two targeted modes (i.e., CM_3 and CM_4) are still present. These modes can still be used to provide an orthogonal third port for the given h with suitable tuning. Specifically, the resonant frequency of CM_3 can be lowered by decreasing d_3 , whereas the resonant frequency of CM_4 can be tuned by a small increase in the chassis size, and its excitation can be modified by increasing d_1 and d_2 . For this extreme case, the bandwidth (with matching) is 8% and the average radiation efficiency is 78% in the operating band.

III. ANALYSIS AND EXCITATION OF OTHER RESONANT MODES

In principle, the remaining tasks in designing the proposed tri-port MIMO antenna are to ensure that CM_1 and CM_2 , are selectively excited by P_2 and P_3 . In particular, the port

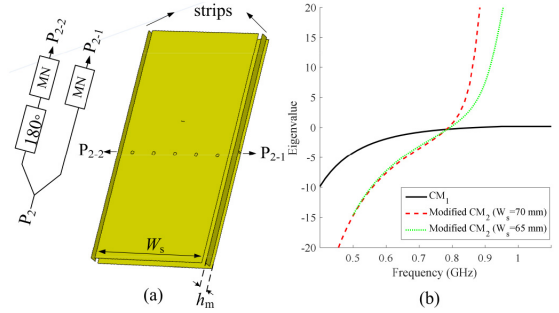


FIGURE 5. (a) Connected plates with metal strips and a feeding network consisting of a power divider with a 180° phase difference in the output ports and matching networks (MNs) ($W_s = 70$ mm, $h_m = 7$ mm), (b) modified eigenvalue for different screen widths.

design for CM_1 and CM_2 must also avoid exciting CM_3 and CM_4 , which are used by P_1 .

A. TUNING AND SELECTIVE EXCITATION OF CM_2 BY THE 2ND PORT

For the connected double-plate chassis, CM_2 has a transversal 0.5λ -dipole far-field pattern (see Fig. 2(b)) and a resonant frequency well above 1 GHz (see Fig. 1(c)). To reduce the resonant frequency to below 1 GHz, the structure can be capacitively loaded along the longer sides of the PCB plate with two center-grounded 150 mm \times 5 mm metal strips (see Fig. 5(a)). The strips are placed 3 mm above the sides. This modification lowers the resonant frequency of CM_2 with respect to Fig. 1(c). Moreover, it can be seen in Fig. 5(b) that as the clearance between the screen and the strips is increased, the slope of the eigenvalue of CM_2 decreases. Thus, to ensure that the bandwidth potential [21] of port 2 (P_2) is acceptable, the screen width W_s is reduced from 75 mm to 70 mm. With these structure modifications, the far-field pattern of each mode remains the same as that of the original double-plate structure (see Fig. 2). However, the characteristic currents are slightly modified due to the two loading strips. For instance, the modified currents of CM_2 and CM_3 are illustrated in Figs. 6(a) and 6(b), respectively. To study the impact of full metal frame, two metal strips were added to the top and bottom edges, with small gaps (e.g., 3 mm) to the metal strips along the longer sides. This addition was found to have limited impact on the utilized modes or their excitation using the existing feed structure.

To excite CM_2 , the feeding port can be placed at a high-current location. One such location is any one of the two shorting pins for the loading strips, as can be seen in Fig. 6(a). Through replacing one of the two shorting pins with a gap feed port, the modal weighting coefficient is calculated and plotted in Fig. 7(a). It can be seen that, by adding one feed, CM_2 will be excited. Moreover, the center location of the feed along the strip helps to prevent the excitation of CM_1 and CM_4 due to their low E-fields at this location, as shown in Figs. 2(a) and 2(d). Nonetheless, as shown in

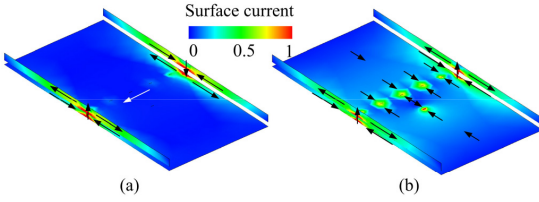


FIGURE 6. Modified surface currents by adding two grounded loading strips for (a) CM_2 , and (b) CM_3 . For clarity, the screen and connecting pins are not shown.

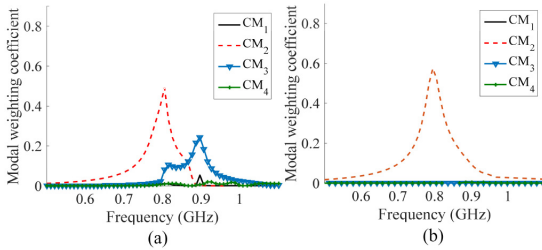


FIGURE 7. Modal weighting coefficient of the modes for P_2 and with: (a) one feed, and (b) two feeds with 180° phase shift ($W_s = 70$ mm). The feed power is kept equal in both cases.

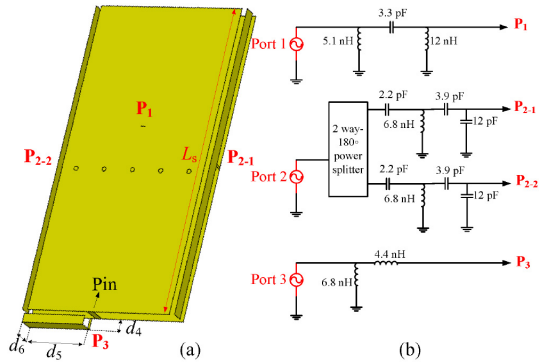


FIGURE 8. (a) Antenna structure with one CCE ($d_4 = 5$ mm, $d_5 = 30$ mm, $d_6 = 6$ mm, $L_s = 145$ mm), (b) matching networks consisting of components connected to the ports.

Fig. 7(a), CM_3 has also been excited by this feed, as it has high current at those locations, as shown in Fig. 6(b).

To selectively excite CM_2 , the currents of CM_2 and CM_3 (in Figs. 6(a) and 6(b), respectively) were compared. As can be seen, although the currents on the shorting pins (of the metal strips) flow in different directions for CM_2 , they are in the same direction for CM_3 . Thus, instead of exciting CM_2 with only one feed, the other pin is also replaced with a feed, with a new port (P_2) feeding them with a 180° phase difference to ensure no excitation of CM_3 (see Fig. 5(a)). The resulting modal weighting coefficient in Fig. 7(b) reveals that CM_3 is no longer excited with this differential feeding scheme. This kind of selective feeding for P_2 is different

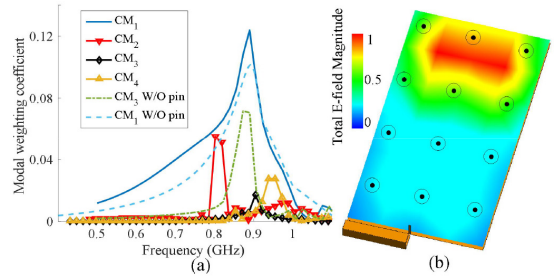


FIGURE 9. (a) Modal weighting coefficient of the modes for P_3 and, (b) electric near-field of the CM_3 mode (half-way between the screen and the PCB) after adding a shorting pin close to the single CCE.

from feeding in [6], in which a single capacitive coupling element (CCE) connected to one of the strips has been used.

Each of the ports in Fig. 5(a) was matched in BetaMatch [22] (see Fig. 8(b)), which yields a 6 dB impedance bandwidth of 15% (830-960 MHz), as depicted in Fig. 11. It is noted that, as the width of the screen W_s decreases, the number of elements needed to match the loading strip port (P_2) is smaller. In addition, as the distance of the screen to the PCB h together with the strip height (h_m) increases, the impedance bandwidth of the port improves.

B. TUNING AND SELECTIVE EXCITATION OF CM_1 BY THE 3RD PORT

Considering the E-field distribution of CM_1 in Fig. 2(a), it is common to use one CCE at a corner of the PCB to excite this mode [23]. To keep the overall length of the structure constant at 150 mm upon adding the CCE, the length of the double-plate model is reduced by d_4 (i.e., ground clearance in Fig. 8(a)). In practice, d_4 should be optimized based on the required ground clearance and achievable bandwidth [23]. Multiple CCEs or more matching elements can be used to reduce the clearance for a given targeted bandwidth. The modal weighting coefficients of CM_1 - CM_4 for a single CCE utilized as the third port are shown in Fig. 9(a). It can be seen in Fig. 9(a) that CM_3 is also excited by the CCE, whereas other modes are only slightly excited in the band of interest.

To remedy this problem, a shorting pin was added between the screen and the PCB at the top center position, near the position of the CCE. This solution was motivated by the E-field behavior seen in Fig. 2, i.e., the E-field of CM_3 is z-oriented whereas that of CM_1 is oriented along the xy -plane. Therefore, the added pin shorted out the E-field of CM_3 in this region (see Fig. 9(b)), without affecting that of CM_1 , such that the excitation of CM_3 notably decreased, as shown in Fig. 9(a). To match the CCE for P_3 , a two-element L matching network with two inductors was used, resulting in the 6 dB bandwidth of 790-960 MHz, as shown in Fig. 11. If the length of the screen L_s is increased beyond 145 mm, the bandwidth of this port will be reduced [16]. Thus, for the final configuration shown in Fig. 8(a), the screen to body ratio is $\sim 90\%$.

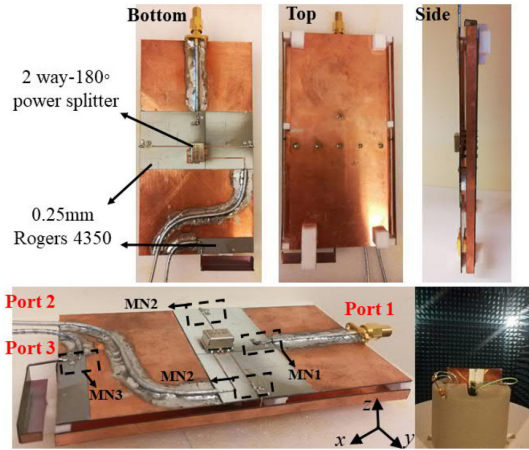


FIGURE 10. Prototype of the proposed tri-port MIMO antenna shown with different viewing angles, and it being mounted for pattern measurement (bottom right).

It is noted that only one CCE is used to excite CM_1 (see Fig. 8(a)), to achieve a compact implementation and allow for more space for possible higher band antennas. It was shown that if the number of properly phased and positioned CCEs (for CM_1) is increased, the complexity of the matching network to achieve a certain bandwidth decreases [23]. Furthermore, multiple CCEs will facilitate more selective excitation of CM_1 , reducing coupling with the other ports.

IV. EXPERIMENTAL RESULTS

To validate the proposed design concept, a prototype of the tri-port antenna was fabricated (see Fig. 10). Two 0.3mm thick copper plates were used to implement the PCB and the screen. The feeding networks were etched on a 0.25mm Rogers 4350 substrate with the relative permittivity of 3.48. To excite the two strips from the middle with the same magnitude and 180° phase difference, a surface mount 2 way- 180° power splitter (Mini-circuits SYPJ-2-222+) was used. To ease the implementation of the feeding network, a substrate is attached on the bottom side of the PCB by using a conductive glue. Alternatively, the network can also be placed between the two plates (see Fig. 14(b)). It is noted that the simple feeding networks in Fig. 10 are only intended to verify the operation of the proposed tri-port antenna. In real implementation, the power splitter and matching elements should be realized with integrated circuits and optimized with respect to the active RF circuitry, to minimize any possible interference. The proposed feeding network in Fig. 10 can be implemented in any advanced multilayer technology, which isolates it from the components between the plates.

Figure 11 shows the simulated and measured S-parameters of the proposed tri-port antenna. S_{13} and S_{23} are higher than S_{12} , since the CCE of P_3 will partially excite the other modes, as illustrated earlier in Fig. 9(a). Nevertheless, the measured isolation is over 13 dB, 20 dB, 17 dB for

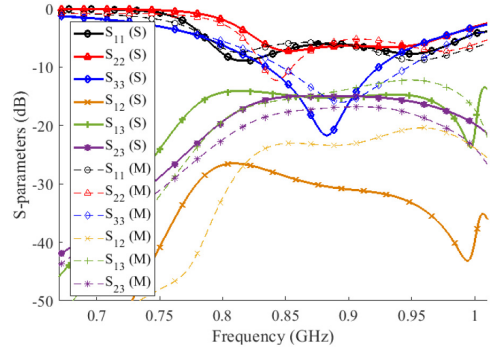


FIGURE 11. Simulated (S) and measured (M) S-parameters of the tri-port antenna.

S_{13} , S_{12} and S_{23} , respectively, which are considered as low enough in terminal applications for frequencies below 1 GHz (e.g., [4]-[13]). The relatively high isolation among the ports was achieved by creating multiple resonant CMs in the low band and selectively exciting them. In contrast, traditional low-band handsets mostly benefit from only one resonant mode (CM_3). The 6 dB impedance bandwidth of P_1 , P_2 and P_3 are 23% (0.79-1 GHz), 17% (0.82-0.98 GHz) and 21% (0.8-0.98 GHz), respectively. Good agreement is observed between the simulated and measured bandwidths. The measured S_{11} and S_{22} have slightly larger bandwidths than the simulated ones, but the in-band matching is slightly worse. S_{33} is slightly shifted at higher frequencies, but it still covers the targeted band. The discrepancies are mainly due to small differences between the nominal and actual values of the Murata components. The nominal values were used in the simulations.

It is further noted that the $|S_{11}|$ result in Fig. 11 is slightly different from that of Fig. 4, even though the same modes are excited. This is because the final prototype of Fig. 8 must be modified from the single-port variant, as described in Section III, to allow for additional modes to be created and selectively excited by two further ports (i.e., P_2 and P_3).

The radiation parameters of the fabricated prototype were obtained from a SATIMO multi-probe spherical near-field system in an anechoic chamber [24]. As expected, it can be observed in Fig. 12 that the total radiation patterns of P_1 - P_3 at 0.9 GHz are very similar to the far-field patterns of CM_3 , CM_2 , and CM_1 , respectively (see Fig. 2), since each port was designed to selectively excite one of these modes. The contribution from CM_4 to the pattern of P_1 only becomes more prominent at higher frequencies, as it contributes to the second/higher resonance of P_1 . The minor differences between the radiation patterns of the fabricated prototype and those of the CMs are primarily due to the presence of a feeding cable, connected to one of the three SMA connectors on the prototype, which was in the near field of the structure. Other reasons for the minor differences include tolerances in the fabrication and possible small phase/amplitude imbalances of the power splitter used.

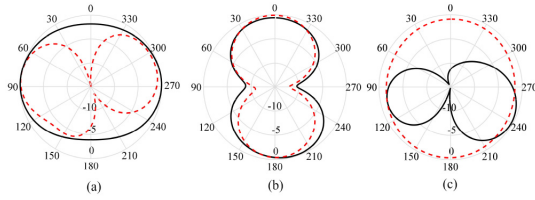


FIGURE 12. Measured radiation patterns of (a) P_1 , (b) P_2 , and (c) P_3 in xy (solid) and yz (dashed)-planes at 0.9 GHz, individually normalized at each port.

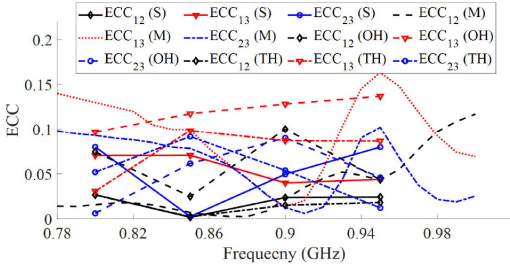


FIGURE 13. Simulated ((S), (OH), (TH)) and measured (M) ECC of the tri-port antenna.

The ECC, as calculated from the measured patterns [25], [26], is below 0.16 for all three ports (see Fig. 13). Simulated and measured ECCs in Fig. 13 were evaluated using a program implemented in MATLAB and antenna correlation tool in the SATIMO software, respectively. The average measured total efficiencies of P_1 - P_3 in their operating bandwidths are 74%, 72%, and 80%, respectively. The total efficiencies of the three ports are over 70% in the common bandwidth (0.82-0.98 GHz). The efficiency values were obtained from the radiation patterns measured using the SATIMO system [24].

The efficiency values are affected by the losses of the power splitters and the feeding networks. The coaxial cables in Fig. 10 were only added for experimental verification of the tri-port antenna design. They were well soldered to the chassis to mitigate cable influence. Coplanar waveguides (CPWs), more suitable for integrated circuits, should be used instead of all the transmission lines (TLs) in practice (Fig. 14(b)). However, the antenna performance was found to be similar for different types of TLs, due to the relatively low operating frequency.

To provide more insight into the system performance and the respective contributions from the total efficiencies and ECCs of the three ports, multiplexing efficiency [27] is used. Essentially, it is an equivalent power loss (for a given MIMO capacity) due to non-perfect total efficiencies and non-zero correlation. Hence, it can be seen as a multi-antenna extension of the single-port total efficiency concept. For a high signal-to-noise ratio (required for MIMO multiplexing transmission) and the reference channel with uniform 3D angular power spectrum, the multiplexing efficiency for a M -port

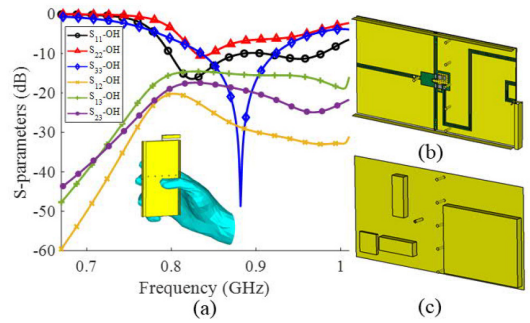


FIGURE 14. (a) Simulated S-parameters of the tri-port antenna in one hand (OH) mode. (b) model with CPW feeding network inside the gap. The screen is not shown for clarity; (c) layout of the antenna in a semi-populated handset device.

MIMO antenna is given by the compact form [27]

$$\eta_{\text{mux}} = \left(\prod_{k=1}^M \eta_k \right)^{1/M} \det(R)^{1/M} \quad (1)$$

where η_k is the total efficiency of port k , R is the correlation matrix, $\det(\cdot)$ is the determinant operator and \prod is the product operator. R for a tri-port antenna is

$$R = \begin{bmatrix} 1 & \rho_{12} & \rho_{13} \\ \rho_{12}^* & 1 & \rho_{23} \\ \rho_{13}^* & \rho_{23}^* & 1 \end{bmatrix}, \quad (2)$$

where ρ_{mn} is the complex correlation coefficient of the far-field patterns for ports m and n , and $*$ denotes the complex conjugate operator [27]. For the proposed antenna, the minimum η_{mux} is calculated to be 67.0% (-1.74 dB) in the common bandwidth. Based on (1), the contributions from antenna efficiencies and correlations to η_{mux} are -1.37 dB and -0.37 dB, respectively, indicating that the efficiency dominates and the ECC values are low enough to not have any major impact on the MIMO performance.

V. PRACTICAL APPLICATIONS OF PROPOSED TRI-PORT ANTENNA

One important practical issue for terminal antennas is the effect of the big display screen, which is utilized in an opportunistic manner in this work to form a new antenna port. In this section, three other practical issues affecting terminal antennas are briefly investigated.

A. EFFECT OF USER INTERACTION

Firstly, the performance of the proposed tri-port antenna is studied for two typical user scenarios, i.e., one-hand (OH) data mode (see Fig. 14(a)) and two-hand (TH) mode (see Fig. 15) [28]. In these scenarios, the prototype is confined to a bounding box of dimensions $151 \times 76 \times 9$ mm³, to account for a 0.5mm-thick casing. The simulated S parameters for OH mode (see Fig. 14(a)) show that the proposed antenna covers the same bandwidth as the free space case (see Fig. 11), but with better impedance matching for P_1 . However, P_2 covers 4% less bandwidth (0.81-0.93 GHz) due

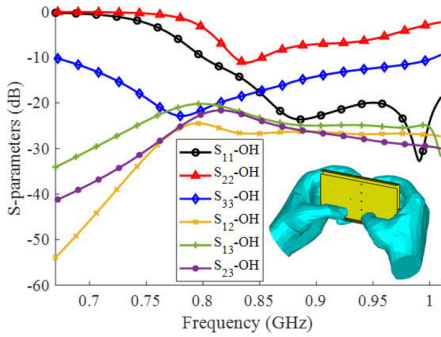


FIGURE 15. Simulated S-parameters of the tri-port antenna in two hand (TH) mode.

to hand loading. The performance of P_2 is more affected by the hand than P_1 , as the palm and fingers were positioned close to the two feeds of P_2 (i.e., P_{2-1} and P_{2-2}) at the metal strips, affecting the near-field radiation of P_{2-1} and P_{2-2} . Moreover, the unbalanced hand loading effect on P_{2-1} and P_{2-2} , which are equipped with the same matching network, leads to higher mismatch. In contrast, P_1 provides more distributed nearfields between the entire chassis and screen for the monopole mode and zero near-field in the center for the patch mode, resulting in the smaller hand effect. Similarly, P_3 is positioned further away from the hand and its nearfields are strongest at the top part of the longer edges, which is less affected by the hand. The hand also marginally affects the isolation between the three ports. However, the isolation remains above 15 dB in all cases.

Concerning efficiency, P_1 and P_2 suffer from slightly higher absorption loss than P_3 due to the position of the feed with respect to the hand, leading to lower radiation efficiency. The average total efficiencies of the P_1 , P_2 , and P_3 in their operating bands are 47%, 40%, and 50%, respectively. The decrease in average total efficiency is mainly due to the radiation efficiency drops of 2.4 dB, 2.7 dB and 2.17 dB, respectively.

In the TH mode, similar to the OH mode, the simulated S parameters (see Fig. 15) show that the proposed antenna can cover the same bandwidth as the free space case, but with better impedance matching for P_1 and P_3 . In the TH case, the palm is closer to the P_3 , whereas in the OH scenario, the palm is closer to either the P_{2-1} or P_{2-2} . Thus, compared with the free space scenario, it can be expected that the resonance of the P_2 is slightly less influenced in the TH case, and that of the P_3 is more affected by the TH case, as has been verified in Fig. 15. P_1 is also more affected in the TH mode than the OH mode, due to the loading effect on the two ends of the handset, which has non-zero nearfield for the monopole and patch modes. In general, the port isolation between the antennas becomes higher as compared with the free space scenario, due to the high absorption loss in the hand tissue. The average total efficiencies of the P_1 , P_2 , and P_3 in their operating bands are 23%, 22%, and 32%, respectively. The decrease in average total efficiency

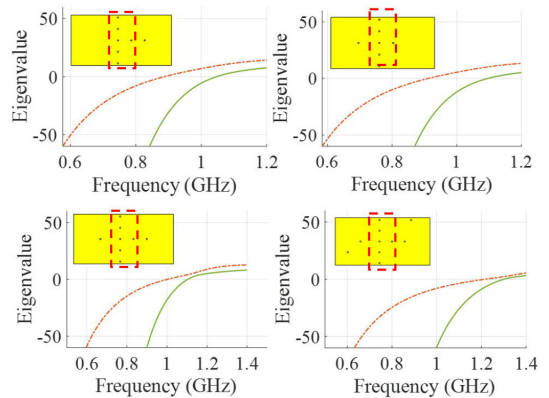


FIGURE 16. Different number of shorting pins added in random locations between the chassis and screen. The red dashed rectangle is showing the original pins we used in Fig. 1(b).

is mainly due to the radiation efficiency drops of 5.8 dB, 4.2 dB and 4.6 dB, respectively.

The slightly higher ECC in Fig. 13 for the OH and TH scenarios are due to the hand impairing efficient excitation of the inherently orthogonal modes as well as the shadowing of the hand causing the far-field patterns to be more alike. However, the simulated far-field ECC is still lower than 0.14 in all cases. The peak specific absorption rate (SAR) values for both OH and TH modes were also simulated for each of the three ports in CST 2018. All the SAR values are below 2 W/kg, implying compliance with the ICNIRP guidelines for hand-only modes [29].

B. EFFECT OF METALLIC COMPONENTS

In the second scenario, since in practice the space between the two connected plates in Fig. 1(b) is populated with metallic components of different sizes (e.g., battery), the impact of these objects (see Fig. 14(c)) was investigated in simulation. It was found that the metallic objects do not have much influence on the operation of the antennas and the introduced modes (CM_1 - CM_4) still exist. However, as the number of objects between the plates is increased, the resonant frequencies of the CM_3 and CM_4 tend to decrease. The resonant frequencies of these modes can be re-tuned using d_2 and d_3 . The operating band of P_1 and P_3 is not significantly affected, whereas P_2 experiences a small mismatch near the upper band edge due to unbalanced loading effect of the battery on the T-strip ports (i.e., P_{2-1} , P_{2-2}). However, by reoptimizing the matching component values, the matching can be restored to the desired level. ECC results are less than 0.1 in the operating band, which shows that the orthogonality of the ports is retained.

C. EFFECT OF ELECTRICAL CONNECTIONS AND GROUNDING

The third scenario considers electrical connections and grounding between the PCB and the screen, used to suppress

unwanted radiation. These connections were modelled using several shorting pins placed at different positions (Fig. 15). It can be seen in Fig. 15 that the CM₃ and CM₄ still exists and can be excited, however, these pins tend to increase the resonant frequencies of CM₃ and CM₄, the extent to which is determined by the modal electric near-fields at the pin positions (see Fig. 2). Therefore, the modes can be retuned by optimizing the number/locations of the pins, including the pins introduced in the initial design (see Fig. 1(b)). If required, a further decrease in the resonances of both modes can be achieved by slightly increasing the chassis length (either physically or electrically by using capacitive loading at one chassis end).

VI. CONCLUSION

Based on new modes introduced by the large metal-covered screen, a tri-port MIMO antenna is proposed for the first time for large-screen smartphones, to cover cellular bands below 1 GHz. The proposed antenna is implemented without any decoupling structure and with the spacing between the feeding locations limited to half the chassis length. The strategy of identifying and selectively exciting available modes facilitates high total efficiencies (above 70%) and low ECC (below 0.16) within the operating bandwidth.

REFERENCES

- [1] L. Sun, H. Feng, Y. Li, and Z. Zhang, "Compact 5G MIMO mobile phone antennas with tightly arranged orthogonal-mode pairs," *IEEE Trans. Antennas Propag.*, vol. 66, no. 11, pp. 6364–6369, Nov. 2018.
- [2] J. Guo, L. Cui, C. Li, and B. Sun, "Side-edge frame printed eight-port dual-band antenna array for 5G smartphone applications," *IEEE Trans. Antennas Propag.*, vol. 66, no. 12, pp. 7412–7417, Dec. 2018.
- [3] M. Abdullah, S. H. Kiani, and A. Iqbal, "Eight element multiple-input multiple-output (MIMO) antenna for 5G mobile applications," *IEEE Access*, vol. 7, pp. 134488–134495, 2019.
- [4] H. Li, Y. Tan, B. K. Lau, Z. Ying, and S. He, "Characteristic mode based tradeoff analysis of antenna-chassis interactions for multiple antenna terminals," *IEEE Trans. Antennas Propag.*, vol. 60, no. 2, pp. 409–502, Feb. 2012.
- [5] S. Zhang, K. Zhao, Z. Ying, and S. He, "Adaptive quad-element multi-wideband antenna array for user-effective LTE MIMO mobile terminals," *IEEE Trans. Antennas Propag.*, vol. 61, no. 8, pp. 4275–4283, Aug. 2013.
- [6] H. Li, B. K. Lau, Z. Ying, and S. He, "Decoupling of multiple antennas in terminals with chassis excitation using polarization diversity, angle diversity and current control," *IEEE Trans. Antennas Propag.*, vol. 60, no. 12, pp. 5947–5957, Dec. 2012.
- [7] H. Li, Z. T. Miers, and B. K. Lau, "Design of orthogonal MIMO handset antennas based on characteristic mode manipulation at frequency bands below 1 GHz," *IEEE Trans. Antennas Propag.*, vol. 62, no. 5, pp. 2756–2766, May 2014.
- [8] Z. Miers, H. Li, and B. K. Lau, "Design of bandwidth-enhanced and multiband MIMO antennas using characteristic modes," *IEEE Antennas Wireless Propag. Lett.*, vol. 12, pp. 1696–1699, 2013.
- [9] K. K. Kishor, and S. V. Hum, "Multiport multiband chassis-mode antenna design using characteristic modes," *IEEE Antennas Wireless Propag. Lett.*, vol. 16, pp. 609–612, 2017.
- [10] I. R. Barani and K.-L. Wong, "Integrated inverted-F and open-slot antennas in the metal-framed smartphone for 2 × 2 LTE LB and 4 × 4 LTE M/HB MIMO operations," *IEEE Trans. Antennas Propag.*, vol. 66, no. 10, pp. 5004–5012, Oct. 2018.
- [11] D. Huang, Z. Du, and Y. Wang, "A quad-antenna system for 4G/5G/GPS metal frame mobile phones," *IEEE Antennas Wireless Propag. Lett.*, vol. 18, pp. 1586–1590, 2019.
- [12] S. Xiao and Z. Du, "Decoupled dual-antenna system using crossed neutralization lines for LTE/WWAN smartphone applications," *IEEE Antennas Wireless Propag. Lett.*, vol. 14, pp. 523–526, 2015.
- [13] H. Aliakbari and B. K. Lau, "Low-profile two-port MIMO terminal antenna for low LTE bands with wideband multimodal excitation," *IEEE Open J. Antennas Propag.*, vol. 1, pp. 368–378, 2020.
- [14] J. Callaham, *The Race to 100 Percent: Smartphone Screen-to-Body Ratios Over the Years*, Jun. 25, 2018. Accessed: Aug. 26, 2021. [Online]. Available: <https://www.androidauthority.com/smartphone-screen-to-bodyratio-878835/>
- [15] *Specifications Samsung Galaxy S9 and S9+*, Off. Samsung Galaxy Site, Suwon-si, South Korea, Mar. 2018. Accessed: Aug. 26, 2021. [Online]. Available: <https://www.samsung.com/global/galaxy/galaxy-s9/specs/>
- [16] B. Xiao, H. Wong, B. Wang, and K. L. Yeung, "Effect of the screen to metal-frame smartphone antennas," in *Proc. IEEE Int. Workshop Antenna Technol. (iWAT)*, Miami, FL, USA, Mar. 2019, pp. 29–32.
- [17] K. Payandehjoo and R. Abhari, "Compact multi-band PIFAs on a semi-populated mobile handset with tunable isolation," *IEEE Trans. Antennas Propag.*, vol. 61, no. 9, pp. 4814–4819, Sep. 2013.
- [18] B. Xiao, H. Wong, D. Wu, and K. L. Yeung, "Metal-frame antenna for big-screen smartphones using characteristic mode analysis," *IEEE Access*, vol. 7, pp. 122224–122231, 2019.
- [19] R. Harrington and J. Mautz, "Theory of characteristic modes for conducting bodies," *IEEE Trans. Antennas Propag.*, vol. 19, no. 5, pp. 622–628, Sep. 1971.
- [20] J. Liu, Q. Xue, H. Wong, H. W. Lai, and Y. L. Long, "Design and analysis of a low-profile and broadband microstrip monopolar patch antenna," *IEEE Trans. Antennas Propag.*, vol. 61, no. 1, pp. 11–18, Jan. 2013.
- [21] J. Villanen, J. Ollikainen, O. Kivekäs, and P. Vainikainen, "Coupling element based mobile terminal antenna structures," *IEEE Trans. Antennas Propag.*, vol. 54, no. 7, pp. 2142–2153, Jul. 2006.
- [22] Betamatch. (2019). *MNW Scan Pte Ltd, Version 3.7.6*. Accessed: Aug. 26, 2021. [Online]. Available: <http://www.mnw-scan.com/>
- [23] H. Aliakbari and B. K. Lau, "On modal excitation using capacitive coupling elements and matching network," in *Proc. IEEE Int. Symp. Antennas Propag. (APS)*, Atlanta, GA, USA, Jul. 2019, pp. 731–732.
- [24] Satimo Stargate. (2019). *Measurement System*. Accessed: Aug. 26, 2021. [Online]. Available: <http://www.satimo.com>
- [25] M. B. Knudsen and G. F. Pedersen, "Spherical outdoor to indoor power spectrum model at the mobile terminal," *IEEE J. Sel. Areas Commun.*, vol. 20, no. 6, pp. 1156–1168, Aug. 2002.
- [26] R. Vaughan and J. B. Andersen, *Channels, Propagation and Antennas for Mobile Communications*. London, U.K.: Inst. Elect. Eng., 2003.
- [27] R. Tian, B. K. Lau, and Z. Ying, "Multiplexing efficiency of MIMO antennas," *IEEE Antennas Wireless Propag. Lett.*, vol. 10, pp. 183–186, 2011.
- [28] I. Vasilev and B. K. Lau, "On user effects in MIMO handset antennas designed using characteristic modes," *IEEE Antennas Wireless Propag. Lett.*, vol. 15, pp. 758–761, 2016.
- [29] ICNIRP Guidelines, "Guidelines for limiting exposure to time-varying electric, magnetic, and electromagnetic fields (up to 300 GHz)," *Health Phys.*, vol. 74, no. 4, pp. 494–522, 1998.

Paper III

Low-Band MIMO Antenna for Smartphones With Robust Performance to User Interaction

Hanieh Aliakbari ¹, Graduate Student Member, IEEE, and Buon Kiong Lau ¹, Senior Member, IEEE

Abstract—This letter proposes a two-port multiple-input-multiple-output smartphone antenna for frequency bands below 1 GHz, which is robust to user effects. The design is achieved by first analyzing the characteristic modes of a chassis that includes the large screen. Two modes predicted to be less affected by the user than other commonly used modes are selected. The modal currents and near-fields of the two desired modes then guide the design: The monopole-like mode introduced by the screen is tuned to resonance using shorting pins and selectively excited using the center feed location. The nonresonant loop mode is selectively excited for the first time by four inductive feeds added along the longer sides of the chassis, with proper phase shifts provided by a feeding network. The proposed antenna features isolation of above 19 dB and envelope correlation coefficient of below 0.12 in the considered scenarios. The measured bandwidth is above 15% for both ports, and the average radiation efficiency is 2 and 4.57 dB higher for two user scenarios with respect to a reference design. Moreover, no adaptive matching is needed as the impedance matching is robust to the user hand/head.

Index Terms—Characteristic modes, feeding network, handset antennas, multiple-input-multiple-output (MIMO) systems, user effect.

I. INTRODUCTION

MULTIPLE-INPUT-multiple-output (MIMO) antenna design for smartphones is very challenging, especially in frequency bands below 1 GHz (i.e., LTE low band), since sufficiently large bandwidth and low correlation are required for an electrically compact chassis [1]. Fortunately, characteristic mode analysis (CMA) can be used to design uncorrelated MIMO antennas of up to 30% bandwidths by using the chassis' modal properties to tune several modes and excite them [1]–[4].

Another challenging issue is that smartphone antennas are traditionally designed and characterized for free-space (FS) operation, rather than actual use cases that involve the close proximity of user hands and head [5]. The high permittivity and high conductivity of the human tissue can result in severe detuning of the antenna and significant power absorption, respectively, which deteriorate antenna efficiency [6]. For instance, the effect of user hand on the operation of a single port antenna is presented in [7], indicating a 7–11 dB drop in antenna efficiency in a LTE low band, compared to FS. In a few studies on the performance

of MIMO handsets in the low band [8]–[11], the proximity of the human body is shown to severely affect both efficiency and correlation of two-port MIMO antennas. Depending on the position of the index finger, the variation in mutual coupling of two-port MIMO antennas can be up to 10 dB [8]. In [9], the far-field patterns of a MIMO antenna are found to be more correlated when the head is in proximity. Another investigation in [10] found that the total efficiency can be as low as –19.1 dB, due to the absorption and mismatch by the user's hand and head, compared to –1.9 dB in FS. In [11], a user hand causes a 4 dB loss in the average total efficiency of a highly correlated MIMO antenna at 0.75 GHz.

Due to the aforementioned significant user effects on MIMO antenna performance, it is important to not only evaluate the performance of completed antenna prototypes in different user scenarios after the design stage [8]–[11], but to also account for user interactions at the design stage. For instance, some design techniques have been found to be effective for mitigating user effects in terminal antennas in LTE low band [12]–[23]. However, existing contributions focus on single-antenna design [12]–[20] and only a few consider MIMO antennas [21]–[23].

In [21], the least affected antenna of four identical elements located at four edges of the chassis is dynamically selected to overcome user effects. Using adaptive matching, significant capacity gains have been achieved in the presence of user by targeting low correlation [22]. However, these methods [21], [22] require complex adaptive circuits and the MIMO antennas utilize only the traditional fundamental dipole mode of the chassis, which is known to be vulnerable to user effects [19].

A comparison study in [23] reveals that the CMA-based MIMO terminal antennas are in general more robust to user effects in the low band, in terms of impedance matching and correlation. Moreover, it has been found that the excited modes of an antenna can substantially influence its user effects [18]–[20]. Since the antenna pattern is a linear combination of the far-fields of the characteristic modes (CMs) excited by the antenna, the user effects on a given CM can be found. In [19], it is observed that the characteristic far-field patterns with a null at the boresight are less affected by a user hand, by comparing the modal weighting coefficients of the antenna in FS with those in the hand grip. This result can be understood by the severe shadowing by the palm and fingers at the boresight. It is not uncommon in the literature to utilize far-field properties to guide antenna designs involving proximity of human tissue, due to the lack of consensus on a suitable near-field figure-of-merit [24]. Subsequently, this insight is applied using CMA to synthesize a desired antenna pattern consisting of several chassis modes [20]. However, the design is single-port and the achieved bandwidth is small (6%).

Manuscript received February 15, 2021; revised April 1, 2021; accepted April 20, 2021. Date of publication April 23, 2021; date of current version July 7, 2021. This work was supported by Vetenskapsrådet (Dnr 2018-04717). (Corresponding author: Buon Kiong Lau.)

The authors are with the Department of Electrical and Information Technology, Lund University, 22100 Lund, Sweden (e-mail: hanieh.aliakbari_abar@eit.lth.se; buon_kiong.lau@eit.lth.se).

Digital Object Identifier 10.1109/LAWP.2021.3075240

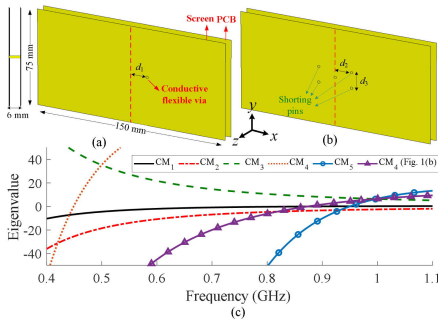


Fig. 1. (a) Geometry of the connected metal plates. (b) Geometry with $d_1 = 0$ mm and four-metal pins added ($d_2 = 9$ mm, $d_3 = 5$ mm). (c) Eigenvalues λ_n of the modes of interest for the dual-plate model in (a) and (b). Eigenvalues of CM_1 – CM_3 , CM_5 are similar for (a) and (b).

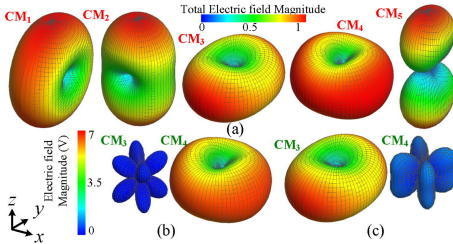


Fig. 2. (a) Normalized characteristic far-field patterns for CMs in Fig. 1(c). E-field magnitude of (b) theta and (c) phi components of CM_3 and CM_4 .

In this letter, we extend this promising concept to design a robust two-port MIMO smartphone antenna in a systematic manner using CMA. The proposed design offers $>15\%$ bandwidth and <0.07 envelope correlation coefficient (ECC) in free space, in LTE low band. Since the screen-to-body ratio of smartphones is increasing nowadays [25]–[27], the two CMs utilized in the design are based on a chassis model that includes a large metal-backed screen. The two modes are selectively excited by the two ports, yielding the desired antenna patterns that have nulls at the boresight. Finally, the MIMO antenna is confirmed to be robust to two common user scenarios.

II. CMA OF CONNECTED DOUBLE PLATE MODEL

Two connected parallel metal plates are used as a model for a large screen smartphone [28] [see Fig. 1(a)]. As shown in the smartphone model, there is a conductive flexible via (represented by a conductive pin of 1 mm in diameter, located d_1 above the center of each plate) that connects the screen assembly to the printed circuit boards (PCB) [25]–[27]. In this section, CMA is performed using 2019 Altair FEKO to explore the modes of this connected perfect electric conductor double-plate model.

For the initial analysis, the screen size is set to be the same as the PCB size [see Fig. 1(a)]. We denote the first mode (CM_1) as the longitudinal half-wave (0.5λ) dipole mode, the second one (CM_2) as the transversal 0.5λ -dipole mode, and the third one (CM_3) as the loop mode [see Fig. 2(a)], all of which also exist in single-PCB models [1]. On the other hand, two new CMs (CM_4 , CM_5) are found for the double-plate model in

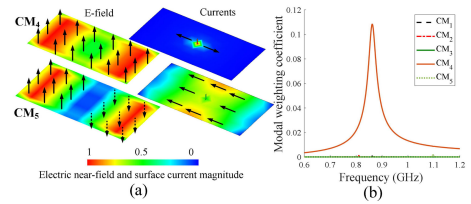


Fig. 3. (a) z -directed electric near-field in between two plates and modal current for CM_4 and CM_5 . (b) Modal weighting coefficient for the first port (P_1).

Fig. 1(a). The lowest-order mode (CM_4) is a monopole-like mode that is due to two connected plates and the fifth-mode (CM_5) is a patch-like mode due to the added screen at the distance of h to the PCB [see Fig. 1(a)]. According to the concept in [29], shorting pins can be introduced to shorten the current paths and hence increase the resonant frequency of the zeroth-order mode. Four shorting pins were introduced [see Fig. 1(b)] to increase the low resonant frequency (0.45 GHz) of CM_4 to the desired low LTE band [27]. The eigenvalues of CM_1 – CM_5 for the models in Fig. 1(a) and (b) with the four shorting pins are shown in Fig. 1(c). The corresponding far-field patterns are presented in Fig. 2(a). It is noted that apart from CM_4 , the eigenvalues and far-fields of the four other modes are identical between the two models shown in Fig. 1. The reason is that the pins are located in the minimum near-field region of the four other modes [e.g., see Fig. 3(a) for that of CM_5]. Most of the existing terminal antennas in LTE low band use the longitudinal 0.5λ -dipole mode (CM_1) and/or the transversal 0.5λ -dipole mode (CM_2) [1]–[17], [21]–[27]. The patterns of these dipole modes are omni-directional on the planes perpendicular to the PCB, i.e., yz and xz planes [see Fig. 2(a)]. Similarly, a patch-like mode (CM_5) also has more directional patterns on the planes perpendicular to the PCB. If the terminal antenna utilizes these modes (CM_1 , CM_2 , CM_5), then the antenna will illuminate the user in both near- and far-fields and suffers more from user effects [19].

To reduce the user effect, an omni-directional pattern with radiation nulls in the boresight direction, i.e., along the positive and negative of z -axis, is preferred [20]. As shown in Fig. 2(a), CM_3 and CM_4 are good candidates for this goal as they provide the desired omni-directional pattern on the xy plane, with the nulls along the z -axis. Despite having similar gain patterns, CM_3 and CM_4 are orthogonal. This due to polarization diversity [see Fig. 2(b) and (c)], with the phi and theta components being dominant for CM_3 and CM_4 , respectively. Consequently, they are good candidates for implementing two orthogonal ports with less effects from user. Therefore, in contrary to previously reported multiport terminal antennas in the low band, the excitation of commonly used modes of CM_1 , CM_2 , and CM_5 are avoided in the proposed MIMO antenna (PMA).

III. SELECTIVE EXCITATION OF CM_4 BY PORT 1 (P_1)

As explained in Section II, CM_4 is tuned to the desired band by adding several shorting pins. The next task is to excite this mode using P_1 , and to prevent the same port from exciting other resonant modes. The characteristic electric field (E-field) distribution half-way between the two plates (i.e., 3 mm from either plate) and current distributions are shown for CM_4 and CM_5 in Fig. 3(a). The characteristic E-field of CM_4 is almost

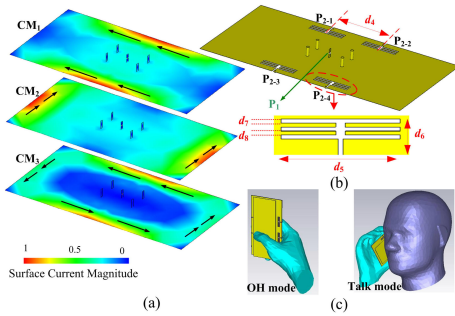


Fig. 4. (a) Surface current on PCB for CM₁–CM₃. (b) Four added slots (ICE) with parameters on the PCB ($d_4 = 40$ mm, $d_5 = 23$ mm, $d_6 = 10$ mm, $d_7 = d_8 = 1$ mm). Screen is not shown for clarity. (c) Antenna in two user scenarios.

consistently in the z -direction in the volume between the plates. The E-field for CM₅ is in both positive (top half) and negative (bottom half) z -directions, with the minimum E-field occurring around the center. So the center feed [i.e., P₁ in Fig. 4(b)] can be used to prevent excitation of CM₅. This is the reason initially for setting $d_1 = 0$ in Fig. 1(b). Moreover, using this single feed should not excite CM₁, CM₂, and CM₃, as their currents are very small along the via between the plates, as shown in Fig. 4(a). This is different from the feeding consideration in [27], where the goal is to simultaneously excite CM₄ and CM₅. In contrast, the goal here is to selectively excite CM₄, to provide the desired omni-directional pattern on the xy plane for P₁ in the low band, with the nulls along the z axis.

The shorting pins are located around the feed in the center as shown in Fig. 1(b), instead of being placed in a single row [27]. The more symmetrical structure helps to prevent the excitation of undesired modes in the final design. The selective excitation of CM₄ was verified by using the modal weighting coefficients for P₁, shown in Fig. 3(b). The selective excitation strategy allows another CM with radiation nulls in the boresight (i.e., CM₃) to be used for the other port, and low correlation with the other port is guaranteed as long as that port does not excite CM₄.

IV. SELECTIVE EXCITATION OF CM₃ BY PORT 2 (P2)

CM₃ is a loop mode, which also exists for a single chassis. CM₃ has long been recognized as an inherently nonresonant inductive mode [1], and hence, it has not been considered practical for antenna design. To our knowledge, this letter represents the first time this mode is successfully utilized for MIMO terminal antenna design. The surface current distribution of CM₁–CM₃ on the PCB is shown in Fig. 4(a). The directions of the surface currents on the screen [not shown in Fig. 4(a)] are the same as those on the PCB for CM₁–CM₃, and the current is minimum on the conductive flexible via. To excite the loop-like surface currents of CM₃ on the PCB, four small inductive coupling elements (ICEs) are implemented symmetrically along the longer sides of the PCB, as depicted in Fig. 4(b). Four voltage ports [i.e., P₂₋₁–P₂₋₄ in Fig. 4(b)] are directly positioned across each of the ICEs. By this arrangement, the two shorter sides of the chassis can be used by other antenna elements to cover other bands. The configuration of the ICE in Fig. 4(b) is the cascaded version of that in [30], which is used to ease the matching of CM₃ across the band. The ICEs have no noticeable effect on the eigenvalues

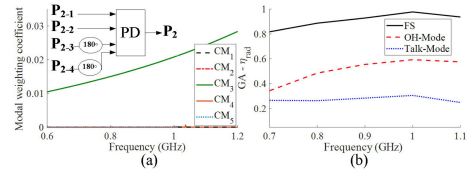


Fig. 5. (a) Modal weighting coefficient of the modes for P₂ and its four feeds with PS. Power divider (PD) is used. (b) GA- η_{rad} for three scenarios.

[Fig. 1(c)] and far-fields [Fig. 2(a)] of the CMs. To excite the desired modes, the correct relative amplitudes and phase shifts (PSs) corresponding to the modal currents in Fig. 4(a) should be applied to P₂₋₁–P₂₋₄. Accordingly, P₂₋₁ and P₂₋₂ should be phase shifted by 180° relative to P₂₋₃ and P₂₋₄, as seen in the inset of Fig. 5(a). The modal weighting coefficients [see Fig. 5(a)] confirm the correct selective feeding of CM₃. If no PS is applied, then the ICEs will excite CM₁ and CM₅ instead, due to their in-phase currents at these feed positions.

To explain how CM₃ can be used by port 2 despite being non resonant, it can be seen in Fig. 1(c) that the eigenvalue of the CM₃ at 0.9 GHz is about 8.68. However, due to the use of more coupling elements the modal excitation coefficient of CM₃ can be increased accordingly [31]. Therefore, efficient excitation of CM₃ by the feeds that are well-aligned to the modal properties has partly compensated for the relatively large eigenvalue of CM₃. Consequently, this letter offers the new insight that additionally flexibility can be gained for antenna design using CMA by considering the feeding structure. Specifically, the possible use of a given CM not only depends on the magnitude of its eigenvalues, but also on how the feed can be designed to enhance the excitation of a CM to compensate for relatively large eigenvalues. This insight will allow more CMs to be chosen as candidate modes for antenna design.

V. USER EFFECT AND SIMULATED RESULTS

The robustness of the proposed two-port design is evaluated in FS and two user scenarios [one-hand (OH) browse mode and talk mode [23], see Fig. 4(c)] using the time-domain solver of CST 2018. The radiation efficiencies of P₁ and P₂ are 94% and 91% in FS at 0.9 GHz, and they drop to 60% and 52%, respectively, in OH. The radiation efficiencies of the proposed design are less affected than the design with broadside pattern in [15] (1.94/2.4 dB drop for P₁/P₂ vs. 4 dB in [15]). The geometric average of radiation efficiencies (GA- η_{rad}) over the two ports as defined in [23] is shown in Fig. 5(b) for the PMA. Since [15] only considers a single-port antenna and an OH mode, better benchmarking can be obtained using the CMA-based two-port antenna evaluated in [23] [see Fig. 6(a)] as a reference MIMO antenna (RMA). The RMA uses modes with no null in the broadside for both ports (i.e., port 1 excites full-wave loop mode and port 2 excites the fundamental dipole mode). To ensure fair comparison, the positions of the coupling element and feeding lines in the chosen RMA are similar to those of the PMA. As can be seen in Fig. 6(b), the drop in the radiation efficiencies of the RMA are 2 and 4.57 dB higher than those of the PMA, in the OH mode and talk mode, respectively. Moreover, the matching efficiency [23] of the RMA is reduced more than that of the PMA in the two user scenarios [see Fig. 6(b)] over 836–968 MHz. Figs 6(b) and 7 show that the S -parameters for the PMA is more stable

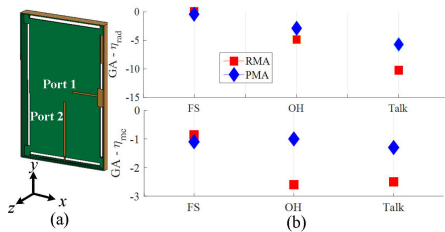


Fig. 6. (a) RMA (i.e., prototype 1 in [23]). (b) Comparison of $GA-\eta_{rad}$ and $GA-\eta_{mc}$ over operating bands in three scenarios for RMA and PMA.

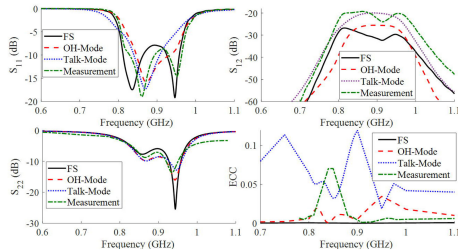


Fig. 7. S-parameters and ECC for three scenarios and measurement results.

TABLE I
COMPARISON OF THE PMA AND TWO-PORT ANTENNAS IN LOW BAND

Ref.	Common BW(MHz)	Ave. $GA-\eta_{rad}$ (OH)	Ave. $GA-\eta_{rad}$ (Talk)	Ave. ECC (OH/Talk)	Adaptive network
[21]*	750–960	-6.88 dB	-10.57 dB	0.13/0.17	Yes
[22]	815–875	-5.5 dB	N/A	0.03/NA	Yes
[23]**	824–894	-7.5 dB	-12.77 dB	0.03/0.15	No
[23]***	818–896	-4.5 dB	-14 dB	0.04/0.02	No
[32]	829-960	-6.59 dB	N/A	0.05/NA	No
[10]*	746 - 787	N/A	-14.6 dB*	NA/0.05	No
PMA	836-968	-3.9 dB	-7 dB	0.02/0.06	No

*Best prototypes (i.e., Antenna34 in [21], and P₂ in [10]), **Prototype 1 (i.e., RMA), and ***Prototype 2 in [23].

with acceptable matching and isolation in different scenarios, indicating its robustness to user effects. The ECC is below 0.12 in all the scenarios (see Fig. 7). The slightly higher ECC in the talk mode is mainly due to the shadowing of the patterns by the user, which increases the similarity between the two patterns. It is noted that the comparison of η_{rad} of the individual ports also shows better performance for the PMA ports. Comparisons with other two-port antennas are also provided in Table I.

VI. MEASURED RESULTS

In real implementation, microstrip lines are used to feed the ICES instead of direct voltage ports (see Fig. 8). The ICES are etched on the top side of the chassis, with matching elements placed on the substrate. The feeding network realized by microstrip lines is printed on the back side of the chassis. The matching elements shown in Fig. 8 are used to widen the bandwidth. The substrate used is Rogers RO4003C (thickness of 1.524 mm, relative permittivity of 3.38, and loss tangent of 0.0027). Three PDs with different PSs are used in Fig. 8 to feed the ICES. As all the ICES are similar and distributed in a mirror symmetric manner, there is ideally no power dissipation in the PDs. The advantage of using PDs over T-divider, despite

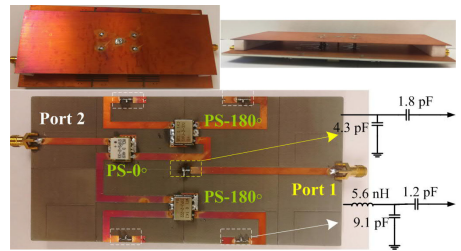


Fig. 8. Prototype of the PMA shown with different viewing angles.

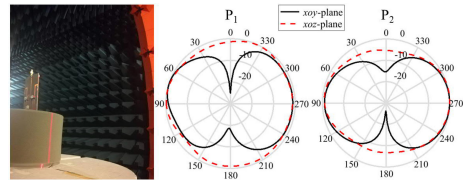


Fig. 9. Measured radiation patterns in two planes for two ports.

the earlier being more space consuming, is that the matching is more controllable due to the isolation between the PDs' ports [33], [34]. It is noted that the simple feeding networks in Fig. 8 are only intended to verify the operation of the PMA. In real implementation, the PD, PS, and off-chip matching elements should be realized with compact integrated circuits for the sake of practicality and compactness, and optimized with respect to the active RF circuitry. The feeding network in Fig. 8 can be realized in any advanced multilayer technology [35].

For the final layout in Fig. 8, the size of the screen is slightly decreased to increase the potential bandwidth [36] of CM₃. The measured bandwidths are 18% (805–967 MHz) and 15% (836–968 MHz) for P₁ and P₂, respectively, which agree well with the simulation results (see Fig. 7). The measured isolation is over 19 dB. The average in-band total efficiencies are 81% and 68% (minimum of 65% and 63%) for P₁ and P₂, respectively. The lower total efficiency in P₂ is mainly due to the PD's loss in the feeding network of Fig. 8. The measured radiation patterns of the two ports (see Fig. 9) show that the radiation nulls are successfully retained at the boresight and backward directions as for CM₃ and CM₄ in Fig. 2. Finally, the ECC of the measured patterns (see Fig. 7) is below 0.07 in the operating band.

VII. CONCLUSION

Using the connected metal-backed screen and chassis model, two new modes are selected and excited for the first time using CMA, resulting in a two-port MIMO terminal antenna for LTE low band. The two ports are more robust in two user scenarios than a reference design, due to the selected modes having a desirable property. Therefore, the proposed antenna does not require any adaptive circuit to compensate for user effects.

ACKNOWLEDGMENT

The authors would like to thank A. Johansson of Lund University and D. Pugachev of Sigma Connectivity AB for their help in prototype fabrication and pattern measurement.

REFERENCES

- [1] H. Li, Z. Miers, and B. K. Lau, "Design of orthogonal MIMO handset antennas based on characteristic mode manipulation at frequency bands below 1 GHz," *IEEE Trans. Antennas Propag.*, vol. 62, no. 5, pp. 2756–2766, May 2014.
- [2] S. Zhang, K. Zhao, Z. Ying, and S. He, "Investigation of diagonal antenna-chassis mode in mobile terminal LTE MIMO antennas for bandwidth enhancement," *IEEE Antennas Propag. Mag.*, vol. 57, no. 2, pp. 217–228, Apr. 2015.
- [3] C. Deng, Z. Feng, and S. V. Hum, "MIMO mobile handset antenna merging characteristic modes for increased bandwidth," *IEEE Trans. Antennas Propag.*, vol. 64, no. 7, pp. 2660–2667, Jul. 2016.
- [4] H. Aliakbari and B. K. Lau, "Low-profile two-port MIMO terminal antenna for low LTE bands with wideband multimodal excitation," *IEEE Open J. Antennas Propag.*, vol. 1, pp. 368–378, 2020.
- [5] R. Khan, A. Al-Hadi, and P. J. Soh, "Recent advancements in user effect mitigation for mobile terminal antennas: A review," *IEEE Trans. Electromagn. Compat.*, vol. 61, no. 1, pp. 279–287, Feb. 2019.
- [6] B. K. Lau, "Multiple antenna terminals," in *MIMO: From Theory to Implementation*. New York, NY, USA: Academic, 2010, pp. 267–298.
- [7] J. Holopainen, O. Kiveks, J. Ilvonen, R. Valkonen, C. Icheln, and P. Vainikainen, "Effect of the user's hands on the operation of lower UHF band mobile terminal antennas: Focus on digital television receiver," *IEEE Trans. Electromagn. Compat.*, vol. 53, no. 3, pp. 831–841, Aug. 2011.
- [8] A. A.-H. Azreimi, J. Ilvonen, C.-H. Li, J. Holopainen, and P. Vainikainen, "Influence of the user's hand on mutual coupling of dual-antenna structures on mobile terminal," in *Proc. 6th Eur. Conf. Antennas Propag.*, Prague, Czech Republic, 2012, pp. 1222–1226.
- [9] A. Hussain, P.-S. Kildal, U. Carlberg, and J. Carlsson, "Correlation between far-field patterns on both sides of the head of two-port antenna on mobile terminal," in *Proc. Int. Symp. Antennas Propag.*, Nanjing, China, 2013, vol. 1, pp. 288–289.
- [10] E. Buskgaard, A. Tatomirescu, S. C. Del Barrio, O. Franek, and G. F. Pedersen, "User effect on the MIMO performance of a dual antenna LTE handset," in *Proc. 8th Eur. Conf. Antennas Propag.*, The Hague, Netherlands, 2014, pp. 2006–2009.
- [11] R. Tian, B. K. Lau, and Z. Ying, "Multiplexing efficiency of MIMO antennas with user effects," in *Proc. IEEE Int. Symp. Antennas Propag.*, Chicago, IL, 2012, pp. 1–2.
- [12] R. Valkonen, J. Ilvonen, K. Rasilainen, J. Holopainen, C. Icheln, and P. Vainikainen, "Avoiding the interaction between hand and capacitive coupling element based mobile terminal antenna," in *Proc. 5th Eur. Conf. Antennas Propag.*, Rome, Italy, 2011, pp. 2781–2785.
- [13] M. Berg, M. Sonkki, and E. T. Salonen, "Absorption loss reduction in a mobile terminal with switchable monopole antennas," *IEEE Trans. Antennas Propag.*, vol. 59, no. 11, pp. 4379–4383, Nov. 2011.
- [14] J. Ilvonen, R. Valkonen, O. Kiveks, P. Li, and P. Vainikainen, "Antenna shielding method reducing interaction between user and mobile terminal antenna," *Electron. Lett.*, vol. 47, no. 16, pp. 896–897, 2011.
- [15] J. Lee, J. Lee, K. Min, and Y. Cheon, "Miniaturized antennas with reduced hand effects in mobile phones using magneto-dielectric material," *IEEE Antennas Wireless Propag. Lett.*, vol. 13, pp. 935–938, 2014.
- [16] A. Andujar, J. Anguera, Y. Cobo, and C. Picher, "Distributed antenna systems for wireless handheld devices robust to hand loading," *IEEE Trans. Antennas Propag.*, vol. 60, no. 10, pp. 4830–4837, Oct. 2012.
- [17] M. R. Islam and M. Ali, "Ground current modification of mobile terminal antennas and its effects," *IEEE Antennas Wireless Propag. Lett.*, vol. 10, pp. 438–441, 2011.
- [18] S. J. Kim *et al.*, "Ground plane with loop structure for reducing user's hand effect," *IEEE Antennas Wireless Propag. Lett.*, vol. 11, pp. 450–452, 2012.
- [19] M. Wu, B. Wang, H. Li, and Y. Yu, "Reducing user effects on mobile handset antennas using mode mapping," in *Proc. 14th Eur. Conf. Antennas Propag.*, Copenhagen, Denmark, 2020, pp. 1–4.
- [20] H. Li, S. Sun, W. Li, M. Wu, and C. Zhou, "Systematic pattern synthesis for single antennas using characteristic mode analysis," *IEEE Trans. Antennas Propag.*, vol. 68, no. 7, pp. 5199–5208, Jul. 2020.
- [21] S. Zhang, K. Zhao, Z. Ying, and S. He, "Adaptive quad-element multi-wideband antenna array for user-effective LTE MIMO mobile terminals," *IEEE Trans. Antennas Propag.*, vol. 61, no. 8, pp. 4275–4283, Aug. 2013.
- [22] I. Vasilev, V. Plicanic, and B. K. Lau, "Impact of antenna design on MIMO performance for compact terminals with adaptive impedance matching," *IEEE Trans. Antennas Propag.*, vol. 64, no. 4, pp. 1454–1465, Apr. 2016.
- [23] I. Vasilev and B. K. Lau, "On user effects in MIMO handset antennas designed using characteristic modes," *IEEE Antennas Wireless Propag. Lett.*, vol. 15, pp. 758–761, 2016.
- [24] J. Felício, J. Biucas-Dias, J. Costa, and C. Fernandes, "Antenna design and near-field characterization for medical microwave imaging applications," *IEEE Trans. Antennas Propag.*, vol. 67, no. 7, pp. 2142–2153, Jul. 2019.
- [25] B. Xiao, H. Wong, B. Wang, and K. L. Yeung, "Effect of the screen to metal-frame smartphone antennas," in *Proc. IEEE Int. Workshop Antenna Technol.*, Miami, FL, USA, 2019, pp. 29–32.
- [26] B. Xiao, H. Wong, D. Wu, and K. L. Yeung, "Metal-frame antenna for big-screen smartphones using characteristic mode analysis," *IEEE Access*, vol. 7, pp. 122224–122231, 2019.
- [27] H. Aliakbari, L. Nie, and B. K. Lau, "Large screen enabled tri-port MIMO handset antenna for low LTE bands," [Online]. Available: <https://doi.org/10.36227/techrxiv.12058776.v1>
- [28] "Specifications | Samsung Galaxy S9 and S9+," The Official Samsung Galaxy Site. [Online]. Available: <https://www.samsung.com/global/galaxy/galaxy-s9/specs/>
- [29] J. Liu, Q. Xue, H. Wong, H. W. Lai, and Y. L. Long, "Design and analysis of a low-profile and broadband microstrip monopolar patch antenna," *IEEE Trans. Antennas Propag.*, vol. 61, no. 1, pp. 11–18, Jan. 2013.
- [30] R. Martens and D. Manteuffel, "Systematic design method of a mobile multiple antenna system using the theory of characteristic modes," *Microw. Antennas Propag.*, vol. 8, no. 12, pp. 887–893, Sep. 2014.
- [31] H. Aliakbari and B. K. Lau, "On modal excitation using capacitive coupling elements and matching network," in *Proc. IEEE Int. Symp. Antennas Propag.*, Atlanta, GA, USA, 2019, pp. 731–732.
- [32] J. Choi, W. Hwang, C. You, B. Jung, and W. Hong, "Four-element reconfigurable coupled loop MIMO antenna featuring LTE full-band operation for metallic-rimmed smartphone," *IEEE Trans. Antennas Propag.*, vol. 67, no. 1, pp. 99–107, Jan. 2019.
- [33] N. Peitzmeier and D. Manteuffel, "Systematic design of an ultra-wideband six-port multi-mode antenna element using symmetry properties of characteristic modes," in *Proc. IEEE Int. Conf. Electromagn. Adv. Appl.*, Granada, Spain, 2019, pp. 466–471.
- [34] T. Y. Shih and N. Behdad, "Bandwidth enhancement of platform-mounted HF antennas using the characteristic mode theory," *IEEE Trans. Antennas Propag.*, vol. 64, no. 7, pp. 2648–2659, Jul. 2016.
- [35] H. Aliakbari, M. Mosalanejad, C. Soens, G. A. E. Vandenbosch, and B. K. Lau, "Wideband SIW-based low-cost multilayer slot antenna array for E-band applications," *IEEE Trans. Compon., Packag., Manuf. Technol.*, vol. 9, no. 8, pp. 1568–1575, Aug. 2019.
- [36] J. Villanen, J. Ollikainen, O. Kiveks, and P. Vainikainen, "Coupling element based mobile terminal antenna structures," *IEEE Trans. Antennas Propag.*, vol. 54, no. 7, pp. 2142–2153, Jul. 2006.

Paper IV

Co-Designed Millimeter-Wave and Sub-6 GHz Antenna for 5G Smartphones

Qiuyan Liang, Hanieh Aliakbari ^{1b}, Graduate Student Member, IEEE, and Buon Kiong Lau ^{1b}, Fellow, IEEE

Abstract—This letter proposes a co-designed millimeter-wave (mm-wave) and sub-6 GHz antenna system. The antenna system consists of four 28 GHz mm-wave arrays with reconfigurable radiation patterns and two sub-6 GHz antennas fed with two corner capacitive coupling elements (CCEs). Each corner CCE is formed by the connected ground planes of two mm-wave arrays in the shared-aperture configuration. The two CCEs are separately matched to cover two sub-6 GHz bands. Each mm-wave array consists of an active patch element and two parasitic patch elements loaded with PIN diodes, realizing 90° beam scanning range with two states of the PIN diodes. The measured results of the fabricated prototype show good agreement with the simulated ones. The prototyped mm-wave arrays cover the band 27.5–28.35 GHz, and each achieves 90° beam scanning at 28 GHz, with measured peak realized gain of 7.9 dBi. The CCE ports cover the two sub-6 GHz bands of 0.79–0.96 GHz and 1.7–5 GHz, with measured isolation of above 17 dB and 20 dB, respectively. The mm-wave band isolation is above 26 dB.

Index Terms—Co-designed antennas, millimeter-wave antennas, reconfigurable antennas, terminal antennas.

I. INTRODUCTION

WITH the widespread adoption of smartphones and the increasing use of bandwidth-hungry apps, there is demand for ever higher data rates in cellular communications. Millimeter wave (mm-wave) technology can facilitate higher data rates, due to more bandwidth being available at higher frequencies [1], [2]. But to compensate for high path loss in mm-wave bands to ensure sufficient coverage area, mm-wave antennas need to form steerable beams with high gains.

One popular approach for mm-wave beam-steering is to use conventional phased array antennas [3]–[7]. However, phase shifters can incur considerable insertion loss and phased array elements can occupy a relatively large volume in a smartphone [8]. To facilitate a compact radiator and avoid the use of phase shifters, a 28 GHz array with parasitic elements is proposed [8]. The beam-steering is realized by shorting the parasitic elements via four transmission lines of different lengths. However, no real switch is used in the measurement and the transmission lines occupy considerable printed circuit board (PCB) space.

Manuscript received 8 May 2022; accepted 31 May 2022. Date of publication 1 July 2022; date of current version 6 October 2022. This work was supported in part by Vetenskapsrådet under Grant 2018-04717. (Corresponding author: Buon Kiong Lau.)

Qiuyan Liang is with the Department of Electrical and Information Technology, Lund University, 22363 Lund, Sweden, and also with the National Key Laboratory of Antenna and Microwave Technology, Xidian University, Xi'an 710071, China (e-mail: qiuyan.liang@eit.lth.se).

Hanieh Aliakbari and Buon Kiong Lau are with the Department of Electrical and Information Technology, Lund University, 22363 Lund, Sweden (e-mail: hea.4080@yahoo.com; bklaui@ieee.org).

Digital Object Identifier 10.1109/LAWP.2022.3187782

To fit multiple antennas working in widely separated bands into the limited space of a smartphone, co-design of the mm-wave antenna and sub-6 GHz antenna has been studied [9]–[17]. In [9] and [10], the mm-wave arrays with feeding networks and the sub-6 GHz antennas (chip antennas/ monopoles) are designed in separate spaces. In [11] and [12], the slot structure acting as an mm-wave connected array is cleverly reused as a defected ground structure to improve the isolation between the sub-6 GHz antennas. However, the array and sub-6 GHz antennas still occupy separate spaces.

To improve aperture utilization, a frequency-reconfigurable slot antenna with a varactor diode working in a fourth-generation (4G) band is reused as an mm-wave antenna based on the connected slot array concept [13]. However, its 4G band is limited to 2.05–2.7 GHz. As another share-aperture approach, the mm-wave array module is embedded into the metal bezel present in some smartphones, with the bezel serving as the sub-6 GHz antenna [14]–[16]. This method helps to reduce the blockage of the mm-wave antenna radiation due to the metallic frame. Similarly, the addition of grating strips facilitates the reuse of the PCB space occupied by a low-band planar inverted-F antenna (PIFA) for implementing an mm-wave antenna array [17]. However, the mm-wave antennas in [14]–[17] are still phased arrays with lossy feeding networks, and some sub-6 GHz antennas (e.g., PIFA) occupy relatively large spaces.

In this letter, a co-designed smartphone antenna system is proposed to accommodate four mm-wave arrays and two sub-6 GHz antennas in a compact space. The mm-wave array employs parasitic elements loaded with PIN diodes to achieve beam-steering, in the same manner as Yagi–Uda antenna [18]. Instead of using self-resonant elements, the sub-6 GHz antennas are excited by non-resonant capacitive coupling elements (CCEs) [19], which are becoming popular to realize low cellular band antennas due to their compactness and simple structure (see [20] and references therein). The metal ground planes of the mm-wave arrays are shared by the corner CCEs that excite the sub-6 GHz bands. This shared-aperture configuration with compact mm-wave arrays on the corner CCEs facilitates sleek integration into 5G smartphones. The fabricated prototype confirms that each mm-wave array can realize 90° scanning range with good impedance matching in the desired frequency band of 27.5–28.35 GHz. Therefore, the four mm-wave arrays on the two CCEs enable full 360° coverage. The two sub-6 GHz antennas are well matched in the operating bands of 0.79–0.96 GHz and 1.7–5 GHz, respectively.

II. CO-DESIGNED ANTENNA SYSTEM

Fig. 1 provides the three-dimensional (3-D) view and top view of the proposed co-designed antenna system. It consists of four

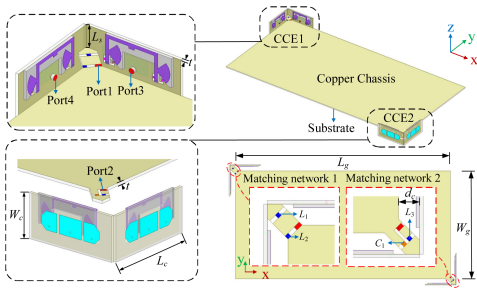


Fig. 1. Overall structure of proposed co-designed antenna ($L_s = 4$ mm, $L_c = 17$ mm, $W_c = 8$ mm, $t = 0.508$ mm, $L_g = 120$ mm, $W_g = 60$ mm, $d_c = 3$ mm).

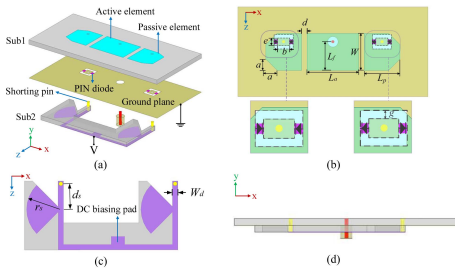


Fig. 2. Geometry of mm-wave array fed by Port3. (a) Three-dimensional exploded view. (b) Top view ($a = 1$ mm, $b = 1.1$ mm, $d = 0.5$ mm, $e = 0.7$ mm, $L_a = 4.6$ mm, $L_f = 2.6$ mm, $L_p = 3.2$ mm, $W = 3.3$ mm, $g = 0.3$ mm). (c) DC biasing lines ($r_s = 1.8$ mm, $d_s = 2.2$ mm, $W_d = 0.6$ mm). (d) Side view.

mm-wave arrays mounted on two corner CCEs and a $120 \text{ mm} \times 60 \text{ mm}$ chassis excited by the two CCEs to cover two sub-6 GHz bands. The proposed antenna system is further described below.

A. MM-Wave Antenna Array

As shown in Fig. 2, the antenna array uses two layers of substrate (Rogers 5880, with thickness of 0.508 mm, relative permittivity of 2.2, and loss tangent of 0.0009) for the radiating layer (Sub1) and the direct current (dc) control layer (Sub2). The array is composed of an active element fed with a 50Ω coaxial cable and two passive elements symmetrically located on two sides of the active element. Each passive element is loaded with two PIN diodes bonded over a square slot etched on the ground. The dc biasing lines are printed on the bottom layer of Sub2. Two shorting pins connect the dc biasing lines, the passive elements and the metal sheets within the etched slots. The two sets of PIN diodes for the two passive elements are installed with opposite bias directions and their dc biasing lines with isolation fan stubs are connected in parallel to share a dc feeding pad. The opposite bias ensures that, when a dc voltage is applied, the PIN diodes of one passive element will always be in the opposite state to those of the other passive element (i.e., ON and OFF states for passive elements 1 and 2, respectively, or vice-versa). The PIN diodes, produced by MACOM (Model no. MA4GP907), allow for operation up to millimeter frequencies [21]. Its equivalent circuits for the ON and OFF states in mm-wave bands, as shown in Fig. 3, were used in the simulation model, where the insertion

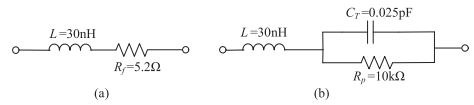


Fig. 3. Equivalent circuits of PIN diode in (a) ON state and (b) OFF state.

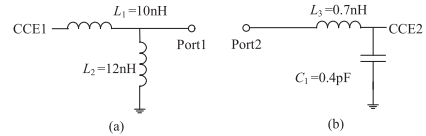


Fig. 4. Schematics of matching networks for (a) CCE1 and (b) CCE2.

loss of the PIN diode in the ON and OFF state is modeled with a 5.2Ω and a $10 \text{ k}\Omega$ resistor, respectively.

The parasitic element is connected to/disconnected from the ground plane when the beneath PIN diodes are turned ON/OFF, which decreases/increases its effective electrical size, such that it acts as a director/reflector [22]. The beam of this array is steered to the director and away from the reflector based on the principle of Yagi-Uda antenna. By applying positive or negative dc voltage between the dc biasing pad and the ground, two symmetrical beams can be achieved.

The effects of the structural parameters were investigated using ANSYS HFSS 2021. The simulation results show that the beam deflection angle and sidelobe level (SLL) are mainly dependent on the size of the parasitic elements (controlled by a) and the distance between the parasitic elements and the active one (d) [see Fig. 2(b)]. For example, decreasing a or increasing d will lead to increased beam deflection angle and SLL, as well as narrower main beam. The appropriate a and d values were then optimized to obtain $\pm 45^\circ$ beam deflection (i.e., mirror symmetric beams for the two possible states of the diodes) and low SLL. The impedance bandwidth of the antenna becomes wider when d decreases, which is because of that a second (higher) resonance is introduced by the parasitic element in the ON state. Considering the radiation pattern performance and the fabrication tolerance requirements, the distance $d = 0.5$ mm was finally chosen.

B. Sub-6 GHz Antennas

Since the CCE should be placed in the region of maximum electric field maximum strength of the mode to be excited (i.e., the fundamental dipole mode) [23], two CCEs are placed at two diagonally opposite corners of the chassis. In addition, these corner locations enable the four mm-wave antennas on the two CCEs to cover the entire field of view and mitigate blockage from the user's hand(s). CCE1 and CCE2 excite the chassis through matching networks (see Figs. 1 and 4) designed in Betamatch [24] to realize two sub-6 GHz antennas, i.e., Ports 1 and 2 cover the low band (LB) of 0.79–0.96 GHz and the high band (HB) of 1.71–5 GHz, respectively. A larger CCE size facilitates broader bandwidth of Port1, thus the CCE parameters are chosen considering the tradeoff between the bandwidth and size [25]. The bandwidth of Port1 and the isolation between Port1 and Port2 in the LB mainly depend on the inductance L_1 . With decreasing L_1 , the LB bandwidth increases whereas the Port1-Port2 isolation decreases. To achieve a good tradeoff between bandwidth and



Fig. 5. Proposed antenna system with metal frame.

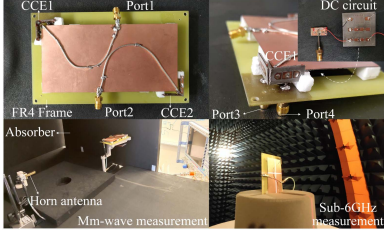


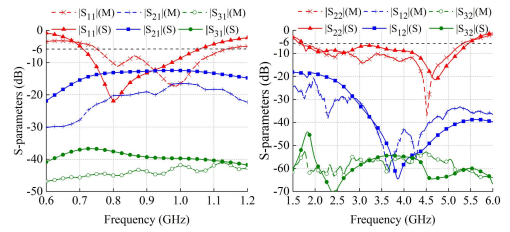
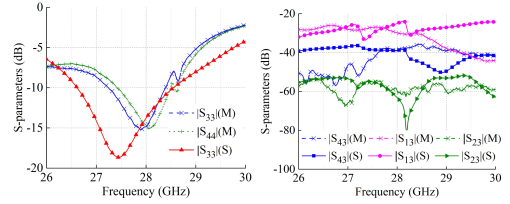
Fig. 6. Prototype of proposed antenna system and measurement setups.

isolation, the matching elements in matching network 1 were chosen to be $L_1 = 10$ nH and $L_2 = 12$ nH. The bandwidth of Port2 in the HB mainly depends on the capacitance value C_1 . The Port1-Port2 isolation in HB is not significantly affected by the matching elements. The optimized matching elements in matching network 2 are $C_1 = 0.4$ pF and $L_3 = 0.7$ nH. It is noted that the loading effect of the mm-wave connectors has been included in the design of matching networks, to facilitate experimental validation. In practice, these connectors are not needed and the matching network can be updated by changing the matching circuit parameter values (e.g., $L_1 = 18$ nH and $L_2 = 10$ nH for port 1). Moreover, more matching elements can give a larger Port2 bandwidth (e.g., 1.37–6.71 GHz using five elements) [24].

In practical applications, smartphones are equipped with a touch screen and some come with metal bezels (side frames). It is found that adding a metal plate (of the same size as the chassis) 4 mm above the chassis (and grounded through a shorting pin at the chassis center) to model the screen does not affect the fundamental mode of the chassis [26], and the impedance matching in the sub-6 GHz bands can be restored by updating the matching networks. To study the effect of metal bezels, four separate vertical metal strips of 8 mm width were located along (but not connected to) the four sides of the chassis, as depicted in Fig. 5. When the distance d_1 between the strips and the CCE1 is larger than 5 mm (0.015 wavelength in free space at 0.875 GHz), Port1 retains over 90% of the original bandwidth (i.e., the case with no strip). The distance d_2 for the CCE2 to retain at least 90% of the original bandwidth is 2 mm (0.023 wavelength in free space at 3.5 GHz).

III. SIMULATED AND MEASURED RESULTS

A prototype of the smartphone antenna system was fabricated (see Fig. 6). The mm-wave CAB.058 coaxial cables are used to feed the mm-wave arrays on CCE1 in the measurement, which are intended to verify the beam scanning range of the mm-wave arrays on each CCE. In real implementation, the feeding of the mm-wave antenna should be realized with more advanced integrated technology to minimize any possible interference. The dc voltage is applied through a substrate with the dc circuits,

Fig. 7. Simulated (S) and measured (M) S -parameters of sub-6 GHz antennas.Fig. 8. Simulated (S) and measured (M) S -parameters of mm-wave array.

which is attached to the back side of the chassis. An FR4 frame is designed to support the antennas in the measurement.

A. S -Parameters

Fig. 7 shows the S -parameter results of the two sub-6 GHz antennas. The measured 6 dB impedance bandwidth (VSWR of 3:1) of Port1 is 0.38 GHz (0.75–1.13 GHz), covering the LTE800/850/900 bands. In the operating band (i.e., LB), the measured isolation of the sub-6 GHz ports $|S_{21}|$ is larger than 17 dB and that between Port1 and mm-wave port Port3 $|S_{31}|$ is larger than 43 dB. The measured 6 dB impedance bandwidth of Port2 is 3.6 GHz (1.70–5.30 GHz), covering the LTE1700-2600 and 5G NR n77-79 bands. In this upper band (i.e., HB), the measured isolations with other ports are over 20 dB.

The S -parameter results of the mm-wave array are shown in Fig. 8. Port3 and Port4 have the same simulation results for reflection coefficient due to symmetry. The simulated 10 dB bandwidth of the mm-wave antenna is around 2 GHz (26.56–28.54 GHz). It is noted that, if needed, the mm-wave antenna bandwidth can be significantly enhanced (e.g., to 3 GHz) by using a stacked patch as the active element. The measured resonances are slightly higher than those in simulation and the measured bandwidths are narrower than the simulated ones, due to the tolerance in the soldering of the mm-wave cables. Such discrepancy is common in mm-wave bands due to the relatively small wavelengths [13]–[17]. The measured 10 dB bandwidths of Port3 and Port4 are 1.15 GHz (27.25–28.4 GHz) and 1.1 GHz (27.4–28.5 GHz), respectively, covering the 5G NR n261 band. In the operating mm-wave band, the measured isolations with other ports are over 26 dB.

B. Radiation Patterns

The radiation pattern results of the fabricated prototype in the sub-6 GHz bands were obtained from a SATIMO multiprobe spherical near-field system [27]. Fig. 9 shows the normalized simulated and measured 2-D pattern cuts at $\theta = 90^\circ$ (azimuth cut), $\varphi = 0^\circ$ (elevation cut), and $\varphi = 90^\circ$ (elevation cut) for Port1

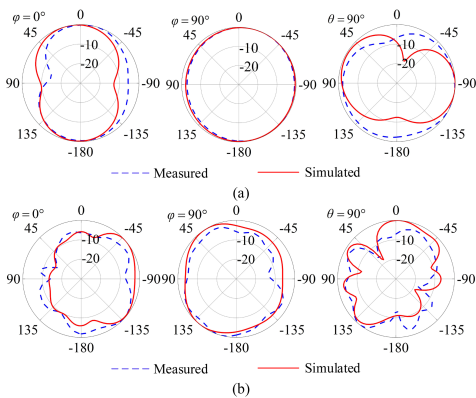


Fig. 9. Simulated and measured normalized radiation patterns at sub-6 GHz band in (a) LB (0.875 GHz) and (b) HB (3.5 GHz).

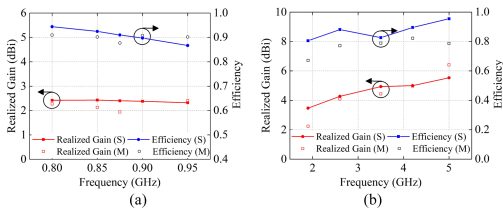


Fig. 10. Simulated (S) and measured (M) realized gain and efficiency in sub-6 GHz in (a) LB and (b) HB.

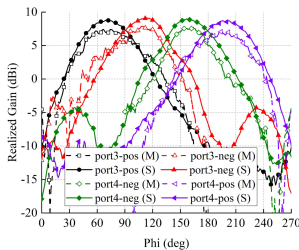


Fig. 11. Simulated (S) and measured (M) radiation patterns of mm-wave arrays with positive (pos) and negative (neg) voltage at 28 GHz.

and Port2 at 0.875 GHz in LB and 3.5 GHz in HB, respectively. The fundamental mode of the chassis is excited by the CCEs in the two sub-6 GHz antennas.

The discrepancies between the simulated and measured patterns are primarily due to the presence of a feed cable in the near field of the structure. The simulated and measured realized gain and efficiency in the sub-6 GHz bands are shown in Fig. 10. The measured efficiencies are higher than the simulated ones at some frequency points due to the discrepancies between the measured and simulated S -parameters.

Fig. 11 shows the radiation patterns of two mm-wave arrays on CCE1 at 28 GHz, which were measured with an in-house pattern measurement system utilizing the Rohde & Schwarz vector network analyzer ZVA67. Applying the positive/negative voltages on the dc biasing pads of the two mm-wave arrays,

TABLE I
COMPARISON BETWEEN THE PROPOSED AND PREVIOUS 4G/5G DESIGNS

	Frequency range (GHz)	Total antenna volume (mm ³)	Phased array (mm-wave)	Diodes
[13]	2.05-2.7 and 23-29	35×12.28×0.381	yes	yes
[14]	0.7-0.96, 1.71-2.69 and 25-30	75×10×7	yes	no
[16]	0.76-0.98, 1.24-2.87, and 22-28.4	21.7×7.75×0.64	Active and dummy elements	no
[17]	0.74-0.96, 1.7-2.2, and 22-31	70×9×0.764	yes	no
This work	0.75-1.13, 1.7-5.3 and 27.5-28.35	34×8×1.016×2	no	yes

four deflected beams were realized. The two mm-wave arrays on CCE1 can achieve 180° coverage range with half power beamwidth. The peak measured realized gains are 7.4 dBi or 7.9 dBi (Port3 with positive or negative voltage) and 7.1 dBi or 7.7 dBi (Port4 positive or negative voltage). The peak measured realized gains are less than the simulated ones by 1.4 dBi (Port3 positive), 1.2 dBi (Port3 negative), 1.6 dBi (Port4 positive), and 1.3 dBi (Port4 negative), respectively. The realized gain difference is primarily due to the loss in the mm-wave cables and slight pattern shape discrepancy, the latter of which was caused by inaccuracies in the PIN diode’s equivalent circuits and the tolerance of the measurement system.

C. Comparison With Other Sub-6 GHz/mm-Wave Antennas

A comparison of recent co-designed antennas for sub-6 GHz and mm-wave bands is presented in Table I. The sub-6 GHz antennas in [14] and [17] employ self-resonance structures, which occupy larger volumes. Phased arrays, which require feeding networks, are used for the mm-wave antennas in [13], [14], and [17]. The proposed antenna system can cover wider sub-6 GHz bands despite the use of two compact CCEs. With the parasitic elements, the proposed mm-wave array achieves beam scanning without the need for complex feeding networks. Moreover, the shared-aperture configuration of the corner CCEs and mm-wave arrays enables a compact antenna volume.

IV. CONCLUSION

A co-designed mm-wave and sub-6 GHz antenna system for 5G smartphone application are proposed in this letter. Each mm-wave array antenna uses two parasitic elements loaded with PIN diodes to realize beam scanning. The four mm-wave arrays share the aperture of the CCEs, with the latter providing coverage of two sub-6 GHz bands, which facilitates a compact antenna structure. The measured results show that the sub-6 GHz antennas cover the bands of 0.79–0.96 GHz and 1.71–5 GHz. The mm-wave array provides 90° scanning range with measured realized gain of up to 7.9 dBi at 28 GHz. Possible future work includes adding ports in the sub-6 GHz bands for MIMO operation by means of creating and exciting more resonant modes [20] as well as using more parasitic elements and reconfigurable states for higher gain in mm-wave bands.

ACKNOWLEDGMENT

The authors would like to thank A. Johansson of Lund University and D. Pugachev of Sigma Connectivity for their help in prototype fabrication and pattern measurement.

REFERENCES

- [1] T. S. Rappaport, et al., "Millimeter wave mobile communications for 5G cellular: It will work!," *IEEE Access*, vol. 1, pp. 335–349, 2013.
- [2] W. Hong, K.-H. Baek, and S. Ko, "Millimeter-wave 5G antennas for smartphones: Overview and experimental demonstration," *IEEE Trans. Antennas Propag.*, vol. 65, no. 12, pp. 6250–6261, Dec. 2017.
- [3] N. Ojaroudiparchin, M. Shen, S. Zhang, and G. F. Pedersen, "A switchable 3-D-coverage-phased array antenna package for 5G mobile terminals," *IEEE Antennas Wireless Propag. Lett.*, vol. 15, pp. 1747–1750, 2016.
- [4] S. Zhang, X. Chen, I. Strytsin, and G. F. Pedersen, "A planar switchable 3-D-coverage phased array antenna and its user effects for 28-GHz mobile terminal applications," *IEEE Trans. Antennas Propag.*, vol. 65, no. 12, pp. 6413–6421, Dec. 2017.
- [5] I. Strytsin, S. Zhang, G. F. Pedersen, and A. S. Morris, "Compact quad-mode planar phased array with wideband for 5G mobile terminals," *IEEE Trans. Antennas Propag.*, vol. 66, no. 9, pp. 4648–4657, Sep. 2018.
- [6] W. Hong, K. Baek, Y. Lee, and Y. G. Kim, "Design and analysis of a low-profile 28 GHz beam steering antenna solution for future 5G cellular applications," in *Proc. IEEE MTT-S Int. Microw. Symp.*, 2014, pp. 1–4.
- [7] N. Ojaroudiparchin, M. Shen, and G. F. Pedersen, "A 28 GHz FR-4 compatible phased array antenna for 5G mobile phone applications," in *Proc. Int. Symp. Antennas Propag.*, 2015, pp. 1–4.
- [8] S. Zhang, I. Strytsin, and G. F. Pedersen, "Compact beam-steerable antenna array with two passive parasitic elements for 5G mobile terminals at 28 GHz," *IEEE Trans. Antennas Propag.*, vol. 66, no. 10, pp. 5193–5203, Oct. 2018.
- [9] C. Lee, M. K. Khattak, and S. Kahng, "Wideband 5G beamforming printed array clutched by LTE-A 4×4 -multiple-input-multiple-output antennas with high isolation," *Microw., Antennas Propag.*, vol. 12, no. 8, pp. 1407–1413, Mar. 2018.
- [10] R. Hussain, A. T. Alreshaid, S. K. Podilchak, and M. S. Sharawi, "Compact 4G MIMO antenna integrated with a 5G array for current and future mobile handsets," *Microw., Antennas Propag.*, vol. 11, no. 2, pp. 271–279, Jan. 2017.
- [11] M. Ikram, R. Hussain, and M. S. Sharawi, "4G/5G antenna system with dual function planar connected array," *Microw., Antennas Propag.*, vol. 11, no. 12, pp. 1760–1764, Sep. 2017.
- [12] M. S. Sharawi, M. Ikram, and A. Shamim, "A two concentric slot loop based connected array MIMO antenna system for 4G/5G terminals," *IEEE Trans. Antennas Propag.*, vol. 65, no. 12, pp. 6679–6686, Dec. 2017.
- [13] M. Ikram, E. A. Abbas, N. Nguyen-Trong, K. H. Sayidmarie, and A. Abbosh, "Integrated frequency-reconfigurable slot antenna and connected slot antenna array for 4G and 5G mobile handsets," *IEEE Trans. Antennas Propag.*, vol. 67, no. 12, pp. 7225–7233, Dec. 2019.
- [14] J. Kurvinen, H. Kähkönen, A. Lehtovuori, J. Ala-Laurinaho, and V. Viikari, "Co-designed mm-wave and LTE handset antennas," *IEEE Trans. Antennas Propag.*, vol. 67, no. 3, pp. 1545–1553, Mar. 2019.
- [15] R. M. Moreno, J. Ala-Laurinaho, A. Khripkov, J. Ilvonen, and V. Viikari, "Dual-polarized mm-wave endfire antenna for mobile devices," *IEEE Trans. Antennas Propag.*, vol. 68, no. 8, pp. 5924–5934, Aug. 2020.
- [16] R. Rodriguez-Cano, S. Zhang, K. Zhao, and G. F. Pedersen, "mm-wave beam-steerable endfire array embedded in a slotted metal-frame LTE antenna," *IEEE Trans. Antennas Propag.*, vol. 68, no. 5, pp. 3685–3694, May 2020.
- [17] M. M. S. Taheri, A. Abdipour, S. Zhang, and G. F. Pedersen, "Integrated millimeter-wave wideband end-fire 5G beam steerable array and low-frequency 4G LTE antenna in mobile terminals," *IEEE Trans. Veh. Technol.*, vol. 68, no. 4, pp. 4042–4046, Apr. 2019.
- [18] J. Huang and A. C. Densmore, "Microstrip Yagi array antenna for mobile satellite vehicle application," *IEEE Trans. Antennas Propag.*, vol. 39, no. 7, pp. 1024–1030, Jul. 1991.
- [19] J. Villanen, J. Ollikainen, O. Kivekas, and P. Vainikainen, "Coupling element based mobile terminal antenna structures," *IEEE Trans. Antennas Propag.*, vol. 54, no. 7, pp. 2142–2153, Jul. 2006.
- [20] H. Aliakbari and B. K. Lau, "Low-profile two-port MIMO terminal antenna for low LTE bands with wideband multimodal excitation," *IEEE Open J. Antennas Propag.*, vol. 1, pp. 368–378, 2020.
- [21] MACOM, "MA4GP907: GaAs flip chip PIN," 2022. Accessed: May 8, 2022. [Online]. Available: <https://www.macom.com/products/product-detail/MA4GP907>
- [22] W.-Q. Deng, X. Yang, C.-S. Shen, J. Zhao, and B.-Z. Wang, "A dual-polarized pattern reconfigurable Yagi patch antenna for microbase stations," *IEEE Trans. Antennas Propag.*, vol. 65, no. 10, pp. 5095–5102, Oct. 2017.
- [23] R. Valkonen, M. Kaitiokallio, and C. Icheln, "Capacitive coupling element antennas for multi-standard mobile handsets," *IEEE Trans. Antennas Propag.*, vol. 61, no. 5, pp. 2783–2791, May 2013.
- [24] MNW Scan, "Betamatch," Version 3.7.6, 2019. Accessed: May 8, 2022. [Online]. Available: <http://www.mnw-scan.com>
- [25] H. Aliakbari and B. K. Lau, "Impact of capacitive coupling element design on antenna bandwidth," in *Proc. 12th Eur. Conf. Antennas Propag.*, 2018, pp. 1–4.
- [26] H. Aliakbari, L. Y. Nie, and B. K. Lau, "Large screen enabled tri-port MIMO handset antenna for low LTE bands," *IEEE Open J. Antennas Propag.*, vol. 2, pp. 911–920, 2021.
- [27] MVG, "SATIMO is MVG," 2022. Accessed: May 8, 2022. [Online]. Available: <https://www.mvg-world.com/en/satimo-is-mvg>

Paper V

Wideband SIW-Based Low-Cost Multilayer Slot Antenna Array for *E*-Band Applications

Hanieh Aliakbari^{1b}, *Graduate Student Member, IEEE*, Mohammad Mosalanejad, *Student Member, IEEE*,
Charlotte Soens, *Member, IEEE*, Guy A. E. Vandenbosch^{1b}, *Fellow, IEEE*,
and Buon Kiong Lau^{1b}, *Senior Member, IEEE*

Abstract—This paper proposes a substrate integrated waveguide (SIW) slot antenna array for the wideband gigabyte mobile radio application in the *E*-band. The wideband unit cell design is based on simultaneous feeding of four-element radiation slots with a higher order cavity mode directly excited by a simple slot aperture fed by a microstrip fork-like tuning stub. Employing the higher order mode along with the slot aperture facilitates low loss, simple feeding network, and lower sensitivity to fabrication errors. To cancel the beam tilt versus frequency, the higher-order-mode unit cell is used in a 2×2 array along with a differential feeding structure. The array was designed and taped out using a new high-resolution multilayer printed circuit board (PCB) technology and characterized by using the constructed millimeter-wave (mm-wave) measurement setup at KU Leuven/imec. This technology provides the possibility to stack microvias in PCBs and reduces the fabrication cost compared to other multilayer technologies in mm-wave bands. The proposed array in 2×2 array configuration has a measured bandwidth of 11.4 GHz (16%), a total efficiency of 69%, a realized gain of 12 dBi at 72 GHz, and a 3-dB gain bandwidth that covers the entire impedance bandwidth. In comparison with existing *E*-band SIW slot arrays (compensating for array sizes), the proposed design achieves similar or better performance in bandwidth but with lower cost, lower sensitivity to fabrication tolerances, and higher total efficiency.

Index Terms—Advanced multilayer printed circuit board (PCB), differential-fed antenna array, *E*-band, substrate integrated waveguide (SIW) cavity higher order mode.

I. INTRODUCTION

DUE to the large available bandwidth, a broad range of applications is rapidly emerging in millimeter-wave (mm-wave) bands [1]. In particular, the first implementable

fifth-generation (5G) standard for mobile communications, i.e., 5G New Radio (NR), includes the use of mm-wave to deliver robust mobile broadband access [2]. Furthermore, for the higher part of mm-wave bands, ITU has allocated unlicensed/lightly licensed spectra in the 60-/70-/80-GHz bands, intended for a number of applications such as fixed cellular backhaul links, broadband local area networks (LANs), and potential 5G systems with multi-gigabyte data rate [3]. One important criterion to ensure marketplace adoption of wireless systems in this band is the availability of low-cost and mass-producible antennas.

Recently, the CMOS technology capable of low-cost mass production is introduced for the mm-wave transceiver implementation. Thus, the practical realization of an antenna array for mm-wave relies on a suitable interface between the active circuits and the antenna, and it is important to choose an antenna fabrication technology that is easy to integrate with the mm-wave integrated silicon transceiver. Smaller dimensions of antennas in the *E*-band than the conventional 60 GHz or lower bands allow the antennas to be comparable in size with the active circuit blocks (e.g., processor, memory, and radio). This has led to on-chip antennas (OCAs) on standard silicon substrates [4], [5] to eliminate the need for a circuit-antenna interface. However, these antennas do not work very well (e.g., ~ -8.5 -dBi gain at 79 GHz [5]) because of the high permittivity (~ 11.7) and low resistivity ($\sim 10 \Omega \cdot \text{cm}$) of silicon substrate. Other main *E*-band antenna fabrication technologies are low temperature co-fired ceramic (LTCC), liquid crystal polymer (LCP), and printed circuit boards (PCBs) [6]. The LTCC technology has more design freedom with via placement and tight tolerance. However, the antenna in package (AIP) on LTCC substrate is less attractive in the *E*-band because of its high cost and considerable loss caused by the relatively high dielectric constant of the LTCC substrate [7]. Although LCP [8] is cheaper than LTCC, both of them have a long production cycle. On the other hand, for the conventional PCB technology, the minimum spacing and diameter of the machine drilled vias are electrically large in the *E*-band, and the impact of fabrication errors becomes more severe. The above considerations motivate the urgent need for a new or improved *E*-band antenna technology that is both low-cost and low-loss.

Manuscript received October 2, 2018; revised March 7, 2019; accepted March 27, 2019. Date of publication April 11, 2019; date of current version September 3, 2019. This work was supported by the Inter-University Microelectronics Center (imec), Leuven, Belgium. Recommended for publication by Associate Editor Y.-K. Yoon upon evaluation of reviewers' comments. (Corresponding author: Hanieh Aliakbari.)

H. Aliakbari and B. K. Lau are with the Department of Electrical and Information Technology (EIT), Lund University, 221 00 Lund, Sweden (e-mail: hanieh.aliakbari_abar; buon_kiong.lau@eit.lth.se).

M. Mosalanejad and C. Soens are with the Inter-University Microelectronics Center (imec), 3001 Leuven, Belgium (e-mail: mohammad.mosalanejad@esat.kuleuven.be; charlotte.soens@imec.be).

G. A. E. Vandenbosch is with the Electrical Engineering Department (ESAT), KU Leuven, 3001 Leuven, Belgium (e-mail: guy.vandenbosch@kuleuven.be).

Color versions of one or more of the figures in this article are available online at <http://ieeexplore.ieee.org>.

Digital Object Identifier 10.1109/TCPMT.2019.2910385

2156-3950 © 2019 IEEE. Personal use is permitted, but republication/redistribution requires IEEE permission. See http://www.ieee.org/publications_standards/publications/rights/index.html for more information.

In the higher part of mm-wave bands, substrate integrated waveguide (SIW) has become a key technology in the realization of antennas. This is because it has the advantages of rectangular waveguide features, such as lower loss in mm-wave and ease of connection to active components and coplanar waveguide (CPW) lines. Several SIW-based antenna structures have been proposed for the *E*-band [3], [8]–[14]. In [9], longitudinal slots are utilized to feed circular patches. However, the used resonant feeding technique leads to a narrow bandwidth. On the other hand, the SIW-fed antipodal linearly tapered slot antenna in [8] has a large operating bandwidth, but its endfire radiation characteristic limits its application in wireless communications since the broadside radiation pattern is often required. Moreover, the proposed design cannot be extended for planar 2-D array application. In [10], the fundamental cavity mode is used in the proposed 8×8 slot array, resulting in a substantial insertion loss (~ 3 dB) of the mode excitation feeding network at 60 GHz. In the same way, the 4×4 slot array reported in [12] provides low total efficiency in the *E*-band (i.e., $\sim 38\%$) because of the use of a large and lossy feeding network. A more simplified antenna feeding network is reported for the fundamental mode cavity in [11], and all resonant cavities are connected with inductive windows. However, the achieved bandwidth, considering both gain and impedance, is relatively small (i.e., $\sim 10\%$) [3], [13], [14].

In comparison with arrays that utilize the fundamental cavity mode, arrays that utilize higher order mode(s) can provide simpler feeding structure. Most existing SIW antennas that utilize higher order mode(s) are designed for lower bands [15]–[17]. However, the feeding network used for the excitation of the mode is still complex in [15], and the impedance bandwidth is small ($\sim 5.5\%$). In addition, the direct excitation probe feed used in [16] and [17] is not suitable for integration with active circuits in higher mm-wave bands.

This paper focuses on the design and implementation of wideband and simple-feed SIW slot antenna array suitable for the *E*-band applications by using an advanced low-cost PCB technology. To realize the boresight radiation and simple feed in the unit cell, two parallel higher-order-mode resonant cavities are simultaneously excited in a wide bandwidth, only by a slot aperture and a modified 50- Ω line. The aperture excitation is utilized rather than direct feed for better circuit integration in this frequency band. Using the TE_{201} mode in the unit cell simplifies the lossy power divider network in larger slot array design and also reduces the number of SIW metal posts, which reduces the metal loss and fabrication cost in the *E*-band. Moreover, using TE_{201} facilitates relaxed fabrication tolerance and higher accuracy, leading to enhanced stability in performance, properties that are more important in the *E*-band than lower frequencies. A differential feeding network is also designed and utilized to mitigate the beam deviation problem in [16]. The measured results of the fabricated unit cell and 2×2 array in the mm-wave measurement setup agree well with the full-wave simulation results.

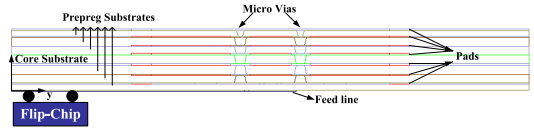


Fig. 1. Schematic of an advanced multilayer PCB technology connected to the MMIC for system-level assembly by solder bump flip-chip technology.

TABLE I
PROPERTIES SPECIFICATIONS OF THE “ANY-LAYER
HDI PCB TECHNOLOGY”

Material	Dielectric constant	Tangent delta	Thickness (um)
Copper 8 (cavity bottom layer)			23
Sub7: Prepreg Substrate (metal post)	3.26	0.006	60
Copper 7 (internal plane 3)			16
Sub6: Prepreg Substrate (metal post)	3.22	0.006	104
Copper 6 (Signal)			16
Sub5: Prepreg Substrate (metal post)	3.22	0.006	104
Copper 5 (Signal)			23
Sub4: Laminate core substrate (metal post)	3.37	0.006	100
Copper 4 (internal plane 2)			23
Sub3: Prepreg Substrate (metal post)	3.22	0.006	104
Copper 3 (Signal)			16
Sub2: Prepreg Substrate (metal post)	3.22	0.006	104
Copper 2 (internal plane 1 and slots)			16
Sub1: Prepreg Substrate	3.25	0.006	60
Copper 1 (modified microstrip line)			23

II. ADVANCED MULTILAYER PCB TECHNOLOGY

A PCB with eight-layer stack-up, as shown in Fig. 1, is used in this paper. This stack-up has seven Panasonic Megtron 6 substrates [18] and eight metal layers, with the properties listed in Table I. The substrate properties were characterized by measurement at 50 GHz. To the best of the authors’ knowledge, these measured properties are the closest available in frequency to the *E*-band. Internal planes 1, 2, and 3 are ground planes, and others are signal planes. This PCB technology is called “any-layer high definition interconnect (HDI) PCB technology,” and it is the most advanced PCB technology in the world, with very high resolution down to 40- μm linewidth [19].

The “any-layer HDI PCB technology” is an improvement of the standard multilayer PCB technology [20], which is significantly more cost-effective than LTCC. In this technology, laser-drilled stacked microvias are used instead of machine drilled vias in the standard PCB technology, for all electrical connections between the two nonstacked metal layers in Fig. 1. In general, conventionally blind or through holes are replaced by copper-filled microvias of significantly smaller dimensions: The minimum hole and pad size of machine drilled vias are 200 and 400 μm , while for laser-drilled microvias are 75 and 175 μm . This means that each layer or connection on a specific layer can be connected with every other layer within the PCB stack-up without using big via holes, resulting in space saving and increased routing density for a given product dimension. The pad sizes are 0.23 mm. Microvias are cone-shaped [see Figs. 1 and 3(a)] with approximate large and small diameters of 0.075–0.14 and 0.055–0.1 mm, respectively.

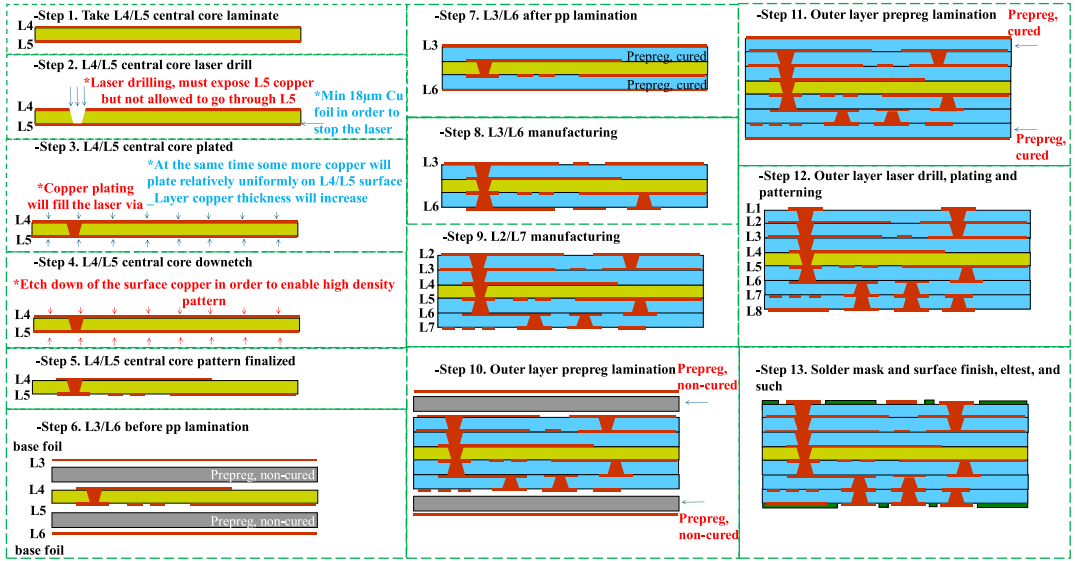


Fig. 2. 13 steps in the fabrication process of “any-layer PCB technology” [21].

The steps of the fabrication process are summarized in Fig. 2 [21]. The process starts with the core layer (i.e., fourth layer in Table I). The “prepreg” substrates work as glue to paste substrates together, so first, they are cured (melted), and then they are laminated on the previously laminated substrates. After curing (when the prepreg substrates become cold), then substrates are ready for the mapping of metal routes or the making of laser-drilled microvias through them.

This technology has a high resolution close to LTCC and can be used for the mm-wave applications up to 100 GHz. Since this technology has lower tape-out cost and fewer fabrication difficulties than other technologies at mm-wave bands (e.g., LTCC and LCP), it is attracting significant interest in the industry

III. CAVITY-BACKED UNIT CELL DESIGN

Fig. 3(a) and (b) shows the simulated electric field (E -field) and magnetic field (H -field) distribution along the yz and xy cross sections of a cavity operating in the TE_{201} mode, respectively. The simulation was performed with Ansys HFSS 15's finite-element solver. The xz plane of the cavity in Fig. 3 can be considered as a virtual ground plane, and the cavity is separated into two independent cavities. According to the waveguide theory [22], the resonant frequency of the TE_{201} mode in the aforementioned resonant cavity is

$$f_{TE_{201}} = \frac{ck_{TE_{201}}}{2\pi\sqrt{\mu_r\epsilon_r}} = \frac{c}{2\pi\sqrt{\mu_r\epsilon_r}} \sqrt{\left(\frac{2\pi}{L}\right)^2 + \left(\frac{\pi}{W}\right)^2} \quad (1)$$

where μ_r and ϵ_r are the equivalent relative permeability and permittivity of one multilayer cavity substrate, respectively. c is the speed of light, and $k_{TE_{201}}$ is the effective wavenumber.

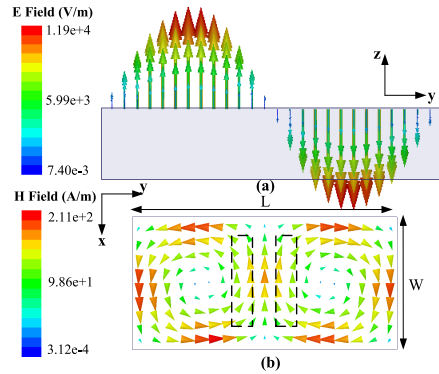


Fig. 3. (a) E -field and (b) H -field distributions of the TE_{201} mode, along yz and xy cross sections of the cavity as an elementary unit cell, respectively.

L and W are the length and the width of the corresponding resonant cavity in Fig. 3. The field distribution of TE_{201} mode in the cavity is given by [22]

$$E_x = E_y = H_z = 0 \quad (2)$$

$$E_z = E_0 \sin(2\pi y/L) \cdot \sin(\pi x/W) \quad (3)$$

$$H_x = j\pi E_0/k\eta L \cdot \cos(2\pi y/L) \cdot \sin(\pi x/W) \quad (4)$$

$$H_y = -jE_0/Z_{TE} \cdot \sin(2\pi y/L) \cdot \cos(\pi x/W) \quad (5)$$

which show that the fields in the cavity form standing waves. E_0 is the amplitude constant. When two slots are approximately etched on the top of the TE_{201} mode resonant cavity, as shown in Fig. 3(b), one elementary unit cell

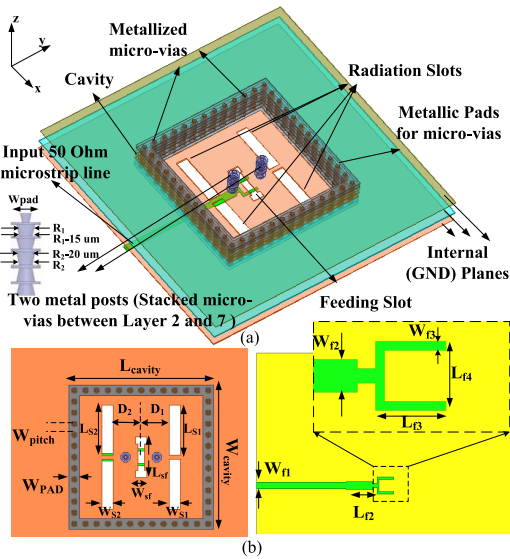


Fig. 4. Unit cell slot antenna structure comprised two parallel TE_{201} resonant cavities. (a) Perspective view and (b) top view with design parameters. The corresponding layers are listed in Table I.

(of 1×2 slot elements) can be realized without the need for any power divider to individually feed the independent cavities. Based on this principle, two parallel TE_{201} -mode resonant cavities and four slots are embedded in the stack-up of Fig. 1, and the resulting antenna can be regarded as a new unit cell consisting of two side-by-side 1×2 slot array, 1-D antenna unit cells on the yz plane. The layout of the four-element slot antenna (one-unit cell) is illustrated in Fig. 4. Here, the effective length/width (i.e., L_{cavity}/W_{cavity}) of the whole resonant cavity is chosen to be one guided wavelength of the resonant frequency ($=c/(f_{TE_{201}}(\mu_r \epsilon_r)^{1/2})$) to support the TE_{201} mode in each resonant cavity. As depicted in Fig. 4(a), the input microstrip line is etched on the first copper layer of the PCB in Table I, whereas the first internal plane forms the ground plane. The higher-order-mode resonant cavity is located at the top of the internal plane 1, and the cavity's side walls are formed by rows of stacked microvias between the internal plane 1 and copper 8 layer. It is noteworthy that by using the cavity microvias in Fig. 3(a), the resulting TE_{201} mode is not as perfect as the cavity with solid planes, especially at higher frequencies, thus (1)–(3) offer only approximations of the real values.

A small H-shaped coupling slot aperture is cut at the center of the internal plane 1, which effectively couples the energy from the modified microstrip line to the cavity. In this way, the two parallel TE_{201} resonant cavities are simultaneously excited by the single-slot aperture without the need for any complex power divider to individually feed the four radiating resonant slots. In order to improve the front-to-back ratio (FTBR) of the array, the resonant slots are

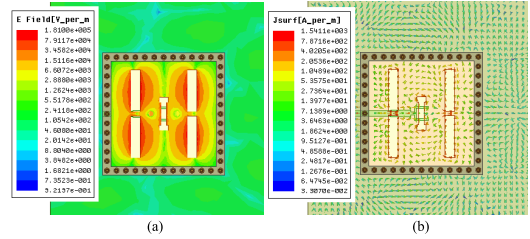


Fig. 5. (a) E -field magnitude distribution and (b) current vector distribution at 73 GHz. (For clarity only internal plane 1 is shown.)

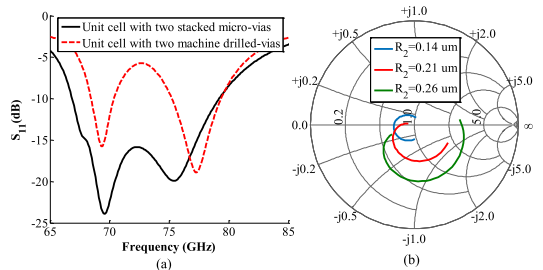


Fig. 6. (a) Simulated S_{11} of the unit cell with two stacked microvias in comparison with the machine-drilled vias and (b) impact of a different R_2 on S_{11} in the Smith chart over 71–76 GHz.

located on the same side with the aperture coupling slot [23]. The antenna is fed by a $50\text{-}\Omega$ microstrip line followed by a fork-shaped feeding structure, positioned symmetrically with respect to the centerline of the yz plane. The fork-shaped feed comprises one horizontal and two vertical stubs, which realizes more effective coupling with the slot for achieving bandwidth enhancement [24].

Two metal posts including cone-shaped stacked microvias are introduced on both sides of the coupling slot in Fig. 4(a) for splitting the electromagnetic (EM) power between the slots and improving the impedance matching. As shown in Fig. 5(a), the EM energy is coupled from the fork-shaped line, split into two parts by the H-slot aperture, and fed into the TE_{201} mode of the multilayer cavity. Fig. 5(b) shows that the radiation slots are excited in phase since the directions of the current flow at the two sides of each slot are identical, and in this way, the broadside radiation can be achieved.

To show the importance of the small stacked microvias provided by the “any-layer HDI PCB technology” in our design, the matching stacked microvias in the middle of the unit cell cavity were replaced by machine-drilled vias in the conventional PCB technology (i.e., with double hole and pad size compared to microvias as indicated in Section II), and the achieved results are compared in Fig. 6. The impedance bandwidth of the unit cell and the locus of S_{11} on the Smith chart are illustrated in Fig. 6(a) and (b), respectively. As can be seen from Fig. 6(b), smaller microvias (i.e., parameters of R_1 and R_2 in Fig. 4) are important to achieve a larger

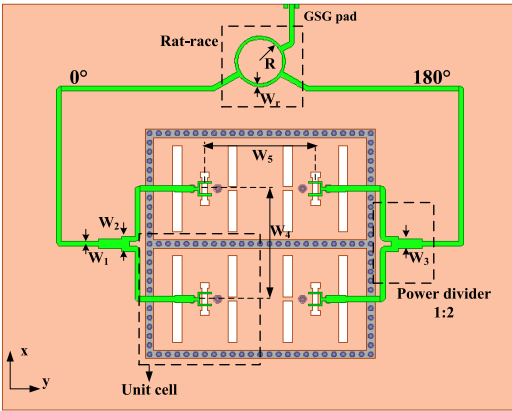


Fig. 7. Schematic of the differentially-fed slot antenna array. The dimensions are: $L_{\text{cavity}} = 3$ mm, $W_{\text{cavity}} = 3.25$ mm, $L_{S1} = L_{S2} = 1.12$ mm, $D_1 = D_2 = 0.75$ mm, $W_{SF} = 0.25$ mm, $L_{SF} = 0.9$ mm, $W_{S1} = W_{S2} = 0.2$ mm, $W_{\text{pitch}} = 0.25$ mm, $W_{\text{PAD}} = 0.23$ mm, $W_{F1} = 0.14$ mm, $W_{F2} = 0.18$ mm, $W_{F3} = 0.05$ mm, $L_{F2} = 0.575$ mm, $L_{F3} = 0.370$ mm, $L_{F4} = 0.4$ mm, $W_r = 0.08$ mm, $R = 0.61$ mm, $W_1 = 0.14$ mm, $W_2 = 0.41$ mm, $W_3 = 0.25$ mm, $W_4 = W_5 = 3$ mm, $R_1 = 0.085$ mm, and $R_2 = 0.14$ mm.

input impedance bandwidth. It can be observed that by making the microvia diameter wider and wider (i.e., close to machine drilled vias in the conventional PCB technology), the corresponding locus gets farther and farther away from the center of the Smith chart. Furthermore, as a result of the larger vias, the electromagnetic field in the cavity will be disrupted and the radiation pattern will be changed significantly in the band of operation.

Moreover, the minimum distance between the machine-drilled vias in the conventional PCB process is two times the distance between stacked microvias in “any-Layer HDI PCB technology,” which by itself makes the performance of the SIW cavity more nonideal, which can lead to worse results. However, for the proof of concept, we have just demonstrated the negative effects of applying machine-drilled vias instead of microvia matching sets in Fig. 6.

IV. DIFFERENTIALLY FED SLOT ANTENNA ARRAY

The higher-order-mode unit cell in Fig. 4 can be arranged to realize a larger array of 2×2 unit cells with higher gain and a simple feeding network (see Fig. 7). In an ideal case, the E -field in the cavity is antisymmetric about the xz plane in the unit cell and symmetric about yz plane (see Fig. 3). In practice, especially due to the nonideal antenna setup, such as the use of microvias instead of solid plane in the cavity and the placing of feedline on the top of the slot unit cell shown in Fig. 4, the E -field in the cavity is not fully symmetric, especially in wide mm-wave bands. Thus, the excited E -field and voltage in the slots are not exactly the same, which leads to far-field beam tilts within the large operating bandwidth, particularly in the yz plane. Similarly, the beam deviation will be even more severe if a higher order cavity mode (TE₄₀₁)

is excited to allow the 2×2 unit cells to be replaced by a single unit cell with a single feed. To avoid any beam tilt during frequency scanning of the slot array in Fig. 7, one side of the array is fed with an in-phase signal, whereas the opposite side of the array is fed with the same signal but shifted in phase by 180° . This differential feeding method can be easily integrated with differential devices, and it also improves the cross polarization [25]. To form the two feeding signals, two T-junction power dividers and a modified rat-race coupler are designed and connected to the fork-like stub in the first copper layer (see Fig. 7). In comparison with the other feeding methods, this method does not need a resistive load, which is actually problematic at mm-wave frequencies. A $150\text{-}\mu\text{m}$ -pitch ground-signal-ground (GSG) pad is used to feed the rat-race. With the differential feeding, the symmetric plane of the cavity in Fig. 7 acts as a ground plane. Therefore, the microvias along the xz plane could be removed without affecting the field distribution. In order to have less interference with slot radiation, a stripline feeding network may be chosen instead of the microstrip line feeding network as shown in Fig. 7. However, the thickness of the SIW cavity and consequently the bandwidth will be reduced by using stripline feeding network in the inner layers of Table I. Moreover, the stripline circuits are more lossy than those of microstrip line. For this reason, the microstrip line feeding network is proposed in Fig. 7. However, this choice does not change the generality of the concept, which is the ability of the unit cell to be extended to larger differentially-fed array structures.

V. SIMULATION AND MEASUREMENT RESULTS

One unit-cell slot antenna and one 2×2 array are designed and optimized in the E -band using the finite-element solver of Ansys HFSS 15. The operation frequency is higher than the characterization frequency in Table I. Therefore, to have more realistic results, the loss tangent of 0.01 (as derived from experience) was used in the simulations. To check for possible emission at and around the fundamental mode, the performance of the unit cell was also simulated in the range 20–60 GHz. Poor matching is found in this lower frequency range; hence, very little unwanted emission is expected. Each of the proposed antennas is etched on a multilayer advanced PCB that provides low-cost implementation for the E -band applications. The multilayer antenna prototypes are shown in Fig. 8(a) and (b). In the proposed structure, a broadband microstrip-to-waveguide transition [26] is not needed for the measurement (see Fig. 1), unlike [10]–[13]. The main part of the mm-wave antenna measurement system is shown in Fig. 8(c). The functional frequency band of the constructed antenna mm-wave on-probe measurement setup is from 30 to 90 GHz [27]. A metal table that is suspended in the center is used as a holder for the micropositioner and the probe. The on-probe antenna under test (AUT) is fixed in the center of the table. A scanning arm fabricated from a nonconducting material, such as polyvinyl chloride (PVC), is used to carry the horn antenna. The whole measurement system fits into a volume of about 1.5 m^3 .

The final antenna reflection coefficient is shown in Fig. 9. The antenna unit cell and array exhibit a relatively large 10-dB

TABLE II
COMPARISON AMONG SOME E-BAND SIW SLOT ARRAYS WITH BROADSIDE PATTERNS USING DIFFERENT TECHNOLOGIES

Ref.	f_0 (GHz)	No. of Unit cells and Feeding Method	BW (%)	GBW(%)	Gain (dBi)	TE(%)	Technology and Cost	Resolution
[3]	81.75	2×8-Open ended pentagonal array, power divider.	11.6	10	15	50	PCB, low	low
[10]	60	8×8 array, power divider.	17.1	17.1	22.1	44	LTCC, high	high
[12]	79	4×4 array, power divider.	10.7	6	11	38	Flexible PCB foil, low	high
[13]	60	12×12 array, power divider.	5	5	22	68	PCB, low	low
Proposed	73	Unit cell, direct aperture feed.	16.4	16	7.15	83	Any layer PCB, low	high
Proposed	72	2×2-unit cell array, differential aperture feed.	16	16	12	69	Any layer PCB, low	high

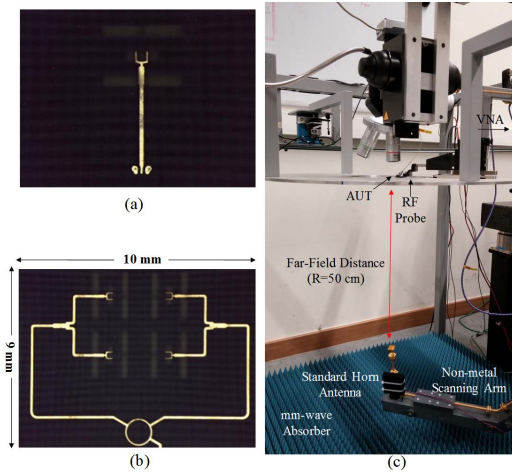


Fig. 8. (a) Bottom view of the fabricated multilayer antenna unit cell. (b) 2 × 2 array with advanced PCB technology. (c) Constructed on-probe antenna measurement system.

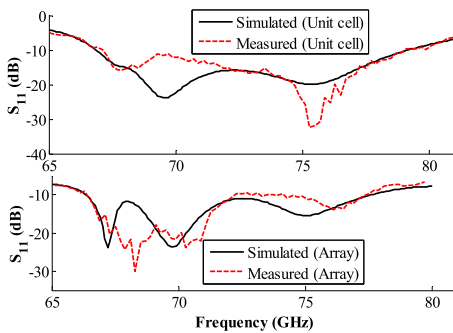


Fig. 9. Simulated and measured S_{11} of the slot antenna unit cell and 2 × 2 array.

impedance bandwidth from 67 to 79 and 66.3 to 77.7 GHz, respectively. It can be seen that reasonable agreement is achieved between measured and the simulated results and they both give the same impedance bandwidth. The difference

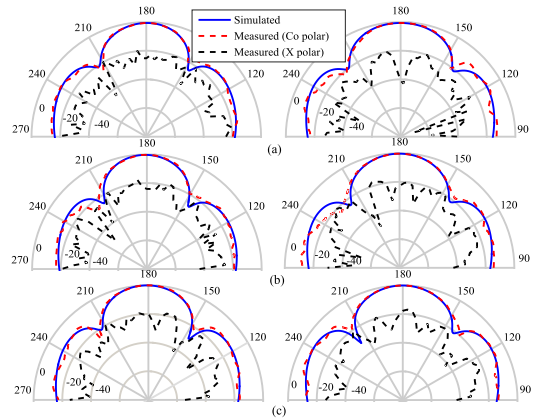


Fig. 10. Radiation patterns of the antenna array in xz (left) and yz (right) plane at (a) 68, (b) 73, and (c) 78 GHz. (Cross polarization is low in simulation.)

between them is mainly due to the tolerance of the thickness and permittivity of the materials. The radiation patterns are shown in Fig. 10 at three different frequencies within the bandwidth. As can be seen, broadside radiation is obtained in both xz and yz planes, and the patterns have narrower beam in the xz plane compared to the yz plane. The peak gain is 7.15 and 12 dBi at the center frequency, for the unit cell and array, respectively. The cross-polarization levels are below -18 dB in the yz plane and xz plane at the center frequency. It is noteworthy that this cross-polarization level and the pattern ripples are normal in the mm-wave measurements and is not different from other works in [8] and [12]. Discrepancies in the radiation patterns between the simulation and measurement may be caused by fabrication tolerance, misalignment between the AUT and the standard horn. The total efficiencies of the unit cell and the slot array are 83% and 69%, respectively. The lower efficiency of the slot array is mainly due to the feeding network loss. The total efficiency is increased to 78% when the differential feeding network is excluded and different phase shifts are applied directly from two separate feeding points. Moreover, thanks to the specific feeding scheme, the antenna’s simulated FTBR is higher than 20 dB.

It is found out that there is a tradeoff involved in choosing between the use of higher-order-cavity-mode technique with single feed and lower order mode(s) with multiple feeding lines. The tradeoff is between lower cost, higher resolution, and efficiency versus more flexibility in feed control, less beam deviation, and simpler matching.

Finally, Table II shows the comparison of the performance of some *E*-band SIW-based slot antennas in terms of feeding technique, 10-dB impedance bandwidth, 3-dB gain bandwidth (GBW), realized gain at the center frequency, total efficiency (TE), cost of technology, and resolution (i.e., fabrication accuracy). All the arrays in Table II (except [13]) offer 10% or more operating bandwidth. However, considering operating bandwidth, possibility for planar 2-D array application, cost, and efficiency, this paper gives the largest operating bandwidth in the targeted band. It is noteworthy from Table II that although the series-fed slot array antenna in [12] has a thinner substrate, it suffers from a large variation in gain (i.e., up to 11 dB) within the impedance bandwidth. Moreover, the bandwidth of a series-fed slot array antenna tends to decrease as the number of antenna elements increases [28].

VI. CONCLUSION

A 2×2 unit cell wideband differential-fed slot array is proposed in this paper for the *E*-band multi-gigabits-per-second applications. Based on the electric field properties of the higher order cavity mode, both the resonance cavity and the antenna feeding network for the unit cell can be realized efficiently, resulting in a simplified feeding network and relatively low loss in the *E*-band.

Moreover, the use of higher order mode makes the structure less sensitive to fabrication errors, desirable for the *E*-band applications. A new and low-cost fabrication method with high accuracy (i.e., "any-layer HDI PCB technology") is used for the antenna realization. The antenna can be readily combined with active circuits [e.g., monolithic microwave integrated circuits (MMICs)].




In summary, the proposed low-cost *E*-band SIW antenna array has the merits of simple feeding structure, wide bandwidth, low loss, and ease of integration with active circuits.

REFERENCES

- [1] M. Marcus and B. Pattan, "Millimeter wave propagation: Spectrum management implications," *IEEE Microw. Mag.*, vol. 6, no. 2, pp. 54–62, Jun. 2005.
- [2] *User Equipment (UE) Radio Transmission and Reception. Part 2: Range 2 Standalone (Release 15)*, document 3GPP TS 38.101-2 v1.0.0, Dec. 2017.
- [3] Z.-C. Hao, M. He, K. Fan, and G. Luo, "A planar broadband antenna for the E-band gigabyte wireless communication," *IEEE Trans. Microw. Theory Techn.*, vol. 65, no. 3, pp. 1369–1373, Mar. 2017.
- [4] D. Hou, Y. Z. Xiong, W. L. Goh, S. Hu, W. Hong, and M. Madhian, "130-GHz on-chip meander slot antennas with stacked dielectric resonators in standard CMOS technology," *IEEE Trans. Antennas Propag.*, vol. 60, no. 9, pp. 4102–4109, Sep. 2012.
- [5] N. Demirel *et al.*, "Codesign of a PA-antenna block in silicon technology for 80-GHz radar application," *IEEE Trans. Circuits Syst., II, Exp. Briefs*, vol. 60, no. 4, pp. 177–181, Apr. 2013.
- [6] Z. Tong, A. Fischer, A. Stelzer, and L. Maurer, "Radiation performance enhancement of E-band antenna in package," *IEEE Trans. Compon., Packag., Manuf. Technol.*, vol. 3, no. 11, pp. 1953–1959, Nov. 2013.
- [7] J. Xu, Z. N. Chen, X. Qing, and W. Hong, "140-GHz TE₂₀-mode dielectric-loaded SIW slot antenna array in LTCC," *IEEE Trans. Antennas Propag.*, vol. 61, no. 4, pp. 1784–1793, Apr. 2013.
- [8] Y. Zhang, S. Shi, R. D. Martin, and D. W. Prather, "High-gain linearly tapered antipodal slot antenna on LCP substrate at E- and W-bands," *IEEE Antennas Wireless Propag. Lett.*, vol. 15, pp. 1357–1360, 2016.
- [9] N. Ghassemi and K. Wu, "High-efficient patch antenna array for E-band gigabyte point-to-point wireless services," *IEEE Antennas Wireless Propag. Lett.*, vol. 11, pp. 1261–1264, 2012.
- [10] J. F. Xu, Z. N. Chen, X. M. Qing, and W. Hong, "Bandwidth enhancement for a 60 GHz substrate integrated waveguide fed cavity array antenna on LTCC," *IEEE Trans. Antennas Propag.*, vol. 59, no. 3, pp. 826–832, Mar. 2011.
- [11] K. Gong, Z. N. Chen, X. Qing, P. Chen, and W. Hang, "Substrate integrated waveguide cavity-backed wide slot antenna for 60-GHz bands," *IEEE Trans. Antennas Propag.*, vol. 60, no. 12, pp. 6023–6026, Dec. 2012.
- [12] S. Cheng, H. Yousef, and H. Kratz, "79 GHz slot antennas based on substrate integrated waveguides (SIW) in a flexible printed circuit board," *IEEE Trans. Antennas Propag.*, vol. 57, no. 1, pp. 64–71, Jan. 2009.
- [13] X. P. Chen, K. Wu, L. Han, and F. He, "Low-cost high gain planar antenna array for 60-GHz band applications," *IEEE Trans. Antennas Propag.*, vol. 58, no. 6, pp. 2126–2129, Jun. 2010.
- [14] Y. Miura, J. Hirokawa, M. Ando, Y. Shibuyam, and G. Yoshida, "Double-layer full-corporate-feed hollow-waveguide slot array antenna in the 60-GHz band," *IEEE Trans. Antennas Propag.*, vol. 59, no. 8, pp. 2844–2851, Aug. 2011.
- [15] J. Xu, Z. Chen, X. Qing, and W. Hong, "A single-layer SIW slot array antenna with TE₂₀ mode," in *Proc. Asia-Pacific Microw. Conf.*, Melbourne, VIC, Australia, Dec. 2011, pp. 1330–1333.
- [16] W. Han, F. Yang, and P. Yang, "Slotted substrate integrated cavity antenna using TE₃₃₀ mode with low profile and high gain," *Electron. Lett.*, vol. 50, no. 7, pp. 488–490, 2014.
- [17] W. Han, F. Yang, J. Ouyang, and P. Yang, "Low-cost wideband and high-gain slotted cavity antenna using high-order modes for millimeter-wave application," *IEEE Trans. Antennas Propag.*, vol. 63, no. 11, pp. 4624–4631, Nov. 2015.
- [18] *Panasonic Megtron 6 Substrates*. Accessed: 2014. [Online]. Available: <http://www.matrixellectronics.com/products/Panasonic/megtron-6>
- [19] *Any-Layer HDI PCB Technology*. Accessed: 2014. [Online]. Available: <https://ats.net/products-technology/product-portfolio/hdi-any-layer-pcbs/>
- [20] *Multilayer PCB Technology*. Accessed: 2014. [Online]. Available: <https://ats.net/products-technology/product-portfolio/hdi-microvia-pcbs/>
- [21] *Aspo Company Website*. Accessed: 2014. [Online]. Available: <https://www.aspocomp.com/>
- [22] N. Marcuvitz, *Waveguide Handbook*. New York, NY, USA: Peregrinus, 1985.
- [23] H.-T. Hu, F.-C. Chen, and Q.-X. Chu, "A compact directional slot antenna and its application in MIMO array," *IEEE Trans. Antennas Propag.*, vol. 64, no. 12, pp. 5513–5517, Dec. 2016.
- [24] C. Zhang, J. Zhang, and L. Li, "Triple band-notched UWB antenna based on SIR-DGS and fork-shaped stubs," *Electron. Lett.*, vol. 50, no. 2, pp. 67–69, Jan. 2014.
- [25] H. Jin, K.-S. Chin, W. Che, C.-C. Chang, H.-J. Li, and Q. Xue, "Differential-fed patch antenna arrays with low cross polarization and wide bandwidths," *IEEE Antennas Wireless Propag. Lett.*, vol. 13, pp. 1069–1072, 2014.
- [26] N. Ghassemi, I. Boudreau, D. Deslandes, and K. Wu, "Millimeter-wave broadband transition of substrate integrated waveguide on high-to-low dielectric constant substrates," *IEEE Trans. Compon., Packag., Manuf. Technol.*, vol. 3, no. 10, pp. 1764–1770, Oct. 2013.
- [27] M. Mosalanejad, S. Brebels, I. Ocket, V. Volski, C. Soens, and G. A. E. Vandebosch, "A complete measurement system for integrated antennas at millimeter wavelengths," in *Proc. 9th Eur. Conf. Antennas Propag. (EuCAP)*, Lisbon, Portugal, Apr. 2015, pp. 1–5.
- [28] J. F. Xu, W. Hong, P. Chen, and K. Wu, "Design and implementation of low sidelobe substrate integrated waveguide longitudinal slot array antennas," *Microw., Antennas Propag.*, vol. 3, no. 5, pp. 790–797, Jul. 2009.

Paper VI

79 GHz Multilayer Series-Fed Patch Antenna Array With Stacked Micro-Via Loading

Hanieh Aliakbari , *Graduate Student Member, IEEE*, Mohammad Mosalanejad, Charlotte Soens, Guy A. E. Vandenbosch , *Fellow, IEEE*, and Buon Kiong Lau , *Fellow, IEEE*

Abstract—A wideband compact series-fed patch subarray is proposed for 79 GHz multiple-input—multiple-output (MIMO) radar. The proposed subarray is, for the first time, loaded with stacked microvias (SMVs). Two sets of patches in the subarray are fed 180° out-of-phase. A low-cost, high-resolution multilayer printed circuit board (PCB) technology, called “any-layer PCB,” is used to implement the SMVs, which cannot be done by standard high-definition interconnect PCB technology. Moreover, the technology supports small SMVs on different layers; hence, thick machine-drilled vias can be avoided. For comparison, a series-fed patch subarray with no SMV loading is designed. It is shown that SMV loading facilitates a larger overlap of the impedance and gain bandwidths, leading to a larger operating bandwidth. The measured 10 dB impedance and 3 dB gain bandwidths are 15% and 9.6%, respectively. The sidelobe suppression is above 12.9 dB, and the maximum array gain is 12.67 dBi at 79.1 GHz. This subarray is suitable for MIMO radar, as its width is around half-wavelength and the SMVs around it mitigate the crosstalk between the transmitting and receiving arrays.

Index Terms—79 GHz, advanced multilayer printed circuit board (PCB), impedance bandwidth, series-fed patch array, stacked microvias (SMVs) loading.

I. INTRODUCTION

TO ACHIEVE high resolution for radar sensors, the use of millimeter-wave (mm-wave) spectrum is essential [1]. Specifically, 77–81 GHz has been allocated for short/medium-range multiple-input—multiple-output (MIMO) automotive radar sensors, which are installed in cars to enable emergency braking, collision warning, blind-spot detection, and precrash vehicle preparation systems.

For radar designers, antenna arrays with compact structure, high efficiency, low sidelobe level (SLL), and ease of integration are very attractive [2]. Moreover, flat gain (e.g., by having a wider-than-specified impedance band) is desirable for automotive radar signal processing, as it gives designers more control over the transmit and receive filter design; alternatively, it offers

higher range resolution [3], [4]. Wider bandwidth also increases the robustness of the prototype in covering the specified band amidst fabrication tolerances.

Different array topologies have been proposed for mm-wave automotive radar [5]–[14]. However, very few structures offer the above desired performance while also fulfill practical requirements, such as low cost and mass reproducibility. For example, the hybrid thin film design in [5] has efficiency below 40% due to losses in the feeding network. In addition, it has high SLL levels in the E -plane and a limited beamwidth (i.e., 40°) in the H -plane, which is not suitable for automotive radars. The array-fed lens in [6] has narrow bandwidth (~5%). Low-temperature cofired ceramic (LTCC) technology is used in [7] and [8], but it is costly and unsuitable for mass production. Furthermore, the radiation efficiency of the array design in [7] is lower than 30% due to the loss associated with the LTCC substrate materials. In [8], the patch array design uses WR12-to-laminated-waveguide transition in the feeding network, which is not compact and not attractive for automotive radars.

Microstrip patch antenna is suitable for array design in mm-wave automotive radar, as it is structurally simple, light weight, easy to fabricate at a low cost using printed circuit board (PCB) technology, and can be integrated in low-profile frontends [8]–[14]. In [9], parallel-fed patch array is designed using a standard PCB fabrication process. However, above 30 GHz, the losses in the feeding network of the parallel-fed patch arrays increase significantly, resulting in relatively low overall efficiencies (around 20%) [9]. Despite the broadband behavior of parallel-fed patch structures, series-fed structures are often used in patch array antennas for radar systems. This is because the lower complexity and loss of the feeding circuit are favorable for antenna gain enhancement in the E -band. However, the impedance bandwidths of series-fed patch arrays are limited [10]–[18]. The patch array bandwidth can be improved either by modifying the patch element size [19] or shape [20]. This leads to improved bandwidth but also degraded radiation performance across the band due to added higher order modes. On the other hand, the radiation characteristics can be preserved by using only the fundamental array mode across the bandwidth and the impedance bandwidth can be improved by loading the entire array [21], or patches in parallel-fed array [22], at lower bands.

The focus of this letter is to enhance the operating bandwidth of the fundamental mode of a series-fed patch array using vertical loading. For the first time, stacked microvias (SMVs) are loaded on the nonradiating edges of the patches to increase the array impedance bandwidth while preserving the array radiation characteristics. This design is visioned for 79 GHz automotive MIMO radar; however, the proposed bandwidth enhancement concept can be used for a general series-fed

Manuscript received 2 June 2022; accepted 19 June 2022. Date of publication 1 July 2022; date of current version 6 October 2022. This work was supported in part by Vetenskapsrådet under Grant 2018-04717. (Corresponding author: Buon Kiong Lau.)

Hanieh Aliakbari and Buon Kiong Lau are with the Department of Electrical and Information Technology, Lund University, 221 00 Lund, Sweden (e-mail: hea.4080@yahoo.com; bkiau@ieee.org).

Mohammad Mosalanejad and Charlotte Soens are with the Inter-University Microelectronics Center, B-3001 Leuven, Belgium (e-mail: mohammad.mosalanejad@esat.kuleuven.be; charlotte.soens@imec.be).

Guy A. E. Vandenbosch is with the Department of Electrical Engineering, KU Leuven, B-3001 Leuven, Belgium (e-mail: guy.vandenbosch@kuleuven.be).

Digital Object Identifier 10.1109/LAWP.2022.3187764

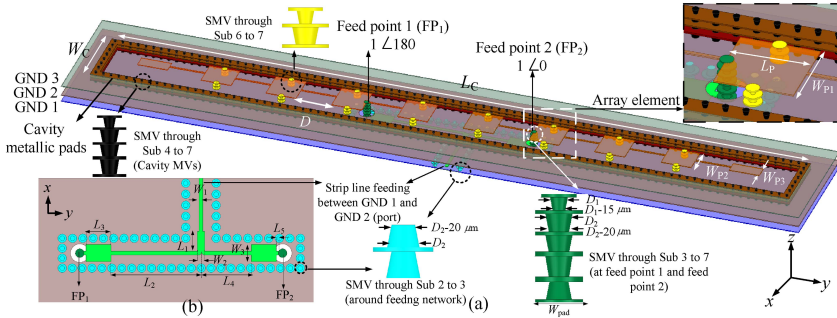


Fig. 1. (a) Three-dimensional view of series-fed patch antenna array and single patch element with four types of SMVs, and (b) feeding network at the bottom layer (GND 1 and Sub 1) is not shown for clarity. The corresponding layers are listed in Table I. Dimensions (mm): $L_C = 22.5$, $W_C = 2.15$, $D = 1.16$, $W_{P1} = 1$, $W_{P2} = 0.85$, $W_{P3} = 0.4$, $L_P = 0.98$, $D_1 = 0.085$, $D_2 = 0.13$, $W_{pad} = 0.23$, $W_1 = 0.1$, $L_1 = 0.53$, $W_2 = 0.19$, $L_2 = 2.42$, $W_3 = 0.45$, $L_3 = 0.67$, $L_4 = 0.335$, and $L_5 = 0.17$.

patch array in other applications/frequency bands. A prototype array, intended for integration as a subarray, has been fabricated with a low-cost “any-layer PCB” technology, which is suitable for mass production [4], [23]. As opposed to standard multi-layer PCB technologies, the “any-layer PCB” technology can implement SMVs between layers.

II. ANTENNA ARRAY DESIGN

A. Single-Element Patch With SMVs

To design the series-fed patch antenna array on a multilayer PCB, the first step is to design the array element. The enlarged version of an array element is shown in Fig. 1(a). The element is composed of a radiating rectangular patch, loaded by two SMVs (in yellow) on its nonradiating edges. It is noted that the SMVs in the design are small pieces of a metal (copper fillings) that can be used to connect a specific layer to every other layer, enabling very low metallic loss that can be neglected in normal circumstances. The electrical model of a single SMV can be broken into three sections: the upper pad, cone, and lower pad. Generally, similar to machine-drilled vias, each section consists of both capacitance and inductance. At higher frequencies, the equivalent circuit of each section will become more distinct, i.e., the pads will mainly contribute to the capacitance (i.e., capacitor between the pads and GND, and capacitor between pads), whereas the cone will contribute to the inductance. Thus, a single SMV can be approximated by a lumped equivalent circuit consisting of a series inductor and two parallel capacitors connected to the ground. The radiating patch is resonant, corresponding to the length (L_P) of $\lambda_g/2$ at 79 GHz (λ_g is the guided wavelength). The generic PCB used in this section has the same multilayer substrate properties, as given in Table I. The specific technology needed to realize the design involving the desired SMVs will be discussed in Section II-B.

Characteristic-mode analysis (CMA) [24] of the array element is performed using 2019 Altair FEKO to explore the modal significance (MS) of the single patch’s broadside fundamental mode (TM_{01}) around the resonant frequency. As Fig. 2(a) shows, the addition of the two SMVs in three layers has very little impact on the MS of the fundamental mode (>0.7), as is the case for the characteristic currents and fields. However, the above-mentioned SMVs’ equivalent circuit has a capacitance and inductance loading effect that can help to match the input

TABLE I
ANY-LAYER HDI PCB BUILD-UP

Material	Dielectric constant	Tangent delta	Thickness (um)
Copper layer 8 (patch array, cavity pad)			16
Sub7: Prepreg	3.26	0.01	68
Copper layer 7 (GND 3, cavity pad)			16
Sub6: Prepreg	3.22	0.01	104
Copper layer 6 (Signal, cavity pad)			16
Sub5: Prepreg	3.22	0.01	104
Copper layer 5 (Signal, cavity pad)			16
Sub4: Laminate core	3.37	0.01	100
Copper layer 4 (GND 2-two feeding holes)			23
Sub3: Prepreg	3.22	0.01	104
Copper layer 3 (Feeding network)			16
Sub2: Prepreg	3.22	0.01	104
Copper layer 2 (GND 1)			16
Sub1: Prepreg	3.25	0.01	68
Copper layer 1 (Signal)			23

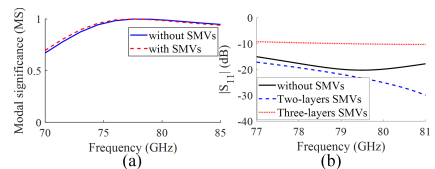


Fig. 2. (a) MS of the single patch fundamental mode. (b) Impact of SMV loading in different layers on the reflection coefficient of a single patch.

impedance of the single element over a larger frequency band and increase the single series patch element’s impedance bandwidth substantially, as shown in Fig. 2(b). The exact change of the input impedance depends on the number of layers used by the SMVs [see Fig. 2(b)], which changes the equivalent capacitance and inductance of the SMVs’ equivalent circuit. Consequently, the number of layers used by the SMVs should be optimized for the largest impedance bandwidth of the fundamental mode. For example, Fig. 2(b) shows that, by adding two-layer SMVs, better matching and, hence, a larger impedance bandwidth is achievable. However, by using three-layer SMVs, the matching condition is degraded, indicating a smaller bandwidth. It is noted that the single patch simulation model in Fig. 1(a) is designed with two strip lines connected to its radiating edges to prepare for the later array configuration. These lines are deembedded from the $|S_{11}|$ in Fig. 2(b). The next step is to choose a technology to implement SMVs in the array, which is suitable for the E-band.

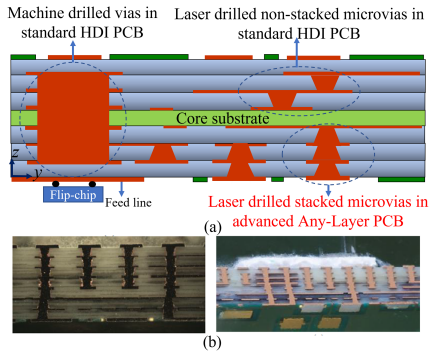


Fig. 3. (a) Different implementation of vias. (b) SMVs implemented in “any-layer PCB” technology (cross-sectional views).

B. SMV Implementation Challenge

The via process was not mature before 2000. Specifically, stacked vias were extremely challenging for fabrication or even impossible to fabricate and would increase drastically the final cost of the antenna while spoiling its reliability [25].

Furthermore, as a result of physically small wavelengths, fabrication tolerances are severe in the mm-wave band, especially at higher frequencies. Thus, accurate and cost-efficient fabrication processes are needed in this band to embed mass-producible antennas in multilayer substrates. To realize the antenna and SMVs in this letter, a new PCB technology, called “advanced any-layer PCB,” is used [4], [23]. The fundamental technical advancement of the “any-layer PCB” over standard high-definition interconnect (HDI) PCB technology [26] is that stacking micro-vias is possible. This facilitates the possible connection of a specific layer to every other layer within the PCB build-up (see Fig. 3). Thus, the huge restriction that the laser-drilled micro-vias used in the HDI PCB design process cannot be stacked is removed. Moreover, conventionally drilled, blind, or through-hole vias created by machine drilling (see Fig. 3) deliver minimum hole and pad sizes of 200 μm and 400 μm , respectively. These dimensions are not suitable for high resolution and higher routing density in PCBs designed for the E-band. For laser-drilled micro-vias in “any-layer PCB” technology, these values are smaller (i.e., 75 and 175 μm), enabling higher routing density and more compact final PCBs.

LTCC technology can also realize small stacked vias in mm-wave, but the cost is higher than the standard multilayer PCB fabrication. Higher dielectric constant of LTCC materials and higher cost for mass production with respect to any-layer PCB make LTCC technology less attractive [27]. It is noted that the “any-layer PCB” technology has been used before, e.g., [4] and [23]. However, this was the first time to use this benefit of the “any-layer PCB” in the design process.

C. Series-Fed Patch Array With SMVs in “Any-Layer PCB”

The proposed SMV-loaded series-fed array of microstrip patches are illustrated in Fig. 1(a). It consists of two sets of patches, each with five SMVs loaded patch elements, as described in Section II-A. The two sets of five resonant patches are fed by two SMVs and two transmission lines that provide

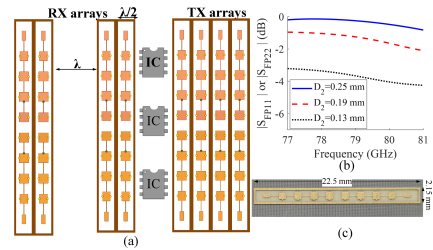


Fig. 4. (a) 4×4 MIMO medium-range automotive radar module. (b) Impact of wider loading SMVs on the reflection coefficient of an array before adding the matching network and splitter in Fig. 1(b) (i.e., $|S_{FP11}|$ or $|S_{FP22}|$). (c) Fabricated prototype in advanced any-layer PCB technology.

180° phase difference of the input signal, which are equally split (using a power splitter made from strip lines and matching quarter wave lines) from a single transmission line [see Fig. 1(b)]. The length of the interconnecting lines between the patches must be $\lambda_g/2$. The widths of the two patches at each outer end of the array are optimized to achieve the desired radiation conductance and to retain bandwidth [28]. Four types of SMVs [shown in four different colors in Fig. 1(a)] are used in the array to connect different layers. The dimension and the direction (i.e., larger diameter at the top or bottom) of each cone-shaped micro-via within a given SMV depend on the layer in which it is placed, as depicted for the green SMV in Fig. 1(a). Metallic pads [see Fig. 1(a)] are used to improve the electrical contact of the micro-vias stacked on different layers. The loading SMVs connect layers 8–6 within the PCB build-up in Table I. The two feeding SMVs connect the patches in layer 8 to the two endpoints of the power splitter embedded in layer 3.

Since three ground planes (GND 1, 2, and 3) are used in the build-up in Table I, there is a potential for the excitation of parallel-plate modes and surface waves. Thus, the antenna array is surrounded by a metallic cavity, implemented by SMVs connecting layer 8–4. The SMVs that are around the strip lines of the power splitter connect layer 2–4. The metallic walls significantly suppress the crosstalk between the transmitting and receiving arrays upon integration into a MIMO module and they do not change the array radiation pattern. In addition, the cavity width is very close to $\lambda_0/2$ at 79 GHz, which suppresses sidelobes in the MIMO array. To our knowledge, no existing design (e.g., [5]–[11]) fulfills these MIMO radar requirements. Fig. 4(a) shows an example of a MIMO radar module, which realizes the virtual array concept in the receiving end.

Similar to Section II-A, CMA is performed for the array with and without the SMV loading in Fig. 1(a), before adding the matching section in Fig. 1(b). Again, the MS curves in Fig. 5(a) show that the bandwidth of the array fundamental mode is not affected. However, as before, SMVs enable less impedance change over the frequency band, which corresponds to a larger intrinsic impedance bandwidth [see Fig. 5(b)].

Finally, the reflection coefficient of the array for different SMV sizes [D_2 in Fig. 1(a)] is plotted for the same band in Fig. 4(b). D_1 is set to $D_1 = D_2 - 0.045$ mm. Fig. 4(b) shows that, by making the SMV diameter wider, the intrinsic impedance bandwidth degrades, which complicates matching and reduces achievable impedance bandwidth.

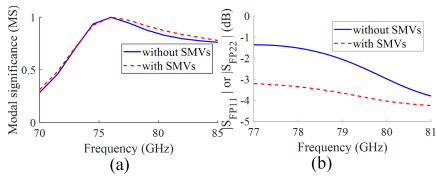


Fig. 5. (a) MS of the fundamental mode of an array. (b) Impact of SMVs on the reflection coefficient of an array before adding matching network and splitter in Fig. 1(b)(i.e., S_{FP11} or S_{FP22}).

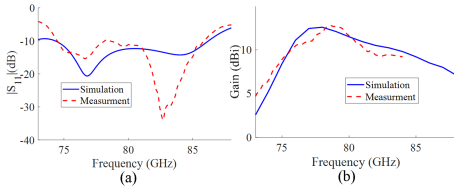


Fig. 6. Simulated and measured array (a) $|S_{11}|$ and (b) gain versus frequency.

By increasing the SMV size, the total equivalent capacitance of the SMVs will increase. This is because the surface area of the via is increasing and the capacitance is proportional to the surface area. Thus, the reactance part of the input impedance will increase, which makes the input impedance harder to match. It is noted that the area of the pad in machine-drilled vias is about four times the pad areas in SMVs. This highlights the matching benefit of the SMVs provided by the “any-layer PCB” technology, which cannot be realized with machine-drilled vias. Fig. 4(c) shows the fabricated prototype of the series-fed patch with SMVs using the “any-layer PCB” technology.

III. MEASUREMENT

The simulated and measured results of reflection coefficient magnitude ($|S_{11}|$) and gain of the array in Fig. 4(c) are shown in Fig. 6. The measured $|S_{11}|$ is lower than -10 dB for 74.50–85.81 GHz (15%). The measured maximum gain is 12.67 dB at 79.1 GHz and the 3 dB gain bandwidth is 75.4–83 GHz. Furthermore, the maximum gain drop is less than 0.8 dB within 77–81 GHz. This flat-gain behavior with matched condition is attractive for radar designers [1]. The discrepancies between the simulated and measured results are mainly due to the fabrication tolerances in the geometrical and material parameters in this technology. These tolerances are unavoidable, especially in multilayer PCB and at high frequencies [15]. The simulated total radiation efficiency of the full array, including the feeding losses, is 63%.

The setup in [23] was used to measure the radiation pattern. In Fig. 7, the simulated and measured patterns are shown at 76, 79, and 83 GHz. The simulated and measured SLLs are under -16.4 dB and -12.9 dB, respectively, for all frequencies. Considering the reflection loss, 3 dB gain bandwidth, and SLL, this antenna can be used for 75.4–83 GHz (9.6% bandwidth).

The measured 3 dB beamwidths in azimuth and elevation are 72° and 12° , respectively, which satisfy the requirements for automotive radars [1]. Finally, a comparison of the proposed design with other mm-wave series-fed patch arrays is given in Table II. The proposed design offers a notably larger impedance bandwidth and very stable gain within the band. As expected, the array gain is proportionally higher for larger arrays.

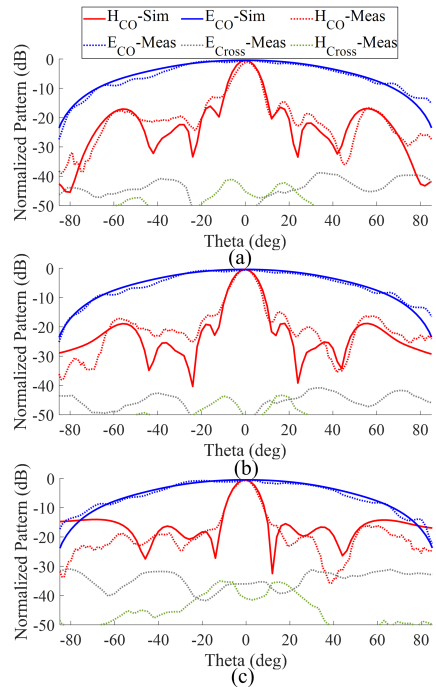


Fig. 7. Simulated (Sim) and measured (Meas) radiation patterns at (a) 76, (b) 79, and (c) 83 GHz.

TABLE II
COMPARISON OF SOME RECENT MM-WAVE SERIES-FED PATCH ARRAYS

Ref.	Frequency (BW)	Gain	Gain variation	Efficiency	Array architecture
[14]	77 GHz (6%)	20 dBi	>2 dB	66%	6×10 (1×10 series fed subarrays)
[10]	79 GHz (5%)	22 dBi	2.5 dB	NA	8×6 (1×6 series fed subarrays)
[18]	24 GHz (3%)	18 dBi	NA	NA	8×8 (1×8 series fed subarrays)
[13]	77 GHz (4%)	15 dBi	>1.5 dB	NA	1×16 series fed subarray
This Work	79 GHz (9.6%)	12.67 dBi	0.8 dB	63%	1×10 series fed subarray

IV. CONCLUSION

A novel compact patch antenna array loaded with SMVs has been presented. The SMV loading enables an array topology with wide combined impedance–gain bandwidth. The proposed array has been realized by the low-cost high resolution “any-layer PCB” technology. This technology has a unique feature that allows the designer to distribute stacked and staggered vias. The small size SMVs compared with the machine-drilled vias facilitate a more compact antenna by enabling the implementation of a compact structure using vertical configuration. The proposed series-fed patch array topology is a good candidate for 79 GHz MIMO automotive radar due to the low cost, compact size, ability to suppress surface waves, as well as relatively wide impedance and flat-gain bandwidths.

REFERENCES

- [1] J. Hasch, E. Topak, R. Schnabel, T. Zwick, R. Weigel, and C. Waldschmidt, "Millimeter-wave technology for automotive radar sensors in the 77 GHz frequency band," *IEEE Trans. Microw. Theory Techn.*, vol. 60, no. 3, pp. 845–860, Mar. 2012.
- [2] S. Yoo, Y. Milyakh, H. Kim, C. Hong, and H. Choo, "Patch array antenna using a dual coupled feeding structure for 79 GHz automotive radar applications," *IEEE Antennas Wireless Propag. Lett.*, vol. 19, no. 4, pp. 676–679, Apr. 2020.
- [3] F. Bauer and W. Menzel, "A 79-GHz planar antenna array using ceramic-filled cavity resonators in LTCC," *IEEE Antennas Wireless Propag. Lett.*, vol. 12, pp. 910–913, 2013.
- [4] M. Mosalanejad, I. Ocket, C. Soens, and G. A. E. Vandenbosch, "Multilayer compact grid antenna array for 79 GHz automotive radar applications," *IEEE Antennas Wireless Propag. Lett.*, vol. 17, no. 9, pp. 1677–1681, Sep. 2018.
- [5] O. Khan, J. Meyer, K. Baur, and C. Waldschmidt, "Hybrid thin film antenna for automotive radar at 79 GHz," *IEEE Trans. Antennas Propag.*, vol. 65, no. 10, pp. 5076–5085, Oct. 2017.
- [6] P. Hallbjörner, Z. He, S. Bruce, and S. Cheng, "Low-profile 77-GHz lens antenna with array feeder," *IEEE Antennas Wireless Propag. Lett.*, vol. 11, pp. 205–207, 2012.
- [7] F. Bauer and W. Menzel, "A 79-GHz resonant laminated waveguide slotted array antenna using novel shaped slots in LTCC," *IEEE Antennas Wireless Propag. Lett.*, vol. 12, pp. 296–299, 2013.
- [8] X. Wang and A. Stelzer, "A 79-GHz LTCC patch array antenna using a laminated waveguide-based vertical parallel feed," *IEEE Antennas Wireless Propag. Lett.*, vol. 12, pp. 987–990, 2013.
- [9] Y. J. Cheng, Y. X. Gui, and Z. G. Liu, "W-band large-scale high-gain planar integrated antenna array," *IEEE Trans. Antennas Propag.*, vol. 62, no. 6, pp. 3370–3373, Jun. 2014.
- [10] Y. Liu, G. Bai, and M. C. E. Yagoub, "A 79GHz series fed microstrip patch antenna array with bandwidth enhancement and sidelobe suppression," in *Proc. Int. Conf. Radar, Antenna, Microw., Electron., Telecommun.*, Tangerang, Indonesia, 2020, pp. 155–158.
- [11] I. Aziz, W.-C. Liao, H. Aliakbari, and W. Simon, "Compact and low cost linear antenna array for millimeter wave automotive radar applications," in *Proc. 14th Eur. Conf. Antennas Propag.*, Copenhagen, Denmark, 2020, pp. 1–4.
- [12] J. R. James and P. S. Hall, *Handbook of Microstrip Antennas (IEE Electromagnetic Waves Series)*. London, U.K.: Peregrinus, vol. 2, 1989.
- [13] J. Yan, H. Wang, J. Yin, C. Yu, and W. Hong, "Planar series-fed antenna array for 77 GHz automotive radar," in *Proc. 6th Asia-Pacific Conf. Antennas Propag.*, Xi'an, China, 2017, pp. 1–3.
- [14] J. Xu, W. Hong, H. Zhang, G. Wang, Y. Yu, and Z. H. Jiang, "An array antenna for both long- and medium-range 77 GHz automotive radar applications," *IEEE Trans. Antennas Propag.*, vol. 65, no. 12, pp. 7207–7216, Dec. 2017.
- [15] T. Yuan, N. Yuan, and L.-W. Li, "A novel series-fed taper antenna array design," *IEEE Trans. Antennas Propag.*, vol. 7, pp. 362–365, 2008.
- [16] N. Ojaroudiparchin, M. Shen, S. Zhang, and G. F. Pedersen, "A switchable 3-D-coverage-phased array antenna package for 5G mobile terminals," *IEEE Antennas Wireless Propag. Lett.*, vol. 15, pp. 1747–1750, 2016.
- [17] V. Semkin et al., "Beam switching conformal antenna array for mm-wave communications," *IEEE Antennas Wireless Propag. Lett.*, vol. 15, pp. 28–31, 2016.
- [18] K. Wincza and S. Gruszczynski, "Microstrip antenna arrays fed by a series-parallel slot-coupled feeding network," *IEEE Antennas Wireless Propag. Lett.*, vol. 10, pp. 991–994, 2011.
- [19] Y. Luo, Z. N. Chen, and K. Ma, "A single-layer dual-polarized differentially fed patch antenna with enhanced gain and bandwidth operating at dual compressed high-order modes using characteristic mode analysis," *IEEE Trans. Antennas Propag.*, vol. 68, no. 5, pp. 4082–4087, May 2020.
- [20] J.-Y. Sze and K.-L. Wong, "Slotted rectangular microstrip antenna for bandwidth enhancement," *IEEE Trans. Antennas Propag.*, vol. 48, no. 8, pp. 1149–1152, Aug. 2000.
- [21] P. C. Strickland, "Series-fed microstrip patch arrays with periodic loading," *IEEE Trans. Antennas Propag.*, vol. 43, no. 12, pp. 1472–1474, Dec. 1995.
- [22] L. Han and K. Wu, "24-GHz bandwidth-enhanced microstrip array printed on a single-layer electrically-thin substrate for automotive applications," *IEEE Trans. Antennas Propag.*, vol. 60, no. 5, pp. 2555–2558, May 2012.
- [23] H. Aliakbari, M. Mosalanejad, C. Soens, G. A. E. Vandenbosch, and B. K. Lau, "Wideband SIW-based low-cost multilayer slot antenna array for E-band applications," *IEEE Trans. Compon., Packag., Manuf. Technol.*, vol. 9, no. 8, pp. 1568–1575, Aug. 2019.
- [24] R. Harrington and J. Mautz, "Theory of characteristic modes for conducting bodies," *IEEE Trans. Antennas Propag.*, vol. 19, no. 5, pp. 622–628, Sep. 1971.
- [25] T. Potelon, M. Ertorre, L. L. Coq, T. Bateman, J. Francey, and R. Sauleau, "Reconfigurable CTS antenna fully integrated in PCB technology for 5G backhaul applications," *IEEE Trans. Antennas Propag.*, vol. 67, no. 6, pp. 3609–3618, Jun. 2019.
- [26] AT&S, "HDI microvia PCBs," 2022. [Online]. Available: <https://ats.net/products-technology/product-portfolio/hdi-microvia-pcb/>
- [27] F. F. Manzano et al., "A multilayer LTCC solution for integrating 5G access point antenna modules," *IEEE Trans. Microw. Theory Techn.*, vol. 64, no. 7, pp. 2272–2283, Jul. 2016.
- [28] S. Sengupta, D. R. Jackson, and S. A. Long, "A method for analyzing a linear series-fed rectangular microstrip antenna array," *IEEE Trans. Antennas Propag.*, vol. 63, no. 8, pp. 3731–3736, Aug. 2015.

